Fault Tolerant Control of a Hydraulic Servo-System

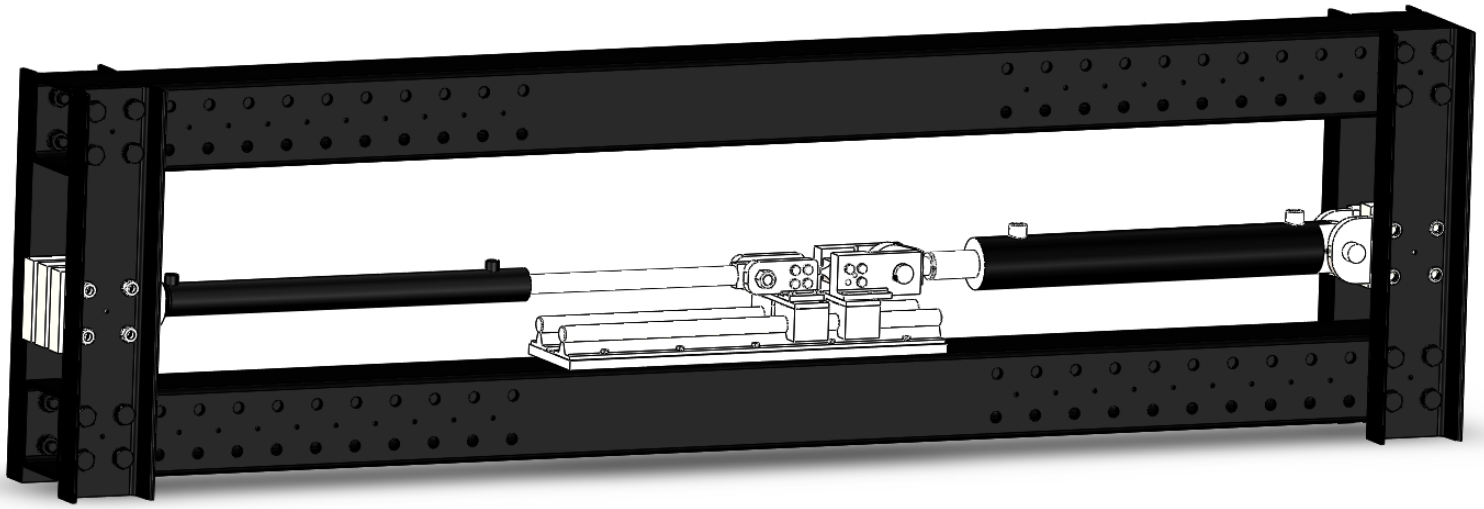

Viktor Donkov & Kasper Ahlbeck
MCE4-1022
School of Engineering and Science, Mechatronic Control Engineering
Department of Energy Technology Aalborg University
Denmark, Aalborg - June 2016

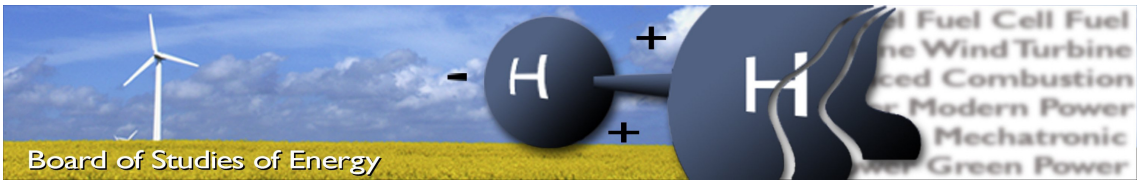

Title:	Fault Tolerant Control of a Hydraulic Servo-System
Semester:	Master Thesis
Project period:	02.02.16 to 01.06.16
ECTS:	30 ECTS
Supervisors:	Henrik C. Pedersen
Project group:	MCE4-1022

SYNOPSIS:

This project analyses the possibility of Fault Tolerant Control(FTC) for a hydraulic servo-system. Based on an analysis of the state of the art in the field, an Indirect Adaptive Robust Controller (IARC) is selected for implementation and testing. The IARC is designed to be tolerant to faults by being able to handle system parameter changes. The system parameters are estimated on-line by a Least-Square Algorithm and the information is used by the controller. The varying parameters are: Mass, Viscous friction, Coulomb friction and Bulk modulus. Furthermore the controller is able to accommodate internal and external leakages. The IARC has been implemented on a test bench provided by AAU. The set-up consists of two cylinders pushing against each other. The estimation algorithm and the IARC have been implemented on a Real-Time computer. The simulation tests showed good performance and fault tolerance of the IARC. Due to problems regarding sensors, it was not possible to replicate the simulation tests experimentally in a satisfactory manner.

Viktor Donkov

Kasper Ahlbeck

Copies:	2+1
Pages, total:	137 (-15 blanks)
Supplements:	87 pages + Upload files

By signing this document, each member of the group confirms that all group members have participated in the project work, and thereby all members are collectively liable for the contents of the report. Furthermore, all group members confirm that the report does not include plagiarism.

PREFACE

This thesis, "Fault Tolerant Control of a Hydraulic Servo-System", is written by student group MCE4-1022 at Aalborg University, Department of Energy Technology, during the spring semester of 2016.

Differentiation with respect to time is denoted with a dot, e.g. velocity is given by $\dot{x}$. Vectors are denoted with bold italic and are named with small letters, e.g. $\boldsymbol{x}_{ex}$. An exception is made for force and moment, where these instead begin with a capital letter. Matrices are only denoted with bold and capital letter e.g. $\mathbf{A}$.

Sections, figures, equations and tables are referenced by chapter# .index# , e.g. section 5.2, figure 5.2, equation (5.2) and table 5.2.

The material used for this appendix report, has been acquired through research of articles, reports, web-pages, books and feedback from the supervisor.

All sources can be found in the bibliography all sorted in alphabetical order by author. References for these sources use Harvard-style notation so all references are marked with company name or last name of the author as well as year of publication.

The software used for modelling and graphical data presentation are MATLAB®R2015a and Simulink®. Attached files; MATLAB scripts, the Simulink models, LabView project, and a PDF version of the report can be found for those of interest.

SUMMARY

The main topic for this project is an investigation of fault tolerant control of a hydraulic servo-system. The main reason for the investigation is the recently increase in interest of fault tolerant control for wind-turbines. This report will focus on the hydraulic cylinder of the pitch system. First, an investigation of the most common faults in a hydraulic servo-system is reviewed. Secondly, an investigation of previous studies regarding FTC has been made. Based on this investigation, the method Indirect Adaptive Robust Control (IARC) is chosen.
A non-linear model of the system has been established, and verified experimentally. A proof of stability and convergence of the IARC has been made. The optimal control gains and the optimal parameters for an estimation algorithm are found through a genetic optimisation algorithm. Furthermore, the range of the considered faults is chosen.
For emulation of the considered faults, different methods are used. A second cylinder is used to emulate variations in mass and excessive friction forces. Internal and external leakages are emulated by manually operated needle-valves connected to the tank.
Simulation results showed that the IARC was able to compensate for changes in mass, viscous friction, and air-ratio. The IARC was able to compensate for some of the leakage, but could not follow the variations in direction completely. The IARC had troubles identifying variations in Coulomb friction.
When tested experimentally, the force controller emulating force related faults had difficulties following the preset trajectory, and was not able to emulate the faults satisfactory. The IARC was able to estimate and compensate for the leakage fault in a similar manner as in the simulations.

For future work it is proposed that the tests are repeated with a velocity sensor. Currently, the velocity is estimated through a numerical differentiation of the position, which requires heavy filtering. Furthermore, an improved validation of the non-linear model regarding friction parameters and leakage flows is of interest. An improved accuracy of the non-linear model may improve the determination of control- and estimation gains.
Lastly, an investigation of changes to the estimation algorithm regarding leakage flows is desired, together with an improved optimisation.

NOMENCLATURE

Acronyms

FI	Fault Identification
FD	Fault Detection
FTC	Fault Tolerant Control
FMEA	Failure Mode and Effects Analysis
FTA	Failure Tree Analysis
FDI	Fault Detection and Isolation
IARC	Indirect Adaptive Robust Control/Controller
SMC/SMO	Sliding mode controller / Sliding mode observer

Parameters

Symbol	Explanation	Unit
A_p	Piston area	[m^2]
A_{leak}	Leakage opening area used to emulate internal and external leakage	[m^2]
B, θ_2	Viscous damping	[Ns/m]
c_{ad}	Adiabatic constant for air	[−]
C_d	Discharge Coefficient	[−]
D_{1n}, θ_4	Nominal lumped force modelling error	[N]
$\tilde{D}_1$	Lumped force modelling error	[N]
$D_{2in}, \theta_6, \theta_7$	Nominal lumped flow modelling error for chamber 1 and 2 (named $Q_{leak,1}$ during fault emulation)	[m^3/s]
$\tilde{D}_{2i}$	Lumped flow modelling error for chamber 1 and 2	[m^3/s]
F_c, θ_3	Coulomb Friction	[N]
h_2, h_3	Non-linear control gains	[-]
k_c	Coulomb friction discontinuity constant	[m/s]
K_v	Gain of the valve from supplied voltage to position of the spool	[m/V]
k_q	Flow gain coefficient	[$m^3/(s\sqrt{Pa})$]
k_1, k_2, k_3, k_{scale}	Control law gains	[-]
L	Length of piston movement	[m]
M_{eq}, θ_1	Equivalent Mass	[kg]
$Q_{leak,i}$	Leakage flow in chamber 1 and 2 (called D_{2in} in estimation algorithm)	[m^3/s]
Q_N	Rated flow of Moog-valve	[m^3/s]
Re	Reynolds Number	[-]
V_0	Initial Volume	[m^3]
α_i	Forgetting factor, i = 1,2,3	[-]
$\beta_{eff}, \theta_5^{-1}$	Effective bulk modulus	[Pa]
$\boldsymbol{\Gamma}$	Estimation algorithm gain	[-]
ε_{A0}	Volumetric ratio of free air in the fluid at atmospheric pressure	[-]
ω_n	Natural frequency	[rad/s]
δ	Standard deviation	[-]
Δp_N	Rated Moog-valve pressure drop	[Pa]
ρ	Density	[kg/m^3]
ρ_{Mi}	Maximum eigenvalues used in estimation algorithm, i = 1,2,3	[-]
ρ_{li}	Minimum eigenvalues used in estimation algorithm, i = 1,2,3	[-]
$\dot{\boldsymbol{\theta}}_{max}$	Maximum rate of convergence of parameters	[-]
ζ	Damping ratio	[-]
$\boldsymbol{\theta}$	Vector of seven uncertain parameters	[-]
$\boldsymbol{\theta}_{range}$	Vector of ranges for the seven uncertain parameters	[-]
ε_2, ε_3	Control law parameter for α_2 and Q_L	[-]
$\boldsymbol{\varphi_{i,max}}$	Maxmimum magnitude of vector of variables used in calculation of h_2 and h_3, i = 2,3	[-]
ν_i	Normalisation factor, i = 1,2,3	[-]
ν_{oil}	Kinematic viscosity of the oil	[m^2/s]

CONTENTS

Part I

Introduction & Problem Definition

CHAPTER 1

INTRODUCTION

In this chapter general background information for fault tolerant control will be given. The system that will be considered in this project will be presented.

1.1 Background Information

One of the important benefits of industrial automation is the possibility for an automated process to be continuous for long time periods. This is further reinforced for autonomous processes where constant supervision can be omitted and around the clock operation is desired. In these cases the possibility of an unnoticed change in operation is present. These changes can arise from wear or unplanned conditions. The result of such a change can lead to potentially negative consequences. The possibility of a reduction in production quantity and quality, or damages to equipment and personnel, necessitates that these issues are addressed. The scientific field of Fault Identification (FI) concerns itself with detecting that a fault has occurred. Fault Diagnostics (FD) focuses on determining which fault has occurred. Fault Tolerant Control (FTC) uses the information provided by FI or FD to compensate for the fault, and in so doing ensures that the aforementioned issues are prevented. With the increase in automation and the desire for increased reliability and reduction in downtime, a lot of work has been devoted to the subject. Automotive and aircraft applications have received a lot of attention, due to the critical part safety plays in these industries. The area of FTC for industrial hydraulic application has less publications, but there appears to be an increased interest in the past years [Odgaard and Johnson, 2013], [Amirat et al., 2009]. Some of these methods will be presented and discussed in the state of the art in Chap. 3. To help readers that have not previously encountered the subject, some basic information and classification will be presented here.

Definition of a Fault

An important part in these subjects is the definition of a fault. According to [Mogens Blanke and Staroswiecki, 2016] a fault can be defined as "a deviation of the system structure or the system parameters from the nominal situation". This deviation can be caused by any number of factors such as wear or outright failure of components in the system and it can usually results in an inability of the system to execute the action for which it was designed.

A system effectiveness is measured in its ability to complete a task. Efficiency on the other hand is the ration between the useful work done by a system versus the energy expended by the system. If a fault only reduces the efficiency, but not the effectiveness of the system and furthermore it does not propagate further, then it is classified as a simple fault [Mogens Blanke and Staroswiecki, 2016]. On the other hand if the system is unable to fulfil its design criteria then the fault has resulted in a failure. This distinction is important, because the field of FTC deals with accommodating faults and determining, when a fault is about to propagate into a failure.
Faults can occur in the actuators of a system, in the plant or in the sensors of the system as seen in fig. 1.1. In the first case the ability of the controller to affect the plant has been changed. In the second case the properties of the system have change and the controller might not ensure stability. In the third case the incorrect or missing information the controller receives can result in incorrect operation. If one of these faults occurs it is desirable that the process continues in the most efficient way. In order for this to be possible the control structure should accommodate the fault.

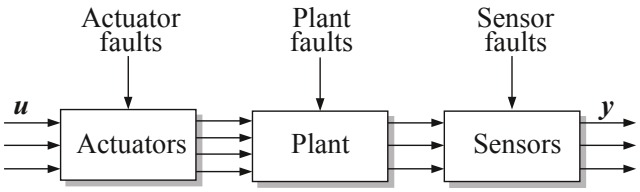

Figure 1.1: Figure distinguishing between types of fault. [Mogens Blanke and Staroswiecki, 2016]

Fault Detection

Fault occurrence can be disruptive to any operation even if it does not propagate into a failure. This is why finding and treating faults is a major research issue. A common systematic approach in literature revolves around the construction of a table linking predicted faults and describing their effects on the system. This technique is called a Failure Mode and Effects Analysis (FMEA).
This approach depends on the analysis of the most basic parts of the system. Finding how they might fail. Finally building a map of how a failure of a component affect the system. To list all of the possible ways the components of a complex system might fail is not a simple task. Then determining the possible ways the failure of a component might propagate through the system requires a rigorous time consuming analysis.
Once all the possible faults are linked to their effects, a unique path might be traced from a fault to its effect [Mogens Blanke and Staroswiecki, 2016]. One might assume then, that if a certain effect is observed in a system the logic can be inverted and a specific fault might be isolated as the cause. This cannot always be ensured, since multiple faults or indeed a combination of faults might produce the same effect in the end. Furthermore listing all possible eventualities, in which a change in a system can occur, is impossible.
To deal with these issues the usual method is to apply risk analysis, so only the more probable faults are included in the design. If all possible component failures are included into a design,

then it can be considered "complete" [Mogens Blanke and Staroswiecki, 2016].
Once a fault is detected, measures may be taken to account for it. The more information about the fault that is available, the better the decision handling. That being said, there are methods of accommodating faults, without the need to find the specific fault, or indeed detect that there is a fault at all.

Fault Handling

There are multiple ways of dealing with faults. They can roughly be divided into active and passive ones. The passive ones can also be describes as robust controllers. In this case the controller is designed in such a way as to be able to ensure stability of the plant provided some conditions are met, without any need for change of controller structure or control parameters. The positive sides of robust controllers are the lack of need for Fault Detection and Isolation (FDI) techniques. This reduces the analytical and component redundancy. On the other hand in order for the controller to be robust a trade-off in the form of reduced performance is required. Larger safety margins and more conservative control design lead to the system being robust to larger faults.

Another method for FTC is adaptive controllers. These can be considered active, in the sense that they vary their control gains in accordance with the changing parameters of the system. These controllers do not need additional supervisor functions from the control structure. The trade-off is that they require time to estimate the system dynamics. This means they have difficulties with dealing with discontinuous changes in the system. In order to detect changes in the system, an estimation algorithm can be used. If the estimation is incorrect, the controller is usually desired robust to obtain stability for all conditions. This can be considered a passive feature.
These controllers are highly dependent on accurate sensor data. If a fault occurs in one of the sensors it is not possible for these control methods to identify that the information is false. If an adaptive controller is to be made tolerant to sensor faults, then additional active FTC methods can be applied.

Active FTC methods require that a fault is detected for them to come into effect. This necessitates the use of FDI techniques and, usually, component or analytical redundancy is required. Component redundancy can be defined as the addition of more actuators and sensors than are technically needed for the system to be effective. These redundant components are utilised to either detect faults or to return the system to nominal operation. For the system of interest, it should be noted that no redundant components will be available, and component redundancy method should therefore not be investigated further. Analytical redundancy can be cheaper and it might be preferred in some cases. These methods have the benefit of possible optimal process performance under the applied conditions. Furthermore, in the occurrence of a fault, the control architecture can make decisions to prevent fault propagation and send messages to schedule maintenance. It could be possible to predict the consequences for the system to be running in a faulted state for a specific amount of time. This could be beneficial for hard to reach systems such as offshore wind turbines, or components of naval or aviation systems. [Mogens Blanke and Staroswiecki, 2016]

1.2 System considered

The desire to reduce maintenance-, and operation costs of wind turbines, together with increased computation power, has lead to an increased interest in FDI and FTC for wind turbines. [Odgaard and Johnson, 2013], [Amirat et al., 2009].
Due to this, this study will focus its investigation on FTC for implementation on the pitch system of a wind turbine. A picture describing the main parts of this system is shown in fig. 1.2.

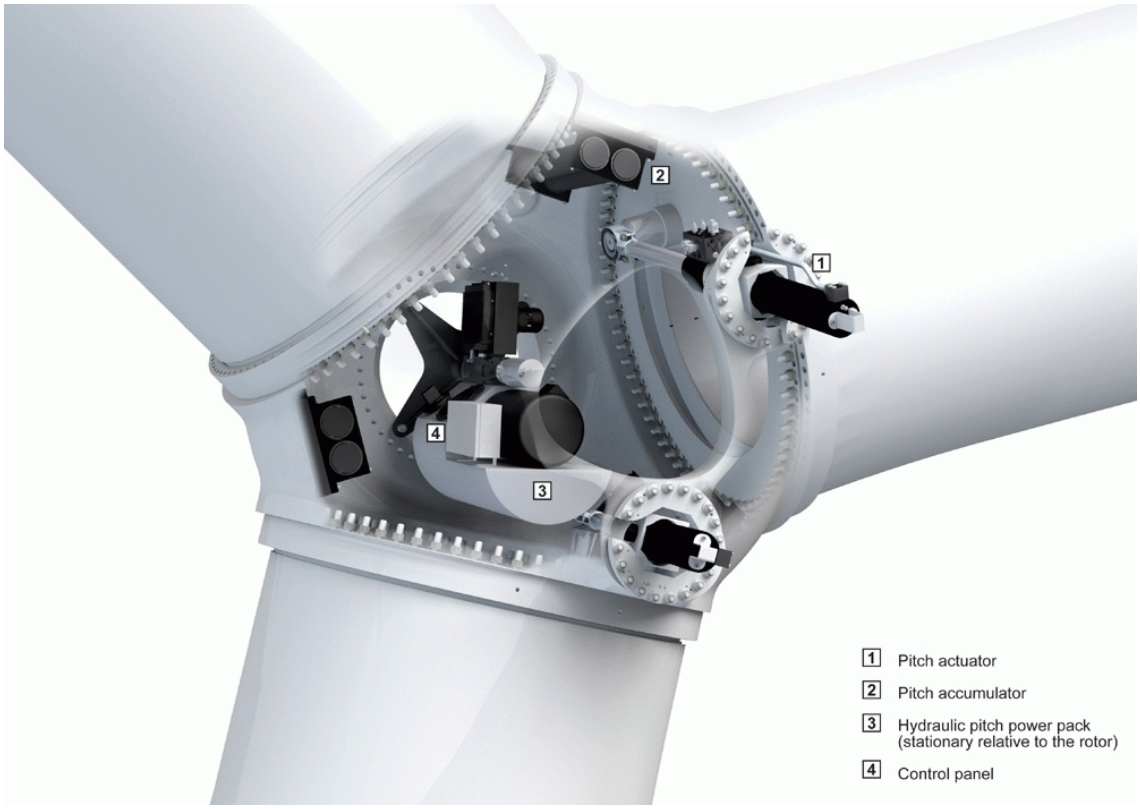

Figure 1.2: Picture of a wind turbine hydraulic pitch system. [HydratechIndustries, 2016]

A full scale pitch system is not available for testing. In order to emulate the movement of the cylinder in a pitch system, a friction test bench will be used. The bench has two cylinders connected back-to-back. One of the cylinders will be acting as a load to emulate conditions similar to what is expected in a pitch-system, more specifically, a large mass. The load cylinder will also provide a load for the test cylinder. FTC will be implemented on the test cylinder. A CAD of the system that will be used can be seen in fig. 1.3.

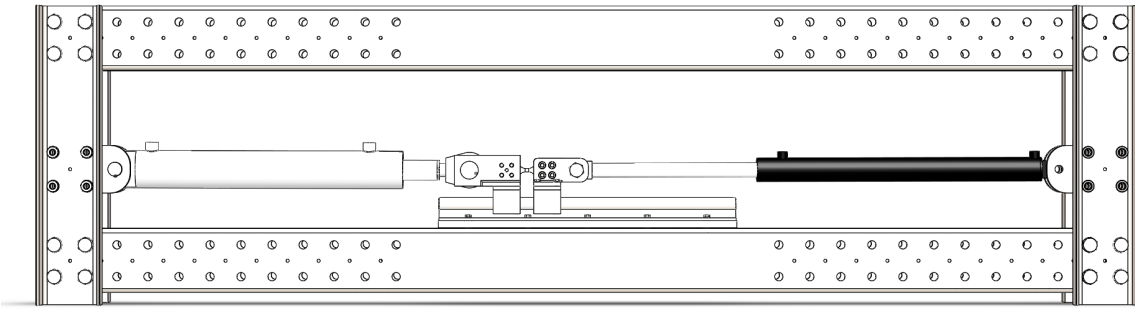

Figure 1.3: CAD of the test bench with test cylinder (left) and load cylinder (right).

The system considered has non-linearities mainly because of the servo-valve, which provides flow depending on the position of the spool and the pressure in the chambers of the cylinder. The possible faults considered include changes in friction parameters. During faults friction can have discontinuous and/or non-linear changes in its parameters. Leakage faults can have non-linear variations because they depend on the pressures in the system, which are non-linear. This should be taken into account when choosing a method, because not all FTC methods are suited for non-linear systems. Accommodations that would handle a fault by increasing or reducing a gain linearly might not be able to handle these changes. The friction test-bench consist of two cylinders:

- Test cylinder (on the left):Stroke length of 500 mm, Piston diameter of 80 mm, Rod diameter of 40 mm
- Load cylinder (on the right):Stroke length of 400 mm, Piston diameter of 40 mm, Rod diameter of 25 mm

The two cylinders are connected to a swash-plate pump capable of delivering pressures up to 180 bar and flows above 60 L/min. The hydraulic schematic can be seen in fig. 1.4

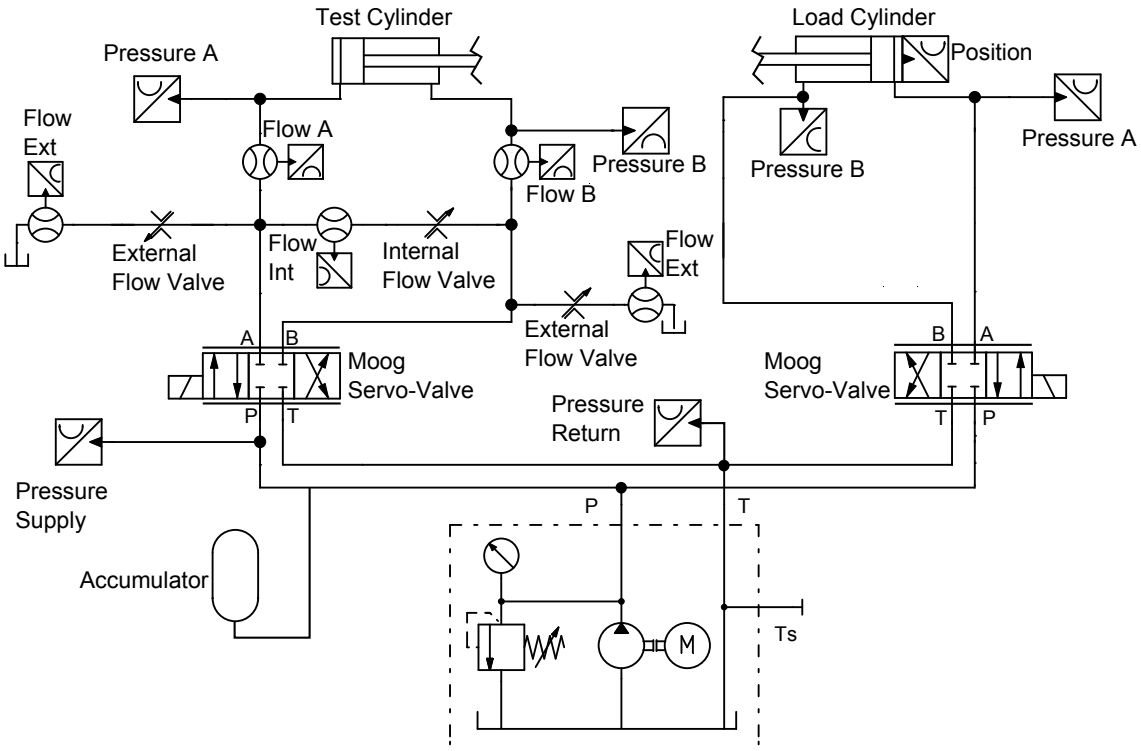

Figure 1.4: Laboratory set-up schematic.

In this figure the Moog Serve-Valve signal denotes the two MOOG-D633 valves, which control the cylinders. The valves are rated to provide 40 L/min of flow. [Inc., 2009] Several variable valves will be used to emulate internal and external leakages. These are needle valves, controllable by hand. The valve used for internal leakage and one of the external leakages (Prolasa-FT 257/2-12) has a maximum flow of 60 L/min flow at 400 bar. The valve for the other external leakage (Prolasa-FT 257/2-38) has a maximum flow of 50 L/min at 400 bar. [Prolasa]. To reduce pressure pulsation, an accumulator is connected to the supply pressure with a capacity of 4 L. Sensors have been added to measure some position, pressures and flows as seen in the figure.

Failure Mode and Effect Analysis

To be able to do fault tolerant control of a system, it is necessary to do an analysis of which faults can occur and what effect these have on the system. A study has been done by [Jesper Linger, 2016] where the faults, their effects, and how often they occur has been made for a pitch system for a wind turbine. The pitch systems in the study are hydraulically actuated, which is why the study can be used for this project.

There are two general approaches to failure analysis, FMEA and failure tree analysis (FTA). FMEA is a bottom up approach, starting with a fault for a given component and determining its effects and causes. FTA is a top down approach, where the analysis starts with an undesired event happening in the system and then working down to determine which components failure is the reason for it. The study [Jesper Linger, 2016] uses a combination of the two, to discover all relevant failure modes. The study uses a Risk Priority Number (RPN) to compare the faults. RPN is defined as a measure combining the chance for a fault to occur and the severity of its

consequences.

Results of the top ten RPN for the system in [Jesper Linger, 2016] is shown in fig. 1.5. From there it can be seen that leakage, internal and external, is a major fault together with valves being stuck. The study also found excessive friction and load/inertia to be a possible fault, however, not in the top ten.

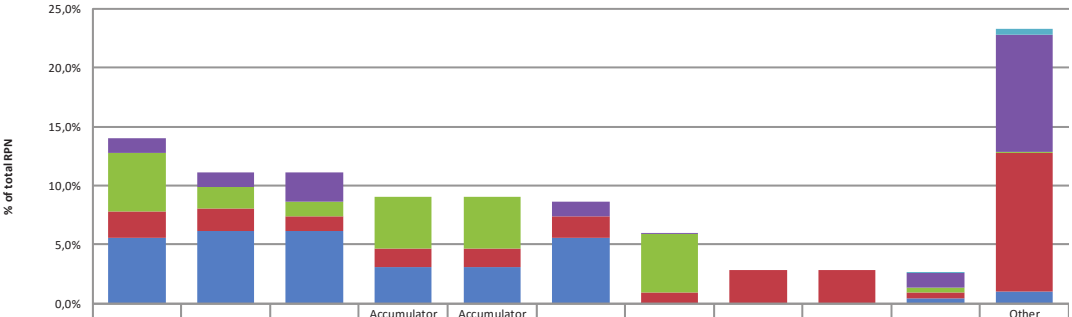

	Valve V8	Valve V7	Valve V9	Accumulator A1	Accumulator A2	Valve V10	Valve V6	Hose H4	Hose H6	Filter F1	Other components
Other	0,0%	0,0%	0,0%	0,0%	0,0%	0,0%	0,0%	0,0%	0,0%	0,0%	0,5%
Electrical fault	1,2%	1,2%	2,5%	0,0%	0,0%	1,2%	0,0%	0,0%	0,0%	1,2%	10,0%
Internal rupture/leakage	5,0%	1,9%	1,2%	4,4%	4,4%	0,0%	5,0%	0,0%	0,0%	0,4%	0,0%
External rupture/leakage	2,2%	1,9%	1,2%	1,6%	1,6%	1,9%	0,9%	2,9%	2,9%	0,5%	11,8%
Internally stuck	5,6%	6,2%	6,2%	3,1%	3,1%	5,6%	0,0%	0,0%	0,0%	0,4%	1,0%

Figure 1.5: Component RPN top ten with failure mode distribution, [Jesper Linger, 2016].

Based on the relevant faults for a wind turbine pitch-system, the faults that will be considered in this study are: Internal- and external leakage, varying friction parameters, varying load/inertia, together with a varying bulk modulus due to air in the oil. The reason for not considering a stuck valve, which according to fig. 1.5 is a common fault, is that the set-up does not have redundant valves applied, making it impossible to control the system with a stuck valve, i.e., it would be considered a system failure.
For the emulation of these faults in the system model, exact consequences of a fault will not be made. The emulation of faults is simplified to be a variation of the system parameters, independently of each other. In the case of leakage, it will be emulated by the opening and closing of a valves to either short circuit the cylinder, or allow flow to the tank. The following faults will be emulated:

- Change in Mass by applying a load force in synch with the acceleration
- Change in Friction parameters by applying a load force in synch with the velocity
- Change in Disturbance force by applying a load force
- Change in Bulk Modulus by increasing the Air-ratio in the oil
- Change in Internal and External Leakages by varying the opening area of a valve

CHAPTER 2

INITIAL PROBLEM FORMULATION

Initial Problem formulation

This project will investigate FTC for wind-turbines hydraulic pitch systems. Currently, only relatively few studies have been made with a focus on FTC for hydraulic systems. A majority of the studies are mainly focused on aeroplanes and vehicles, however, recently there has been an increase in interest and studies regarding wind-turbines [Amirat et al., 2009], [Odgaard and Johnson, 2013]. Some of the common faults that affect wind-turbines are leakage flows, valves being stuck, sensor malfunction, and to some degree, a varying load and friction parameters [Jesper Linger, 2016]. The studies focused on aeroplane or vehicle FTC do not specifically target the afore mentioned faults, but some of these algorithm can deal with a loss of efficiency in actuators i.e. reduction in area of control surfaces for an aeroplane. It is expected that these more general terms encompass some of these faults. For instance it can be considered that an internal leakage in a cylinder would result in a proportional loss in pressure and limit the force output and velocity of the piston. The two faults will affect the dynamics of the respective systems differently, but a similarity can be seen in the sense that the performance of the actuator will be impaired in both cases. This leads to the initial problem:

- Which FTC algorithm can be implemented on a hydraulic servo-system considering the possibility of faults like leakage, and varying load/friction being present?
- Which of the considered FTC algorithms shows the most promise of successfully handling these faults?

CHAPTER 3

LITERATURE REVIEW

In this chapter, articles regarding different FTC methods will be reviewed. For the interested reader, more elaboration on each article can be found in App. H.

The First part will include different passive fault tolerant control (PFTC) and active fault tolerant control (AFTC) methods, with a focus on their effectiveness and where they have been applied, rather than the underlying theory.

The second part will contain a closer look at 2 of these articles. These have been chosen, because they were deemed more suitable for the task at hand.

The final section will contain a discussing about the pros and cons of the two articles. Based on the discussion, the best FTC method and strategy for the system of interest is chosen.

3.1 Broad Review

Classifying which method an article has chosen in order to achieve fault tolerance is not a trivial task, because many of the presented methods incorporate parts of each other. The division used here is by no means exact, but it serves the purpose of alleviating some of the difficulty of categorising the amount of information available on the subject.

H_∞ Control

A common design methodology for PFTC, is to use robust controllers in order to obtain stability and disturbance attenuation, both when the system operates normally and when faults occur. As discussed in the introduction chapter, passive FTC methods do not change the control structure or controller parameters when a fault occurs. Instead they are designed in a way, which is robust to faults, disturbances and modelling errors within certain bounds. H_∞ is but one of the methods that can be used to obtain robust control. It is used as an example of what can be achieved with such methods, because Linear Quadratic Regulators and other optimal control methods share many of the same limitations.

The H_∞ method has been used in [Veillette et al., 1992], [Zhou and Ren, 2001], and [Huang

et al., 2014].
[Veillette et al., 1992] and [Zhou and Ren, 2001] are only theoritical, with no verification of their performance, and is therefore not considered for this project.

The article [Huang et al., 2014] considers H_∞ for a linear system with an example for a vertical take-off and landing vehicle. The article considers a new way to process the faults, called semi-Markov process which is able to consider a larger variation of fault processes. The design is tested for the vehicle with a 50% actuation fault. The controller was able to reduce the effect from the fault to a small steady error. It was proposed to use a higher order feedback to remove the steady error. The main issue with this method is the requirement of a linear system which may introduce large uncertainties when the highly non-linear dynamics in a hydraulic system are linearised.

Quantitative Feedback Theory

The FTC method Quantitative Feedback Theory (QFT) has been used both as a passive and active FTC for hydraulic systems in studies from 2002-2010. Their findings are mentioned below:

The studies [Niksefat and Sepehri, 2002], [Karpenko and Sepehri, 2003], [Karpenko and Sepehri, 2005], and [Karpenko and Sepehri, 2010] proposes methods to use Quantitative Feedback Theory (QFT) for hydraulic systems. [Niksefat and Sepehri, 2002] considers faults in both sensors, supply pressure, and servo-valve. However, the method is only able to achieve robustness, and requires a conservative design to cope with all the faults without any adaptation. The study [Karpenko and Sepehri, 2003], and [Karpenko and Sepehri, 2005] considers leakage faults, with leakages of up to 25% of the piston seal. These studies are not investigated further due to the lack of severe non-linear faults considered and their conservative control design.

The study [Karpenko and Sepehri, 2010] investigates an approach to reduce the conservativeness of QFT algorithms due to the linearisation. The proposed method is using a Linear Time Invariant Equivalent (LTIE) modelling approach, where LTIE models are defined as models generating the same output as non-linear systems given the same input. Two QFT control laws are proposed for different fluid power applications. The first controller uses a proportional control structure and is well suited for applications with noisy sensors or highly dynamic reference commands. The second controller incorporates an integrator and is suited for applications where static errors due to un-modelled non-idealities are present. The controllers were tested on a hydraulic ram where different load springs (0-80 kN/m) were attached. The controllers were also tested with various parameter uncertainties, but no specific values have been mentioned. The proposed controller worked well for all tests, with the proportional having a slight overshoot and able to be within 5 % of the desired value and the integrator being more tight and having zero steady state error due to the integrating term.

QFT has also been proposed as a control strategy for aircraft, the studies concerning these are: [Keating et al., 1997] and [Wu et al., 1999]. Here QFT is used to compensate for loss of elevator surface area of up to 50 %. These have however not been investigated further due to only linear faults being investigated.

Adaptive Control

A large number of studies regarding adaptive control design used for FTC have been made, because of the inherent properties of the adaptation theory. Different methods have been developed to achieve the desired adaptive properties. Papers describing some of them will be presented in the following section.

The studies [Maybeck and Pogoda, 1989], [Maybeck and Stevens, 1991], and [Maybeck, 1999] investigates the use of multiple models for aircrafts. Loss of efficiency of actuators is considered, but the design requires redundant hardware to compensate for the faults and failures tested. Due to this, the method proposed is not investigated further.

The article [Tong et al., 2014] involves observer-based adaptive decentralised fuzzyfied FTC of a non-linear large-scale system with actuator failures. The article considers unmeasured states, unknown non-linear functions, and actuator faults modelled as loss of effectiveness. The control design method is done by combining a backstepping technique with the non-linear tolerant-fault control theory. The simulated system used for testing is a model of two inverted pendulums connected by a spring. The existing adaptive decentralised control approaches made prior to this study are able to control the same system, however, only if no actuator faults occurs, which is where this approach is superior. The future work proposed is to simplify the design. Other studies using similar methods have been made for hydraulic systems. Because of this, this study will not be investigated further.

The studies [Yao et al., 2000] [Bu and Yuo, 2001], [Yao et al., 2001], [Bu and Yao, 2001], [Yao and Palmer, 2002], [Mohanty and Yao, 2006], and [Mohanty and Yao, 2011] investigates the use of Adaptive Robust Controller (ARC) for hydraulic systems in the form of 3-DoF robot with seven uncertain parameters, hard to model non-linearities, and disturbances. These includes parameters such as bulk modulus, leakage and friction forces. For testing and examples, a three degree of freedom robot has been used. The study [Mohanty and Yao, 2011] proposes to use indirect ARC, (IARC), which is able to separate parameter estimation and control law. By doing this, the estimation of seven parameters has been improved regarding estimation time to 1.5-10 seconds. A requirement for the proposed algorithm is a known range on the parameters investigated and an adaptation rate. The resulting IARC is shown to be superior to both industrial controllers, and the direct ARC, (DARC), used in the previous studies. The test for the comparison of IARC and DARC consisted of slowly moving a load of 22.7 kg in a swinging motion. The reference is a pulse of 0.3 radians with a frequency of approx 4 seconds. Because of the system similarities with this article and the promising results this article has been selected for further investigation.

The article [Balle et al., 1998] investigates FTC for heat-exchanger. The method used is based on fuzzy controller and observers. The faults considered were sensor faults. The method described is not investigated further due to no actuator faults being investigated.

A lot of work has been devoted to FTC for aviation purposes: [Tao et al., 2002],[Tao et al.,

2001], [Bošković, 2014], [Wise et al., 1999], [Bodson and Groszkiewicz, 1997], [Bodson and Groszkiewicz, 1997], [Gao et al., 2015], [Zhou et al., 2014], [Ahmed-Zaid et al., 1991]. The studies [Tao et al., 2002] [Tao et al., 2001], [Bošković, 2014], [Wise et al., 1999] all consider situations in which redundant hardware is available making them unsuitable for this project. The articles [Gao et al., 2015] and [Zhou et al., 2014] consider only linear faults. The method in [Bodson and Groszkiewicz, 1997] requires the estimation of 45 parameters. Furthermore none of these articles have laboratory test due to the expensive nature of the systems they are investigating. For these reasons these methods have not been chosen.

The study [Yao et al., 2014] is regarding internal leakage for a single-rod hydraulic actuator. The article proposed two controllers, one for the nominal system with small faults, and a FTC for the severe faults. The controller designed is based on parameter adaptive methodology, with a learning mechanism. For the system investigated in the article the learning mechanism only has one uncertain parameter, internal leakage. The designed controller is simulated on a double-rod hydraulic actuator model. The internal leakage faults tested were abrupt and incipient cases with a leakage parameter corresponding to an increase of 50 to 200 % of the nominal leakage (calculated under the assumption the load pressure is equal to supply pressure), which was detected in 6 seconds and compensated for a few seconds later. An issue with this method is the lack of friction related faults and only considering one uncertain parameter.

The article [Yin et al., 2014] investigates an integrated design of FTC systems with application to Tennessee Eastman (TE) benchmark. The proposed fault-tolerant architecture is a data driven design whose core is an observer/residual generator based realisation of the Youla-parametrisation of all stabilisation controllers. The FTC is then achieved by an adaptive residual generator for the on-line identification of the fault diagnosis relevant vectors, and an gradient based optimisation approach for the on-line configuration of the parameter matrix. The faults considered were actuator faults, process faults and sensor faults. The performance and effectiveness of the proposed schemes has been demonstrated by using the TE benchmark model. Based on simulations the FTC was found superior to a standard PI-controller at faulty situations. The system considered in the article diverted too much from a hydraulic servo-system to be considered for further studies.

[Plummer and Vaughan, 1996] proposes an adaptive control based on pole placement for electro-hydraulic positioning systems. For the design, a linearisation of the system is required. The method is considered indirect and switches off adaptation if the trace of the covariance matrix is too large. To reduce the magnitude and variance of uncertainties in the parameters, an off-line initial system identification is proposed. Faults tested include a change in supply pressure from 160 to 40 bar and vice-versa. Dead oil was introduced into the circuit reducing the natural frequency equivalent to an increased load mass. Another test was done removing the dead oil. The test results showed the adaptation happens rapidly and the control is able to compensate for the fault. This study shows promise, however, [Mohanty and Yao, 2011] uses a similar method. The difference being that [Plummer and Vaughan, 1996] uses the estimated system parameters to create a linear controller, while [Mohanty and Yao, 2011] utilises a non-linear control design with Lyapunov proof of stabilty if the estimation fails.

The studies [Jin, 2015] and [Jin, 2016] analyses FTC for MIMO non-linear systems. The design method used is based on the backstepping approach, and the proposed controller is tested on a 2 DoF robot. The method is not investigated further, due to the system of interest being SISO. The method is similar to the one used in [Mohanty and Yao, 2011], but the latter one has the benefit of it having been tested on a SISO system.

[Yang and Ye, 2006] investigates FTC for linear time-invariant systems. The proposed control is based on adaptive H_∞ design. The new indirect adaptive FTC design method is made via state feedback and is presented for actuator fault compensations. The design is developed in the framework of linear matrix inequality approach. A comparison between the proposed adaptive gain controller and a fixed gain version was tested on both a nominal system and a system with a failure on the first actuator. From the simulation, the proposed adaptive H_∞ has better performance in both situations and has more relaxed conditions than the standard H_∞ design with a fixed gain. This study is not considered due to it being based on a linear time-invariant system.

The article [Chen et al., 2016] involves FTC for an ocean surface vehicle. The method used is based on a backstepping approach. The article is not investigated further due to it being based on a system with multiple actuators, which is not the case for the system considered in this report.

Sliding Mode Control

Sliding Mode theory has received a lot of research attention, due to its relatively simple design and implementation and highly robust properties making it a good candidate for FTC applications. Application using sliding mode controllers (SMC) or observers (SMO) are presented here.

In [Kim et al., 2001] a SMC is investigated as a FTC for a combustion engine. The article investigates valve and sensor faults, but not for a hydraulic cylinder or faults in the form of friction or similar. Due to this, the proposed control law is not found of interest.

The article [Moradi and Fekih, 2014] is regarding FTC for a full-scale car suspension. The proposed control is an adaptive PID for each subsystem, one for each wheel. A tracking signal is made from a sliding mode controller to each of the subsystems to mitigate the 3 degree of freedom arising from road undulations. The proposed controller is tested on a full-scale vehicle dynamic model with active suspension system with 7 degrees of freedom. The faults considered are actuator faults and uncertainties. To test the uncertainties, 20 % uncertainty was added to 18 parameters, and a 1 % uncertainty to tire stiffness. From this test, the system was able to handle the system with only slightly less tracking performance than for a nominal model. For faults, a test for each of the wheel subsystem was made where one received zero control signal. Further tests were made were a varying efficiency was applied to the actuators. The result from these tests were that the proposed controller was found superior to those used in previous studies. For further studies, the use of observers instead of measuring states is

desired.
This has not been considered further due to a 20 % uncertainty of the system parameters being smaller than the ones in [Mohanty and Yao, 2011].

SMC FTC has also receive a lot of attention from aviation industry [Shtessel et al., 2002], [Hess and Wells, 2003], [Liu et al., 2011], [Zhao et al., 2014b]. [Zhao et al., 2014a] is based on the availability of redundant hardware. [Zhao et al., 2014a] considers a near space vehicle. [Zhao et al., 2014b] requires 50 sec to accommodate to a loss in actuator efficiency fault. For these reasons the methods in these articles has not been investigated further.

[Patton et al., 2010] proposes a method where a sliding mode observer is combined with a sliding mode controller in order to deal with abrupt actuator faults. The authors propose the use of this method to deal with the hard to model friction effect such as Stribeck effect and Coulomb friction. The system considered was a linear inverted pendulum. The authors of the article claim that the proposed methods are less complex, than constructing accurate friction models, while still being able to deal with the problem. Laboratory test show that the method is viable and shows promising results. The article proposes further study of this method on a non-linear system. The focus on discontinuous faults in this article makes a good candidate for implementation in this project. The article has been chosen for further study.

Linear Parameter Variation

The study [Sloth et al., 2011] investigates FTC for wind turbines. The method used is Linear Parameter Variation (LPV), where different design strategies are compared. The strategies used are active, passive, and nominal. Furthermore, a robust controller is designed. For the optimisation problem involved in the passive and robust controllers, bilinear matrix inequalities are solved instead of linear matrix inequalities due to parameter variations not being estimated. For comparing the controllers, a non-linear simulation model of a wind turbine is used. A nominal and a faulty case were simulated, with the fault being a low pressure in the pitch system. From the tests, the active strategy had a superior performance for the faulty case, at the cost of a fault diagnosis. For the nominal case, similar performances were observed. This study is not considered for further analysis, due to only faults regarding low pressures being investigated.

[Shin et al., 2002] and [Ganguli et al., 2002] investigates FTC for aircraft with actuator failures. The method used is a LPV controller based on LMI optimisations and LPV using a quasi-LPV model. The strategy described in the articles requires multiple actuators to react to the faults, and the strategies are therefore not investigated further.

Intelligent Systems

The articles [Sami and Patton, 2013], [Diao and Passino, 2001], [Diao and Passino, 2002], [Zhang et al., 2004], [Farrell et al., 1993], [Reveliotis and Kokar, 1995], [Polycarpou and Helmi, 1995], [Polycarpou, 2001] and [Musgrave et al., 1996] have investigated the possibility of applying machine learning in order to obtain FTC. While the proposed methods work theoretically, not all have been tested in a laboratory setting where the conditions could affect the learning process. Due to the complexity of these algorithm, they have been deemed not suited for the

task at hand.

Findings Table

Based on the literature made, a table has been constructed to give an overview of which faults each method has been able to handle and for what system type they have been tested.

Control Method	Non-linear system	Actuator fault	Sensor fault	Non-linear faults	Simplicity	Tested on hydraulic sys.
Passive QFT	-	+	-	-	++	+
Active QFT	-	+	-	-	+	+
SMC	+	+	+	+	-	-
Adapt. Backstepping	+	+	-	+	-	+
Adapt. MM	-	+	+	+	-	-
Passive LPV	-	+	-	-	++	+
Active LPV	-	+	-	-	+	+
IC	+	+	+	+	- -	+

Based on the literature review it has been concluded that it is very difficult to accommodate for sensor faults without redundant sensors. Furthermore, methods which can accommodate for sensor faults often cannot accommodate actuator faults. Alternatively a multiple model approach can be taken. Then the decision if a fault has occurred in an actuator, the plant or a sensor can be taken based on statistical information and probability theory. This method has not been tested on hydraulic system and it has been concluded that the large non-linearities present in a hydraulic system might not allow for correct implementation of such a method. Based on this reasoning this project will not attempt to accommodate sensor faults, instead focusing on actuator faults. The conclusion is that two methods have the most promise, based on the consideration that the method has to be applied on a non-linear system with non-linear actuator faults. These are the SMC and the Adaptive Backstepping methods. Two specific articles have been chosen for further study representing each method, [Patton et al., 2010] and [Mohanty and Yao, 2011] respectively. The Intelligent system methods also show promise, but have been rejected due to the complexities associated with the learning process.

3.2 Indirect Adaptive Robust Control

In this section, a deeper analysis of the article [Mohanty and Yao, 2011] will be conducted. The article concerns a hydraulic system and uncertainties similar to the ones this project is interested in. Furthermore the article shows promising results. Based on this analysis and 3.3, a choice of method for the system in this report will be made.

The system considered in [Mohanty and Yao, 2011] is a hydraulic system in the form of a three degree of freedom hydraulic robot with uncertain non-linearities and disturbances. Two of the three DOF are locked, leaving a single cylinder to be controlled. The uncertainties considered are bulk modulus, inertia, non-linear friction forces, leakage, and lumped modelling errors.

These are similar changes to what effect uncertainties/faults can have on the hydraulic system considered in this report. Two of the major faults for the system of interest in this report are the leakage and friction, which are both included. The objective of the proposed control law, Indirect Adaptive Robust Controller (IARC), is to achieve precision control while maintaining a fast parameter estimation in order to make the controller applicable for non-linear systems with uncertain non-linearities and disturbances. The authors of the article propose that the method can be used for FTC, but have not simulated faulty conditions.

The adaptation law requires an estimation of the system parameters. The article uses a least squares method, because it can lead to faster convergence of the estimates to the correct parameters.

The article uses a backstepping method to design the control law. The resulting controller has three linear and three non-linear control gains. For the estimation algorithm, the authors mention that the improvement compared to the previous method is a generally faster estimation. The estimation is based on measurements filtered through a stable low pass filter with a relative degree of no less than three. This removes the need for a acceleration measurement, because the stable filter removes the noise from the measurements and outputs a smooth signal. In this way the filter velocity measurement can be derived to acquire the filtered acceleration.

Based on this, the article continues to show a numerical example where a comparison of DARC and IARC is made. The result is that IARC has a faster converge of the uncertain parameters and better steady state tracking accuracy which was the desired result from the articles problem formulation. The article does not test how the estimator handles parameters which vary over time, but the theory supports the assumption that the algorithm will be able to converge to the new parameter values. The algorithm is only able to accommodate faults which affect the system parameters in a way that can be estimated.

3.3 Combining Sliding Mode Observer and Controller

In this section a deeper analysis of the article [Patton et al., 2010] will be conducted. A step-by-step presentation, of the method and what conclusions can be derived from it for further use in this project, will be given. Based on them together with the conclusions from 3.2, a decision will be made for the final choice of method. The study is focused on accurately estimating the non-smooth, non-linear nature of friction in mechatronics systems as a motivation for its research into FTC. On-line estimation of friction is complex and degradation of components can drastically change friction dynamics. Patton et al. propose a controller that estimates this friction based on the sliding term of a sliding mode observer (SMO) and then compensate for it through a sliding mode controller (SMC).

A canonical linear state space representation is used to design an observer and then a discontinuous term, dependent on the sign of the error, is added to keep the plant output on the sliding surface.

According to the article the friction will be seen as a disturbance by the linear system. When perfect sliding occurs the system is guaranteed to be robust to a certain type of uncertainty and the system behaves as a reduced order motion independent of the control. The article does

not discuss it, but when applied to a non-linear system any differences that appear between the system and its linear approximation will produce the same error. This error would also be lumped with the difference due to friction forces. The controller will then have to take care of the faults, non-linearities and the friction terms.

[Patton et al., 2010] continues by designing a SMC. First a sliding hyperplane is defined based on the design in [Dorling and Zinober, 1988]. By dividing the control law in a linear and a discontinuous part the system stability can be proven by designing the control law for the reduced order motion system. In this article a Quadratic Minimisation method is chosen for the linear part of the control law. For the discontinuous part a single parameter has to be chosen large enough to ensure reachability of the sliding surface. Patton et al. also prove that by augmenting the design of the sliding surface and the variable structure control law stable sliding motion can be achieved even though some states are not available for measurement. Overall this design method can be beneficial, because velocity or acceleration measurement are not always available and furthermore a large part of the controller design is linear, with a single non-linear control gain to be tuned.

The article tests the theory on an inverted pendulum. The cart in the test was driven by a DC motor. Friction has been modelled by the discontinuous Stribeck friction model [Putra and Nijmeijer, 2004]. The available measurement were cart and pendulum position and cart velocity. Another test was done with only the cart and pendulum position available in the feedback loop. The method worked in both cases and a noticeable result is visible in Fig. 3.1 when the compensation is activated.

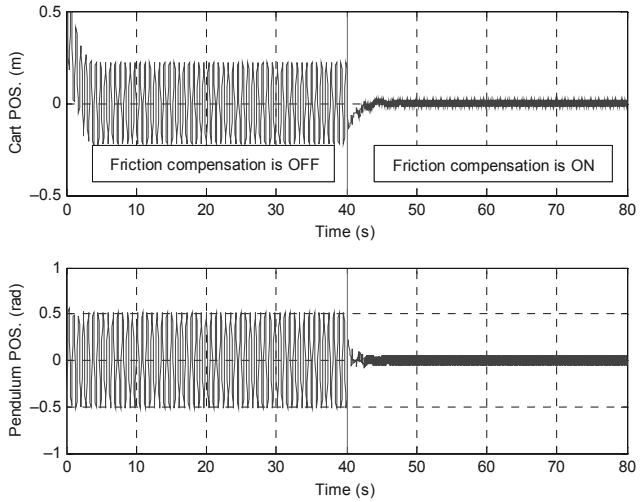

Figure 3.1: Figure presenting [Patton et al., 2010] results of SMO-SMC with a 25 N friction force.

3.4 Discussion

It is difficult to determine, which method holds more potential. On the one hand it is a well known problem for SMC that once the system converges to the sliding surface, a chattering occurs. In order to reduce this phenomenon a number of methods have been proposed like the inclusion of a boundary layer or the nesting of the sliding controller in the derivatives of the control law, so by integration the chatter can be reduced. The inclusion of these methods

can degrade the robustness of the controller or increase the complexity of the implementation and the proof of stability.
Furthermore, the SMC requires a linearisation of the system. A linearisation may be possible for some non-linear system, but the effectiveness of the control law will depend on the severity of the non-linear tendencies in the system.
Some positive points of the SMC/SMO are:

- Does not need velocity sensor, due to the way the SMO is designed.
- Fewer design parameter can make for a simpler implementation.

While the negative points are:

- The controller hasn't been tested on a non-linear system.
- The controller only accounts for differences between the linear and non-linear model. It is not possible to determine why these differences have arisen.
- Due to the difference between the system in the article and the hydraulic system considered in this report, the mathematical proof ensuring stability of the controller will require reworking.

On the other hand adaptive control is based on a gradual convergence to the values of a system, with the size of the error depending on the performance of an estimation algorithm. Adaptive algorithm are however not dependent on a linearised model, possibly increasing the performance on non-linear systems.
Some of the positive features of the IARC are:

- Similarity between the system used in the article and the one that will be used in this report.
- The same parameters will have to estimated.
- Possible future work in using the estimated system parameters for diagnosis.

The main negative points of the IARC is the larger amount of parameters which have to be tuned.

Based on these considerations, and the general idea of how the two methods described in the previous section work, the IARC method is chosen to design a control law for this project. One of the major reasons is that it is based on a non-linear model, allowing the control structure to be used for more complex non-linear systems compared to SMC.
Mohanty et al. have proposed that the method can be used for FTC, but have only tested the method for an initial error in estimation. In this project the ability of the IARC to operate under faulty conditions, that is, the system parameters will vary with time, will be tested.

CHAPTER 4

PROBLEM STATEMENT

The goal of this project is to select and implement FTC on a hydraulic servo-system emulating conditions and faults that a wind turbines pitch system might experience. Based on the initial problem formulation and the literature review, an Indirect Adaptive Robust Controller (IARC) has been chosen as the most suited FTC for the system, and will be implemented.
The project will answer the following questions:

- What performance can an IARC achieve on the hydraulic servo-system provided by AAU?
- Can the IARC still handle the faults if the change in the mass, friction parameters, the bulk modulus of the oil, and the leakages in the hydraulic servo-system is occurring continuously over time?
- What is the effect of designing the IARC to handle larger variations in the aforementioned parameters?
- How fast does the algorithm accommodate faults and how much performance is lost during faulty operation?

Solution Strategy

Before the performance of the IARC can be determined, a non-linear model of the system is constructed. This model will be used to design the IARC, which is based on the system dynamics. The model will then be used to test the behaviour of the algorithm in a safe environment, before the actual implementation of the controller is considered. Based on a Failure Mode and Effect Analysis, made by [Jesper Linger, 2016], and the limitations of the IARC, the faults that will be looked into are chosen.
A force controller is designed for a load cylinder connected to the test cylinder, as seen in fig. 1.3. It will emulate conditions similar to what a cylinder in a wind turbine pitch system experiences. The force controller is also used to emulate faults such as varying mass and friction parameters. Faults concerning leakage will be emulated by varying an opening area of needle-valves placed on the set-up. Both external and internal leakage can be emulated in this way.
The user defined parameters used in the IARC structure will depend on the size of faults the IARC can handle. A number of parameter variation ranges will be investigated. The user defined parameters will be determined by using an optimisation algorithm.

To obtain a benchmark which will be used to evaluate the performance under faulty condition, a simulation and experimental test of the IARC, under fault-less conditions will be made.
To obtain a realistic simulation, the noise and delays from the measurement equipment available will be used. The noise levels have first been taken from the data sheets for the respective sensors. Later on, laboratory measurements show that the standard deviation of the simulated noise is similar in magnitude to noise samples obtained during tests.
Further simulations will be made where faults are introduced to the system to determine how the IARC will perform under faulty situations.
To validate the simulations, similar tests will be made on the experimental set-up.
Based on the analysis of the IARC structure, the simulation results, and experimental results, the answers to the problems above will be obtained if the following tasks are completed:

- Modelling of the system to be used as a preliminary test bench
- Determination of possible faults and which system parameters are affected
- IARC design for the system and proof of stability
- Choice of estimation algorithm required for the optimal operation of the IARC
- Design of estimation algorithm for the system parameters affected by the considered faults: Mass, Coulomb and Viscous Frictions, Bulk Modulus and Leakage
- Determination of optimal parameters for the IARC and the estimation algorithm through an optimisation algorithm
- Simulation tests to verify the IARC works under realistic conditions i.e noise and delays
- Simulation tests to determine the performance of the IARC under nominal conditions
- Simulation tests to investigate the amount of time needed to accommodate a fault and the reduction in performance during faulted operation
- Writing of IARC and estimation algorithm program in LabView to be implemented on a Real Time Machine
- Testing of IARC and estimation algorithm on the set-up in order to verify simulation results

Part II

Modelling

CHAPTER 5

SYSTEM MODEL

In this chapter, a model of the experimental set-up will be determined. Faults will be emulated in the non-linear model of the system based on chap. 1.2, and at a later time they will be replicated in the lab.

5.1 Non-linear System Model

To simulate the faults considered and their effects, it is desired to obtain a precise model. Flow calculations due to leakage, system dynamics due to mass and friction parameters need to be precise enough to simulate the faults. For the bulk modulus calculation, the air-ratio in oil should be included. Furthermore, to include the limitations from the servo-valves, the dynamics and flow limitations will be included.
The desired precision is linked to the accuracy of the sensors. Simulation with more precision than sensor accuracy cannot be validated in the lab and do not benefit the project.

A sketch of the full hydraulic system that will be used for experimental purposes is shown in fig. 5.1.

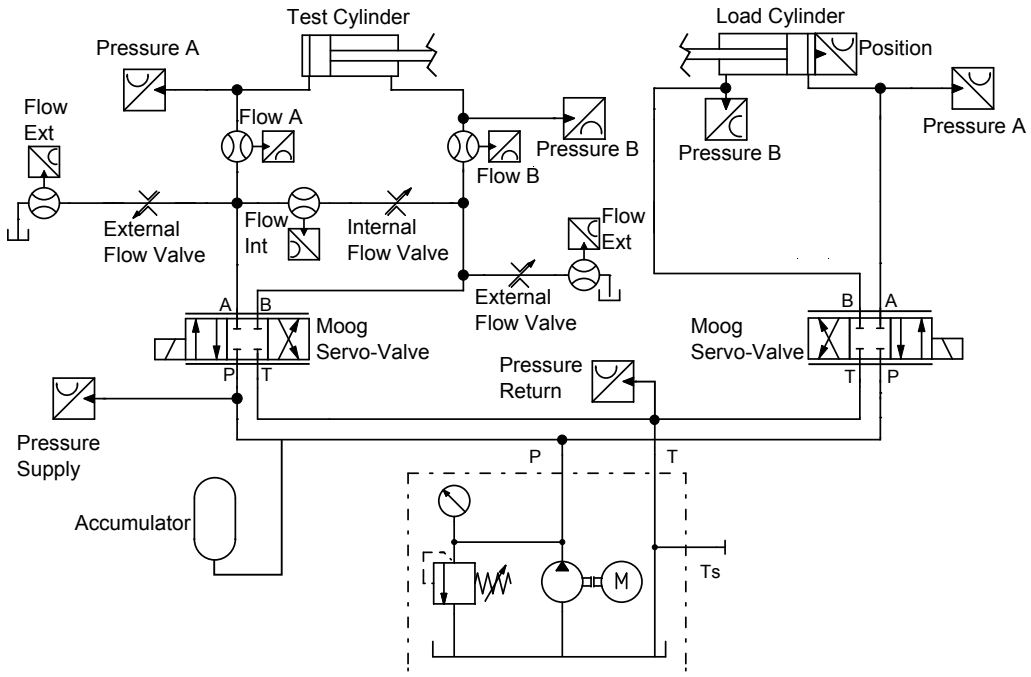

Figure 5.1: Schematic of the hydraulic system

In fig. 5.1 both a test cylinder and a load cylinder is shown, where the load cylinder will be used to emulate a load, faults, and time-varying parameters. Components used to emulate leakages are shown as flow valves in fig. 5.1, a description of these will be made later in Chap. 10. The components and relevant info for the measurements will be described in the experimental set-up chapter, Chap. 10.

The description of the non-linear model in this chapter will be for the test cylinder, but the same equations can be applied to the load cylinder if required. A simplified sketch showing the components required in the modelling of the test cylinder is shown in fig. 5.2.

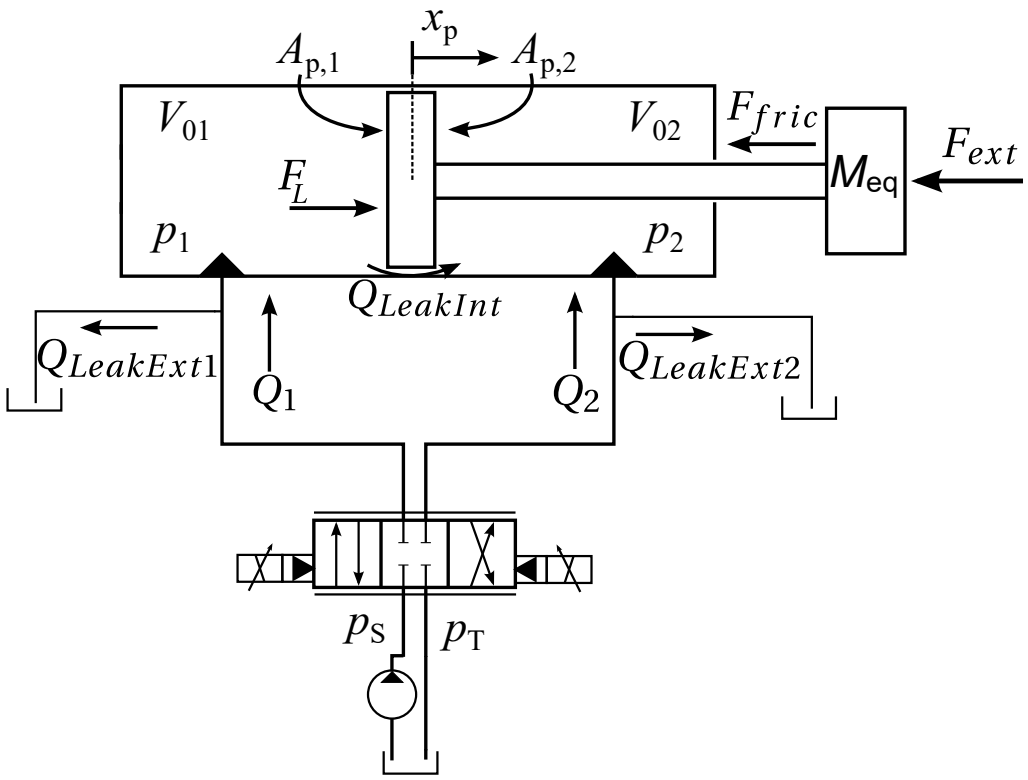

Figure 5.2: Sketch of the cylinder and valve with component parameters

Based on the components and parameters shown in 5.2, a description of the established model will be made in the following, starting with the cylinder and the forces applied to it. From this, the equations for each force will be described, and the underlying dynamic models will be shown, which includes the continuity equation and valve dynamics.

Forces Acting on the Piston

From the cylinder shown in fig. 5.2, a force equation is determined based on Newtons 2nd Law eq. (5.1):

$$\begin{aligned} \sum F_x &= M_{eq}\ddot{x}_p = F_L - F_{fric} - F_{ext} \\ &= M_{eq}\ddot{x}_p = p_1 A_{p,1} - p_2 A_{p,2} - F_{fric} - F_{ext} \end{aligned} \tag{5.1}$$

where

M_{eq}	is the mass of the piston	[kg]
x_p	is the position of the piston	[m]
F_L	is the pressure force acting on the piston	[N]
F_{fric}	is the friction forces acting on the piston	[N]
F_{ext}	is a disturbance force	[N]
p_i	is the pressure in chamber 1 and 2	[Pa]
$A_{p,i}$	is the piston area for chamber 1 and 2	[m^2]

The pressures acting on the piston will be determined based on the continuity and orifice equations, see section 5.1.1. The disturbance force F_{ext} is controlled by an actuator, and can

deliver different force trajectories. The load force will be used to test for different scenarios of mass, disturbances and emulating varying friction force related parameters. The control law used for the load cylinder is described in App. B.
The IARC will be able to compensate for variations in the load and mass by estimating the system parameters: M_{eq} and F_{ext} with the estimation algorithm explained in Sec. 7.2.

The friction force will be modelled by (5.3). Here, only the Coulomb friction and viscous friction are included, due to these being the dominating factors for the speeds that will be used during testing. If very low speeds were considered, then the Stribeck effect should be considered. For the Coulomb friction, a sign function of the piston speed is needed. A sign function may give numerical problems, due to discontinuities that will occur. To avoid this, a tanh function is used instead, which uses a steep slope when a sign change occurs, making the function continuous.

$$F_{fric} = B\dot{x}_p + F_c \cdot S(\dot{x}_p) \tag{5.2}$$

$$F_{fric} = B\dot{x}_p + F_c \cdot \tanh\left(\frac{\dot{x}_p}{k_c}\right) \tag{5.3}$$

where k_c is a user defined constant to choose at what velocity the Coulomb friction will have its full effect.
A nominal value of the parameters B, and F_c will be determined experimentally. For the initial system model and IARC parameter determination, the nominal system parameters will be based on a previous project [Henriksen, 2009]. The previous project used the same load cylinder, but a different test cylinder, resulting in expected differences in the magnitudes. These should however give a decent baseline for the friction parameters. The previously estimated parameters are approximately: $B = 18000$, $F_c = 200$.
The IARC will be able to compensate for variations in the friction force related parameters by estimating the system parameters: B and F_c, with the estimation algorithm described in Sec. 7.2.

A comparison of the use of sign function and tanh function can be seen in fig. 5.3, where the viscous friction is also included. The parameters used are: $B = 18000\ N\frac{s}{m}$, $F_c = 200\ N$, $k_c = 1\frac{mm}{s}$.

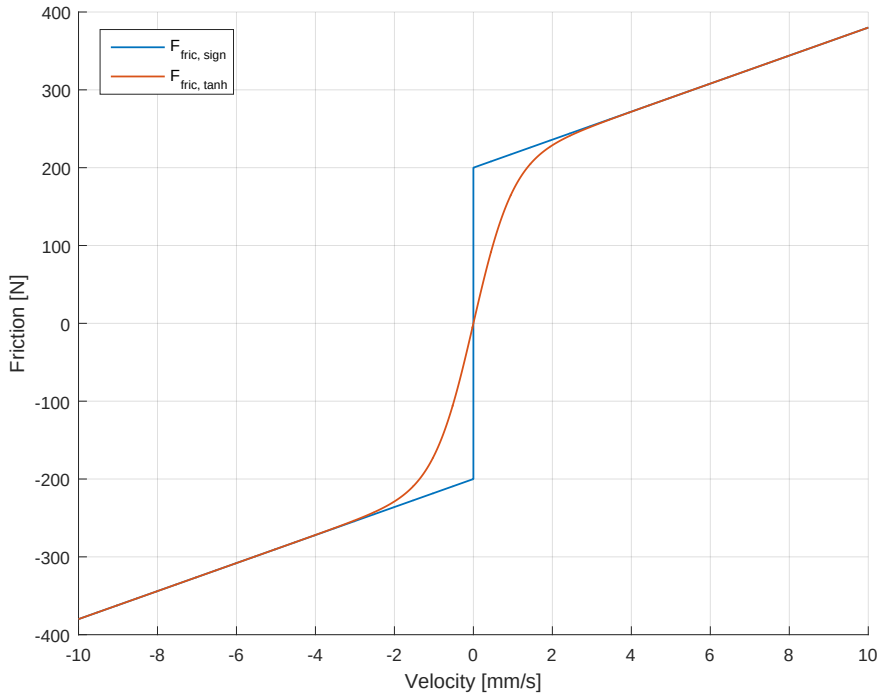

Figure 5.3: Combined friction model using parameters mentioned above.

In fig. 5.3 the comparison of tanh and sign function shows that the error introduced by using a tanh in simulations will only be relevant for velocities smaller than ≈ 2 mm/s. The trajectory used for this project will mainly operate with speeds of 20-150 mm/s, meaning the error introduced by using tanh will only have an effect in the transition period between two directions. The use of tanh is therefore found acceptable.

5.1.1 Cylinder Dynamics

The dynamics of the pressures in the chambers of the cylinder p_1 and p_2 can be determined based on the continuity equation shown in eq. (5.4) and (5.5).

$$Q_1 - Q_{LeakInt} - Q_{LeakExt1} = A_{p,1}\dot{x}_p + \frac{V_1}{\beta_1}\dot{p}_1 \tag{5.4}$$

$$Q_{LeakInt} + Q_2 - Q_{LeakExt2} = -A_{p,2}\dot{x}_p + \frac{V_2}{\beta_2}\dot{p}_2 \tag{5.5}$$

where

$$V_1 = V_{0,1} + A_{p,1}x_p \tag{5.6}$$

$$V_2 = V_{0,2} - A_{p,2}x_p \tag{5.7}$$

where $V_{0,1}$, $V_{0,2}$ are defined as the volumes in each chamber when the piston is in middle position together with the volume in the hoses connecting the valve and cylinder.

The flows Q_1 and Q_2 can be calculated based on the orifice equation and valve dynamics, see Sec. 5.1.2.

The set-up used for this project will have needle valves emulating the leakages. Flows across valves can usually be assumed turbulent. However, at low pressure drops and small openings, which may be the case when emulating small leakage flows, the Reynolds number may become sufficiently low to permit laminar flow. The minimum Reynolds number for a flow to be considered turbulent depends on the shape of the cross section area, ≈ 600 for valves. [T.O.Andersen, 2007]
The Reynolds number can be calculated by eq. (5.8), [T.O.Andersen, 2007].

$$Re = \frac{\bar{u} d_h}{\nu_{oil}} = \frac{d_h}{A \nu_{oil}} Q \tag{5.8}$$

where

$\bar{u}$	is the average velocity of flow	[m/s]
d_h	is the hydraulic diameter	[m]
ν_{oil}	is the kinematic viscosity of the oil	[m^2/s]
A	is the opening area	[m^2]

where ν_{oil} is 50 cSt, $1cSt = 10^{-6} \frac{m^2}{s}$, based on [T.O.Andersen, 2007].

To determine the maximum Reynolds number that can be achieved under test conditions, the range of leakage flows is used, which is up to ≈ 10 L/min, or 25 % of the maximum flow supplied to the system. By sweeping across the range of valve openings that will be used to simulate leakage flows, together with a range of pressures from 1-180 bar as pressure difference, the leakage flow is found to be turbulent for flows larger than 0.6 L/min. However, if the maximum valve opening is used in the simulation, then a minimum of 4 L/min is observed. In order to simulate leakages below 0.6 L/min the Reynolds numbers is above 600 unless the pressure difference is close to 0 bar. The error introduced for those cases is found to be negligible because the flows are very small. Based on this, the discharge coefficient used in the orifice equation can be kept constant at 0.6, corresponding to a turbulent flow.

The leakage flow can then be calculated by an orifice equation as:

$$Q_{LeakInt} = C_d A_{LeakInt} \sqrt{|(p_1 - p_2)|} S(p_1 - p_2) \tag{5.9}$$

$$Q_{LeakExt1} = C_d A_{LeakExt1} \sqrt{|(p_1 - p_t)|} S(p_1 - p_t) \tag{5.10}$$

$$Q_{LeakExt2} = C_d A_{LeakExt1} \sqrt{|(p_2 - p_t)|} S(p_2 - p_t) \tag{5.11}$$

where $S(\bullet)$ is a sign function and C_d = 0.6. The value of $A_{LeakInt}$, $A_{LeakExt1}$, $A_{LeakExt2}$ will initially be 0, due to the valves being closed. The valves can be opened during testing, to emulate faults causing a change in the leakage flow.
For the IARC to compensate for the varying leakage flow, the leakage flow will be estimated directly through an estimation algorithm described in Sec. 7.2.

The bulk modulus, β, in (5.4) and (5.5) can be approximated based on (5.13) as described in

[T.O.Andersen, 2007].

$$\beta_{eff,i}(t, p_{a,i}, \varepsilon_A) = \frac{1}{\frac{1}{\beta_F} + \varepsilon_A \left(\frac{1}{\beta_A} - \frac{1}{\beta_F}\right)} \approx \frac{1}{\frac{1}{\beta_F} + \frac{\varepsilon_A}{\beta_A}} \quad i = 1,2 \tag{5.12}$$

$$\beta_A = c_{ad} p_{a,i}, \quad i = 1,2 \tag{5.13}$$

where

β_{eff}	is effective stiffness of the fluid-air mixture	[Pa]
ε_A	is the volumetric ratio of free air in the fluid, (5.14)	[-]
β_F	is the stiffness of the pure fluid according to β_A	[Pa]
β_A	is the air stiffness according to the pressure, $p_{a,i}$	[Pa]
t	is the temperature of the oil	[$^\circ C$]
$p_{a,i}$	is the absolute pressure in each chamber	[Pa]
c_{ad}	is the adiabatic constant for air, 1.4	[-]

From eq. (5.13), bulk modulus is a varying parameter, depending on the pressure, temperature, and air volume ratio in the oil. In fig. 5.4, different scenarios of air volume ratios have been shown, where ε_A is calculated based on (5.15). The result is that if the oil contains no air, then the bulk modulus can be considered constant, assuming constant density, and with an increasing reference volumetric ratio of free air in the fluid at atmospheric pressure, ε_{A0}, the bulk modulus reaches a constant value at a higher pressure, assuming constant density.

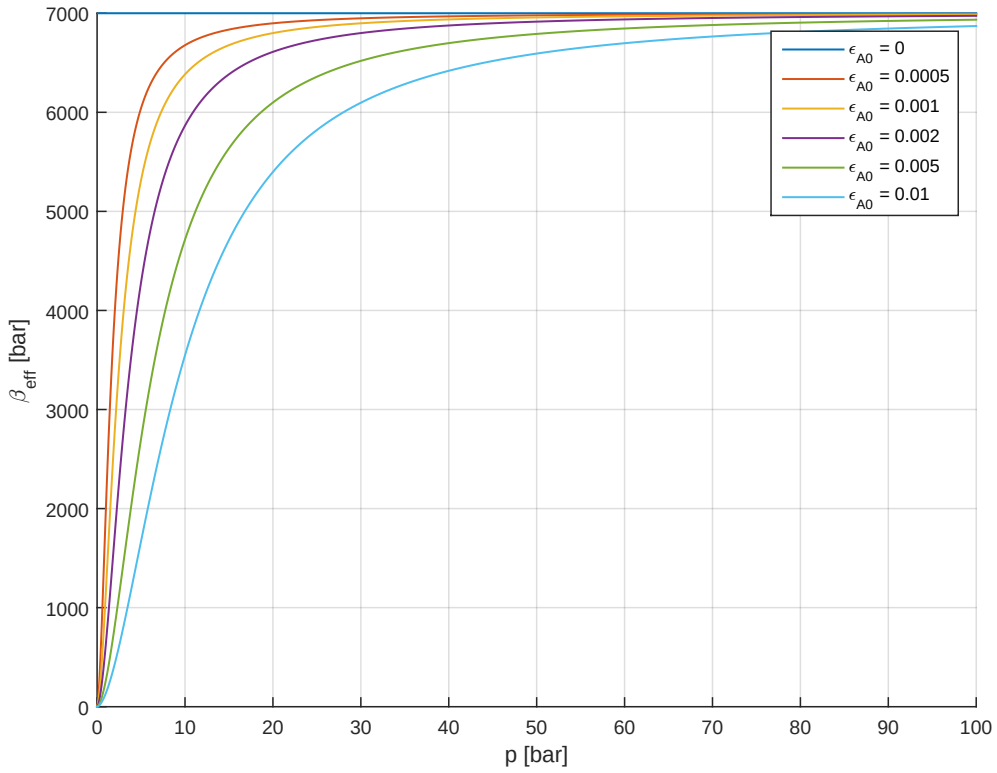

Figure 5.4: Effective bulk modulus build up for different air to oil ratios.

During faulty situations, the ratio of air in the oil, ε_{A0}, may not be constant, resulting in a

varying bulk modulus when the pressures are relatively small. To calculate ε_A based on ε_{A0}, eq. (5.14) will be used [T.O.Andersen, 2007].

$$\varepsilon_A(t,p,p_a) = \frac{1}{\left(\frac{1.0-\varepsilon_{A0}}{\varepsilon_{A0}}\right)\frac{\rho_0(t_0)}{\rho(t,p)}\left(\frac{p_{\text{atm}}}{p_a}\right)^{\frac{-1}{c_{ad}}} + 1.0} \tag{5.14}$$

where

ε_{A0}	is the volumetric ratio of free air in the fluid at atmospheric pressure	[-]
p_{atm}	is the atmospheric pressure	[Pa]
p	is the pressure in each chamber	[Pa]
$\rho_0(t_0)$	is the mass density at atmospheric pressure	[kg/m^3]
$\rho(t,p)$	is the pressure in each chamber	[kg/m^3]
t_0	is the reference temperature	[$^\circ C$]

For the modelling, eq. (5.14) is simplified by assuming $\rho_0(t_0)$=$\rho(t,p)$. The assumption is based on that the temperature variations expected on the system will not have a significant impact on the density of the oil. During experimental testing, the temperature of the oil varied from 36-56 $^\circ C$, which corresponds to an ≈ 2 % variation in the density. Furthermore, the pressure variation in the system are not significant enough to result in significant density variations (supply of 180 bar). The resulting equation is:

$$\varepsilon_A(t,p_a) = \frac{1}{\left(\frac{1.0-\varepsilon_{A0}}{\varepsilon_{A0}}\right)\left(\frac{p_{\text{atm}}}{p_a}\right)^{\frac{-1}{c_{ad}}} + 1.0} \tag{5.15}$$

The IARC will be able to compensate for a varying air-ratio by estimating the size of Bulk-modulus with an etimation algorithm described in Sec. 7.2

5.1.2 Valve Dynamics

The valve used in this project is a MOOG D633 directly actuated servo valve. The spool actuation is achieved with a voltage input. The valve posses a 40 L/min capacity seen in fig. 5.5. The valves frequency response is given by the producer as fig. 5.5.

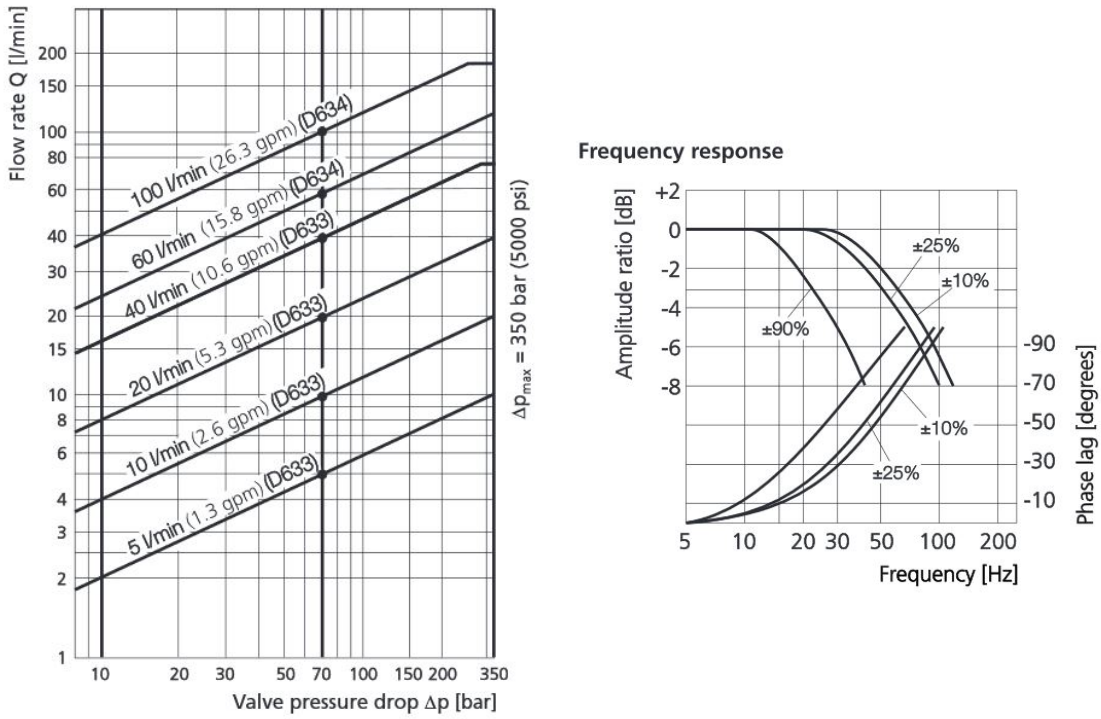

Figure 5.5: Flow rate of MOOG D633 (left) and Frequency response of MOOG D633 servo valve (right) [Inc., 2009]

The flows from the valve, Q_1 and Q_2, can be described by the orifice equation, eq. (5.16) and (5.17).

$$Q_1 = k_q x_v \sqrt{|\Delta p_1|} S(\Delta p_1) \tag{5.16}$$

$$Q_2 = -k_q x_v \sqrt{|\Delta p_2|} S(\Delta p_2) \tag{5.17}$$

where k_q is a flow gain coefficient defined as eq. (5.18), x_v is the normalised spool displacement which is controllable by a voltage input, and has the dynamics (5.21). $S(\bullet)$ is a sign function. Δp_i depends on which chamber is connected to the tank, controlled by the valve input, defined as eq. (5.19) and (5.20):

$$k_q = \frac{Q_N}{\sqrt{p_N}} \tag{5.18}$$

$$\Delta p_1 = \begin{cases} p_s - p_1, & x_v \geq 0 \\ p_1 - p_t & x_v < 0 \end{cases} \tag{5.19}$$

$$\Delta p_2 = \begin{cases} p_2 - p_t, & x_v \geq 0 \\ p_s - p_2 & x_v < 0 \end{cases} \tag{5.20}$$

where the nominal flow and pressure, Q_N and p_N, can be found in the datasheet, [Inc., 2009]. The values are 40 L/min and 35 bar.

For the purposes of this project the valve dynamics will be modelled as a 2nd order system with a transfer function:

$$\frac{x_v}{u_{ref}} = \frac{K_v \omega_n^2}{s^2 + 2\zeta\omega_n s + \omega_n^2} \tag{5.21}$$

where

u_{ref}	is the voltage control signal	[V]
K_v	is the gain of the valve from supplied voltage to position of the spool	[m/V]
ω_n	is natural frequency of the valve	[rad/s]
ζ	is the damping ratio of the valve	[-]

From fig. 5.5, the natural frequency will depend on the opening of the valve, ranging from ≈ 22.5-60.0 Hz.

5.1.3 Discussion of Natural Frequencies of the System Components

To get an understanding of how the hydraulic cylinder frequency compares with the valve frequency, the following calculations are made. Furthermore, a short description of the dynamics and system effects of the force controller used to emulate an increase in mass and force related faults will be made.

The values for the transfer function are estimated based on the frequency response in fig. 5.5.

The valve frequency is determined from fig. 5.5 to be 377 rad/s for a ±10% valve opening. The natural frequency of an asymmetric cylinder can be found by equation (5.22) as proposed by [T.O.Andersen, 2007].

$$\omega_{n,cyl}(x_p) = \sqrt{\frac{K_h(x_p)}{M_{eq}}} \tag{5.22}$$

where $K_h(x_p)$ is a function of the position of the cylinder piston and can be defined as

$$K_h(x_p) = \beta_{eff}\left(\frac{{A_{p,2}}^2}{V_2(x_p)} + \frac{{A_{p,1}}^2}{V_1(x_p)} + \frac{{A_{p,3}}^2}{V_3(x_p)} + \frac{{A_{p,4}}^2}{V_4(x_p)}\right) \tag{5.23}$$

where $_3$, $_4$ corresponds to the piston and rod side of the load cylinder respectively. The result for the natural frequencies of the two cylinders can be seen in fig. 5.6 together with the valve frequency at 10 % corresponding to the fastest natural .

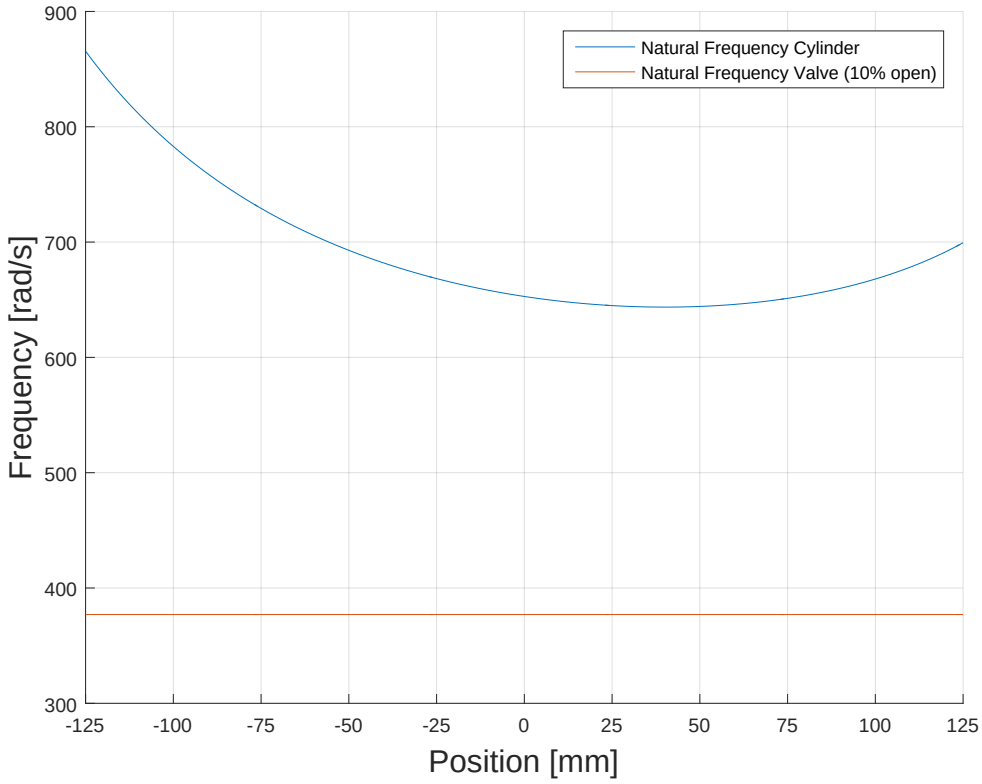

Figure 5.6: Cylinder frequency as a function of position.

The natural frequency of the test cylinder is calculated to be ≈640 rad/s at a linearisation point of 25 mm and 30 mm/s. The reasoning for the linearisation position and the procedure can be seen in appendix A. By comparing the frequencies in fig. 5.6, it is shown that the cylinder natural frequencies are approximately a factor of 2 faster than the fastest case for the valve(10% opening). From this, the fast dynamics of the cylinder will not be excited, and should not be a concern when tuning the controller. However, for the case where the load cylinder is supplying a large force, corresponding to an increased mass of the system, then the natural frequencies of the cylinder may decrease to values where the valve is faster. This is done to emulate conditions for a wind-turbine pitch system. Due to this, the frequencies have been calculated again, with an upper and lower bound of the desired emulated mass, 6000-9000 kg. The result can be seen in fig. 5.7. This range is associated with the ranges of mass uncertainty the non-linear controller will be tuned for.

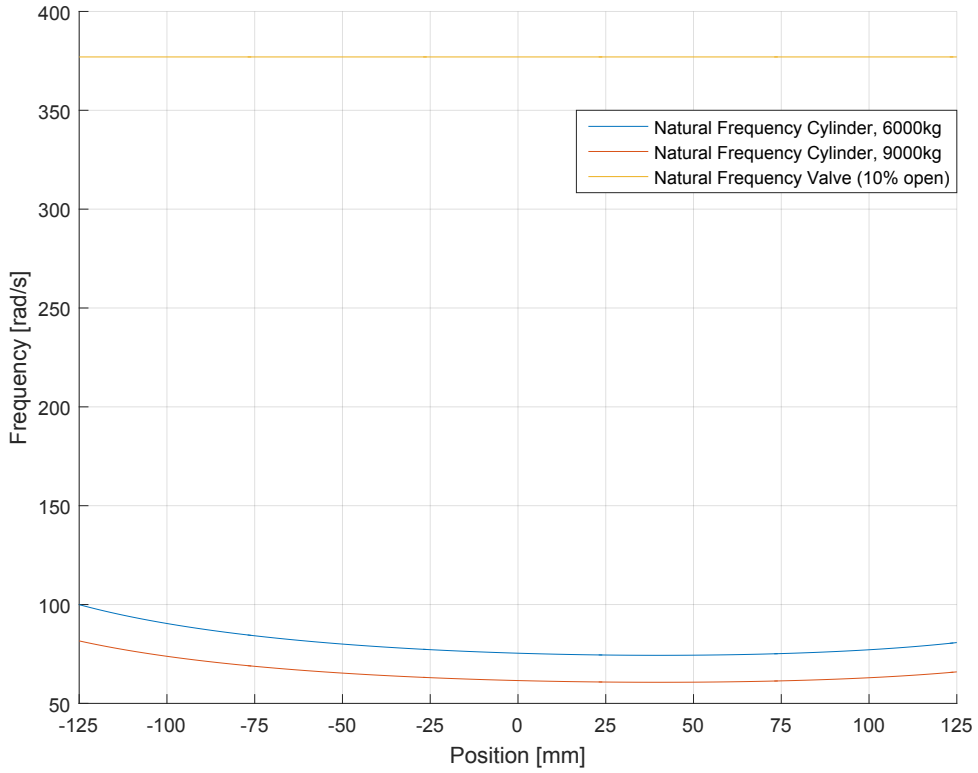

Figure 5.7: Cylinder frequency with a simulation of larger mass as a function of position.

Fig. 5.7 shows that when a large load is applied to the cylinder, the natural frequency is reduced significantly. For the force controller design, the resulting frequency of the load cylinder system should not be faster than the valve, in order to obtain a good response. To make sure the valve frequency will not become a problem, the valve dynamics will be included in the design of the force controller.

In App. A a linear model of the system is defined and verified with the non-linear model described in this chapter. The linear model determined is used to design the force controller, used to emulate an increased mass, together with variations in the mass, load, and friction parameters in the system.

The reference force for the load controller is calculated from a reference mass, viscous friction, and Coulomb friction, together with the position trajectory. Where the reference mass, viscous friction and Coulomb friction are used to emulate time varying parameters. A block diagram of the structure is shown in fig. 5.8.

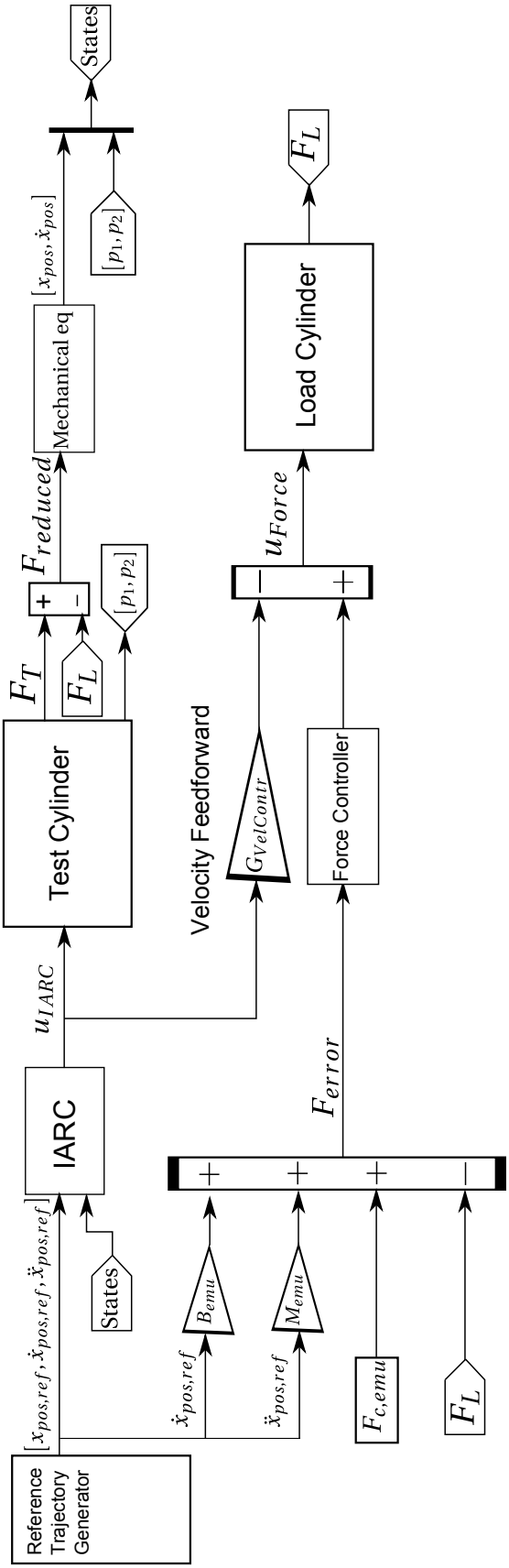

Figure 5.8: Block diagram of force controller structure.

To emulate the variations in force related parameters as realistic as possible, the force controller needs to be able to emulate the variations at least as fast as the reference dynamics. To reduce the limitations the force controller will have emulating on the simulations, the force controller is designed to be as fast as possible. The resulting force controller has a rise-time of 4 ms and a settling time of 36 ms, with an overshoot of 27 %. Applying the force controller to the load cylinder, the resulting bandwidth of the load cylinder subsystem is 78 Hz. The fast controller has the benefit of being able to follow the reference fast enough to for example emulate the increased mass. The load cylinder control will include a velocity feedforward in order to reduce the possible pressure build up when the test cylinder accelerates.

To ensure that the tuning of the IARC does not exceed the bandwidth of the force controller, the force controller will be included in the model used for tuning of the IARC in Chap. 8.

CHAPTER 6

SUB-CONCLUSION

In this part of the report a non-linear model of the hydraulic system has been established. Based on information from an FMEA analysis, the following parameters have been chosen for fault emulation: Mass, Friction parameters, Air-level in the oil, and internal/external leakage. These parameters will be varied in the non-linear model and later on, changes in them will be emulated in the lab. The non-linear model has been linearised in order to investigate the eigenfrequency of the system. Furthermore a force controller is designed for one of the cylinders. This controller will provide the forces, which will emulate parameter changes in the lab. In order to bring the conditions in the lab closer to those expected for a cylinder in a wind-turbine pitch system, the force controller will emulate a minimum mass of 6000 kg.

Part III

Control

CHAPTER 7

CONTROL DESIGN AND PARAMETER ESTIMATION

7.1 Control Design

For the design of the indirect adaptive robust control law, a modularised backstepping design is used [Mohanty and Yao, 2011]. To guarantee transient performance and tracking accuracy the standard design requires that no unknown non-linearities are present in the system. However, this is not the case for the system in this project due to the interest of faulty situations. In order for the method to still guarantee a minimum transient performance and tracking accuracy, [Mohanty and Yao, 2011] proposes to utilise the known, bounded and pre-set adaptation rate for the uncertain parameters, determined in Chap. 8. With the assumption that the parameters will remain within these bounds it is possible to prove the stability of the controller. The control law and estimation algorithm will be explained in the following.

The general idea of the structure of the controller and estimation algorithm can be seen on fig. 7.1, where the estimator sends the estimated parameters, $\hat{\boldsymbol{\theta}}$, to the controller, calculated based on the previous states, $\boldsymbol{x}$, and control input, u. The estimator has a filter added, to make sure the states are smooth and continuous, so the time derivative of velocity and pressures can be calculated. This is done due to the acceleration and time derivative of pressure not being measurable. The controller then sends out a new control input, u, and new plant outputs are obtained. The cycle then repeats.

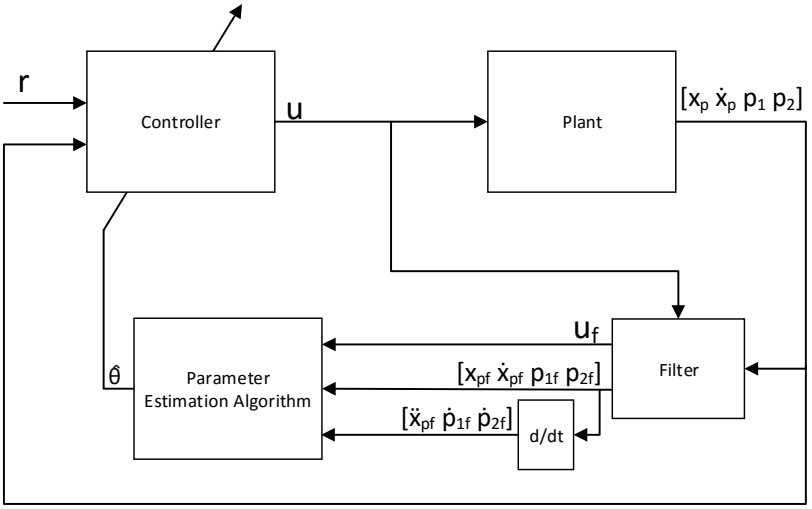

Figure 7.1: Block structure of plant, estimation algorithm, and control law

In this chapter, the following nomenclature is used: $\hat{\bullet}$ is used to denote estimate of $\bullet$, and $\tilde{\bullet}$ is used to denote the error between real and estimate of $\bullet$, e.g. $\tilde{\bullet} = \hat{\bullet} - \bullet$.

Uncertain Parameters

The system model from chapter 5 includes a number of uncertain parameters. The uncertain parameters are defined as:

$\boldsymbol{\theta}$	$= [\theta_1 \quad \theta_2 \quad \theta_3 \quad \theta_4 \quad \theta_5 \quad \theta_6 \quad \theta_7]$		
θ_1	$= M_{eq}$	Equivalent mass of piston and load mass	[kg]
θ_2	$= B$	Viscous friction coefficient and damping	[Ns/m]
θ_3	$= F_c$	Coulomb friction	[N]
θ_4	$= D_{1n}$	Lumped model error in the force equation, i.e. friction	[N]
θ_5	$= \beta^{-1}$	Inverse bulk modulus	[Pa^{-1}]
θ_6	$= D_{21n}$	Nominal lumped model error in the continuity equation, i.e. leakage	[m^3/s]
θ_7	$= D_{22n}$	Nominal lumped model error in the continuity equation, i.e. leakage	[m^3/s]

Accurate off-line estimations can be made for some of these parameters (B, F_c, β^{-1}) through laboratory tests. These estimation will only be correct for specific conditions. Their values can change over time, as a function of other system parameters (pressure for β^{-1}) or during faulty operation. The modelling error D_{1n} is present due to omitted dynamics such as the Stribeck effect. [Mohanty and Yao, 2011] use a 3 DoF robotic manipulator, which means that some coupling effect is probably included in their article, which will not be present here. The D_{21n} and D_{22n} modelling errors contain the internal leakage and external leakages, which can occur. $\tilde{D}_1$, $\tilde{D}_{21}$, and $\tilde{D}_{22}$ are the changes in the lumped model errors from the nominal value in case

of incorrect estimation or faults. The system model can then be expressed by eq. (7.1)-(7.3):

$$\theta_1 \ddot{x}_p = p_1 A_{p,1} - p_2 A_{p,2} - \theta_2 \dot{x}_p - \theta_3 S(\dot{x}_p) + \theta_4 + \tilde{D}_1 \tag{7.1}$$

$$\theta_5 \dot{p}_1 = -\frac{A_{p,1}}{V_1}\dot{x}_p + \frac{Q_1}{V_1} - \frac{\theta_6}{V_1} - \frac{\tilde{D}_{21}}{V_1} \tag{7.2}$$

$$\theta_5 \dot{p}_2 = \frac{A_{p,2}}{V_2}\dot{x}_p + \frac{Q_2}{V_2} + \frac{\theta_7}{V_2} + \frac{\tilde{D}_{22}}{V_2} \tag{7.3}$$

The control law will be designed to cancel out the system dynamics and to force the error dynamics of the closed loop to converge to zero. The stability of the plant depends on the accuracy of the estimated parameters. For this reason certain requirements are imposed on the control law. For the control design and parameter estimation method, a requirement to prove stability and convergence is that the uncertain parameters are bounded to a specific range and rate of change. Larger bounds i.e. more uncertainty and possibility for larger estimation error, lead to larger control gains.

The ranges for the uncertain parameters are determined based on the nominal system parameters and restrictions due to system performance. These will be discussed when choosing the control gains and the parameters used in the estimation algorithm in Chap. 8.

States of the System

Before the control method is explained, the states of the system are introduced, where the piston position, velocity and chamber pressures are assumed measurable. The states are:

$$\begin{aligned}
\boldsymbol{x} &= [x_1 \quad x_2 \quad x_3 \quad x_4]^T \\
x_1 &= x_p \\
x_2 &= \dot{x}_p \\
x_3 &= p_1 A_{p,1} \\
x_4 &= p_2 A_{p,2}
\end{aligned}$$

By inserting the defined states into the system equations (7.1)-(7.3), the time derivatives of the states can be calculated as:

$$\dot{x}_1 = x_2 \tag{7.4}$$

$$\theta_1 \dot{x}_2 = x_3 - x_4 - \theta_2 x_2 - \theta_3 S(x_2) + \theta_4 + \tilde{D}_1 \tag{7.5}$$

$$\theta_5 \dot{x}_3 = -\frac{A_{p,1}^2}{V_1}x_2 - \theta_6 \frac{A_{p,1}}{V_1} + Q_1 \frac{A_{p,1}}{V_1} - \tilde{D}_{21}\frac{A_{p,1}}{V_1} \tag{7.6}$$

$$\theta_5 \dot{x}_4 = \frac{A_{p,2}^2}{V_2}x_2 + \theta_7 \frac{A_{p,2}}{V_2} + Q_2 \frac{A_{p,2}}{V_2} + \tilde{D}_{22}\frac{A_{p,2}}{V_2} \tag{7.7}$$

7.1.1 Backstepping Design

For the backstepping design method, a number of variables and virtual controllers are introduced to prove convergence, and by combining these, a control input is defined. The method starts with a virtual controller for the position error. It then moves through the derivatives until a directly controllable state is found. In this case the derivative of the pressures of the system.

For the position and velocity states, two variables, z_1, z_2 are defined:

$$z_1 = x_1 - x_{1d} \tag{7.8}$$

$$z_2 = \dot{z}_1 + k_1 z_1 = x_2 - x_{2eq} \tag{7.9}$$

$$x_{2eq} \triangleq \dot{x}_{1d} - k_1 z_1 \tag{7.10}$$

where x_{1d} is the reference position and k_1 is a positive gain feedback. The size of the gain k_1 and the following control gains introduced later in this section are chosen based on an optimisation algorithm, described in Chap. 8. (7.8) corresponds to the position error, and (7.9) is the velocity error, with a position feedback. The transfer function for eq. (7.9) is:

$$G_s(s) = \frac{z_1(s)}{z_2(s)} = \frac{1}{s + k_1} \tag{7.11}$$

The transfer function is stable for $k_1 \geq 0$. From the transfer function, it can be seen that z_1 is bounded if z_2 is bounded. Furthermore, it can be seen that making z_2 small or converging to zero is equivalent to making z_1 small or converging to zero. These considerations are needed for the Lyapunov proof of stability for the controller. The next step of the design is then to make z_2 as small as possible.

To prove convergence of z_2 to as small a value as possible with a guaranteed transient performance, a time derivative of (7.9) is inserted into the system eq. (7.5):

$$\theta_1 \dot{x}_2 = \theta_1 \dot{z}_2 + \theta_1 \dot{x}_{2eq} \tag{7.12}$$

$$\theta_1 \dot{z}_2 = x_3 - x_4 - \theta_2 x_2 - \theta_3 S(x_2) + \theta_4 + \tilde{D}_1 - \theta_1 \dot{x}_{2eq} \tag{7.13}$$

Eq. (7.13) becomes the error dynamics of the velocity of the system. The controllable input in this equation is the load force ($F_L = x_3 - x_4$). This load force can be selected with the intention to cancel out the influence of the other parameters in the equation. Furthermore the load force can ensure that $\dot{z}_2$ has an opposite sign to z_2. The load force is dependent on the pressures in the chambers of the actuator. These can be manipulated by the valve input. If this load force is selected with these considerations in mind, it can make z_2 converge to zero. For this purpose F_L is selected as the virtual control law α_2 which is designed as:

$$\alpha_2(x_1, x_2, \hat{\boldsymbol{\theta}}, t) = \alpha_{2a} + \alpha_{2s} \tag{7.14}$$

$$= \alpha_{2a} + \alpha_{2s1} + \alpha_{2s2} \tag{7.15}$$

where the α_{2a} part of the control law, is designed to cancel out the current estimate of $\boldsymbol{\theta}$, and α_{2s} consists of the control gains. The resulting equations for them are:

$$\alpha_{2a} = \hat{\theta}_1 \dot{x}_{2eq} + \hat{\theta}_2 x_2 + \hat{\theta}_3 S(x_2) - \hat{\theta}_4 \tag{7.16}$$

$$\alpha_{2s1} = -k_2 z_2 \tag{7.17}$$

$$\alpha_{2s2} = -k_{2s}(x_1, x_2, t) z_2 \tag{7.18}$$

By inserting the virual control law $\alpha_2 = x_3 - x_4$ into (7.13), the following is achieved:

$$\theta_1 \dot{z}_2 = -k_2 z_2 + (\boldsymbol{\varphi}_2^T \tilde{\boldsymbol{\theta}} + \tilde{D}_1 - k_{2s} z_2) \tag{7.19}$$

where:

$$\boldsymbol{\varphi}_2 = [\dot{x}_{2eq} \quad x_2 \quad S(x_2) \quad -1 \quad 0 \quad 0 \quad 0]^T \tag{7.20}$$

Again the aim is to ensure z_2 converges towards zero, which in this case requires that the term $\tilde{D}_1 + \boldsymbol{\varphi}_2^T\tilde{\boldsymbol{\theta}} - k_{2s}z_2$ is dominated by k_{2s}. The terms $\tilde{D}_1 + \boldsymbol{\varphi}_2^T\tilde{\boldsymbol{\theta}}$ can be seen as a disturbance preventing the error dynamics from converging to zero, since they are not dependent on z_2. If the estimation of the parameters is perfect, then the estimation error $\tilde{\boldsymbol{\theta}}$ will be zero, removing this term. Of course this is not a reliable assumption and the size of k_{2s} has to be selected large enough to reduce the effect of these terms. As z_2 converges towards zero the influence of $k_{2s}z_2$ reduces as well. This means that $z_2 = 0$ is not achievable unless $\tilde{\boldsymbol{\theta}} = \tilde{D}_1 = 0$, but a small value can be reached. In order to ensure that these dynamics are stable and the error will not grow to infinity, steps have to be taken. The expression will be examined at the worst case scenario, where the estimation error is at its maximum and so are the non-linear uncertainties and disturbances. In order to establish bounds for the uncertain non-linearities and uncertain parameters, the following conditions will have to be satisfied when choosing the value of the non-linear gain k_{2s}.

Condition 1	$z_2\left(\alpha_{2s2} + \tilde{D}_1 + \boldsymbol{\varphi}_2^T\tilde{\boldsymbol{\theta}}\right) \leq \varepsilon_2$
Condition 2	$z_2\alpha_{2s2} \leq 0$

Table 7.1: Conditions for the choice of α_{2s2}.

where $\varepsilon_2 \geq 0$ is a design parameter affecting the maximum effect a parameter uncertainty, $\tilde{\boldsymbol{\theta}}$, and uncertain non-linearity, $\tilde{D}_1$ can have on the system. A consideration when choosing the size of ε_2 is, that if chosen too small, a large α_{2s2} is required. Since large values for $\tilde{D}_1 + \boldsymbol{\varphi}_2^T\tilde{\boldsymbol{\theta}}$ increase the size of $\dot{z}_2$ leading to an increasing z_2. In turn z_2 is composed of the current velocity, a velocity reference and a position position error as seen in eq. (7.9). All of these are in practical terms bounded. In that case the control gain k_{2s} can be chosen, so the maximum disturbance cannot exceed the design parameter. The second condition ensures that the term k_{2s} is positive, so the equation for $\dot{z}_2$ minimises the size of z_2.

To chose a value for k_{2s} to satisfy these conditions, a method described in [Yao and Tomizuka, 1997] is used. The method ensures that α_{2s2} satisfies the conditions, while having a smooth non-linear gain function, by utilising a $\tanh(\cdot)$ function. The control law is defined as:

$$\alpha_{2s2} = -h_2 \tanh\left(\frac{h_2 z_2}{\varepsilon_2}\right) \tag{7.21}$$

where the non-linear gain, h_2, is defined as:

$$h_2 \geq ||\boldsymbol{\varphi}_2(x_2)^T\boldsymbol{\theta}_{range}|| + ||\tilde{D}_{1,max}|| \tag{7.22}$$

Here the vector $\boldsymbol{\theta}_{range}$ is defined as maximum error that can occur in the estimation and each element is defined as

$$\theta_{range,i} = \theta_{max,i} - \theta_{min,i} \quad i = 1,2,3,4,5,6,7 \tag{7.23}$$

By using this definition of h_2, the Condition 1 is fulfilled. The use of L_2 norm to calculate the size of h_2 ensures it is a positive scalar. The design parameter ε_2 is also a positive scalar by definition, which means that the sign of (7.21) is determined by z_2. This fulfils Condition 2, because the tanh(·) function will cancel out the sign of z_2 in the condition, equivalent to z_2^2, and the negative sign of (7.21) will give the negative value of the expression. To reduce the effect of noise and the computation required for each iteration, h_2 can be defined as a constant by using the maximum value of $\boldsymbol{\varphi}_2$. The resulting control gain is:

$$h_2 \geq ||\boldsymbol{\varphi}_{2,max}^T \boldsymbol{\theta}_{range}|| + ||\tilde{D}_{1,max}|| \tag{7.24}$$

If α_2 is considered as the desired load force the following of this reference has to be considered. To make sure that the load force F_L will converge to the proposed virtual controller α_2, a third state is introduced, $z_3 = F_L - \alpha_2$, corresponding to a force error. To prove boundedness and convergence of z_2, a Lyapunov candidate is defined as

$$V_2 = \frac{\theta_1}{2} z_2^2 \tag{7.25}$$

$$\dot{V}_2 = \theta_1 z_2 \dot{z}_2 \tag{7.26}$$

Inserting (7.13) in (7.26) gives:

$$\dot{V}_2 = z_2(F_L - \theta_1 \dot{x}_{2eq} - \theta_2 x_2 - \theta_3 S(x_2) + \theta_4 + \tilde{D}_1) \tag{7.27}$$

Using $F_L = z_3 + \alpha_2$ gives:

$$\dot{V}_2 = z_2 \alpha_{2s1} + z_2 \left(\alpha_{2s2} + \tilde{D}_1 + \boldsymbol{\varphi}_2^T \tilde{\boldsymbol{\theta}}\right) + z_2 z_3 \tag{7.28}$$

$$\dot{V}_2 \leq z_2 \alpha_{2s1} + \varepsilon_2 + z_2 z_3 \tag{7.29}$$

$$\dot{V}_2 \leq -k_2 z_2^2 + \varepsilon_2 + z_2 z_3 \tag{7.30}$$

where ε_2 is the user defined constant from the conditions of the virtual control law. This Lyapunov candidate cannot be used to prove stability, because of z_3. At this point the force build up has not been investigated and conclusions about the stability of this error state cannot be drawn. Although, it can be concluded that z_2 is bounded and converges to zero or a small value, if z_3 converges to zero or a small value. This will be investigated later in the chapter, by establishing a combined Lyapunov candidate for z_2 and z_3. In order for this to be possible, the dynamics of z_3 have to be investigated.

The time derivative of z_3 is combined with the time derivative of F_L from eq. (7.6) and (7.7), resulting in:

$$\theta_5 \dot{z}_3 = Q_L - \left(\frac{A_1^2}{V_1} + \frac{A_2^2}{V_2}\right) x_2 - \frac{A_1}{V_1}\theta_6 - \frac{A_2}{V_2}\theta_7 - \theta_5 \dot{\alpha}_{2c} - \theta_5 \dot{\alpha}_{2u} + \tilde{D}_2 \tag{7.31}$$

Once again the aim is to force the dynamics of z_3 so it converges towards zero. The force F_L depends on the load flow determined by valve spool position. The term Q_L can be considered

proportional to the load flow, since it depends on the flows Q_1 and Q_2, but in this case the unit for Q_L is m^2/s. The terms Q_L and $\tilde{D}_2$ are defined as:

$$Q_L = \frac{A_{p,1}}{V_1} Q_1 - \frac{A_{p,2}}{V_2} Q_2 \tag{7.32}$$

$$\tilde{D}_2 = -\frac{A_{p,1}}{V_1} \tilde{D}_{21} - \frac{A_{p,2}}{V_2} \tilde{D}_{22} \tag{7.33}$$

The derivative of α_2 is:

$$\dot{\alpha}_2 = \dot{\alpha}_{2c} + \dot{\alpha}_{2u} \tag{7.34}$$

$$\dot{\alpha}_{2c} = \frac{\delta \alpha_2}{\delta x_1} x_2 + \frac{\delta \alpha_2}{\delta x_2} \hat{\dot{x}}_2 + \frac{\delta \alpha_2}{\delta \hat{\boldsymbol{\theta}}} \hat{\dot{\boldsymbol{\theta}}} + \frac{\delta \alpha_2}{\delta t} \tag{7.35}$$

$$\dot{\alpha}_{2u} = \frac{\delta \alpha_2}{\delta x_2} \tilde{\dot{x}}_2 \tag{7.36}$$

where $\dot{\alpha}_{2c}$ is the calculable part of $\dot{\alpha}_2$. $\dot{\alpha}_{2u}$ is the incalculable part, because acceleration measurement, $\dot{x}_2$, is not available. This means that the estimation error, $\tilde{\dot{x}}_2$ cannot be calculated.
For the calculation of $\dot{\alpha}_2$, a derivation of z_2 as (7.38) is used, which can be derived from (7.9). The values in $\dot{\alpha}_{2c}$ can be defined as the following:

$$z_2 = \dot{x}_1 - \dot{x}_{1d} + k_1(x_1 - x_{1d}) \tag{7.37}$$

$$= x_2 - x_{2d} + k_1(x_1 - x_{1d}) \tag{7.38}$$

$$\frac{\delta \alpha_2}{\delta x_1} = -k_2 k_1 - k_{2s} k_1 \tag{7.39}$$

$$\frac{\delta \alpha_2}{\delta x_2} = \hat{\theta}_2 - k_2 - k_{2s} \tag{7.40}$$

$$\frac{\delta \alpha_2}{\delta \hat{\boldsymbol{\theta}}} = [\dot{x}_{2eq} \quad x_2 \quad S(x_2) \quad -1 \quad 0 \quad 0 \quad 0]^T \tag{7.41}$$

$$\frac{\delta \alpha_2}{\delta t} = \theta_1 \ddot{x}_{2eq} + (k_2 + k_{2s}) \dot{x}_{2d} + (k_2 k_1 + k_{2s} k_1) \dot{x}_{1d} - \dot{k}_{2s} z_2 \tag{7.42}$$

$$= \theta_1 \ddot{x}_{2eq} + (k_2 + k_{2s}) \dot{x}_{2d} + (k_2 k_1 + k_{2s} k_1) \dot{x}_{1d} \tag{7.43}$$

where for the last step, the time derivative of k_{2s} is zero, due to the gain being defined as a constant in eq. (7.24). The equations for $\hat{\dot{x}}_2$ and $\tilde{\dot{x}}_2$ are:

$$\hat{\dot{x}}_2 = \frac{1}{\hat{\theta}_1} \left((x_3 - x_4) - \hat{\theta}_2 x_2 - \hat{\theta}_3 S(x_2) + \hat{\theta}_4 \right) \tag{7.44}$$

$$\tilde{\dot{x}}_2 = \hat{\dot{x}}_2 - \dot{x}_2 \tag{7.45}$$

A virtual control law is applied to select Q_L such that z_3 converges towards zero. The control law should cancel out at least the known part of the derivative of the virtual law α_2 and the pressure dynamics of the system. The virtual control law is:

$$Q_L = Q_{La} + Q_{Ls} = Q_{La} + Q_{Ls1} + Q_{Ls2} \tag{7.46}$$

$$Q_{La} = \left(\frac{A_{p,1}^2}{V_1} + \frac{A_{p,2}^2}{V_2} \right) x_2 - z_2 + \frac{A_{p,1}}{V_1} \hat{\theta}_6 + \frac{A_{p,2}}{V_2} \hat{\theta}_7 + \hat{\theta}_5 \dot{\alpha}_{2c} \tag{7.47}$$

$$Q_{Ls1} = -k_3 z_3 \tag{7.48}$$

$$Q_{Ls2} = -k_{3s}(\boldsymbol{x}, t) z_3 \tag{7.49}$$

where z_2 is introduced in order to cancel out the term $z_2 z_3$ in the Lyapunov candidate (7.30). Similar to α_2, Q_{La} cancels out the known dynamics of the pressures, based on the estimated parameters. Q_{Ls1} drives the z_3 towards zero, since k_3 is a positive control parameter, chosen based on the conditions mentioned for k_1. k_{3s} is a non-linear gain, chosen based on the following two conditions: where

$$\boldsymbol{\varphi}_3 = \begin{bmatrix} 0 & 0 & 0 & 0 & \dot{\alpha}_{2c} & \dfrac{A_{p,1}}{V_1} & \dfrac{A_{p,2}}{V_2} \end{bmatrix}^T \tag{7.50}$$

and ε_3 is s design parameter affecting the maximum effect a parameter uncertainty, $\tilde{\boldsymbol{\theta}}$, uncertain non-linearity, $\tilde{D}_2$, and acceleratoin estimation error, $\dot{\alpha}_{2u}$, can have on the system. Similar to the conditions for k_{2s}, the first condition ensures that the effect from uncertainties will remain bounded and k_{3s} will dominate these errors. The second condition is to make sure the controller Q_{Ls2} follows the desired functionality, e.g. $\dot{z}_3 = -kz_3$. By inserting the proposed control law for Q_L into (7.31) yields:

$$\theta_5 \dot{z}_3 = Q_{Ls1} + Q_{Ls2} + \boldsymbol{\varphi}_3^T \tilde{\boldsymbol{\theta}} - \dot{\alpha}_{2u}\theta_5 + \tilde{D}_2 \tag{7.51}$$

$$= -k_3 z_3 - k_{3s} z_3 + \boldsymbol{\varphi}_3^T \tilde{\boldsymbol{\theta}} + \tilde{D}_2 \tag{7.52}$$

The method used to choose the gain of k_{3s} is the same as for k_{2s}. The control law is defined as:

$$Q_{Ls2} = -h_3 \tanh\left(\frac{h_3 z_3}{\varepsilon_3}\right) \tag{7.53}$$

where non-linear gain is defined as:

$$h_3 \geq ||\boldsymbol{\varphi}_3(x_1, x_2, \hat{\boldsymbol{\theta}}, t)^T \boldsymbol{\theta}_{range}|| + ||\dot{\alpha}_{2u,max}(\theta_{5,max} - \theta_{5,min})|| + ||\tilde{D}_{2,max}|| \tag{7.54}$$

Like h_2, the control gain can be simplified to be using a constant value for $\boldsymbol{\varphi}_3$, to reduce the computation time and noise effect. Due to a lack in acceleration measurement the term $\dot{\alpha}_{2u,max}(\theta_{5,max} - \theta_{5,min})$ will not be zero. It is included here, so the non-linear gain can suppress maximum influence. The resulting control gain is:

$$h_3 \geq ||\boldsymbol{\varphi}_{3,max}^T \boldsymbol{\theta}_{range}|| + ||\dot{\alpha}_{2u,max}(\theta_{5,max} - \theta_{5,min})|| + ||\tilde{D}_{2,max}|| \tag{7.55}$$

The proof of convergence by use of a Lyapunov candidate of z_3 will be shown in sec. 7.3, due to convergence of the estimation algorithm determined in the next section is part of the proof.

Assuming the virtual control law, Q_L, is valid, and z_3 converges to zero, the control law for the system can be defined. Due to Q_L being controllable by the valve input, and the parameters for the valve are known, the virtual control law for Q_L can be used to determine the control input

Condition 1	$z_3\left(Q_{Ls2} + \boldsymbol{\varphi}_3^T \tilde{\boldsymbol{\theta}} - \dot{\alpha}_{2u}\theta_5 + \tilde{D}_2\right) \leq \varepsilon_3$
Condtion 2	$z_3 Q_{Ls2} \leq 0$

Table 7.2: Conditions for the choice of Q_{Ls2}.

to the system by isolating x_v in the following:

$$Q_L = \frac{A_{p,1}}{V_1} Q_1 - \frac{A_{p,2}}{V_2} Q_2 \tag{7.56}$$

$$= \frac{A_{p,1}}{V_1} k_q x_v \sqrt{\Delta p_1} + \frac{A_{p,2}}{V_2} k_q x_v \sqrt{\Delta p_2} \tag{7.57}$$

$$x_v = u = \frac{Q_L}{\frac{A_{p,1}}{V_1} k_q \sqrt{\Delta p_1} + \frac{A_{p,2}}{V_2} k_q \sqrt{\Delta p_2}} \tag{7.58}$$

where for $x_v = u$ it is assumed that the control gains fulfil the condition that the frequency of the controller do not exceed the bandwidth of the servo valve.

A diagram showing how the different states and control laws are connected can be seen on fig. 7.2.

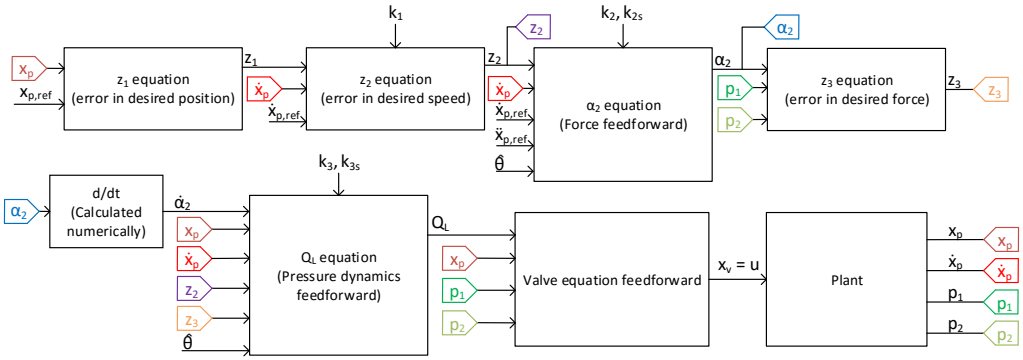

Figure 7.2: Diagram of control structure

From 7.2, the structure of the control law gives an overview of how the final control law is obtained. Furthermore, the two virtual controllers both require the estimated parameters as inputs. Due to this, the convergence speed of the estimation algorithm, introduced in the next section, is correlated to the performance of the IARC.

The requirement for the backstepping design utilised to obtain this control input, is the boundedness of the uncertain parameters and non-linearities. Furthermore, as mentioned above, to accurately cancel out the dynamics of the system, an accurate estimate of its parameters is needed. To achieve this, a parameter estimation algorithm is introduced in the following section, Sec. 7.2. Once that is established the combined Lyapunov candidate can be examined and the stability of the control law can be proven.

7.2 Parameter Estimation

For the IARC algorithm to be fault tolerant and work satisfactory a parameter estimation of the uncertain parameters, $\boldsymbol{\theta}$, is needed. The general idea of parameter estimation is that at each time instant, the parameter estimation algorithm utilises the previous control input and measurements to update the uncertain parameters. The updated parameters are then used in the computation of the next control input. The proposed method in [Mohanty and Yao, 2011] is

an indirect adaptive control, which separates the estimation and control law by first estimating the parameters and then computing the control parameters. The other method is the direct adaptive control which combines the two, and estimates the control parameters directly. Due to the study [Mohanty and Yao, 2011] having shown that the indirect method was superior to the direct method tested on a similar system, the indirect method will be used for this report.

The parameter estimation can be done in various ways, for example gradient or least square estimation methods. This project will use the least square method, because it has proven itself to be more efficient in [Mohanty and Yao, 2011].

Least square estimation is based on regression analysis in order to determine the parameters in a system. Its based on a cost function which contains the prediction error. A simple example of how the parameter estimation is done, based on an example from [Slotine et al., 1991], is: Consider a system where the acceleration can be measured, and the mass is uncertain.

$$m\ddot{x} = F = u \tag{7.59}$$

$$\hat{m}(t) = \frac{u(t)}{\ddot{x}} \tag{7.60}$$

By using this estimation directly, the noise of the measurements may give significant errors. To overcome this problem, the least-square approach can be used. The total prediction error is estimated as:

$$J = \int_0^t e^2(r)\, dr \tag{7.61}$$

where the prediction error is defined as:

$$e(t) = \hat{m}(t)\ddot{x}(t) - u(t)$$

By using this error minimisation, the measurement noise is potentially averaged out. The resulting estimate is:

$$\hat{m} = \frac{\int_0^t wu\, dr}{\int_0^t w^2\, dr} \tag{7.62}$$

where $w = \ddot{x}$. For a time varying parameter, this calculation has to be done for every iteration, which may cause computational problems. To overcome this, an estimation gain is defined as:

$$P(t) = \frac{1}{\int_0^t w^2\, dr} \tag{7.63}$$

where the update can be obtained by:

$$\frac{d}{dt}[P^{-1}] = w^2 \tag{7.64}$$

By inserting this into eq, (7.62), the time derivative of the uncertain parameter is obtained as:

$$P^{-1}\hat{m} = \int_0^t wu\, dr \tag{7.65}$$

$$P^{-1}\dot{\hat{m}} + \frac{d}{dt}[P^{-1}]\hat{m} = wu \tag{7.66}$$

$$P^{-1}\dot{\hat{m}} + w^2\hat{m} = wu \tag{7.67}$$

$$P^{-1}\dot{\hat{m}} = wu - w^2\hat{m} = -we \tag{7.68}$$

$$\dot{\hat{m}} = -P(t)we \tag{7.69}$$

The estimate can then be calculated by numerically integrating eq. (7.69).

With the general idea of parameter estimation introduced, the method can be applied to the system of interest.
To apply the method the first step is to define the output of the system with the assumption that no uncertain non-linearities are present, i.e. $\tilde{D}_1 = \tilde{D}_{21} = \tilde{D}_{22} = 0$. For cases where this assumption is not true, the estimation algorithm will not work optimally, and will not converge to the correct parameters. The reason for this is that the uncertain non-linearities will be seen as an error in the estimation algorithm. The effect this will have on the control algorithm can be seen from the Lyapunov candidate, described in the section 7.3. There it is shown that the states, z_2 and z_3, converges to a value bounded by ε. The value converged to will be proportional to $\tilde{\boldsymbol{\theta}}$. Due to the non-linear uncertainties affecting the estimation algorithm, $\tilde{\boldsymbol{\theta}}$ will only converge to zero, when $\tilde{D}_1 = \tilde{D}_{21} = \tilde{D}_{22} = 0$, and when that is not fulfilled, z_2 and z_3 will converge to a bounded value. This means that the controller will be stable at all times, but performance is depending on the size of $\tilde{\boldsymbol{\theta}}$.

By using this assumption, the system equations can be split up into measurable and known parameters, and uncertain parameters. The left side of the bold equal sign in (7.70)-(7.72) contains the known or measurable components. The right side of the bold equal sign contains the real values of the uncertain parameters and their regressors.

$$y_1 = x_3 - x_4 \mathbf{=} \theta_1 \dot{x}_2 + \theta_2 x_2 + \theta_3 S(x_2) - \theta_4 \tag{7.70}$$

$$y_2 = \frac{-A_{p,1}^2}{V_1} x_2 + \frac{Q_1 A_{p,1}}{V_1} \mathbf{=} \theta_5 \dot{x}_3 - \frac{\theta_6 A_{p,1}}{V_1} \tag{7.71}$$

$$y_3 = \frac{A_{p,2}^2}{V_2} x_2 + \frac{Q_2 A_{p,2}}{V_2} \mathbf{=} \theta_5 \dot{x}_4 + \frac{\theta_7 A_{p,2}}{V_2} \tag{7.72}$$

The acceleration of the system is not available as a direct measurement. To remedy the situation a stable filter of the 3^{rd} order is applied. The reasoning for the third order filter comes from the requirement of velocity, acceleration, and jerk inputs to the estimation algorithm, in (7.70)-(7.72). Due to the acceleration ($\dot{x}_2$), and jerk ($\dot{x}_3$, $\dot{x}_4$) not being measurable they need to be approximated by a time derivative of x_2 and x_3, x_4. To make sure x_2, x_3, and x_4 are smooth and continuous, the third order filter is required. There exists a number of different types of filters that can be used, Bessel, Butterworth, and Chebyshev among others. The filter that will be used for this project is a Butterworth filter due to its flat frequency response, defined as (7.73). When it is applied to previous equations the result is (7.74)-(7.76).

$$H_f = \frac{b_1 s^3 + b_2 s^2 + b_3 s + b_4}{a_1 s^3 + a_2 s^2 + a_3 s + a_4} \tag{7.73}$$

$$y_{1f} = H_f [x_3 - x_4] = \theta_1 s x_{2f} + \theta_2 x_{2f} + \theta_3 S(x_2)_f + \theta_4 (-1)_f \tag{7.74}$$

$$y_{2f} = H_f \left[\frac{-A_{p,1}^2}{V_1} x_2 + \frac{Q_1 A_{p,1}}{V_1} \right] = \theta_5 s x_{3f} - \theta_6 \left(\frac{A_{p,1}}{V_1} \right)_f \tag{7.75}$$

$$y_{3f} = H_f \left[\frac{A_{p,2}^2}{V_2} x_2 + \frac{Q_2 A_{p,2}}{V_2} \right] = \theta_5 s x_{4f} + \theta_7 \left(\frac{A_{p,2}}{V_2} \right)_f \tag{7.76}$$

where the subscript $_f$ denotes that this is a filtered value. The variables $\dot{x}_{2f}$, $\dot{x}_{3f}$, and $\dot{x}_{4f}$ are estimated by sx_{2f}, sx_{3f}, and sx_{4f} in (7.74)-(7.76), where s is a Laplace transformation of the

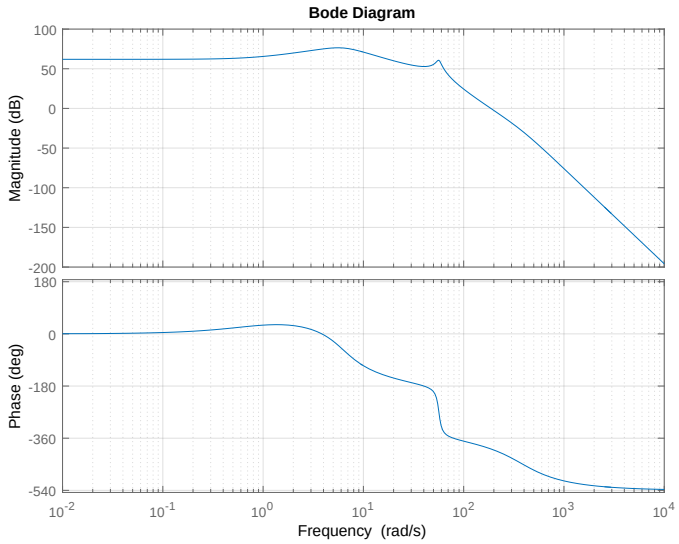

Figure 7.3: Open loop bode diagram of the system with the 3^{rd} order Butterworth filter applied.

derivation function. A bode diagram of the filter H_f applied to the open loop system is shown in fig. 7.3.

The filter is designed in such a way as to allow the system dynamics to be excited, but it will stop the high frequency noise, which will be present in the measured signals. The cut-off frequency of the filter has been chosen as 1 Hz. The relatively low frequency compared with the natural frequency of the system can be explained by the large resonance peak of the open loop system A.3, which has a size of 94 dB that occurs a decade after the cut-off frequency of the valve. Since it is a 3^{rd} order filter the frequency response decays with 60 dB/dec leaving a positive response at the natural frequency and cutting off at ≈ 200 rad/s. The frequency of the noise is 1 kHz or ≈ 3000 rad/s, resulting in the majority of the noise being filtered out.

The second step is to define the regressor matrices from (7.74)-(7.76):

$$\boldsymbol{\varphi}_{1f} = \begin{bmatrix} sx_{2f} & x_{2f} & S(x_2)_f & (-1)_f \end{bmatrix}^T \tag{7.77}$$

$$\boldsymbol{\varphi}_{2f} = \begin{bmatrix} sx_{3f} & \left(\frac{A_{p,1}}{V_1}\right)_f \end{bmatrix}^T \tag{7.78}$$

$$\boldsymbol{\varphi}_{3f} = \begin{bmatrix} sx_{4f} & \left(\frac{A_{p,2}}{V_2}\right)_f \end{bmatrix}^T \tag{7.79}$$

and the vector of uncertain parameters

$$\boldsymbol{\theta}_{1s} = \begin{bmatrix} \theta_1 & \theta_2 & \theta_3 & \theta_4 \end{bmatrix}^T \tag{7.80}$$

$$\boldsymbol{\theta}_{2s} = \begin{bmatrix} \theta_5 & \theta_6 \end{bmatrix}^T \tag{7.81}$$

$$\boldsymbol{\theta}_{3s} = \begin{bmatrix} \theta_5 & \theta_7 \end{bmatrix}^T \tag{7.82}$$

Then the regression model can be defined as

$$y_{if} = \boldsymbol{\varphi}_{if}{}^T \boldsymbol{\theta}_{is} \tag{7.83}$$

where $i = \{1,2,3\}$. The error between the estimated output and the real output can be defined as

$$\epsilon_i = \hat{y}_{if} - y_{if} \tag{7.84}$$

$$\epsilon_i = \boldsymbol{\varphi}_{if}^T \hat{\boldsymbol{\theta}}_{is} - \boldsymbol{\varphi}_{if}{}^T \boldsymbol{\theta}_{is} \tag{7.85}$$

$$\epsilon_i = \boldsymbol{\varphi}_{if}^T \tilde{\boldsymbol{\theta}}_{is} \tag{7.86}$$

In order to update the estimated unknown parameters according to the error defined in 7.86 an adaptation law is used, sat up similar to the simple example in (7.69), with the addition of a normalisation factor, ν, explained below.

$$\dot{\hat{\boldsymbol{\theta}}}_i = -\frac{1}{1+\nu_i \boldsymbol{\varphi}_{if}^T \boldsymbol{\Gamma}_i \boldsymbol{\varphi}_{if}} \boldsymbol{\Gamma}_i \boldsymbol{\varphi}_{if} \epsilon_i \tag{7.87}$$

where $\boldsymbol{\Gamma}_i$ is the adaptation gain, which defines the rate at which the estimation error gets reduced. A large gain ensure a fast convergence but can also lead to overshoot in estimation. For this reason the gain is chosen large initially and is then updated as

$$\dot{\boldsymbol{\Gamma}}_i = \alpha_i \boldsymbol{\Gamma}_i - \frac{\boldsymbol{\Gamma}_{\boldsymbol{i}} \boldsymbol{\varphi}_{if} \boldsymbol{\varphi}_{if}^T \boldsymbol{\Gamma}_{\boldsymbol{i}}}{1+\nu_i \boldsymbol{\varphi}_{if}^T \boldsymbol{\Gamma}_i \boldsymbol{\varphi}_{if}} \tag{7.88}$$

where α_i is the forgetting factor. If chosen properly, this may improve the estimation rate of time-varying parameters. It will reduce the rate at which $\boldsymbol{\Gamma}_i$ converges towards a predetermined minimum value. If the forgetting factor is not used once $\boldsymbol{\Gamma}_i$ and $\dot{\boldsymbol{\Gamma}}_i$ reach a small value, the adaptation algorithm is not able to handle time varying parameters.
ν_i is the normalisation factor that should only take on positive values. If it is equal to 0 the algorithm is not normalised. Two additional requirements on the adaptaion gain, Γ_i, are:

$$\boldsymbol{\Gamma}_i(0) = \boldsymbol{\Gamma}_i{}^T(0) > 0 \tag{7.89}$$

$$\boldsymbol{\Gamma}_i(t_r^+) = \rho_i \boldsymbol{I}_i \tag{7.90}$$

The first is the starting condition for the adaptation gain where it may not be equal to zero, otherwise the derivative of $\boldsymbol{\Gamma}_i$, eq. (7.88), is equal to zero and no adaptation occurs. Furthermore, it needs to be positive, in order to make the error, ϵ_i converge to zero. The second condition states that at the covariance resetting time t_r the value of $\boldsymbol{\Gamma}_i$ will be reset. The time t_r is defined as the time at which Γ reaches its smallest eigenvalue $\lambda_{min}(\boldsymbol{\Gamma}_i(t)) = \rho_{li}$. At that time $\boldsymbol{\Gamma}_i$ is reset in such a way as to make $0 \leq \rho_{li} \leq \rho_i$. $\boldsymbol{I}_i$ is an identity matrix with the appropriate dimensions. By having this, $\boldsymbol{\Gamma}$ never reaches zero, and the estimation algorithm will maintain a minimum adaptation gain.

A practical problem can occur with this implementation, because if the system dynamics are not sufficiently excited, $\boldsymbol{\Gamma}_i$ can become unbounded and this can lead to estimator wind up. In order to prevent this, bounds are set as

$$\dot{\boldsymbol{\Gamma}}_i = \begin{cases} \alpha_i \boldsymbol{\Gamma}_i - \frac{\boldsymbol{\Gamma}_{\boldsymbol{i}} \boldsymbol{\varphi}_{if} \boldsymbol{\varphi}_{if}^T \boldsymbol{\Gamma}_{\boldsymbol{i}}}{1+\nu_i \boldsymbol{\varphi}_{if}^T \boldsymbol{\Gamma}_i \boldsymbol{\varphi}_{if}} & if \lambda_{max}(\boldsymbol{\Gamma}_i(t)) \leq \rho_{Mi} \\ & \&||Proj_{\hat{\boldsymbol{\theta}}}(\boldsymbol{\Gamma}_{\boldsymbol{i}} \boldsymbol{\tau}_i)|| \leq \dot{\boldsymbol{\theta}}_M \\ 0 & otherwise \end{cases} \tag{7.91}$$

Here ρ_M is the preset maximum eigenvalue of $||\boldsymbol{\Gamma}(t)||$. This lead to the following bounds on the adaptation gain: $\rho_{1i} \boldsymbol{I}_i < \boldsymbol{\Gamma}(t) < \rho_M \boldsymbol{I}_i$.

To get an idea of how all the described equations are connected to achieve the estimated parameters a block diagram of the parameter estimation structure has been made, and can be seen in fig. 7.4.

The proof of convergence for the estimation algorithm together with proofs for the IARC will be made in the following section.

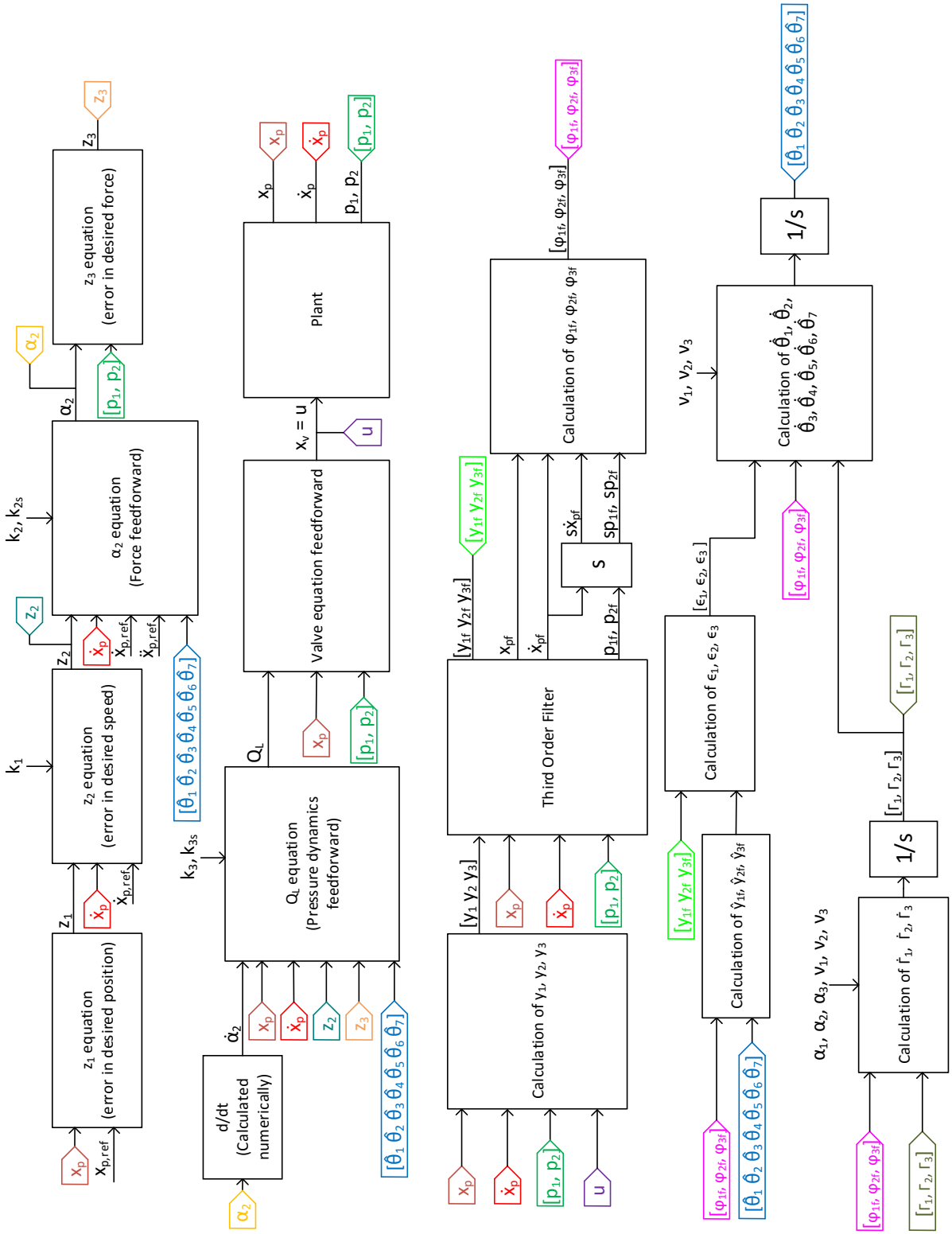

Figure 7.4: Block diagram of the estimation algorithm structure.

7.3 Control Law Proof

In this section the proof that the control law from Sec. 7.1 is stable will be given. Claims for the control on a similar system have been proven in [Mohanty and Yao, 2011]. The Lyapunov functions described in [Mohanty and Yao, 2011] will be used as a basis for the proof.

7.3.1 Boundedness of error

The first step is to establish a Lyapunov candidate function:

$$V = \frac{\theta_1}{2} z_2^2 + \frac{\theta_5}{2} z_3^2 \tag{7.92}$$

The function is positive definite(PD), because θ_1 is the mass of the system and θ_5 is inverse proportional to the bulk modulus. The derivative of (7.92) is

$$\dot{V} = \theta_1 z_2 \dot{z}_2 + \theta_5 z_3 \dot{z}_3 \tag{7.93}$$

Inserting the expressions for $\dot{z}_2$ and $\dot{z}_3$ from eq. (7.13) and eq. (7.31) into eq. (7.93) the result is

$$\begin{aligned} \dot{V} = {} & z_2 \left(z_3 + \alpha_2 - \theta_1 \dot{x}_{2eq} - \theta_2 x_2 - \theta_3 S(x_2) + \theta_4 + \tilde{D}_1 \right) \\ & + z_3 \left(Q_L - \left(\frac{A_{p1}^2}{V_1} + \frac{A_{p2}^2}{V_2} \right) x_2 - \frac{A_1}{V_1} \theta_6 - \frac{A_2}{V_2} \theta_7 - \theta_5 \dot{\alpha}_{2c} - \theta_5 \dot{\alpha}_{2u} + \tilde{D}_2 \right) \end{aligned} \tag{7.94}$$

Then by inserting the expressions for α_2 and Q_L from eq. (7.14) and eq. (7.32) one obtains

$$\begin{aligned} \dot{V} = {} & z_2 \left(z_3 - \theta_1 \dot{x}_{2eq} - \theta_2 x_2 - \theta_3 S(x_2) + \theta_4 + \tilde{D}_1 + \hat{\theta}_1 \dot{x}_{2eq} + \hat{\theta}_2 x_2 + \hat{\theta}_3 S(x_2) - \hat{\theta}_4 - k_2 z_2 + \alpha_{2s2} \right) \\ & + z_3 \Bigg[- \left(\frac{A_{p1}^2}{V_1} + \frac{A_{p2}^2}{V_2} \right) x_2 - \frac{A_1}{V_1} \theta_6 - \frac{A_2}{V_2} \theta_7 - \theta_5 \dot{\alpha}_{2c} - \theta_5 \dot{\alpha}_{2u} + \tilde{D}_2 + \left(\frac{{A_{p1}}^2}{V_1} + \frac{A_{p2}^2}{V_2} \right) x_2 \\ & - z_2 + \frac{A_1}{V_1} \hat{\theta}_6 + \frac{A_2}{V_2} \hat{\theta}_7 + \hat{\theta}_5 \dot{\alpha}_{2c} - k_3 z_3 + Q_{ls2} \Bigg] \end{aligned} \tag{7.95}$$

This can be simplified by noting that $\tilde{\theta} = \hat{\theta} - \theta$, which results in

$$\dot{V} = -k_2 {z_2}^2 + z_2 z_3 + z_2 \left(\alpha_{2s2} + \boldsymbol{\varphi}_2^T \tilde{\boldsymbol{\theta}} + \tilde{D}_1 \right) + z_3 \left(Q_{ls2} + \boldsymbol{\varphi}_3^T \tilde{\boldsymbol{\theta}} - \theta_5 \dot{\alpha}_{2u} + \tilde{D}_2 \right) - z_3 z_2 - k_3 {z_3}^2 \tag{7.96}$$

As stated in Sec. 7.1 the term z_2 is added in the control law Q_L with the purpose of cancelling out the term $z_2 z_3$, which results from the derivation of z_2. This reduces eq. (7.96) to

$$\dot{V} = -k_2 {z_2}^2 - k_3 {z_3}^2 + \underbrace{z_2 \left(\alpha_{2s2} + \boldsymbol{\varphi}_2^T \tilde{\boldsymbol{\theta}} + \tilde{D}_1 \right)}_{\leq \varepsilon_2} + \underbrace{z_3 \left(Q_{ls2} + \boldsymbol{\varphi}_3^T \tilde{\boldsymbol{\theta}} - \theta_5 \dot{\alpha}_{2u} + \tilde{D}_2 \right)}_{\leq \varepsilon_3} \tag{7.97}$$

The last two terms in eq. (7.97) are upper bounded by the definition of the conditions in sec. 7.1, which are presented in tables 7.3 and 7.4.

Since the first two terms in (7.97) are always negative, the upper bound of the function is defined by the worst case scenario, where the terms which can have a positive sign are

Condition 1	$z_2 \left(\alpha_{2s2} + \tilde{D}_1 + \boldsymbol{\varphi}_2^T \tilde{\boldsymbol{\theta}} \right) \leq \varepsilon_2$
Condition 2	$z_2 \alpha_{2s2} \leq 0$

Table 7.3: Conditions for the choice of α_{2s2}.

Condition 1	$z_3\left(Q_{Ls2}+\boldsymbol{\varphi}_3^T\tilde{\boldsymbol{\theta}}-\dot{\alpha}_{2u}\theta_5+\tilde{D}_2\right)\leq\varepsilon_3$
Condition 2	$z_3 Q_{Ls2}\leq 0$

Table 7.4: Conditions for the choice of Q_{Ls2}.

maximum and the ones that are always negative have a minimum value. This scenario will produce the largest possible value for the equation. This can be expressed as

$$\dot{V}\leq -k_2 z_2^2-k_3 z_3^2+\varepsilon_2+\varepsilon_3 \tag{7.98}$$

To consider the worst case scenario the two control gains k_2 and k_3 are considered at their minimum values. Furthermore the first two terms are dependent on square values of the errors z_2 and z_3, similar to the original Lyapunov candidate. A new term $\varepsilon=\varepsilon_2+\varepsilon_3$ is introduced and the derivative of the Lyapunov candidate can be rewritten to

$$\dot{V}\leq -min\{k_2,k_3\}\left(z_2^2+z_3^2\right)+\varepsilon \tag{7.99}$$

The difference between the original Lyapunov candidate $V=\frac{\theta_1}{2}z_2^2+\frac{\theta_5}{2}z_3^2$ and the term $z_2^2+z_3^2$ are the scales $\frac{\theta_1}{2}$ and $\frac{\theta_5}{2}$. These scales are positive scalars so it is possible to multiply with $\frac{2\theta_1}{2\theta_1}$ and $\frac{2\theta_5}{2\theta_5}$, without changing the equation.

$$\dot{V}\leq -\min\{k_2,k_3\}\left(\frac{2\theta_1}{2\theta_1}z_2^2+\frac{2\theta_5}{2\theta_5}z_3^2\right)+\varepsilon \tag{7.100}$$

$$\leq -2\min\left\{\frac{k_2}{\theta_1},\frac{k_3}{\theta_5}\right\}\left(\frac{\theta_1}{2}z_2^2+\frac{\theta_5}{2}z_3^2\right)+\varepsilon \tag{7.101}$$

$$\leq -2\min\left\{\frac{k_2}{\theta_1},\frac{k_3}{\theta_5}\right\}V+\varepsilon \tag{7.102}$$

By defining $\lambda=2\cdot\min\left\{\frac{k_2}{\theta_1},\frac{k_3}{\theta_5}\right\}$ one obtains

$$\dot{V}\leq -\lambda V+\varepsilon \tag{7.103}$$

This result is not negative semi-definite, because it is not possible to determine, which of the two terms is larger at all times. Stability cannot be proven with this Lyapunov candidate by Lyapunov like analysis. But another approach can be taken. The solution of the differential equation eq. (7.103) is

$$V\leq e^{-\lambda t}V(0)+\frac{\varepsilon}{\lambda}\left(1-e^{-\lambda t}\right) \tag{7.104}$$

From (7.104) it can be concluded that as $t\to\infty$ the exponential terms in (7.104) will converge towards zero, because λ is a positive scalar. This makes the equation have an upper bound of $\frac{\varepsilon}{\lambda}$ at $t=\infty$. This is a positive scalar smaller than infinity. Which in turn, when comparing with the original Lyapunov candidate (7.92), leads to the conclusion that z_2 and z_3 are bounded, expressed as (7.105).

$$V(t\to\infty)=\frac{\theta_1}{2}z_2^2+\frac{\theta_5}{2}z_3^2\to\frac{\varepsilon}{\lambda} \tag{7.105}$$

From the fact that z_2 is bounded it can be concluded that z_1 is bounded i.e. $z_1,z_2,z_3\in L_2[0,\infty)$. This still does not show convergence of these values, but it proves the stability of the system. Furthermore by examining

$$\frac{\varepsilon}{\lambda}=\frac{\varepsilon_2+\varepsilon_3}{\lambda}=\frac{z_2\left(\alpha_{2s2}+\boldsymbol{\varphi}_2^T\tilde{\boldsymbol{\theta}}+\tilde{D}_1\right)+z_3\left(Q_{ls2}+\boldsymbol{\varphi}_3^T\tilde{\boldsymbol{\theta}}-\theta_5\dot{\alpha}_{2u}+\tilde{D}_2\right)}{\lambda} \tag{7.106}$$

It can be concluded that the only way for V to be equal to 0 is for z_2 and z_3 to be equal to zero, which can only happen if the term $\left(\alpha_{2s2} + \boldsymbol{\varphi}_2^T\tilde{\boldsymbol{\theta}} + \tilde{D}_1\right)$ and $\left(Q_{ls2} + \boldsymbol{\varphi}_3^T\tilde{\boldsymbol{\theta}} - \theta_5\dot{\alpha}_{2u} + \tilde{D}_2\right)$ are equal to zero, because of the dynamics of z_2 taken from sec. 7.1

$$\theta_1\dot{z}_2 = -k_2 z_2 + (\alpha_{2s2} + \boldsymbol{\varphi}_2^T\tilde{\boldsymbol{\theta}} + \tilde{D}_1) \tag{7.107}$$

Here it can be seen that as z_2 converges to zero the influence of α_{2s2} becomes smaller because $\alpha_{2s2} = -h_2\tanh\left(\frac{z_2 h_2}{\varepsilon_2}\right)$. Then the estimation error and the disturbance can influence the error dynamics. In other words the convergence of the algorithm depends on the accuracy of the estimation. But the stability of the system is ensured within the maximum estimation error. To prove convergence of the error states to zero the following considerations have to be made. The adaptation rates are bounded by definition and the filter H_f is stable. This together with the stability of the error states means that the following bounds exist $z_1, z_2, z_3, \tilde{\boldsymbol{\theta}}, \hat{\boldsymbol{\theta}}, \dot{\hat{\boldsymbol{\theta}}}, \boldsymbol{\varphi}_{if} \in L_\infty[0,\infty)$. Where L_∞ is the L-infinity norm. Furthermore $\dot{z}_2, \dot{z}_3, \dot{\epsilon}_i \in L_\infty[0,\infty)$.

7.3.2 Boundedness and convergence of estimation error

To prove that the estimaton error is stable and will converge to zero another Lyapunov candidate is introduced

$$V_{est}(\tilde{\boldsymbol{\theta}}_i) = \frac{1}{2}\tilde{\boldsymbol{\theta}}_i^T\tilde{\boldsymbol{\theta}}_i \tag{7.108}$$

This Lyapunov candidate is positive definite. The derivative is then

$$\dot{V}_{est} = \tilde{\boldsymbol{\theta}}_i^T\dot{\tilde{\boldsymbol{\theta}}}_i \tag{7.109}$$

By considering θ to be slow varying or at least slower varying than the update frequency of the estimation algorithm, it can be assumed that $\dot{\tilde{\boldsymbol{\theta}}}_i = \dot{\hat{\boldsymbol{\theta}}}_i$. Then by utilising (7.87) the derivative becomes

$$\dot{V}_{est} = \tilde{\boldsymbol{\theta}}_i^T\left(-\boldsymbol{\Gamma}_i\boldsymbol{\varphi}_{if}\epsilon_i\right) \tag{7.110}$$

Furthermore by using the definition of ϵ_i from eq. (7.86)

$$\epsilon_i = \boldsymbol{\varphi}_{if}^T\tilde{\boldsymbol{\theta}}_i \tag{7.111}$$

It can be inserted into the Lyapunov candidate derivative to obtain

$$\dot{V}_{est} = -\tilde{\boldsymbol{\theta}}_i^T\boldsymbol{\Gamma}_i\boldsymbol{\varphi}_{if}\boldsymbol{\varphi}_{if}^T\tilde{\boldsymbol{\theta}}_i \tag{7.112}$$

In eq. (7.112) $\boldsymbol{\Gamma}_i$ is a bounded positive definite matrix by definition. Furthermore the matrix created by the two vectors $\boldsymbol{\varphi}_{if}\boldsymbol{\varphi}_{if}^T$ will always be of the form

$$\begin{bmatrix} a \\ b \\ c \end{bmatrix}\begin{bmatrix} a & b & c \end{bmatrix} = \begin{bmatrix} a^2 & ab & ac \\ ba & b^2 & bc \\ ca & bc & c^2 \end{bmatrix} \tag{7.113}$$

The leading principle minors of the matrix are all non-negative and so are the principle minors. The matrix will be positive semi-definite. This leads to (7.112) being negative semi-definite. This shows that $\tilde{\boldsymbol{\theta}}_i$ is bounded. Since we assumed $\dot{\tilde{\boldsymbol{\theta}}}_i = \dot{\hat{\boldsymbol{\theta}}}_i$, then $\dot{\hat{\boldsymbol{\theta}}}_i \in L_2(0,\infty)$, furthermore $\epsilon_i \in L_\infty[0,\infty)$. No further conclusion can be made based on this result alone. In order to prove

convergence Lyapunov like analysis has to be applied. This involves investigating the second derivative of the Lyapunov candidate

$$\ddot{V}_{est} = -2\tilde{\boldsymbol{\theta}}_i^T \boldsymbol{\Gamma}_i \boldsymbol{\varphi}_{if} \boldsymbol{\varphi}_{if}^T \dot{\tilde{\boldsymbol{\theta}}}_i + \tilde{\boldsymbol{\theta}}_i^T \dot{\boldsymbol{\Gamma}}_i \boldsymbol{\varphi}_{if} \boldsymbol{\varphi}_{if}^T \tilde{\boldsymbol{\theta}}_i + \tilde{\boldsymbol{\theta}}_i^T \boldsymbol{\Gamma}_i \boldsymbol{\varphi}_{if} \dot{\boldsymbol{\varphi}}_{if}^T \tilde{\boldsymbol{\theta}}_i + \tilde{\boldsymbol{\theta}}_i^T \boldsymbol{\Gamma}_i \dot{\boldsymbol{\varphi}}_{if} \boldsymbol{\varphi}_{if}^T \tilde{\boldsymbol{\theta}}_i \tag{7.114}$$

$\dot{\boldsymbol{\Gamma}}_i$ is bounded by definition. $\boldsymbol{\varphi}_{if}$ is bounded and continues, because it is the output of a 3^{rd} order filter, that has been designed with the specific desire to have these signals smooth and derivable. $\tilde{\boldsymbol{\theta}}_i$ was proven bounded in the previous step. This means that $\dot{V}_{est}$ is uniformly continuous in time. Barbalat's Lemma is applied:

- V_{est} is lower bounded by zero
- $\dot{V}_{est}$ is negative semi-definite
- $\ddot{V}_{est}$ exists and is bounded $\Rightarrow \dot{V}_{est}$ is uniformly continuous in time

Then $\dot{V}_{est} \to 0$ as $t \to \infty$. Since $\boldsymbol{\Gamma}_i$ cannot become zero, the only way for $\dot{V}_{est}$ to converge to zero is if $\tilde{\boldsymbol{\theta}}_i \to 0$ or $\boldsymbol{\varphi}_{if} \to 0$ as $t \to \infty$. From the assumption that the system will be persistently exited, it can be concluded that $\boldsymbol{\varphi}_{if}$ cannot be equal to zero and this leaves the only possibility of $\tilde{\theta} \to 0$. To ensure persistent excitation conditions the algorithm should only update if $\ddot{x} \geq$ and $\dot{x} \geq$. Since $\dot{\alpha}_{2u}$ is proportional to $\tilde{\dot{x}}_2$ it also converges towards zero. Then equation 7.98 can be rewritten to

$$\dot{V} = -k_2 z_2^2 - k_3 z_3^2 + z_2 \alpha_{2s2} + z_3 Q_{Ls2} + \left(\boldsymbol{\varphi}_2^T z_2 + \boldsymbol{\varphi}_3^T z_3\right)\tilde{\boldsymbol{\theta}} + \dot{\alpha}_{2u}\theta_5 z_3 \tag{7.115}$$

Since $z_3 Q_{Ls2} \leq 0$ and $z_2 \alpha_{2s2} \leq 0$ from the conditions (7.2) and (7.1), these terms can be omitted. Furthermore, since it was proven that $\tilde{\theta}, \dot{\alpha}_{2u} \to 0$ and $z_1, z_2, z_3 \in L_\infty[0,\infty)$ the terms $\left(\boldsymbol{\varphi}_2^T z_2 + \boldsymbol{\varphi}_3^T z_3\right)$ and $\theta_5 z_3$ will converge to zero. This leaves

$$\dot{V} \leq -k_2 z_2^2 - k_3 z_3^2 \tag{7.116}$$

Since $\boldsymbol{\varphi}_2^T\tilde{\boldsymbol{\theta}}, \boldsymbol{\varphi}_3^T\tilde{\boldsymbol{\theta}}, \dot{\alpha}_{2u}\theta_5 \in L_\infty[0,\infty)$ and $\dot{z}_2$, and $\dot{z}_3$ are bounded and continuous, once again Barbalat's Lemma can be applied and it proves that $z_1, z_2, z_3 \to 0$ as $t \to \infty$. It is important to note that z_3 is a virtual state containing both x_3 and x_4 and while it is stable there are infinite combinations of pressures that satisfy a desired force output meaning that the internal dynamics of degree one can still be unstable. This is a limitation of the algorithm and the fact that the separate pressures cannot be controlled individually. [Mohanty and Yao, 2011] does not provide stability proof of the internal dynamics of the system, but instead test the system experimentally to show stability. This project has done the same. The internal pressures p_1 and p_2 for a simulation of a pulse-like trajectory is shown in fig. 7.5. The parameters used for the IARC in the simulation are the optimised parameters, determined in Chap. 8.

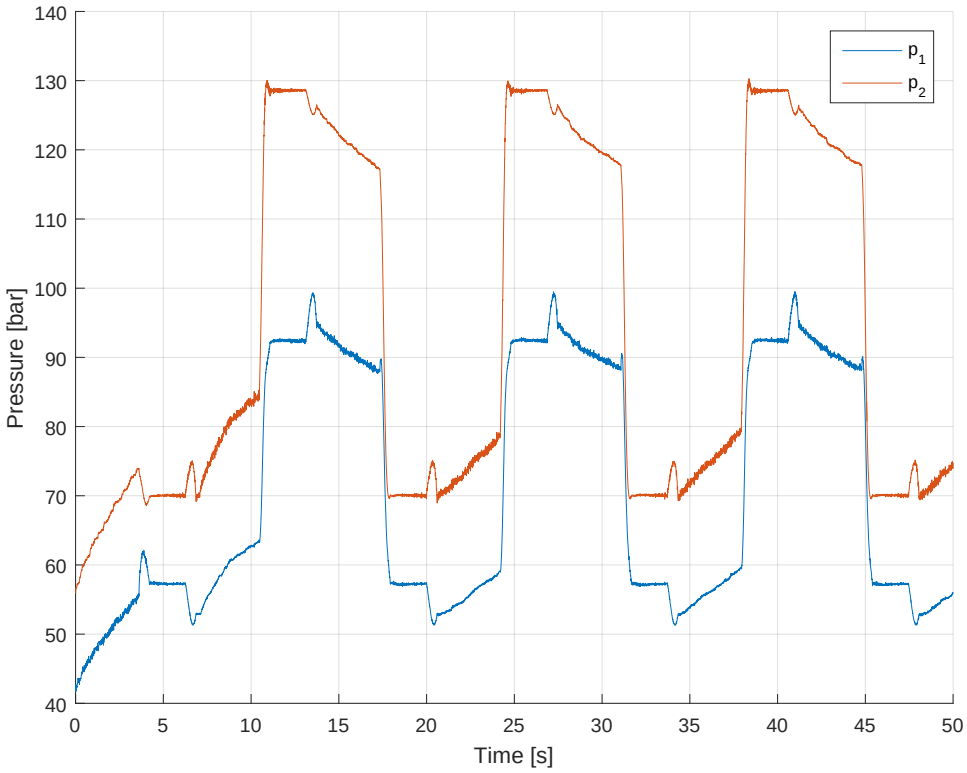

Figure 7.5: Internal pressure dynamics for chamber 1 and 2.

Fig. 7.5 indicates that the system is indeed internally stable. However, since no proof is made together with different trajectories and faulty situations being investigated, the separate pressures should be monitored during testing.

7.3.3 Implementation problems

The first numerical Matlab implementation resulted in an unstable system with the control effort reaching values outside the normalised valve opening and oscillating heavily. This resulted in consecutive hits against the valve opening saturation. In order to determine the most influential parameters in the control law another simulation experiment was conducted. The control gains in the control law were alternately significantly lowered, set to zero and to large values one at a time in order to determine their influence. The uncertain parameters of the system were set to be constants, which were then directly given to the feedforward terms of the controller, so the estimation algorithm could not influence the controller. The result of this sensitivity analysis was the conclusion that z_2, shown in 7.117, was one of the most dominant terms causing the problems.

$$Q_{La} = \left(\frac{A_{p,1}^2}{V_1} + \frac{A_{p,2}^2}{V_2} \right) x_2 - z_2 + \frac{A_{p,1}}{V_1} \hat{\theta}_6 + \frac{A_{p,2}}{V_2} \hat{\theta}_7 + \hat{\theta}_5 \dot{\alpha}_{2c} \tag{7.117}$$

A possible reason for this was found to be that the system velocity, x_2 is scaled down by A^2/V,

where z_2 is used directly. To investigate if this was the problem, a scaling factor, k_{scale} was applied to the z_2, shown in (7.118).

$$Q_{La} = \left(\frac{A_{p,1}^2}{V_1} + \frac{A_{p,2}^2}{V_2}\right) x_2 - \frac{z_2}{k_{scale}} + \frac{A_{p,1}}{V_1}\hat{\theta}_6 + \frac{A_{p,2}}{V_2}\hat{\theta}_7 + \hat{\theta}_5\dot{\alpha}_{2c} \tag{7.118}$$

By including the scaling factor in the optimisation algorithm, the optimisation was able to obtain a stable response, where a scaling factor above 1 was found to be needed.
This indicates that including a scaling factor as a design parameter could improve the system response. To determine if this affects the stability proof of the control law, a new Lyapunov candidate is investigated where k_{scale} will be included.

The new Lyapunov candidate function is:

$$V = \frac{\theta_1}{2}z_2^2 + \frac{k_{scale}\theta_5}{2}z_3^2 \tag{7.119}$$

Once more the derivative of the Lyapunov candidate is:

$$\dot{V} \leq -k_2 z_2^2 + z_2 z_3 + z_2\left(\alpha_{2s2} + \boldsymbol{\varphi}_2^T\tilde{\theta} + \tilde{D}_1\right) + k_{scale}z_3\left(Q_{ls2} + \boldsymbol{\varphi}_3^T\tilde{\theta} - \theta_5\dot{\alpha}_{2u} + \tilde{D}_2\right) - z_3 z_2 - k_{scale}k_3 z_3^2 \tag{7.120}$$

This can be simplified to:

$$\dot{V} \leq -k_2 z_2^2 + \varepsilon_2 + k_{scale}\varepsilon_3 - k_{scale}k_3 z_3^2 \tag{7.121}$$

The solution to this differential equation is:

$$V \leq e^{-\lambda t}V(0) + \frac{\varepsilon}{\lambda}\left(1 - e^{-\lambda t}\right) \tag{7.122}$$

$$\lambda = 2\cdot\min\left\{\frac{k_2}{\theta_1}, \frac{k_3}{\theta_5}\right\} \tag{7.123}$$

$$\varepsilon = \varepsilon_2 + k_{scale}\varepsilon_3 \tag{7.124}$$

The fact that ε_3 is scaled increases the upper bound of the Lyapunov candidate. In the worst case scenario the upper bound of the candidate $\frac{\varepsilon}{\lambda}$ is increased, while the rate of convergence λ is kept the same. This does not change the fact that V is bounded and so z_2 and z_3 are bounded. The rest of the proof showing that z_1, z_2 and z_3 will converge to zero is based on the estimation algorithm forcing the estimation errors $\tilde{\theta}$ to zero. This part will not change, because the estimation algorithm operation is not directly reliant on the control law. Based on this the derivative of the new Lyapunov candidate can be shown to be bounded by

$$\dot{V} \leq -k_2 z_2^2 - k_{scale}k_3 z_3^2 \tag{7.125}$$

Which once more, through the use of Barbalat's Lemma, shows that $z_1, z_2, z_3 \to 0$ as $t \to \infty$. This concludes the controller proof. The conclusion is that as long as the values for k_1, k_2, k_3 and k_{scale} are positive scalar values the errors are convergent as $t \to \infty$. No conclusions can be made about the performance of the algorithm, when a trajectory has to be followed, beyond the fact that the system will be stable. There are no standard procedures for the tuning of a non-linear adaptive controller. For this reason, an optimisation algorithm will be chosen to find the optimal control- and estimation parameter values for this specific system and trajectory.

CHAPTER 8

CONTROL AND ESTIMATION PARAMETER OPTIMISATION

No set procedure is available for the tuning of non-linear controllers. So an optimisation algorithm was selected as the best approach for tuning the IARC and the estimation algorithm parameters. The trajectory that will be used for the optimisations is discussed in the first section. The simulation model will use the force controller determined in App. B, because it will introduce delays in the mass emulation. If the force controller is not used during the optimisation, the IARC may have a higher bandwidth than the force controller, possibly introducing stability problems.
The simulation model will not include noise on the measured states, but the effect from including these will be determined in Chap. 11. Section 8.2 will be concerned with the control gain optimisation. This optimisation is affected heavily by the severity of the faults the controller has to be stable for. To test to what degree the performance is reduced under the worst conditions of the estimation algorithm, an analysis has been made. The analysis consists of a test where the estimation algorithm is completely wrong, for example where the real leakage is maximum, but the minimum is estimated, giving the wrong information to the control law.

In this chapter, the final findings will be described, and the optimum control law parameters and estimation algorithm parameters will be shown together with their performance. For the interested reader, a full description of the method used and discussion of various findings can be found in App. D.

Contents

8.1 Optimisation Trajectory

The trajectory used for the optimisation can be seen in fig. 8.1

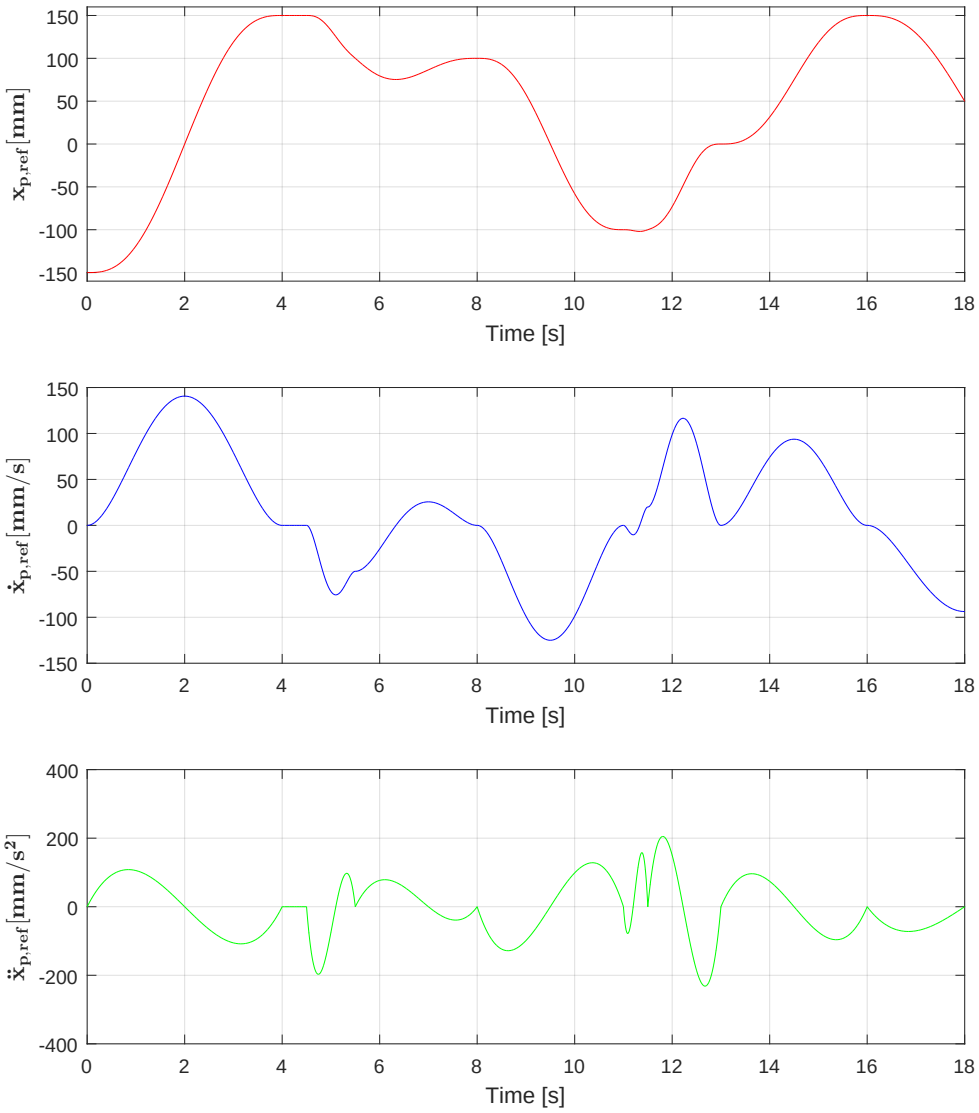

Figure 8.1: Position, velocity, and acceleration trajectory used for the optimisation algorithms

By using this trajectory the system will be tested for dynamic scenarios with frequencies of 1-4 Hz on the acceleration. Higher frequencies have not been included because of a desire to not optimise the controller for a high bandwidth. The reason for this is the valve and force controller limits how fast the IARC can operate. At the maximum velocity, the normalised valve opening is ≈0.8.
Simulations where higher frequencies are used will be made in Chap. 11. These are done to determine if the system is stable with the designed controller, if a higher frequency reference is

required.

8.2 Control Law Parameter Optimisation

The performance of the control law depends on the four control gains, k_1, k_2, k_3, and k_{scale}. k_1 is used for the position control, k_2 for the velocity, and k_3 for the acceleration. k_{scale} was introduced in the control law proof to reduce the impact of the velocity error state z_2. These will be used as the optimisation variables:

$$\boldsymbol{x}_{opti} = \begin{bmatrix} k_1 & k_2 & k_3 & k_{scale} \end{bmatrix}^T \tag{8.1}$$

The desired result of the optimisation is to obtain the best performance, during trajectory tracking under nominal conditions. In App. D it was found the best result was obtained when acceleration error was used for the cost function value. The test starts with an initial error in estimation, shown in table 8.1. The cost function to be minimised is based on a simulation using the trajectory in fig. 8.1 on the non-linear model and it depends on the Root-Mean-Square (RMS) acceleration error ($\ddot{e}_p$), calculated as:

$$f_{min}(\boldsymbol{x}_{opti}) = \sqrt{mean\left(\ddot{e}_p^2\right)} \tag{8.2}$$

$$\ddot{e}_p = \ddot{x}_{pd} - \ddot{x}_p \tag{8.3}$$

The performance of the controller also depends on the estimation algorithm. For this optimisation an initial error is present in the uncertain parameters. The estimation will then converges to the true values over the course of the simulation. It is possible to give the correct values to the control law directly to remove the impact from not having optimal estimation algorithm parameters. The optimisation has not been performed in this manner, because part of the control law is only active when the uncertain parameters have not converged to their real values. The parameters for the estimation algorithm in this optimisation are hand tuned, to achieve a convergence from initial offset to the nominal values. These values are not the optimal values, but the performance is satisfactory for these tests, estimating the correct parameters within 5-10 seconds.

In the non-linear virtual control laws shown in eq. (8.4), two user defined parameters have to be chosen, ε_2 and ε_3.

$$\begin{aligned} \alpha_{2s2} &= -h_2 \tanh\left(\frac{h_2 z_2}{\varepsilon_2}\right) \\ Q_{Ls2} &= -h_3 \tanh\left(\frac{h_3 z_3}{\varepsilon_3}\right) \end{aligned} \tag{8.4}$$

where h_2 and h_3 are the non-linear control gains, defined as:

$$\begin{aligned} h_2 &\geq ||\boldsymbol{\varphi}_{2,max}^T(\boldsymbol{\theta}_{max} - \boldsymbol{\theta}_{min})|| + ||\tilde{D}_{1,max}|| \\ h_3 &\geq ||\boldsymbol{\varphi}_{3,max}^T(\boldsymbol{\theta}_{max} - \boldsymbol{\theta}_{min})|| + ||\dot{\alpha}_{2u,max}(\theta_{5,max} - \theta_{5,min})|| + ||\tilde{D}_{2,max}|| \end{aligned} \tag{8.5}$$

By having a relatively large value of ε_2 and ε_3, the non-linear virtual control laws will only have an effect when there is a larger error, z_2 and z_3. The sizing of ε_2 and ε_3 also correspond to the maximum effect that an error in the estimation and unmodelled non-linear forces will have on the system. Having a very large value of ε_2 and ε_3 means the controller will mainly use the linear control gains when no faults and uncertainties are present. This is desirable, because the tanh function in the non-linear gains can result in a fast changing control law. By increasing the values of ε_2 and ε_3 the non-linear gains switch direction less abruptly. This leads to a lower bandwidth of the controller. The downside of having large ε_2 and ε_3 is that estimation errors and non-linear disturbances can introduce larger errors. Both points should be considered when choosing the size of ε_2 and ε_3. It is difficult to determine the exact effect a chosen value will of ε_2 and ε_3 has. For this reason hand tuned values were initially chosen in order to have a starting point for the investigation of the controller. The resulting controller had instability issues which served to guide its further tuning.

In App. D, different values of ε_3 were investigated, because it was found that part of the instability problems originated from the initial choice of this value. Through further investigation it was found that the initially chosen leakage range of 6 L/min resulted in large h_3 gains. An initial ε_3 value of 1 was too small and needed to be increased. The resulting difference in the two investigations was on the uncertain leakage flow range. By increasing the size of ε_3 it was possible to use a larger leakage flow range. Further investigation of the choice of ε will be discussed later in the chapter. The ranges obtained with different values of ε are shown in table 8.1.

Range	M_{eq}[kg]	B [Ns/m]	F_c [N]	D_{1n} [N]	β^{-1} [bar^{-}1]	D_{21n} [m^3/s]	D_{22n} [m^3/s]	ε_2	ε_3
Nom. Value	6500	18000	200	0	7000^{-1}	$\approx$-2·10^{-6}	$\approx$ -2·10^{-6}	-	-
Ini. est.	7000	16500	120	0	7500^{-1}	0	0	-	-
$\boldsymbol{\theta_{range,1}}$	[10 9000]	[0 30000]	[0 1500]	[-500 500]	$[10000\ 4000]^{-1}$	**[-2 1]/60000**	**[-2 1]/60000**	200	**1**
$\boldsymbol{\theta_{range,2}}$	[10 9000]	[0 30000]	[0 1500]	[-500 500]	$[10000\ 4000]^{-1}$	**[-5 1]/60000**	**[-5 1]/60000**	200	**3**
$\boldsymbol{\theta_{range,3}}$	[10 9000]	[0 30000]	[0 1500]	[-500 500]	$[10000\ 4000]^{-1}$	**[-9 1]/60000**	**[-9 1]/60000**	200	**8**

Table 8.1: Nominal value of uncertain parameters, initial estimate used, uncertain parameter range tested and values of ε_2 and ε_3.

The ranges achieved in table 8.1 are found to be acceptable uncertain parameter ranges for a hydraulic servo-system of this size. For the tests, a large mass will be emulated (6500 kg) to simulate operation conditions of a pitch-system.

To emulate the maximum mass and friction parameters, which exceeds the real values, the force controller is required.
To validate that the load cylinder can deliver enough force to emulate these parameters, the maximum force output is calculated and compared with the required force.
With a supply pressure of 180 bar, the load cylinder can deliver a force of up to $\approx$ 14000 N or $\approx$ 22000 N depending on the direction. Assuming the nominal parameters are zero, and the maximum acceleration and velocity in the trajectory is required together with a maximum Coulomb friction, then a load force of $\approx$ 7750 N is required. This scenario may not be realistic, due to it requiring maximum acceleration at maximum velocity, but it shows that the load cylinder is able to produce the required force. An use of up to 50 % of the possible force from

the load cylinder is found acceptable, and a safety margin of ≈ 2 is achieved. Based on this, the desired range on the uncertain parameters regarding mass and friction are possible to emulate on the experimental set-up available.

A leakage range of 10 L/min corresponds to 25 % of the maximum flow in the system which is also found to be satisfactory. The lower ε_3 tested was due to an initial choice of using ε_3=1. The effect on the system performance when using different values of ε_3 will be shown later in this section.

The optimisation algorithm used to determine the control gains is a standard Genetic Algorithm (GA) from Matlab's Global Optimization Toolbox. The algorithm is slower and more complex than a gradient based optimisation. A gradient based method is not used, because the non-linear nature of the controller and the system prevent the determination of the shape of the cost function. The genetic algorithm has the added benefit of having random initial guesses for the parameters, removing the requirement of having a good user defined initial guess, or multiple tests with different initial guesses. Furthermore the values have been normalised to prevent numerical problems, due to the large difference between the magnitude of k_1 and k_2, and k_3. The values are:

Parameter	Minimum Value	Maximum Value	Normalisation Scale
k_1	1	250	0.05
k_2	1	200	1
k_3	1	1550	$1 \cdot 10^{-10}$
k_{scale}	1	300	1

where the minimum and maximum values have been chosen based on what previous studies have used, [Mohanty and Yao, 2011], and realistic values from hand tuning.

Optimisation Results

The optimum control gains determined for each range are shown in table 8.2.

Range tested	k_1	k_2	k_3	k_{scale}	$f_{min}(acc)$
$\boldsymbol{\theta_{range,1}}$	36.0·0.05	285	$17.0 \cdot 10^{-10}$	471	**39.27**
$\boldsymbol{\theta_{range,2}}$	71.5 ·0.05	294	$1.0 \cdot 10^{-10}$	578	**40.01**
$\boldsymbol{\theta_{range,3}}$	**76.5·0.05**	**129**	$\mathbf{35.0 \cdot 10^{-10}}$	**197**	**40.16**

Table 8.2: Optimisation of control law gains result using RMS of acceleration error as cost function value

The cost function values obtained for the three leakage flow ranges, marked with bold in table 8.2, are very similar. This indicates that under the conditions optimised for, similar performances are obtained. To determine what the difference between the designed controllers are, a comparison is made in the following subsection.

Discussion of Control Law Parameter Variations

To determine the effect of an increased ε_3, a comparison is made where a maximum estimation error is introduced. This is achieved by having the control law use the maximum value of the leakage flow (1 L/min), while the system will be subjected to minimum leakages of -9 L/min.

The comparison can be seen in App. D. A more thorough discussion is made, but the main part is that by having a large ε_3, the control law is allowed to have a larger error in certain conditions. By allowing a larger error, the control law will give a more smooth signal unless a large error occurs. If a smaller ε_3 is used for the large leakage flow range, the control law will try to maintain a very small error, requiring fast changes in the valve position. These fast changes might not be possible, and the system may go unstable, which was observed during some simulations. The performance achieved with a leakage flow range of 10 L/min is found acceptable, and larger leakage flows are not investigated, due to 10 L/min being sufficiently large considering the valve for the system available can deliver 40 L/min.

Control Law Performance

The performance achieved when using the control law parameters for $\boldsymbol{\theta_{range,3}}$ using the trajectory mentioned in the beginning, fig. 8.1, can be seen in fig. 8.2.

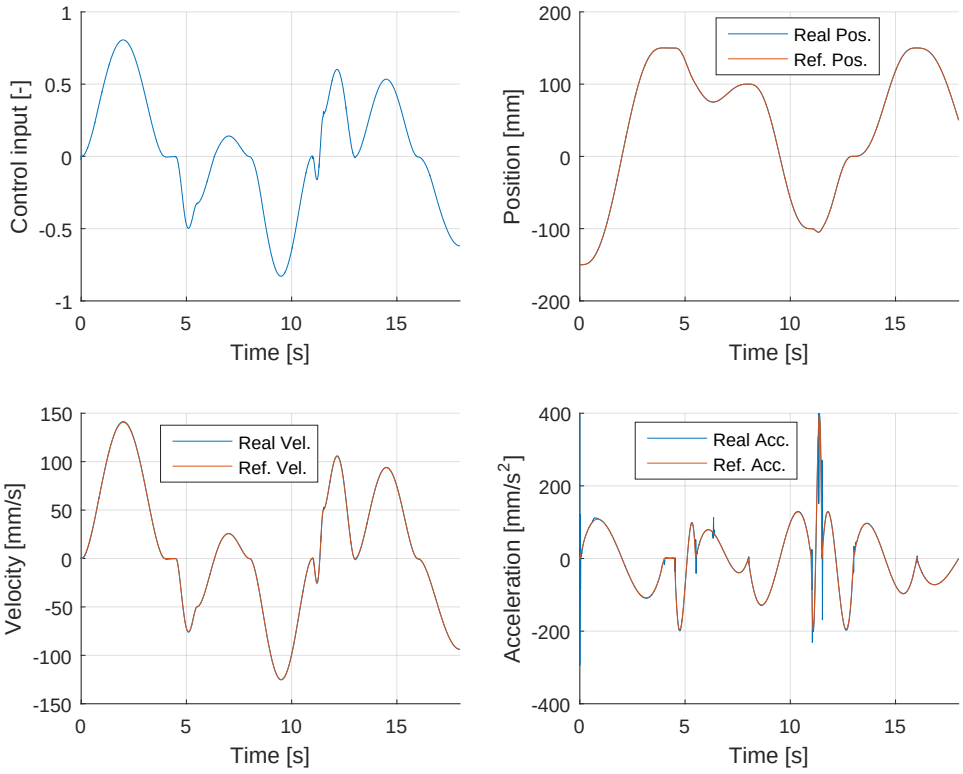

Figure 8.2: System response.

In fig. 8.2 the system follows the reference nicely. The acceleration does have a few spikes in error, which is due to the force controller having some difficulties for fast changes in direction

due to the emulation of mass. The initial spike is due to the initial pressures not corresponding to the initial acceleration reference. The RMS position error for the simulation was 0.22 mm.

The determined control law gains and ranges will be used when determining the estimation algorithm parameters in the following section.

From this, the system parameters ranges that the system can tolerate is determined, and a satisfactory system response has been obtained. For the IARC to achieve similar performance during faulty situations, corresponding to a variations in the system parameters, the optimal parameters for the estimation algorithm has to be determined, which will be done in the following section.

8.3 Estimation Algorithm Parameter Optimisation

For the estimation algorithm, the control parameters determined in the previous section will be used. The piston movement trajectory used is generally the same, it has been extended to last 25 seconds to make it start and stop at the same position. The simulation will last 50 seconds, allowing the trajectory to be run twice, and allow time for multiple changes to the parameters. For the estimation algorithm optimisation, a number of faults have been introduced, to emulate time-varying tendencies of the uncertain parameters. For the emulation of mass-, viscous friction-, Coulomb friction-, and disturbance changes, a load trajectory will be used. To emulate a time-varying bulk modulus, a varying air ratio in the oil is introduced. For the leakage, a varying internal and external leakage area is used. A visual depiction of the parameter trajectory is shown in fig. 8.3 and 8.4.

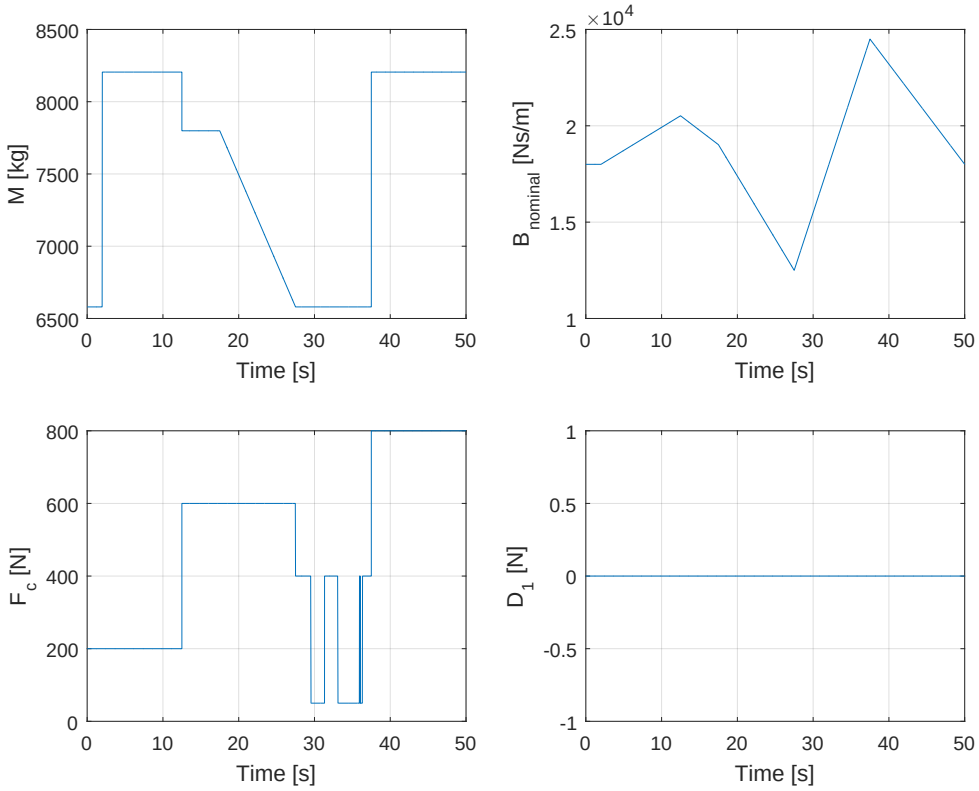

Figure 8.3: Force fault related parameter variations.

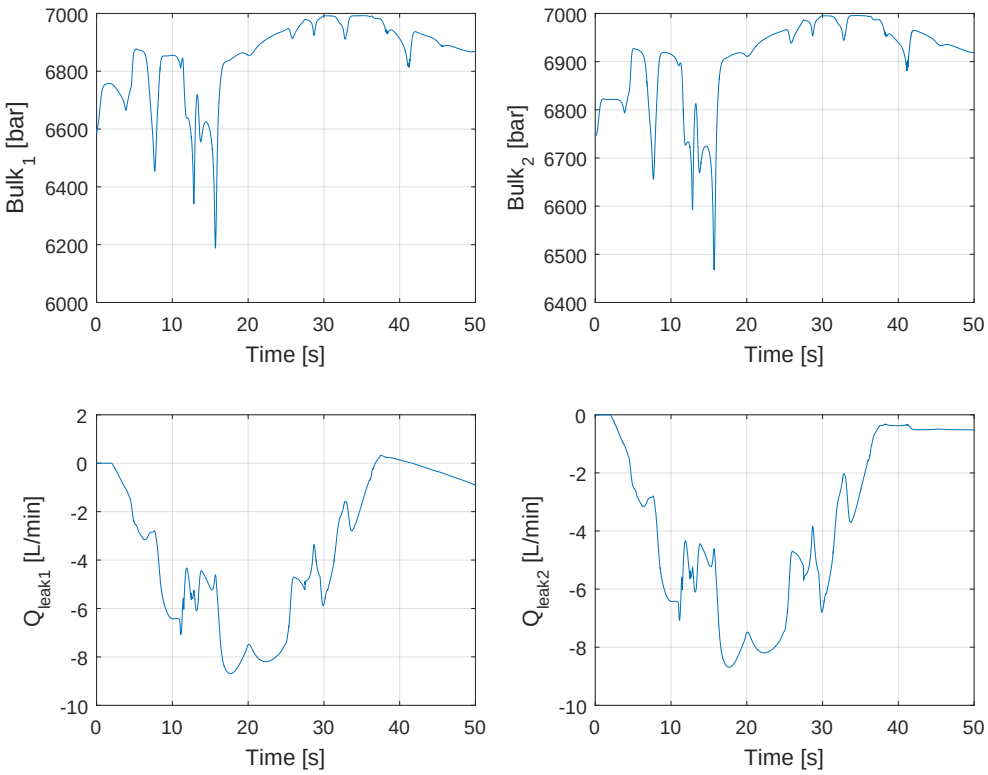

Figure 8.4: Flow fault related parameter variations.

where the terms Q_{leak1} and Q_{leak2} corresponds to D_{21n} and D_{22n} in Chap. 7.
As can be seen in fig. 8.3 and 8.4, all uncertain parameters are varied during the run. This is done because some of the parameters of the estimation algorithm are not independent, and should be chosen simultaneously. This trajectory does not correspond to realistic fault scenarios. Instead it is designed to ensure the algorithm is optimised for a multitude of different situations.

The optimisation variables are:

$$\boldsymbol{x}_{opti} = [\boldsymbol{\Gamma}(0) \quad \dot{\boldsymbol{\theta}}_M \quad \boldsymbol{\nu} \quad \boldsymbol{\alpha} \quad \boldsymbol{\rho}_M \quad \boldsymbol{\rho}_l]^T \tag{8.6}$$

where the variable vectors contain multiple elements, written explicitly in table 8.3. The upper and lower bounds for the optimisation parameters, can be seen in App. D.

The cost function is defined as eq. (8.7), to obtain a minimisation of the error between the real parameters and estimated parameters. A scaling, $weight_i, i = 1:7$, has been applied to make the algorithm weigh the parameter more equally. This is not an optimal way, because some parameters change much faster. The ones like mass, which have a changes in the form of a step introduce error spikes. By using RMS, peak errors may have a larger impact than a small consistent error. This approach was however found to give a decent estimation performance. Furthermore, the D_{1n} error is not included in the cost function due to the reference being zero during the whole run. If this is included, it will interfere in the three other force related

parameters in a negative way, due to it trying to reduce the variations in D_{1n} to become as small as possible. An attempt was made to include D_{1n} in the optimisation. The result was that the convergence time for mass, viscous friction, and Coulomb friction was increased significantly. Because these are found to be more important parameters, it is chosen to not include the D_{1n} in the cost function. A different approach that could be used is a minimax approach, where the optimisation tries to decrease the parameter with the largest error first, then the next and so forth. This was tried to be implemented, however, the results obtained showed significantly worse performance than the GA results.

$$f_{min}(\boldsymbol{x}_{opti}) = \sum_{i=1}^{7} \sqrt{mean\left((\tilde{\theta}_i \cdot weight(i))^2\right)} \tag{8.7}$$

$$weight = \begin{bmatrix} \frac{1}{5000} & \frac{1}{10000} & \frac{1}{900} & 0 & 7000 \cdot 10^5 & 12 \cdot 10^4 & 12 \cdot 10^4 \end{bmatrix}^T \tag{8.8}$$

The optimisation algorithm chosen is the GA, with the same reasoning as for the control law optimisation: The optimisation function is very non-linear, and GA is not dependent on a good initial guess. The simulation required for the estimation algorithm is very time consuming. A full optimisation run with 2600 generations was determined to be unfeasible. Instead, a 10 generations optimisation run which required 4 days was performed. The parameters determined here may not be the optimum due to the relatively low amount of generations. However, the parameters will be analysed and the performance will be determined. The results from the optimisation is shown in tab. 8.3.

type	Parameter	Optimum value	Normalisation scale
Initial estimation gain	$\Gamma_{1;1,1}(0)$	4250	1
	$\Gamma_{1;2,2}(0)$	2690	1
	$\Gamma_{1;3,3}(0)$	2890	1
	$\Gamma_{1;4,4}(0)$	2140	1
	$\Gamma_{2;1,1}(0)$	48.4	10^{-12}
	$\Gamma_{2;2,2}(0)$	3140	10^{-4}
	$\Gamma_{3;2,2}(0)$	3060	10^{-4}
Maximum rate of change	$\dot{\theta}_{M;1}$	279	20
	$\dot{\theta}_{M;2}$	240	70
	$\dot{\theta}_{M;3}$	320	2
	$\dot{\theta}_{M;4}$	197	20
	$\dot{\theta}_{M;5}$	164	10^{-8}
	$\dot{\theta}_{M;6}$	198	10^{-6}
	$\dot{\theta}_{M;7}$	159	10^{-6}
Normalisation factor	ν_1	0.148	1
	ν_2	0.010	1
	ν_3	0.023	1
Forgetting factor	α_1	0.979	1
	α_2	0.639	1
	α_3	0.621	1
Maximum eigenvalue	$\rho_{M,1}$	1190	10^4
	$\rho_{M,2}$	1290	10^4
	$\rho_{M,3}$	1030	10^4
Minimum eigenvalue	$\rho_{l,1}$	9.32	10^{-2}
	$\rho_{l,2}$	6.86	10^{-10}
	$\rho_{l,3}$	14.3	10^{-10}

Table 8.3: Optimised estimation algorithm parameters

The optimum values in table D.14 has a few noticeable factors. The first one is the low initial estimation gain for bulk modulus ($\Gamma_{2;1,1}(0)$) which indicates that the normalisation factor might be set high compared to the others. The optimum value is however not equal to the minimum, indicating the optimum is still inside the bounds used. For the normalisation factors, ν_2 and ν_3 are found to be almost zero, resulting in almost no normalisation being used. ν_1 is optimised to 0.148, indicating the force relevant parameters can benefit from having some normalisation. The forgetting factor has been optimised to 0.979 and ≈0.6, indicating the estimation algorithm is benefiting from having a relative large forgetting factor.

To determine the estimation performance for each parameter without any influence from variations of the others, tests are conducted with a variation in only one parameter for each run.

Estimation Performance

The estimation performance for time-varying variations of each parameter can be seen in fig. 8.5 and 8.6. These figures will show the estimation performance if the possible fault occurring is only affecting one parameter.

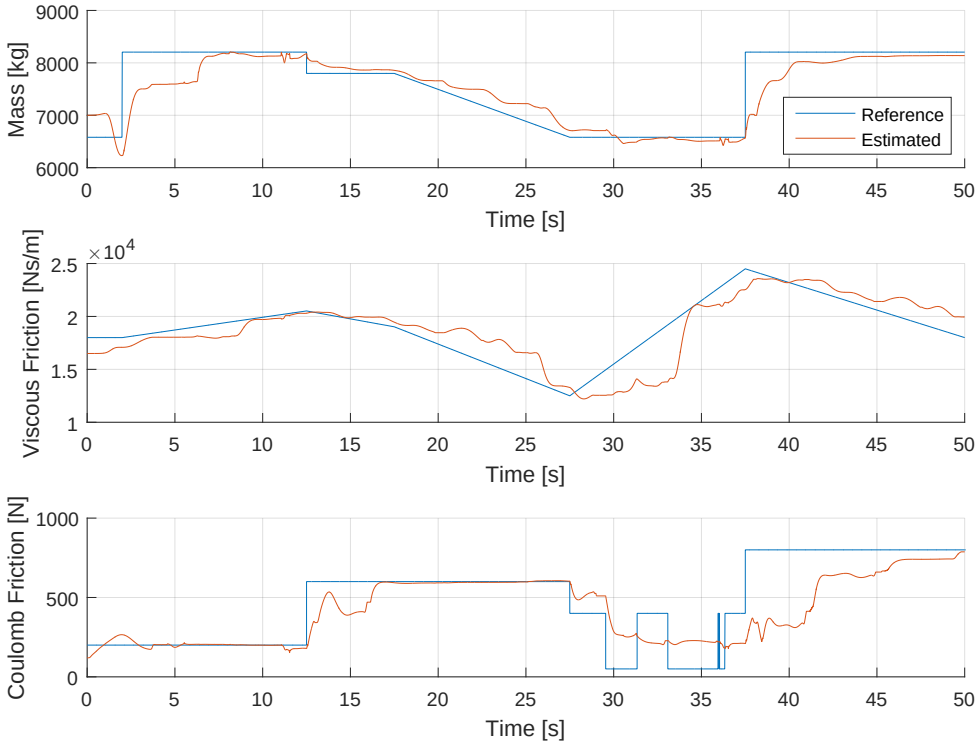

Figure 8.5: Parameter estimation of mass, viscous friction and Coulomb friction

The mass estimation in fig. 8.5 shows that the estimation algorithm is able to follow the variations emulated, with a 2-5 seconds delay for a step variation. It should be noted that the movement trajectory used is the same as for the estimation optimisation, meaning there are time periods with low or no accelerations. Without any acceleration, the estimation algorithm may have difficulties estimating. An example is at time 4 seconds, the reference acceleration is zero for 0.5 seconds, possible resulting in the mass estimation stopping to converge.
For the viscous friction, similar conditions apply, with the estimation algorithm being able to follow the reference, with some issues at ≈27-34 seconds, which is a period in time where a low reference velocity occurs.
The Coulomb friction has some difficulties, however, it follows the tendencies.
The last uncertain parameter D_{1n} is not shown, due to the reference being zero.

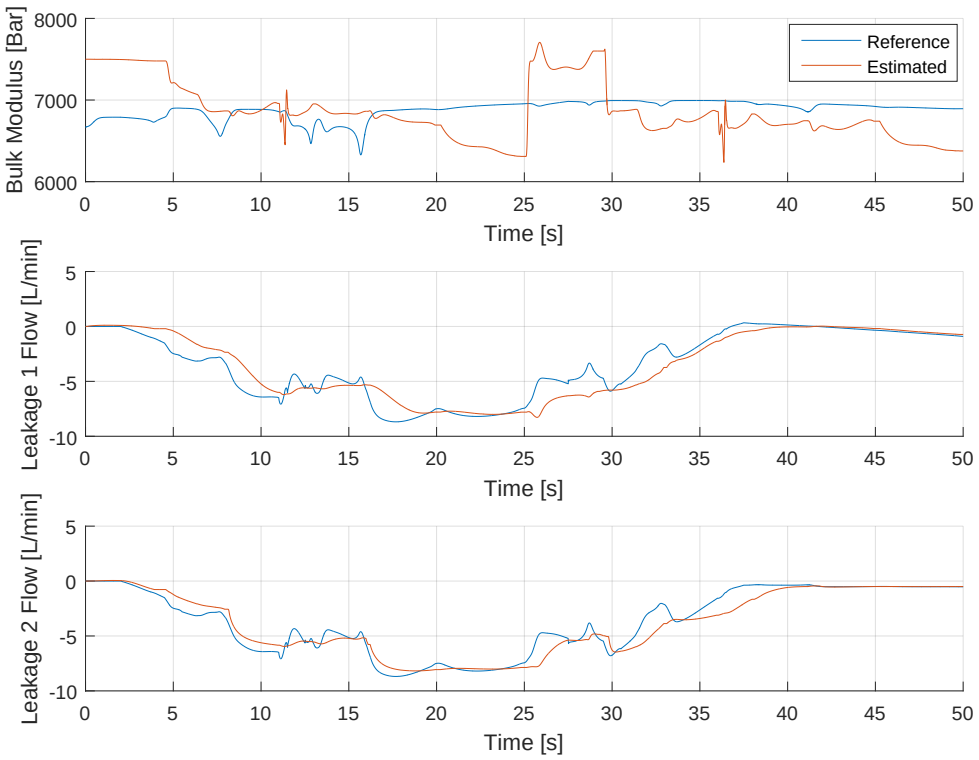

Figure 8.6: Parameter estimation of bulk modulus, leakage flow 1 and leakage flow 2

The bulk modulus estimation in 8.5 shows that the algorithm has some difficulties estimating the reference value, while still being somewhat close to the reference value. A possible explanation to the difficulties is the low pass filter applied on the pressure measurements to allow an approximation of the pressure dynamics removing the high frequency variations. However, if the cut off frequency in the filter is increased too much, problems regarding noise can appear.
The leakage flows follows the reference quite well with a small delay or offset.

A simulation where all parameters are varied as is the case for the fault trajectory used during determining the estimation parameters has also been made. Tendencies were similar, with the only parameters being affected significantly being mass and bulk modulus. The results can be found in App. D.

CHAPTER 9

SUB-CONCLUSION

In this part of the report the IARC structure has been determined for the hydraulic system of interest. The IARC consists of a control law and an estimation algorithm. The effectiveness of the control law is found to depend on accuracy of the estimation algorithm. If the parameter variations are within the defined bounds, the IARC has been proven to be stable.
The IARC tuning requires 4 control gains and two user selected constants. These parameters together with the bubble within which the controller is proven stable, determine the performance of the controller. The influence of the user defined constants ε_2 and ε_3, and the range were investigated. It was found that increasing the parameter range within which the controller is stable also requires larger values for ε_2 and ε_3. The range of parameter variations was determined through considering this compromise, and the result can be found in tab. 9.1. These ranges are found to be suitable for the system available. However, if desired, increased ranges are possible, at the cost of performance, and increased dependency of a good estimation of parameters. To determine the optimal parameters for the IARC, it was found suitable to use a GA optimisation algorithm. The determined control parameters can be seen in table 9.

Range	M_{eq}[kg]	B [Ns/m]	F_c [N]	D_{1n} [N]	β^{-1} [bar$^-$1]	D_{21n} [m^3/s]	D_{22n} [m^3/s]
$\boldsymbol{\theta_{range}}$	[10 9000]	[0 30000]	[0 1500]	[-500 500]	[10000 4000]$^{-1}$	**[-9 1]/60000**	**[-9 1]/60000**

Table 9.1: Uncertain Parameter Range.

Range	k_1	k_2	k_3	k_{scale}
$\boldsymbol{\theta_{range}}$	76.5·0.05	129	$35.0 \cdot 10^{-10}$	197

Table 9.2: Optimised Controller gains

Part IV

Simulation & Experimental Results

CHAPTER 10

LABORATORY SET-UP

In this chapter, a description of the laboratory set-up provided by AAU will be given. The chapter is not only intended to provide the reader with a description of the available hardware, but to also point out specific condition that are present in the laboratory.
The optimised controller, found in sec. 8, will be tested in a simulation that will attempt to emulate these conditions before being applied on the experimental set-up. The simulation tests are made to get an indication of how well the IARC will work when all uncertainties from the lab is included, i.e. noise and delays.
The set-up in the laboratory consists of two connected cylinders. One will act as a controllable load, and the other will be the cylinder controlled by the fault tolerant IARC. A CAD drawing of the set-up can be seen in fig. 10.1, and a schematic of the set-up with sensors and valves included can be seen in fig. 10.2.

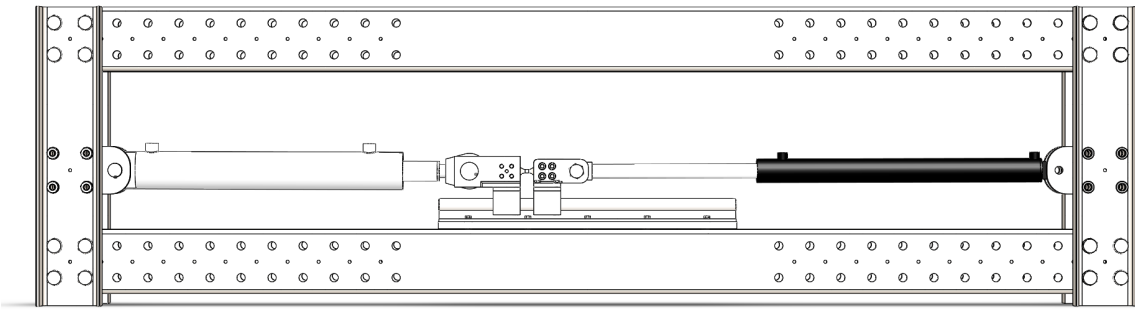

Figure 10.1: CAD of the test bench with test cylinder (left) and load cylinder (right).

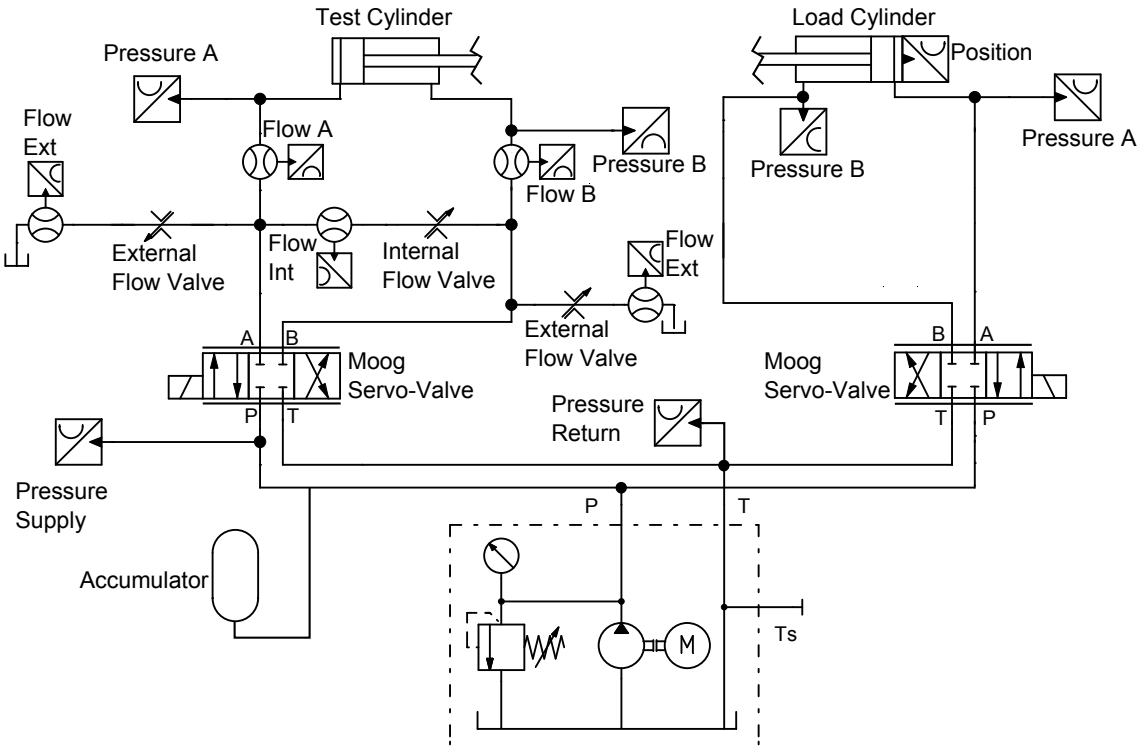

Figure 10.2: Laboratory set-up schematic.

Cylinder and Valve Dimensions

The dimensions for the test cylinder, left cylinder in fig. 10.1, are:

- Stroke length: 500 mm
- Piston diameter: 80 mm
- Rod diameter: 40 mm

The dimensions for the load cylinder, right cylinder in fig. 10.1, are:

- Stroke length: 400 mm
- Piston diameter: 40 mm
- Rod diameter: 25 mm

To control the cylinders, two MOOG-D633 valves are used. The rated flow is 40 L/min. The valves are voltage controlled, 0 to ± 10 V, and have a threshold of less than 0.1%, and a hysteresis of less than 0.2%. The null-leakage at an operating pressure of 140 bar is 1.2 L/min. [Inc., 2009]

The valves used to emulate internal and external leakages are needle valves, controllable by hand. The valve used for internal leakage and one of the external leakages (Prolasa-FT 257/2-12) has a maximum flow of 60 L/min flow at 400 bar. The valve for the other external leakage (Prolasa-FT 257/2-38) has a maximum flow of 50 L/min at 400 bar. [Prolasa].

To control the system a real time computer with an EtherCat slave will be used. The communication between the two real time PC, the EtherCat slave, the sensors and the valves will be achieved with NI's Labview software. This will be discussed in further details in App. E. It is important to note that the control law will be implemented in a loop executed at 1 kHz frequency.

To reduce pressure pulsations on the supply pressure, a 4 L accumulator has been applied after the pump output.

Measurement Equipment

The pressure transducers used are made by Danfoss and are rated to 400 bar (Danfoss-MBS 32-3615-1AB08). The pressure transmitters used are made by Danfoss and are rated for 250 bar (Danfoss-MBS-33-3411-3AB08).
The tolerance is typically ±0.3 % with a max of ±0.8 %. The response time is less than 4 ms.
For the load cylinder, the 400 bar transducer will be used, and for the test cylinder, the 250 bar transmitter will be used for each chamber, return pressure, and supply pressure. [Danfoss]

The flow sensor used are from the Parker and are rated to 15 (Parker-K-SCVF-015-10-07) and ±60 L/min (Parker-SCQ-060-0-02).
For the external leakage, the 15 L/min version will be used. The output is current and it has a tolerance of ±0.5 % and a response time less than 400 ms.
For the flow through the system and internal leakage, the 60 L/min will be used. The sensor has a voltage output and a tolerance of ±2 % and a response time less than 2 ms. [Parker]

The position and velocity sensor used is called Temposonics-RP-M-2000M-D60-1-V61000.6.
The stroke length is 1000 mm and it has an update time of 1 ms, with a resolution of 0.0015 %.
The speed range is ±1 m/s, and has a resolution of 0.1 mm/s, with deviations less than 0.5 %.
Update time is the same as position of 0.5 ms. [Temposonics].

Another position sensor is applied inside load cylinder. The sensor is from Regal, model No. PS6308. The sensor can measure the full stroke length of the cylinder from 0-400 mm with a standard linearity of ±0.1 % [Regal Components AB].

Simulation Considerations

In order to bring the non-linear model of the system, as close as possible to reality. The accuracy of the sensors will implemented as white noise, i.e. a mean of zero and therefore no bias. This is under the assumption that the sensors will be calibrated. The standard deviation of this noise will be selected as the maximum tolerance of the sensors. To implement response time delay of the sensors a low pass filters will be used. These filters have been designed to have a rise time equivalent to the largest response time of the respective sensors they are applied to. To emulate the fact that the control law will be executed once every 1 ms, a delay has been introduced after the control law is calculated. The control loop in the program has been synchronised with the scan engine, so no further delay will be introduced in the feedback signals. The IARC has been designed without the requirement of flow sensors, meaning these will not be used for the control law. The flow sensors will be used when determining the system parameters, described in App. C. The flow sensors will also be used to analyse the effectiveness of the estimation of leakage flows in the system. A test of the controller with these considerations implemented in the model can be seen in the following chapter.

CHAPTER 11

SIMULATION RESULTS

To verify the stability and performance of the IARC with optimised gains a number of simulations are made. First a verification of the non-linear model that will be used in this chapter will be conducted here. Once it has been shown that the model agrees to a degree with the real system, a simulation where no faults are present will be introduced. The conditions used and results from this simulation will serve as a benchmark throughout the chapter, referred to as nominal conditions, and the performance can be seen in App. F.2. Using the nominal conditions as a benchmark the system response will be compared when different faults are introduced. This will give an indication of the fault tolerance of the IARC. During the first tests only one parameter variation will be introduced per simulation.
The considerations from the previous chapter regarding noisy measurement and delays have been implemented in the model used for these tests. Sec. 11.2 will discuss the influence of the measurement noise on the performance of the IARC. The tolerances of the sensors are included in the simulation as white noise with a standard deviation (δ) corresponding to the tolerance value of the respective sensor. The values have been validated experimentally and can be seen in App. E.2.1. Their values are:

- δ_x = 0.1 mm, with a rise time of 0.5 ms
- $\delta_{\dot{x}}$ = 5 mm/s, with a rise time of 0.5 ms
- $\delta_{p_{test}}$ = 0.75 bar, with a rise time of 4 ms
- $\delta_{p_{load}}$ = 1.20 bar, with a rise time of 4 ms

The rise time for position and velocity is not emulated due to the sampling frequency (1 kHz) being slower. The rise time for pressures are emulated as a first order system with an approximate rise time of 4 ms. Since all optimisation was done without noise in the measurements, its effect has to be investigated before a performance benchmark is selected.

11.1 Verification of Non-linear Model

To verify that the non-linear model constructed in chap. 5 is correct and describes the dynamics of the system accurately, a comparison between simulated and measured results is made. The position, pressures, and flows will be compared.
The valve inputs used during the measurement test have been recorded. These time series will be used as inputs to the simulated cylinder models. The measured supply and tank pressures

will also be used in the simulation because it was found that they are varying during the tests. Comparisons of pressures, flow, and position can be seen in fig. 11.1-11.3.

Pressure Dynamics and Flows Comparison

Fig. 11.1 shows similar tendencies have been achieved for the measured and modelled pressures and flows. There are some differences in the pressure magnitudes, for example after the valves are opened at time 1 second, the simulated pressures drop resulting in a smaller pressure difference across the simulated cylinder. Because of the large difference in chamber areas the resulting force is still in the correct direction. The opposite happens when moving in the other direction, seen at time 2 seconds, resulting in a larger force produced by the simulated cylinder compared with the real one. This indicates some differences between the non-linear model and the real system. The differences could for example be friction forces and leakage flows. The friction parameters used in the model are based on test results in the App. C. These were deemed uncertain partly due to their sensitivity to pressure measurement errors, and partly due to the use of a basic friction model only considering Coulomb- and viscous friction. A leakage across the valve is evident on the real system, and is also mentioned in the data sheet. This has been included in the model, but this value has not been validated, due to measurement uncertainties as discussed in App. C.

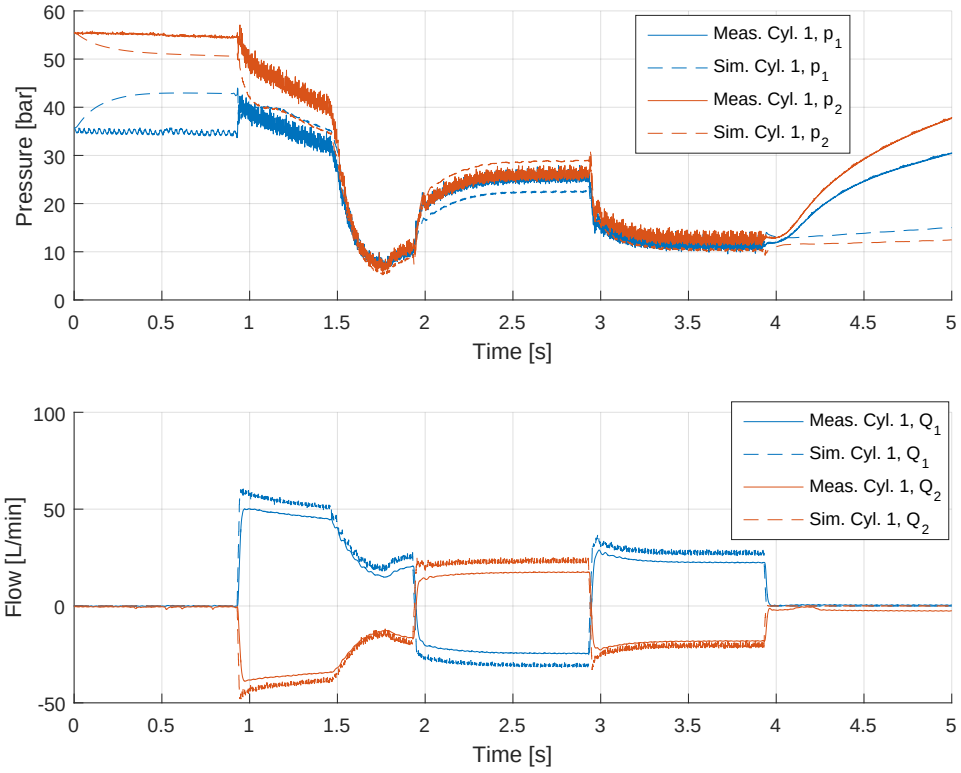

Figure 11.1: Cylinder 1 dynamic comparison of experimental and non-linear model.

For the second cylinder, the flows were not measured, because flow sensors were installed only on the test cylinder. The simulated flows are included, to show their dynamics. The difference

in the simulated pressures for the second cylinder are almost always lower than the measured, with the exception being when the valve is close after time 4 seconds. Similar to the first cylinder, the explanation could be errors regarding friction forces and leakage flows.

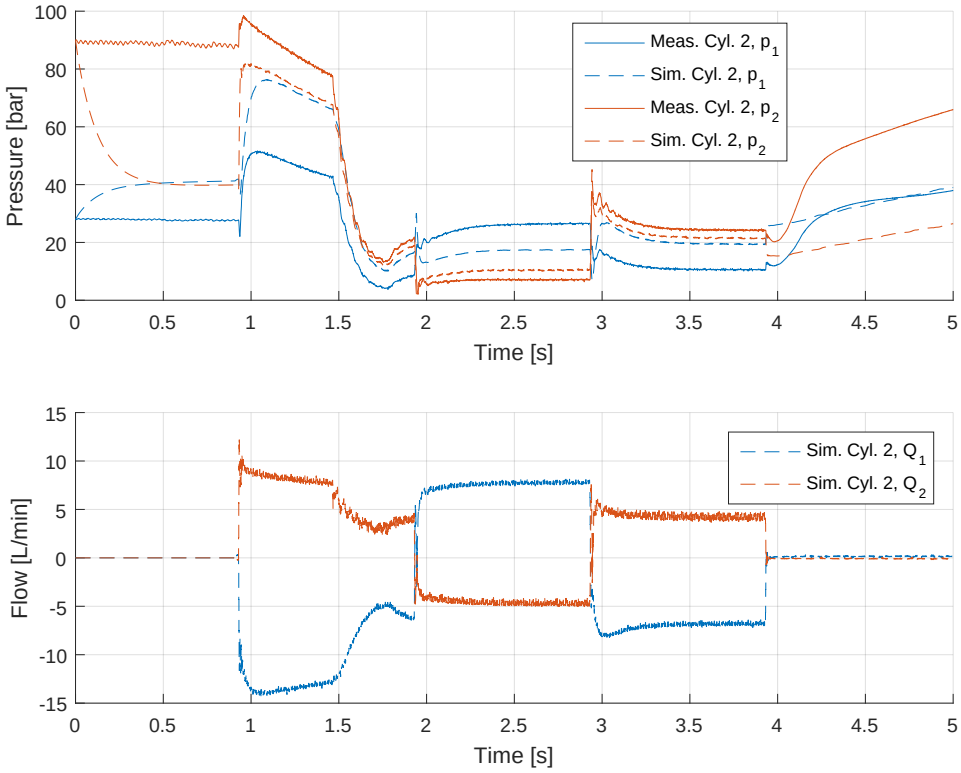

Figure 11.2: Cylinder 2 dynamic comparison of experimental and non-linear model..

Position Comparison

In fig. 11.3, two different simulations are shown. In the first the measured valve inputs are fed to the valves in the complete non-linear model. For the second test, the measured pressures are used directly in the mechanical equation, omitting the orifice equation and continuity equation in the model. This is done to detect if the difference in chamber pressures observed in the previous figures has a significant effect.
In fig. 11.3, the position shows similar tendencies between measured and simulated using the experimental valve openings. The offset could be due to the friction parameters or possible leakage in the system not accounted for.
When using the measured pressures directly, the result is a significant error in the position. This indicates that either the pressure measurements are wrong or the estimated friction parameters are not tuned correctly. By tuning the friction parameters, it was possible to make the position fit when moving in the positive direction, when moving in the negative direction however, the position barely moved, even when setting the friction forces to zero. Since friction forces cannot be negative it is concluded that the pressure measurements are, as mentioned in App. C, uncertain, and might not be correct. Once again a variation of 1 bar in the measurements can result in forces large enough to accelerate the 25kg mass of the system, resulting in the position error seen here.

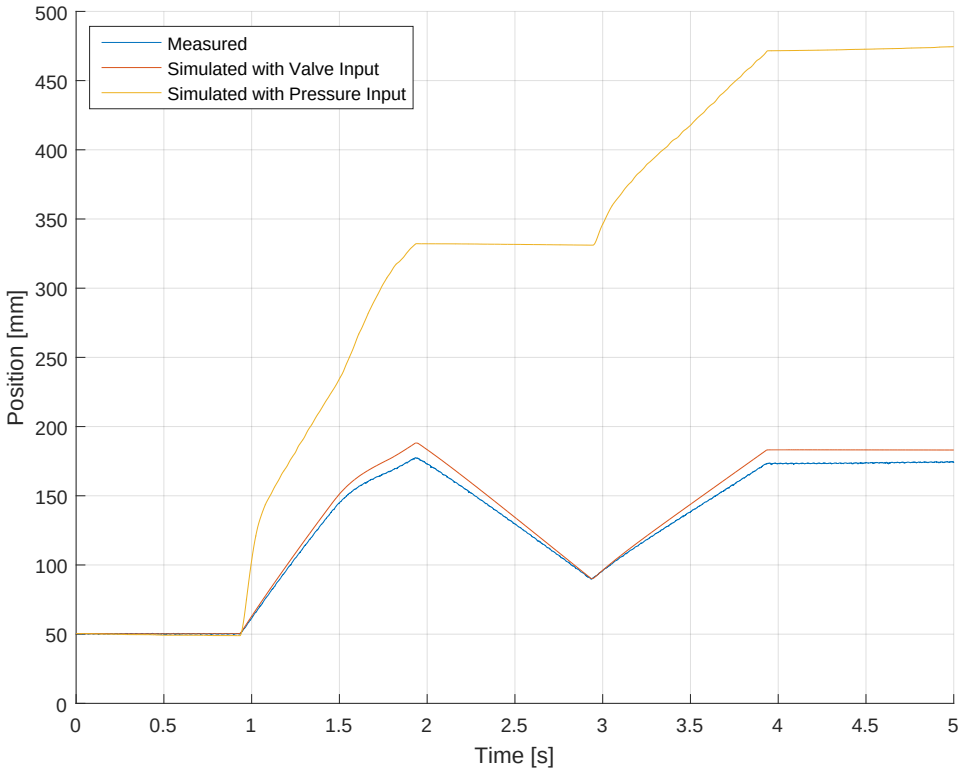

Figure 11.3: Position comparison of experimental and non-linear model.

11.1.1 Verification Conclusion

Based on the measurements and tests discussed in this section, the following can be concluded

- The non-linear model shows tendencies not unlike the real system
- Due to uncertain measurements, and possibly due to a simple friction model it cannot be concluded why the non-linear model does not describe the real system perfectly
- New friction models and further verifications have not be considered due to time constraints
- It is further concluded that the parameter uncertainties are within the fault ranges the IARC is designed for meaning. The controller can be implemented under these conditions

11.2 Noise Influence on System Performance

11.2.1 System Response without Measurement Filters

To determine the effect of noise, a simulation with the noise levels from the datasheet explained in the Chap. 10 is made. In App. F.1, reasoning behind the need of filters is shown.
Based on the results it is found that due to the influence from noise, a low pass filter with a 15 Hz cut-off frequency should be applied to the measured inputs of the IARC. With this filter the estimation is not affected, but the chatter of the IARC is reduced significantly. No filter will be applied to the force controller. Attempts to down-tune the force controller and either reduce

its sensitivity to noise or allow a filter to be applied have not worked. All force controllers tuned with a lower bandwidth have shown stability issues when paired with the IARC.

11.3 System Performance under Faulty Conditions

To determine how much the system performance degrades under faulty situations, different fault scenarios will be tested. To compare the performance, the nominal condition benchmark simulations will be used, described in App. F.2. The nominal values can be seen in tab. 11.1. The system performance may be influenced by the value of each parameter, i.e. the system performance may vary for a mass of 6000 kg and 9000 kg. The comparison will however give an indication of the impact of a fault.

Range	M_{eq}[kg]	B [Ns/m]	F_c [N]	D_{1n} [N]	β^{-1} [bar^{-}1]	D_{21n} [m^3/s]	D_{22n} [m^3/s]
Nom. Value	6525	18000	200	0	7000^{-1}	0	0
Ini. est.	7000	16500	120	0	7500^{-1}	0	0

Table 11.1: Nominal value of uncertain parameters and initial estimate used.

It is expected faults occur one at a time. The fault will be simulated by a change in the system, in the form of: M_{eq}, B, F_c, ε_{A0}, A_{Leak}. The time at which the different changes occur and their magnitude is shown for each test. The nominal test did not have any variations, only an initial error. The values used can be seen in tab. 11.1.
The first results will show the performance for the control law and estimation when the system reference trajectory has a pulse reference, moving from one end to the other. This test will show how the IARC performs under non-optimal conditions for the estimation due to it only being accelerated for short periods of time.
The second part will be tests where a sine curve is used as a reference, resulting in a system which is accelerated at all times. This fulfils the estimations algorithms requirements, allowing it to work constantly. The result from this test can show how fast the estimation algorithm can estimate variations in parameters under optimal conditions. Furthermore it is expected that the cylinder in a wind-turbine's pitch system would have a repeating, possibly sine-like trajectory.
The last test is for conditions where the emulated mass is zero, resulting in a M_{eq} of 25 kg. This is done to make sure the system is stable when no mass is emulated. The estimation algorithm still has an initial mass estimate of 7000 kg.

11.3.1 Pulse Reference

The reference trajectory used for the tests in this section can be seen in fig. 11.4. Furthermore, the time periods where the estimation algorithm will not update has also been shown to give an indication of the conditions for the estimation algorithm.

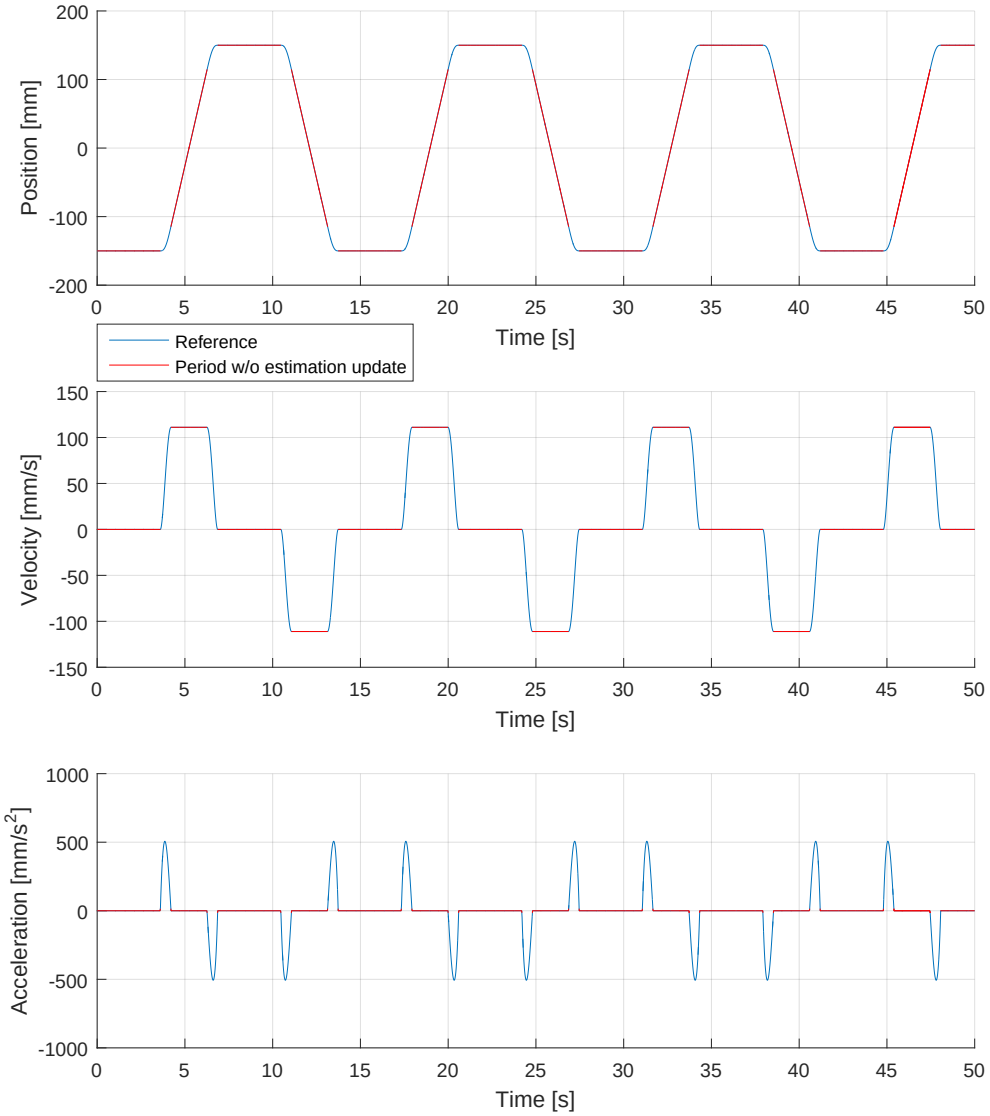

Figure 11.4: System reference.

As mentioned above, pulse like reference affects the efficiency of the estimation, because it will only be effective for small time periods. The pulse train excites the system dynamics better than a sine curve, but anti-wind up implemented in the estimation algorithm prevents it from updating parameters when the velocity and/or acceleration are equal to zero. To get an indication of how well both the control law and estimation algorithm will perform under these conditions, two scenarios are investigated. The first scenario will be where the system is affected by an increase in mass. The second scenario will be where a relatively fast increase in leakage flow opening area is introduced. One scenario will investigate the part of the estimation which is based on the mechanical equation. The other will investigate the part which is based on the continuity and orifice equations.
Simulations for faults of the remaining parameters has also been made. The results from these

tests were similar to what was achieved for faults regarding mass and leakage flow.

Mass Variation

In fig. 11.5 the reference and estimated mass is shown, together with the position error under these conditions compared to having a constant mass at the initial value.

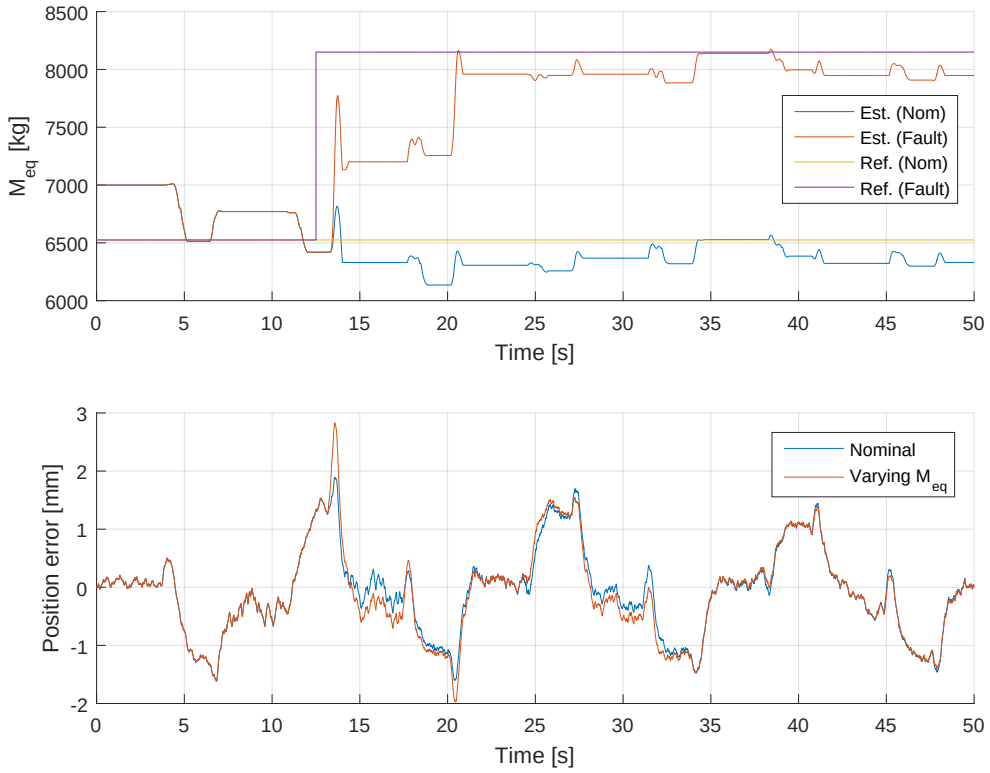

Figure 11.5: Performance when affected by a mass related fault.

In fig. 11.5, the IARC shows that it is fault tolerant to variations in the mass under these working conditions, due to it converging to nominal conditions within three acceleration pulses. Looking at the position error, the mass step introduced an increase in error. After ≈ 10 seconds, the mass change has been estimated, and nominal error response is achieved.
The instant change in mass is not expected to occur in realistic situations. A more realistic scenario would be for a gradual increase in load due to wind changes. Here the mass is varied with a step to investigate the rate with which the algorithm will converge to the correct parameter.
Results from a simulation with more variations during the run, including ramp variations, can be found in App. F.

Leakage Flow Fault

In fig. 11.6 the reference, estimated leakage, and the position error is shown.

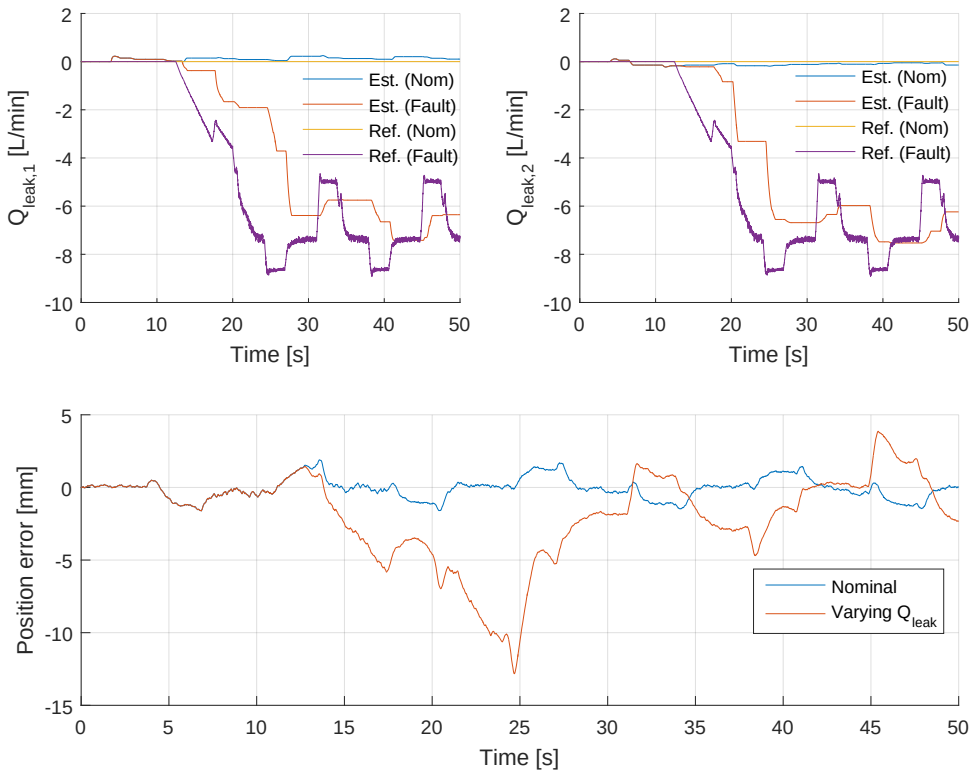

Figure 11.6: Performance when affected by an increased leakage flow.

Fig. 11.6 indicates that the IARC is not completely fault tolerant to faults regarding leakage flows. The reason for it not being considered completely fault tolerant is that it does not converge to nominal conditions, but only reduces the effect from the fault.
In fig. 11.6 the estimation takes longer to converge to the increased leakage flow, due to the estimation algorithm only being able to estimate when the system is accelerating. After ≈3 pulses, the leakage estimation is in the same range as the real leakage. Looking at the position error plot, the initial delay on the leakage estimation resulted in a relative large error of up to 12 mm. After the estimation algorithm has converged to approximately the same value as the real leakage, the position error is reduced to ±4-5 mm. The nominal case has errors up to ±2 mm, indicating the leakage estimation is not perfect, which can also be seen on the comparison of reference and real leakages. The algorithm does however shows that it is able to compensate for part of the introduced fault in the form of leakage flow. If an improved estimation algorithm is used, resulting in a better estimation, the error may be reduced further to nominal like conditions.

Other Faults

The figures for the remaining faults have been omitted here, and are shown in App. F. The main findings are:

A fault introduced in the form of a step change in the viscous friction had a similar response to the mass step. When the change is introduced, the effect was observed as an increased error.

After 4-5 pulses, the estimation algorithm had converged to the correct viscous friction. After 8-9 pulses, the position error signal was the same as the nominal case. Based on this, the IARC is considered fault tolerant to step changes in viscous friction changes under these working conditions.
Continuously varying viscous friction was also simulated in the form of a ramp change increasing and decreasing the size of B. The resulting estimation was poor. Based on the fact that the estimation managed to convert for a step change in 8-9 pulses, a reason for the poor estimation is that the variations are introduced too fast for the estimation to follow the real value.
For the Coulomb friction, the fault was introduced as step changes on the absolute value of the Coulomb friction, resulting in Coulomb friction forces of ±200-1000 N. Based on the simulation, the IARC was not able to compensate completely to the fault, the reason may be it requiring a longer time period at a value to estimate it properly. The estimation algorithm had difficulties estimating the variations in the Coulomb friction, but showed tendencies of converging towards the correct value. The difficulties may be due to it being hard to differentiate between a disturbance and the Coulomb friction when only accelerating for short periods of time. For the position error response, the faulty situation generally had a larger error than the nominal case, with the largest spikes being 9 mm and -6 mm compared to the nominal case of ±2 mm.
Faults introduced as variations in the air-ratio of the oil did not have any noticeable impact on the system response.

11.3.2 Sine-Curve Reference

The reference used in this section is a 0.5 Hz sine-curve, with an amplitude of 35 mm. The resulting control input is up to ≈0.6-0.9 at the maximum speed depending on the size of leakage flow in the system.

Mass Fault

A change in mass can be explained by a change in the load of the system. It not assumed that these kinds of faults can occur abruptly, but this will be done here to show the limits of the algorithm. The fault will be simulated by a step in the trajectory of the load cylinder. A ramp input is also implemented, which could be due to an increase over time in load. Change of these sort are more likely real life. The mass trajectory used to simulate these faults can be seen in fig. 11.7. A comparison of position error between the faulty case and a nominal case with a constant mass of 6525 kg is also shown.

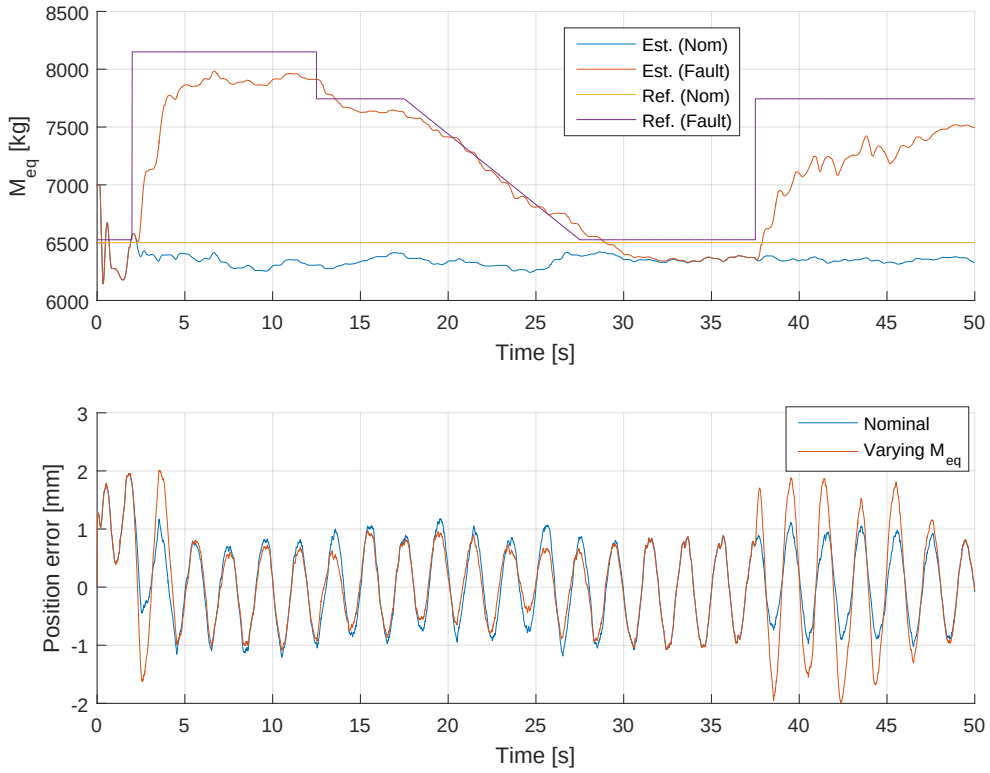

Figure 11.7: Performance for a mass related fault

From fig. 11.7, the IARC is found to be fault tolerant to mass variations under the conditions applied, both to step variations and to ramp variations. Furthermore, there are indications of either the emulated mass or the estimated mas being ≈ 2 % off the reference mass. In fig. 11.7 the position error shows that the steps emulated in mass has a position error effect of up to ≈0.5 mm, before converting to similar performance as obtained with the constant mass of 6525 kg. For some cases, the performance is improved after the estimation has converged to the correct value, which could be due to the increased mass damping the system.

Viscous Friction

In order for the viscous friction of the system to change, the consistency of the oil has to change. Either due to foreign particles or due to temperature variation. Changes of this nature are expected to occur slowly, which is why this parameter will also be varied slowly. The trajectory tracking performance can be seen in fig. 11.8.

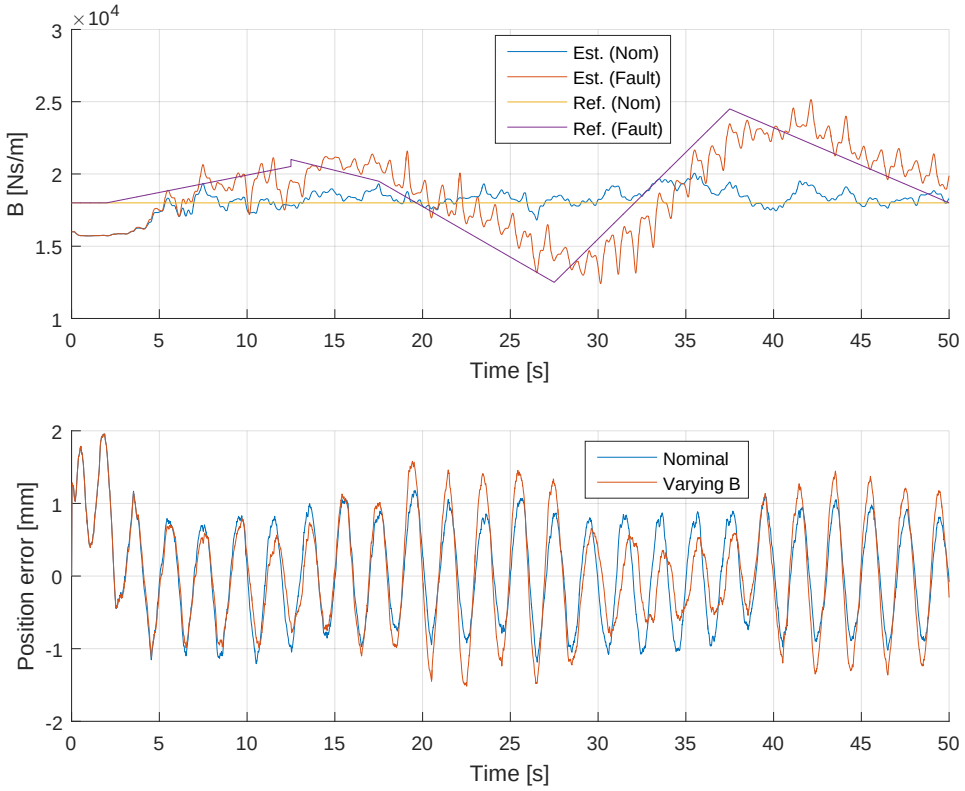

Figure 11.8: Performance for a Viscous friction related fault

Fig. 11.8 indicates that the system when having a large viscous friction has improved performance, possibly due to the increased damping. When a decrease in B is applied, the error is increased, and when it is increased, the error is decreased. This shows that the system works better for an undershoot of the parameter than an overshot. Generally, the estimation algorithm is able to follow the variations, and if the viscous friction coefficient was set to constant for a time period, the correct value should be estimated with similar accuracy as for the nominal case. Based on these findings, the IARC is found to be fault tolerant to variations in the viscous friction under these conditions.

Coulomb Friction

The magnitude of the Coulomb friction parameter will be varied abruptly. The results of the simulation can be seen in fig. 11.9.

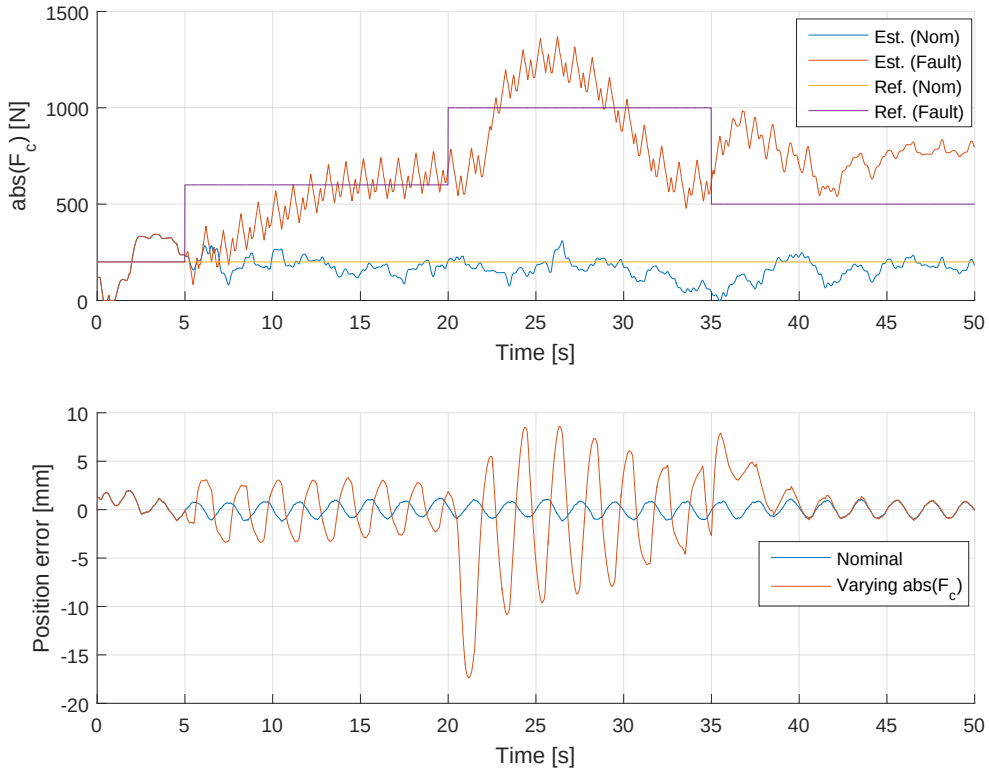

Figure 11.9: Performance for a Coulomb friction related fault

In fig. 11.9, it can be see that the estimation algorithm struggles with estimating the correct Coulomb friction. The problems in estimation result in reduced performance. Furthermore, the problems in estimation may cause problems for the other estimated values. To investigate this, the estimated parameters and corresponding reference is shown in fig. 11.10.

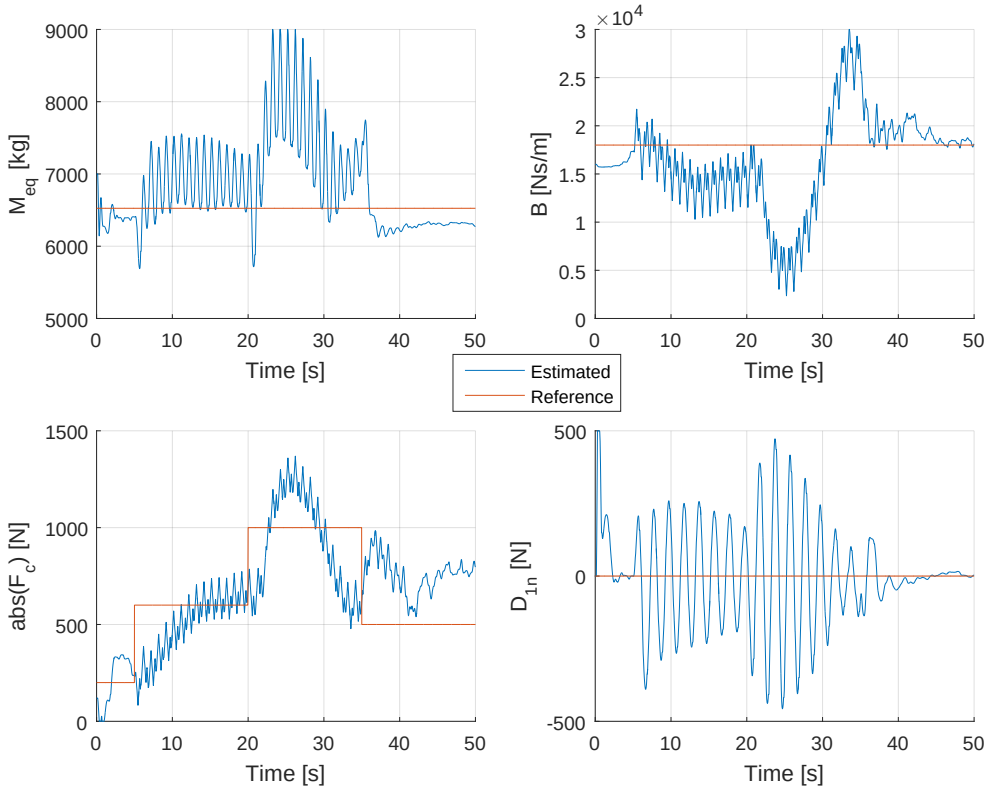

Figure 11.10: Estimated force related parameters

The largest position errors occurred at the time internal 20-35 seconds. In fig. 11.10, this corresponds to the time period with the largest estimation errors of the three other parameters. This indicates that the estimation algorithm has troubles determining if the introduced fault corresponds to a change in Coulomb friction, and not mass or viscous friction. If given a larger time span to converge, the system should learn, for example the mass gives indications of converging back to the reference. At the time internal 35-50 seconds, the Coulomb friction is reduced again. Here, the other estimated parameters converges to their correct values, while the Coulomb friction maintains an error of ≈200 N. For this time internal, fig. 11.9 shows that the position error corresponds to nominal values. Based on these observations, faults due to Coulomb friction are deemed hard to compensate, however, under some conditions, and if given a larger time span, the system will converge to nominal conditions.

Air-Ratio

Faults resulting in a varying air-ratio in the oil will affect the size of the bulk modulus, with the main effect being at pressures below 100 bar. The result from varying the air-ratio in the simulation can be seen in fig. 11.11, where a comparison of the resulting bulk-modulus value and estimated value is shown. A comparison of the performance to a nominal case is also shown.

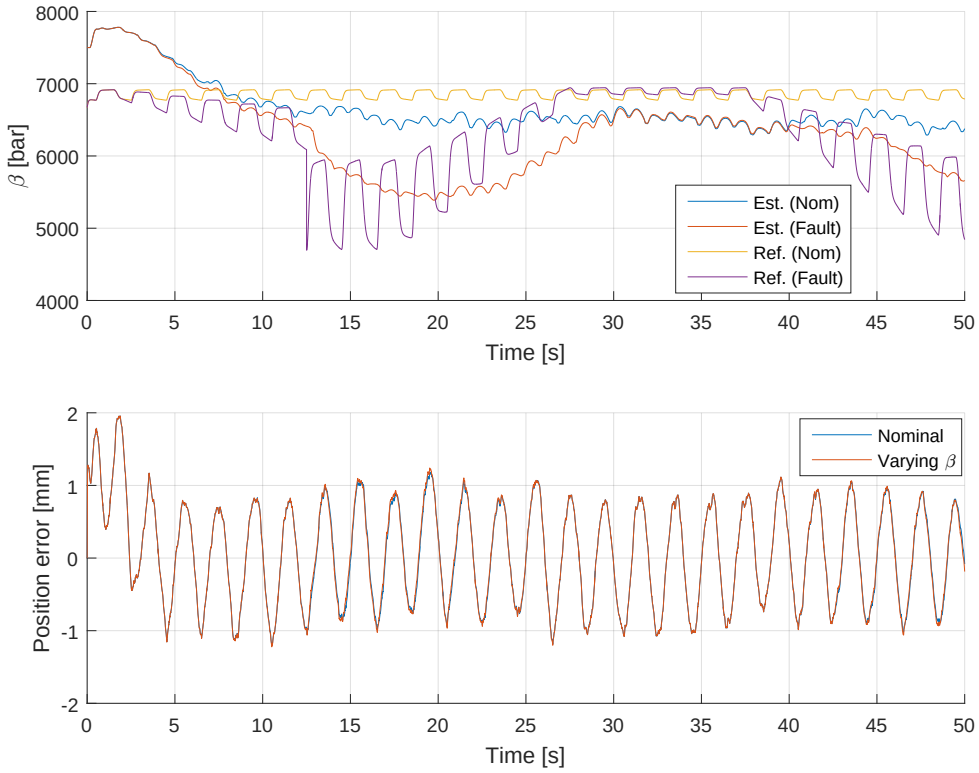

Figure 11.11: Performance for an air-ratio related fault

Fig. 11.11 shows that the estimation follows the reference somewhat. The estimation is not able to follow the relatively fast changes due to direction changes, but it follows the main variations. The effect on the position error is minimal, resulting in the IARC being considered fault tolerant to air-ratio variations under these conditions.

Leakage

Faults resulting in varying leakage flows, both external and internal, has been combined. The emulation of a leakage flow fault will be an increase in leakage area over time, untill ≈ -9 L/min is obtained. A decrease in leakage is also emulated, although this might be uncommon in real systems. The external leakage is increased after ≈ 27 seconds. After this point the difference of the two leakage flows is not zero ergo the leakage leaving one chamber is not entering the other.

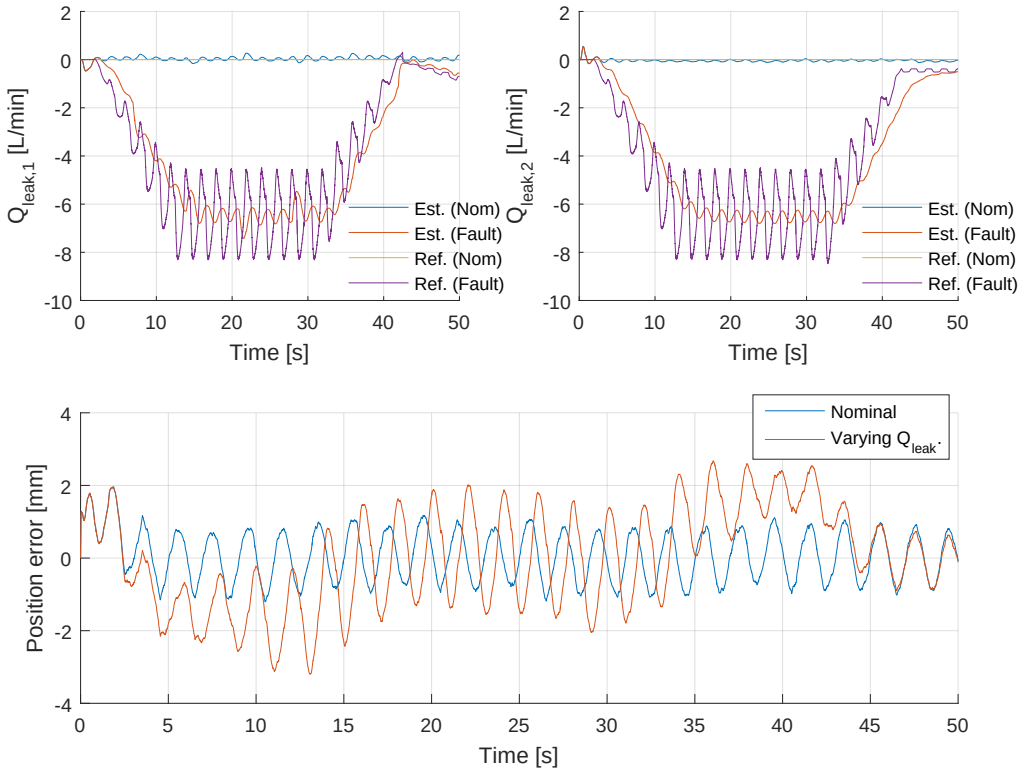

Figure 11.12: Performance for a Leakage related fault

From fig. 11.12, the IARC is not considered to be completely fault tolerant to faults regarding leakage flows. Similar to the pulse-reference test, the estimation algorithm is only able to estimate the average leakage flow, resulting in it not achieving nominal conditions at when a large leakage is applied. For lower leakages, the effect is smaller, and the estimation is able to follow the variations better, for example after time 45 seconds.

No Mass Emulation

For safety reason, a situation where the force controller is not working as intended is simulated. The force controller is given zero reference, which means the equivalent mass in the system is the 25 kg real mass. The initial mass estimate is kept at 7000 kg, to determine how quickly the estimation algorithm can estimate the correct mass of 25 kg. The trajectory used is the pulse-reference. The response can be seen in fig. 11.13.

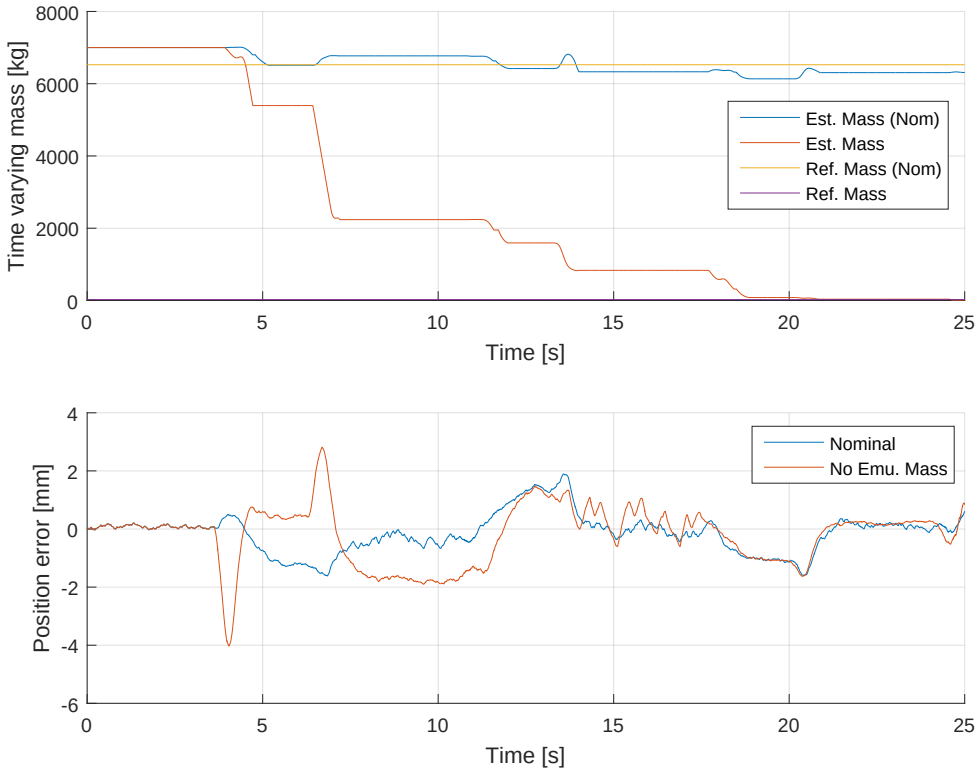

Figure 11.13: Performance with M_{eq} of 25 kg, with initial estimate of 7000 kg.

Fig. 11.13 shows that the estimation algorithm is able to converge to the correct mass within 5 acceleration pulses. The system response shows that the performance is improving as the mass converges to the correct value. Initially an error of up to 4 mm is observed. After the mass has converged, position error is similar to the nominal conditions.

11.4 Discussion of Simulation Results

In this part of the report the optimised controller and estimation algorithm are tested. First the influence of noise is investigated. The conclusion is that the IARC will perform satisfactory provided some of the noise is filtered out. The trade-off is that high frequency trajectories cannot be followed, since the dynamics are lost in the filtering. Since the project focus is on wind-turbine pitch systems and it is not expected for the orientation of the blades to change faster than 1 Hz, it is concluded that the trade-off is acceptable. The second set of tests investigate the influence of a trajectory on the abilities of the controller to estimate parameter changes.

A pulse like trajectory is used, because it has long periods of time where velocity and acceleration are zero. The estimation algorithm was able to estimate changes in parameters even though the operating conditions for the algorithm were sub-optimal. The controller had a larger error when the fault was introduced and then converged to a smaller error when the estimation converged to the real parameter. The test where leakage was introduced showed that the estimation algorithm had some difficulties following the real leakage flow perfectly.

This resulted in position error larger than the one in nominal conditions. It was however able to reduce the error significantly.
For the last test regarding having no mass emulation, the estimation algorithm was able to converge from an initial mass guess of 7000 kg to the correct mass of 25 kg within five acceleration pulses, which resulted in the performance converging to nominal performance.

The tests with a sine curve trajectory, showed better estimation, probably due to the system having a varying velocity and acceleration at all times. This fulfils the estimation algorithm conditions regarding when it updates. The estimation algorithm was able to estimate the parameters well. The most difficulties occurred for the the Coulomb friction estimation. The continuous estimation of parameters resulted in the estimation algorithm being able to estimate the parameters consistently. After the estimation algorithm had converged to the applied variations/faults, the IARC was able to obtain nominal like system responses.

Based on these results, the performance is found to be heavily dependant on how fast the estimation algorithm converged to the real values.

Generally the IARC seemed to be able to compensate for variations in the system, which can occur during faulty situations. To verify that this also works on a real set-up, similar tests will be made experimentally on the set-up described in Chap. 10.

Table 11.2 shows the Root-Mean-Square of the position error, recorded during runs for each parameter estimation for both the pulse train and the sine wave trajectories. The RMS errors will be for fault trajectories used during the Sine-wave trajectories, which has also been applied when using the pulse trajectory.

Trajectory	e_{RMS} Nominal[mm]	e_{RMS} M_{eq} [mm]	e_{RMS} B[mm]	e_{RMS} F_c[mm]	e_{RMS} β^{-1}[mm]	e_{RMS} Leakage[mm]
Pulse train	0.73	0.79	1.49	2.04	0.73	3.58
Sine Wave	0.70	0.82	0.77	3.84	0.70	1.36
Trajectory	$\lvert e_{max}\rvert$ Nominal[mm]	$\lvert e_{max}\rvert$ M_{eq} [mm]	$\lvert e_{max}\rvert$ B[mm]	$\lvert e_{max}\rvert$ F_c[mm]	$\lvert e_{max}\rvert$ β^{-1}[mm]	$\lvert e_{max}\rvert$ Leakage[mm]
Pulse train	1.90	2.29	3.31	9.45	1.90	12.83
Sine Wave	1.96	2.01	1.96	17.38	1.96	3.19

Table 11.2: Root-Mean-Square and maximum of the position error for different parameter faults for pulse train trajectory and a sine wave trajectory.

It is desired to compare the simulated performance with the experimentally obtained one, in order to verify the fault tolerance of the IARC.

CHAPTER 12

EXPERIMENTAL RESULTS

Contents

This chapter will show the experimental results obtained from the laboratory implementation of the IARC and the estimation algorithm. The faults are introduced one at a time and the results from the estimation algorithm and the changes observed in the performance of the IARC are analysed. A number of changes had to be introduced in the algorithm in order to facilitate smooth operation for all conditions. These modification are shown and discussed in the first section. The second section discusses tests which attempt to replicate the nominal conditions benchmark established in App. F.2. Each following section shows the fault operation of the estimation algorithm and the IARC for a specific parameter variation.

12.1 Filtering and Parameter changes

Based on the estimated friction parameters in App. C, the initial guesses of friction parameters that were used in the non-linear model were not chosen correctly. According to the tests the friction parameters change according to direction.
The estimated viscous friction was significantly lower than assumed, ≈7670 Ns/m in one direction and ≈859 Ns/m in the other, which is significantly different than the initial assumption of 18000 Ns/m. These values are within the defined estimation range of [0 30000] Ns/m. Since this is the case it is expected that the estimation algorithm will converge to the real value.
The Coulomb friction found through the tests in App. C was larger than expected. Values of up to 1384 N and 198 N in the other direction were calculated, compared to the initial guess of 200

N.
The initial assumed size of Coulomb friction led to an initial range of [0 1500] N for the estimation algorithm. The upper bound of the range is close to the calculated values. It is not desirable to have the upper bound so close to the actual value, because it would be difficult to distinguish between an overshoot of the estimation and an incorrect estimation, if in both cases the estimation shows a saturated value. The range of the Coulomb friction has been increased to [0 3000] N to prevent this.
A new optimisation is required to ensure that the controller is stable for this range. The new friction values have been added in the non-linear model as well as the expanded range. Since the friction parameters calculated from the tests are considered uncertain an average value has been chosen. This can result in a less than optimal controller performance-wise, but it also results in more robust controller. The friction parameters used are 600 N for Coulomb friction and 3000 Ns/m for viscous friction. The resulting controller is shown in table 12.1. The estimation range is shown in table 12.2.

Range tested	k_1	k_2	k_3	k_{scale}
$\boldsymbol{\theta_{range,exp}}$	77.2·0.05	5.11	$545 \cdot 10^{-10}$	27.5

Table 12.1: Control Law Parameters used for experimental testing

Range	M_{eq}[kg]	B [Ns/m]	F_c [N]	D_{1n} [N]	β^{-1} [bar^{-}1]	D_{21n} [m^3/s]	D_{22n} [m^3/s]
$\boldsymbol{\theta_{range,exp}}$	[10 9000]	[0 30000]	[0 3000]	[-500 500]	[10000 4000]$^{-1}$	[-9 1]/60000	[-9 1]/60000

Table 12.2: Parameter Ranges used for experimental testing.

An increased filtering of the measured data that is fed into the IARC was needed in order to obtain a smooth response. Runs with position and pressure filters set to 15 Hz resulted in near instabilities. It was concluded that the signals were not smooth enough for derivation after they were filtered. This resulted in spikes in velocity and acceleration estimation. The controller compensated for this acceleration which leads to problems during the run. The sudden drop in position observed in fig. 12.1 is the result of one of these problems. This drop in position could be easily heard and a pressure spike could be observed in the hoses. Because of safety concerns associated with the possibility of larger spikes when faults are introduced, it was concluded that the feedback signal have to be filtered more.

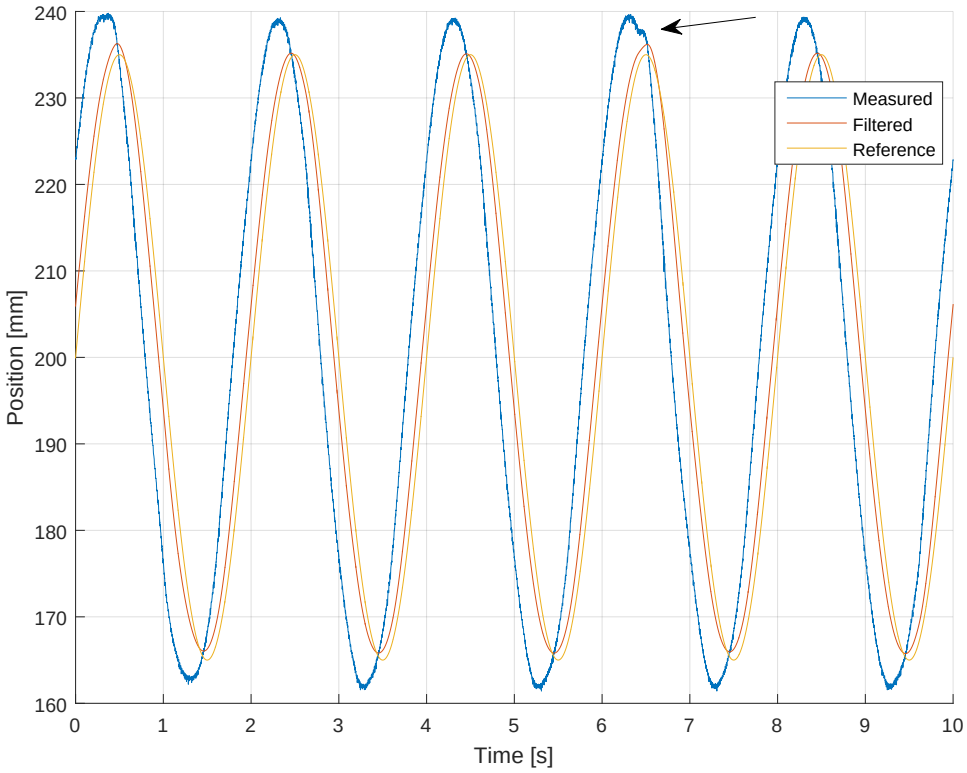

Figure 12.1: Results with initial filters.

The cut-off frequency for positions and pressures was reduced to 1 Hz. Velocity was found through the derivation of the position signal after it is filtered. The IARC will attempt to follow the velocity profile provided from the derivation. It was found that if the velocity is not smooth the IARC provided unneeded forces to attempt to follow the velocity reference. The filter on the velocity reference was also a 1 Hz first-order low-pass filter.
The estimation algorithm also requires that the position and pressures are filtered, but through a different filter. According to the theory discussed in Sec. 7.2 the signals have to be filtered through at least a third order filter. Instead of the 1st order 1 Hz filter, a 15 Hz third-order filter has been used for position and pressures signal in the estimation algorithm. The velocity was obtained through the differentiation of the 15 Hz filtered position signal and was further filtered with a first order 5 Hz filter. This extra filtering was required, because the velocity estimate is further differentiated to obtain an acceleration estimate. The original design in Sec. 7.2 originally intended one less differentiation.
The excessive filtering resulted in a stable controller without any chatter, but a poorer performance. It is expected that this issue can be solved after the velocity sensor is installed on the system and no numerical differentiation is required to provide velocity for the IARC. The consequence of the heavy filtering can be seen in fig. 12.2.

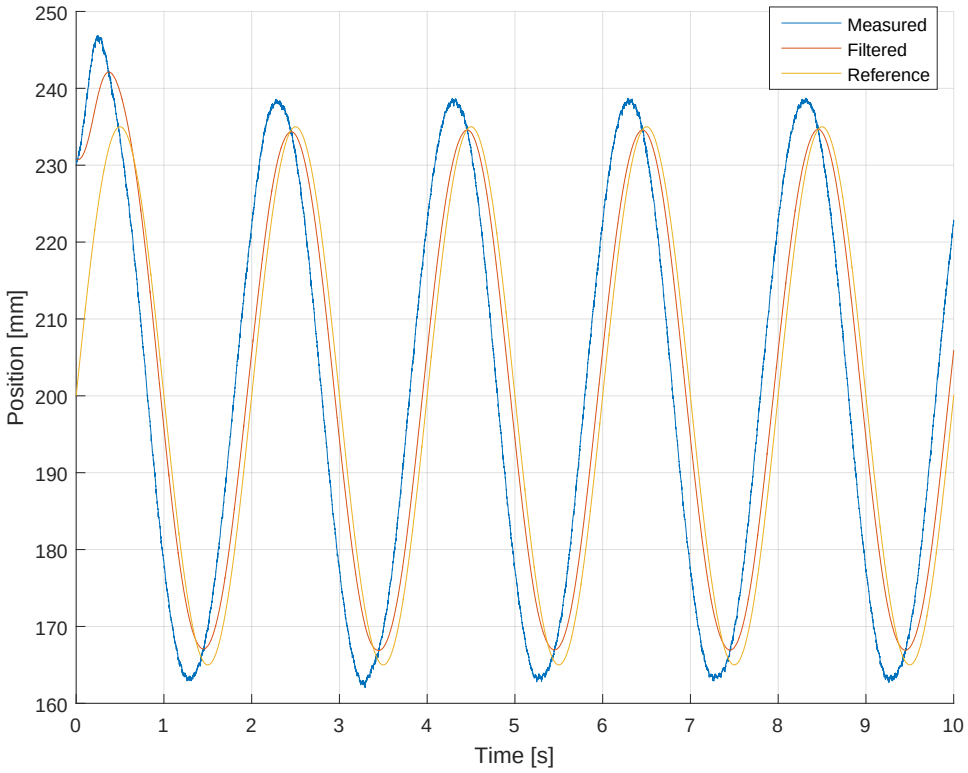

Figure 12.2: Results from increased signal filtering.

It can easily be noticed that there is a large difference between the measured position and the filtered one. It can also be observed that the filtered position, which is the signal that the IARC sees, follows the reference with some success. The conclusion from this test is that the excessive filtering has resulted in a large error in position if the reference is compared with the measured position. It can also be argued that the IARC is performing to some extent, considering the comparison between the filtered value and the reference. From these two observations it can be argued that the algorithm itself is not wrong. It is expected that some of these issues will be solved and a better performance will be obtained, when the velocity sensor is installed on the test-stand. In order to evaluate the performance of the IARC despite the situation **error will be considered as the difference between the reference and the filtered position**. This is not the real error during the test, but this method will potentially better show the effect faults have on the performance of the algorithm.

12.2 Nominal Performance and Estimation of Nominal Uncertain Parameters

For the nominal tests, the force controller is given a 0 N reference. This is done to determine if the estimated parameters converge to constant values, corresponding to the nominal parameters of the system. The nominal test is done for both the pulse reference and sine reference, to verify that they converge to the same values. The force related parameters can be seen in fig. 12.3, and the flow related parameters in fig. 12.4.

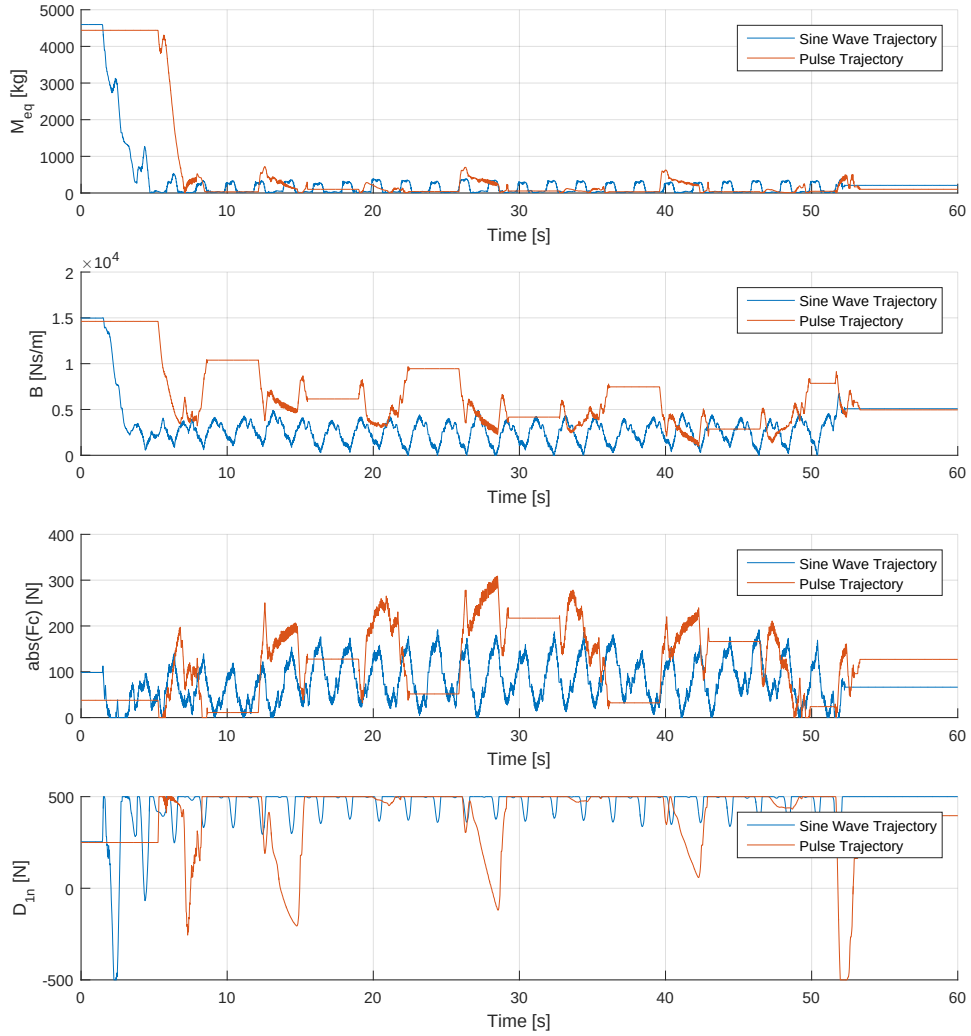

Figure 12.3: Nominal estimation of uncertain parameters estimated from the mechanical equation.

Fig. 12.3 shows that for these tests, the mass is estimated towards the lower limit. This can be expected, since the actual mass of the system is close to 25 kg. There are some variations during the run, where the mass goes up to 200 kg for the sine trajectory, and 800 kg for the pulse trajectory. This estimation error can be explained by errors in the other force parameters due to the difficulties the estimation algorithm has with estimation of the friction parameters. Tests in App. C show that a linear calculation of the friction parameter solely based on velocity results in different parameters according to the direction of movement. It can be expected that the on-line estimator would also see the difference as a sudden error when a switch in direction occurs. This can result in the 200 kg spikes. It is also possible that part of the problem is the fact that the estimation algorithm uses acceleration as the regressor associated with mass. Since this acceleration is obtained through double derivation of position the value of it is uncertain

at best.
An alternative explanation is also that the poorly performing force controller introduces force errors above the 500 N D_{1n} ranges. This can also be a valid assumption when considering that this parameter is at either saturation limit for nearly the entire run. No conclusion can be made based on the available information. It is proposed that as future work a comparison between results with a different force controller and the same estimation algorithm, and the same force controller but an expanded estimation algorithm are compared. Due to time limitation this analysis has not been conducted in this report. Instead the general trend of the estimation towards convergence is accepted as satisfactory.

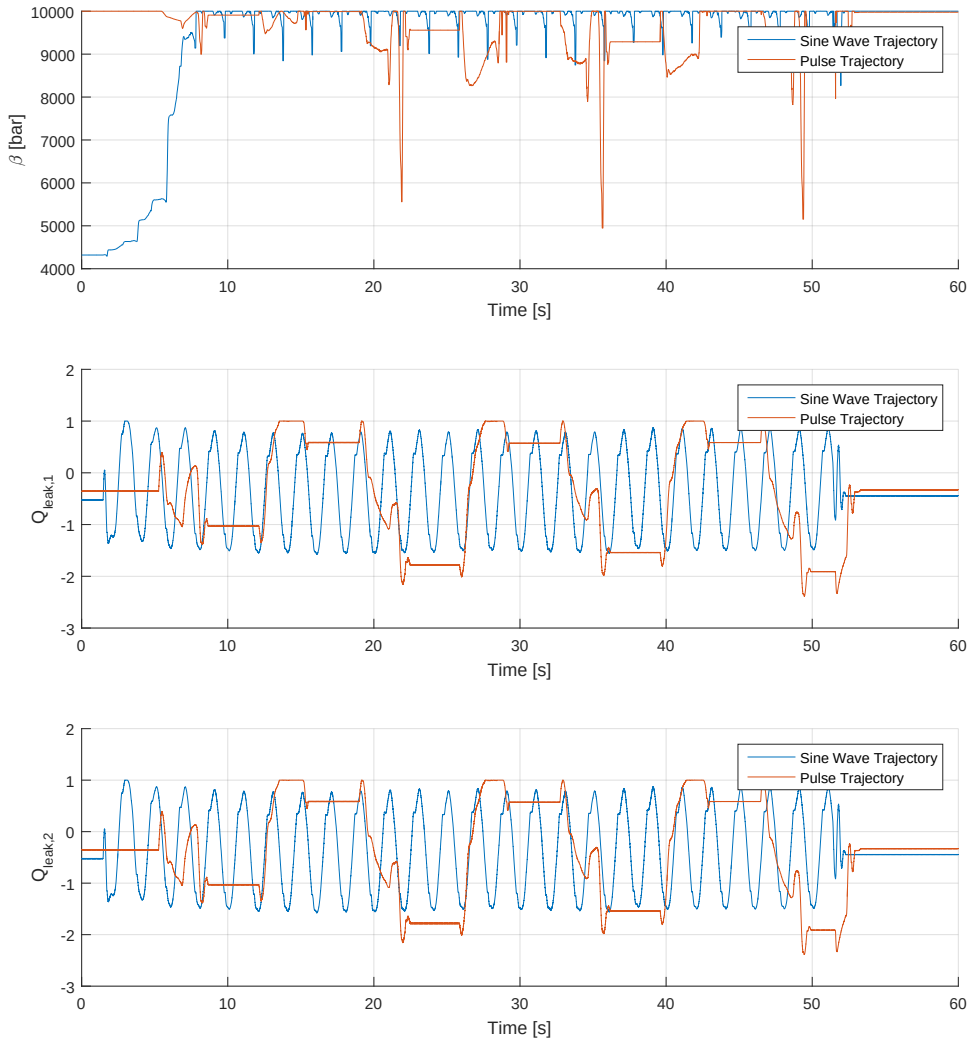

Figure 12.4: Nominal estimation of uncertain parameters estimated from the continuity and orifice equations.

Table 12.3 shows the mean values estimated during the sine and pulse trajectory following. The

information is averaged over the time period from 20 to 50 seconds . It can be noticed that the estimated values are not far-off from the values calculated in App. C. The exception is Coulomb friction, which shows much smaller values than the expected ones. It is possible that some of the force error has been redistributed to other parameters in an attempt to estimate the real system. It can also be noticed that excluding viscous friction, the estimated mean values have not been changed significantly for the two trajectories.

Trajectory	M_{eq}[kg]	B [Ns/m]	F_c [N]	mD_{1n} [N]	β [N]	$Q_{leak,1}$ [L/min]	$Q_{leak,2}$ [L/min]
Sine	120.0	2470	85	477	9930	0.788	0.789
Pulse	120.4	5470	137	427	9470	0.947	0.947

Table 12.3: Mean nominal parameter estimation.

12.3 Performance for a Mass variation

First an attempt was made to emulate, estimate and compensate for changing mass. The mass variation has been introduced as a change in the force controllers trajectory. The goal was to emulate a step of 4000 kg. The mass step occurs at ≈ 25 s. A small difference can be noticed in the estimation of mass in fig. 12.5. The algorithm consistently estimates a higher mass value with results between 400 kg and 1000 kg. This is a fraction of the desired step of 4000 kg. Two explanations for this lack of mass increase are the most obvious. Either the estimation algorithm cannot converge to the new value or the mass is not estimated in the first place. Since the estimation algorithm showed better results in the nominal test, the force controller performance was examined.

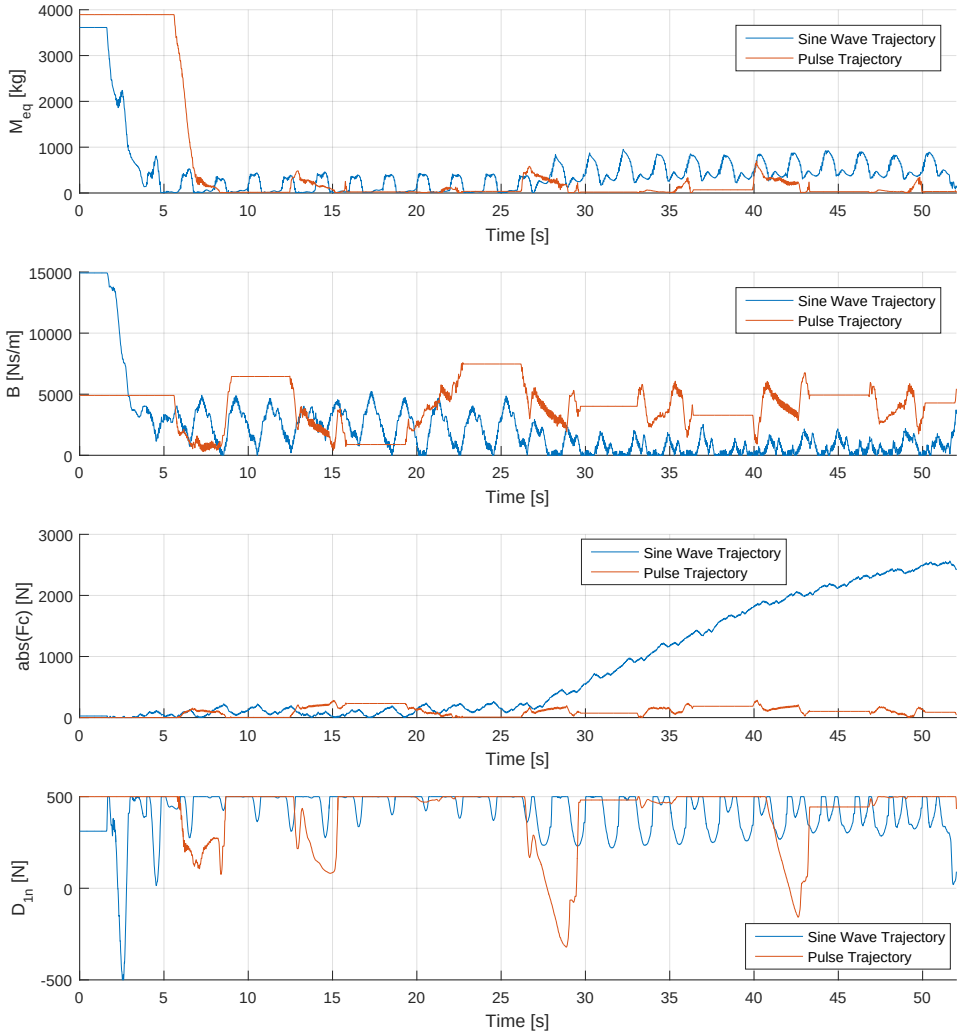

Figure 12.5: Filtered position trajectory following during mass parameter variation.

The performance of the force controller during mass step emulation for a sine curve trajectory can be seen in fig. 12.6. It can easily be observed that the force controller is not following the trajectory in a satisfactory manner. Error spikes consistently occur in one movement direction. After the step in mass the controller follows the reference to some extent between the error spikes. Since the force controller is not providing the correct force at the correct time the estimation algorithm is unable to link it to any of the variables and the error is estimated as a change in the Coulomb friction for a sine curve trajectory. For the pulse trajectory following changes can be observed in the D_{1n} parameter and a slight increase in viscous friction. Based on these results the force controller is not able to emulate a change in mass. No conclusions can be made about the performance of the estimation algorithm as far as this test goes.

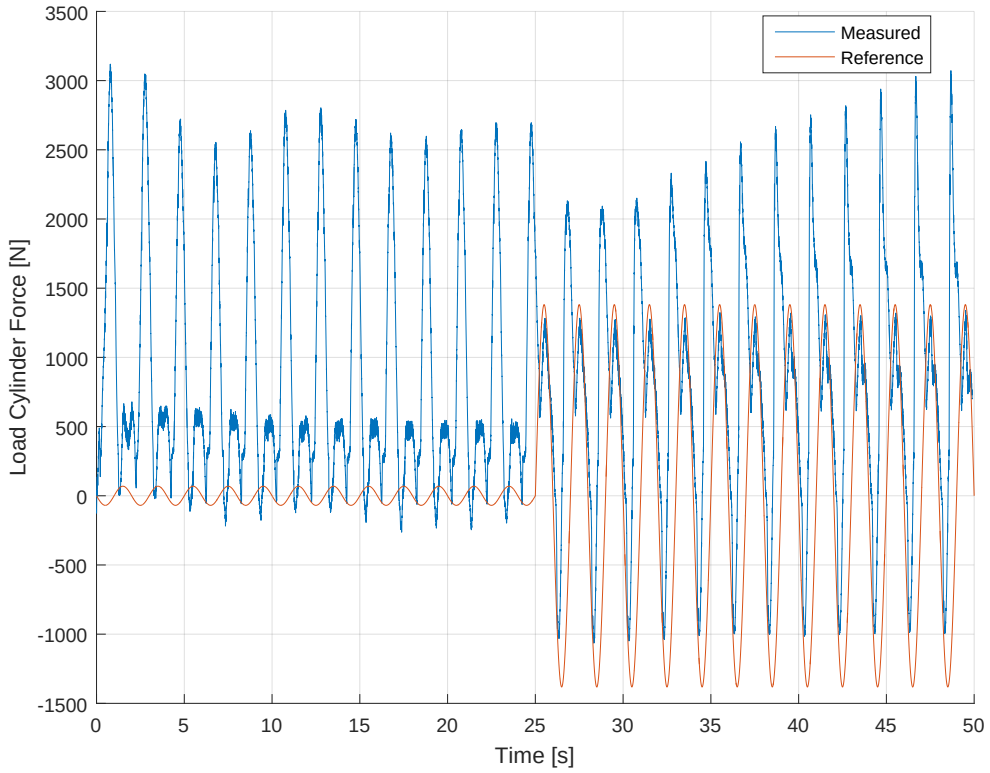

Figure 12.6: Trajectory following performance of the force controller during mass step emulation.

The performance of the IARC concerning fault tolerance cannot be examined thoroughly since an actual mass change is not emulated consistently, but the estimation algorithm does attempt to incorporate the disturbances the force controller delivers, which means that the force can potentially be accounted for in the feedforward of parameters to the IARC. To see if this is the case the reference following of the filtered position signal is examined for both trajectories. In fig. 12.7 the results from a run with the sine curve trajectory can be seen. Two of the graphs show the performance of the IARC with a higher resolution. One shows a time period just after the fault has occurred and one after it has occurred and the estimation algorithm has had some time to converge to some values that should describe the situation better. Changes in the performance can be noticed, but they are not necessarily better. No conclusion can be drawn from this test as far as the performance of the IARC and the estimation algorithm are concerned.

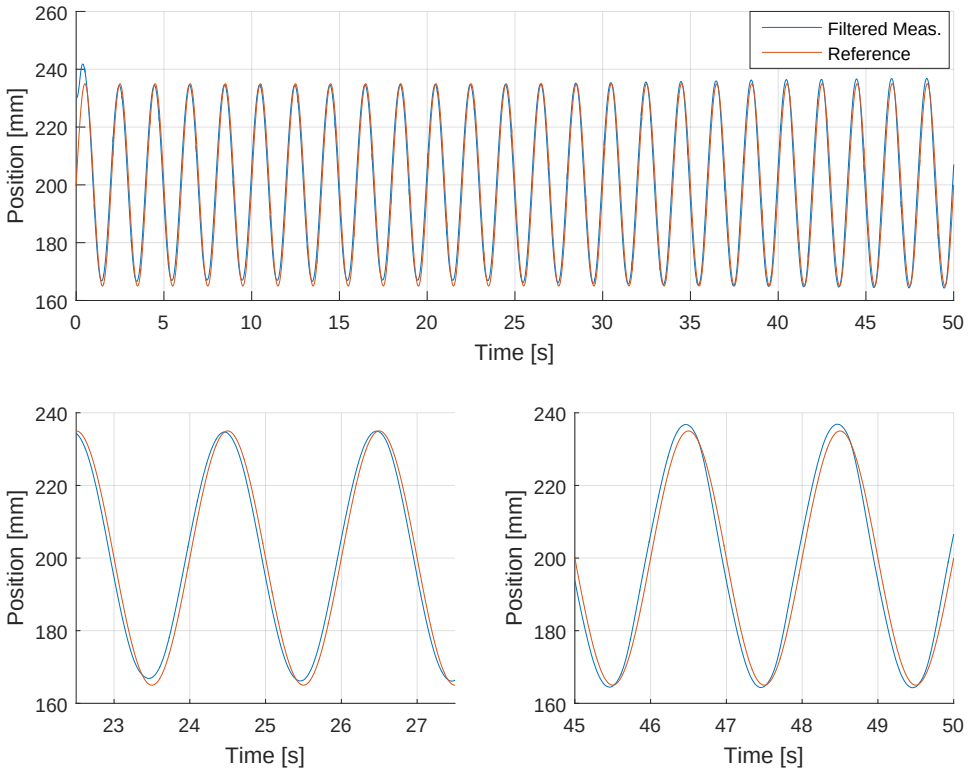

Figure 12.7: Filtered position trajectory following during mass parameter variation with a sine curve trajectory.

In fig. 12.8 the same can be seen for the pulse trajectory. No noticeable changes can be observed in the performance during the operation.

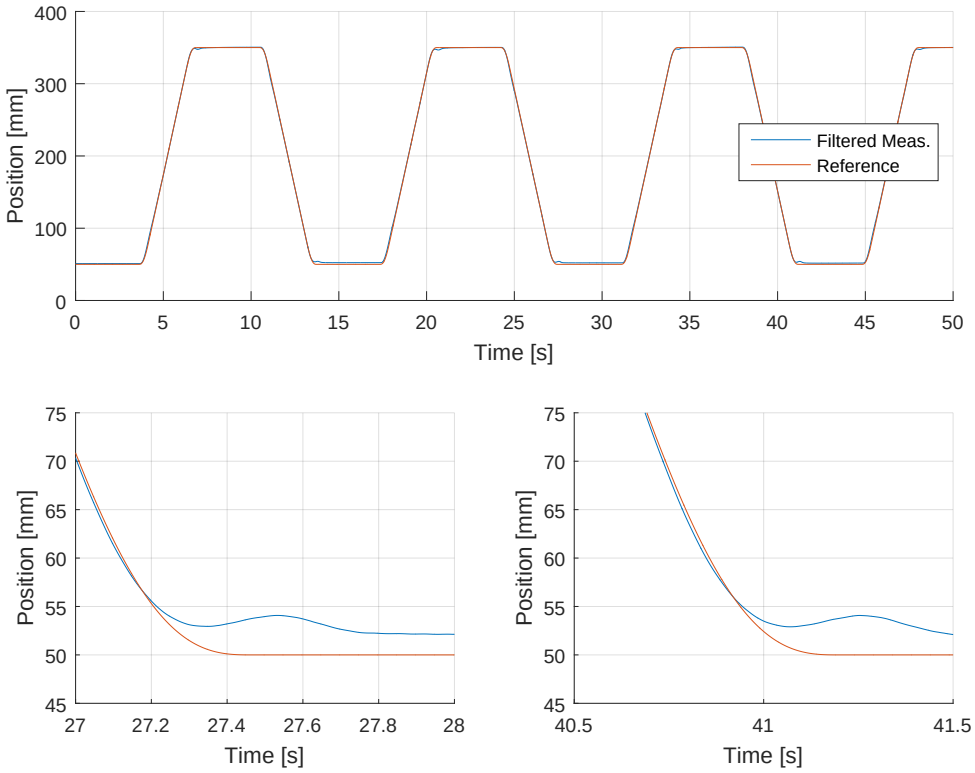

Figure 12.8: Filtered position trajectory following during mass parameter variation with a pulse trajectory.

12.4 Performance for a Viscous friction variation

The second parameter variation test shows the ability of the IARC to handle changes in viscous friction. The change in viscous friction is introduced through the force controller trajectory. An increase of 10000 Ns/m is desired during this run. Figure 12.9 shows that indeed the estimation algorithm sees the force delivered by the force controller as an increase in viscous friction.

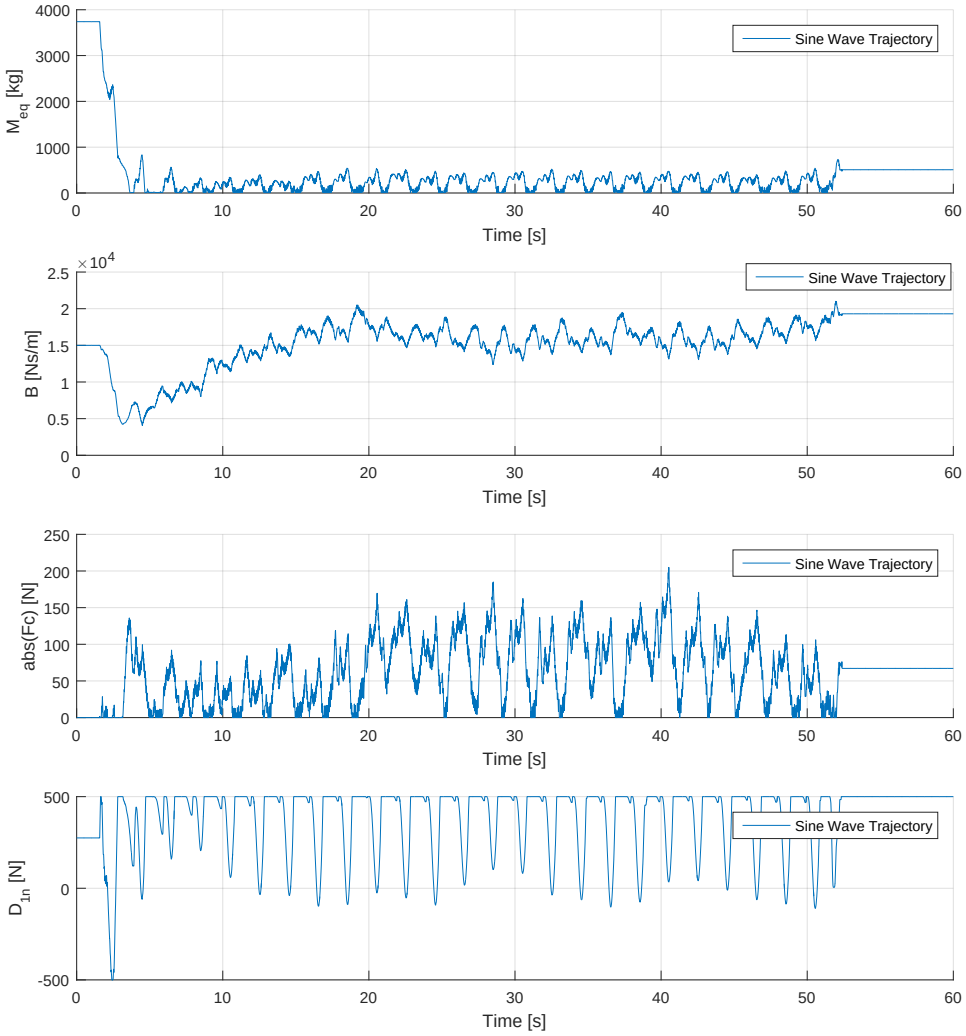

Figure 12.9: Estimation of parameters estimated from force equation during viscous friction parameter variation.

The performance of the IARC improves over time as can be seen in fig. 12.10. The change in error is not large but a positive trend can be observed. The overshoot when moving in the negative direction is reduced from 1.5 mm to 0.5 mm. Slight tremors were observed during this test. They cannot be seen in the result shown here due to the heavy filtering applied to the variables. Since the simulations result chapter and the theory behind the estimation algorithm conclude that the performance of the IARC will be poorer for a pulse trajectory, this test has been omitted due to safety concerns.

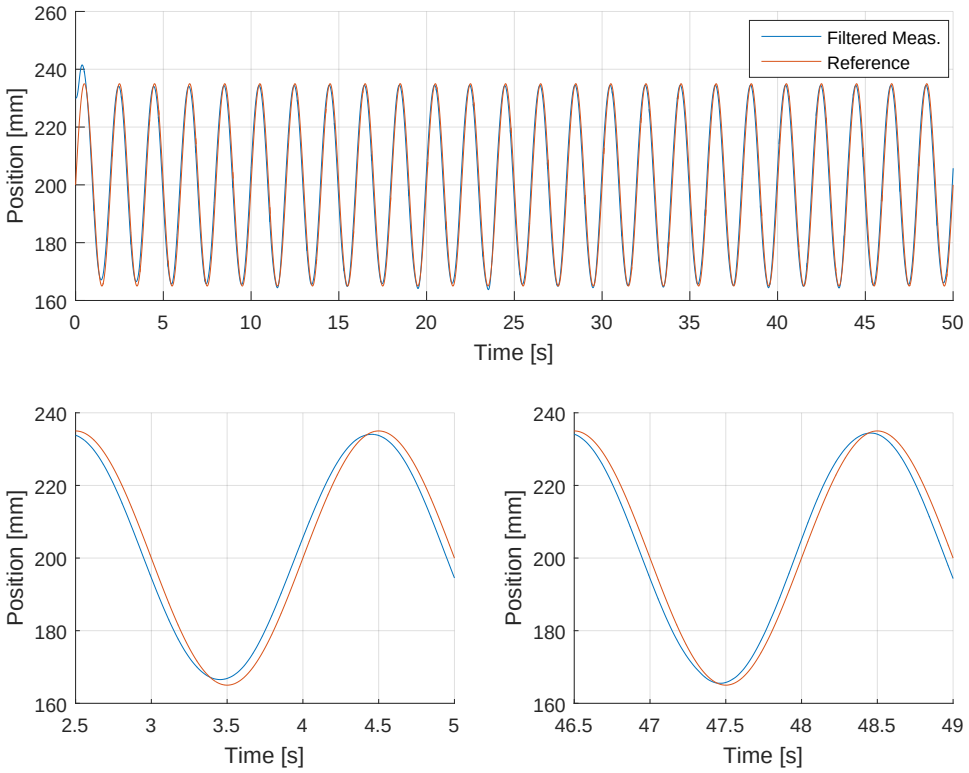

Figure 12.10: Filtered position trajectory following during viscous friction parameter variation.

12.5 Performance for a Coulomb friction variation

A test, investigating the ability of the IARC to handle changes to Coulomb friction, can be seen in fig. 12.11. The Coulomb friction variation has been introduced through the trajectory of the force controller. The controller is supposed to increase the Coulomb friction by 1000 N for the entire run. It can be observed that the estimation algorithm cannot distinguish between Coulomb and Viscous friction in this case. It can be seen in the mass variation test shown previously, that the algorithm estimates an increase in Coulomb friction when an increase in mass is desired. It is assumed that the excessive filtering of regressor parameters and the force controller problems resulted in a general inability of the test stand to emulate Coulomb friction.

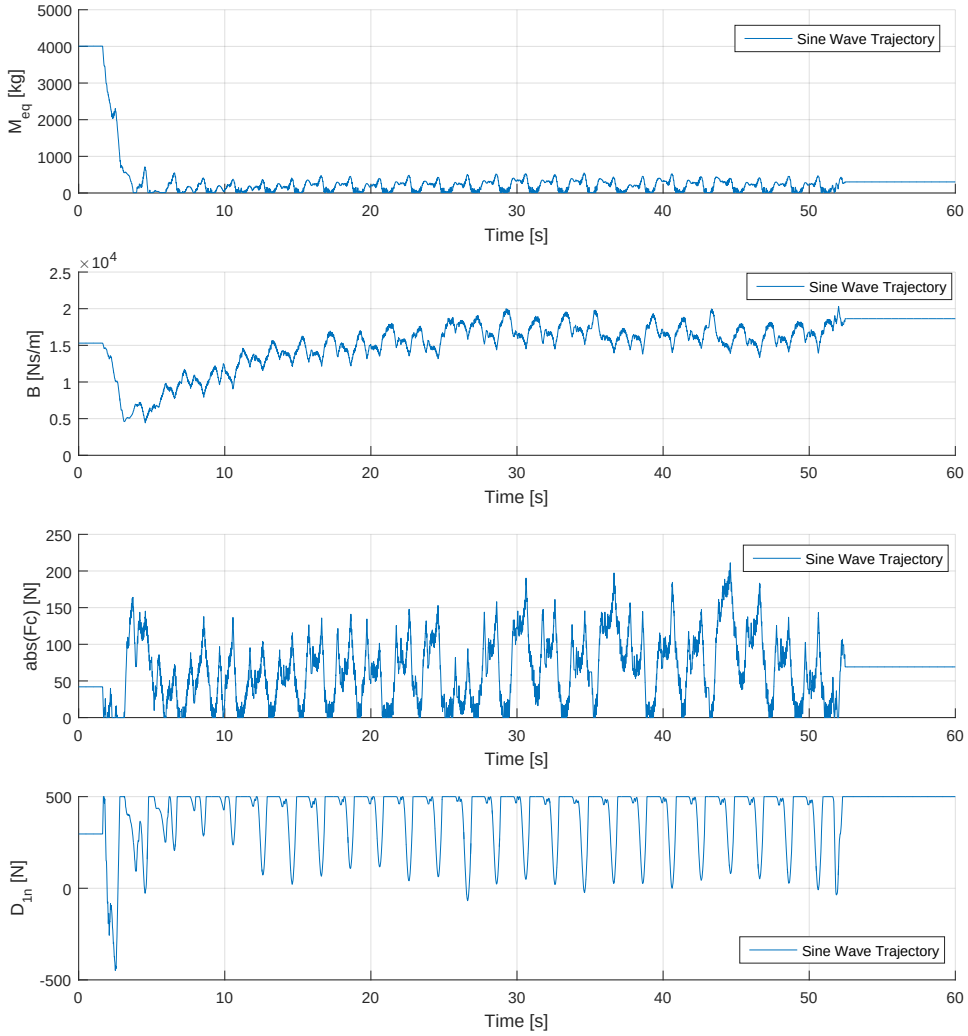

Figure 12.11: Estimation of parameters associated with the mechanical equation during Coulomb friction parameter variation.

12.6 Performance for a Leakage fault

Both internal and external leakages were tested. Results for internal leakage will be shown here, because they are more conclusive. The results for external leakage can be seen in App. G. The leakage fault was introduced into the system through a user operated needle valve. Since the leakage through the valve is both dependent on the opening of the valve and pressure difference across the cylinder chambers it is difficult to get a specific leakage flow fault. The opening of the needle valve was increased steadily while looking at the measurement graphs until an internal leakage of close to 6 L/min was achieved. The estimation of the leakage can be seen in fig. 12.12. The estimation follows the real leakage to some extent. The simulation results showed that leakage estimation cannot follow the leakage perfectly as the changes occur

too fast when the cylinder switches movement direction. Similar tendencies can be seen here.

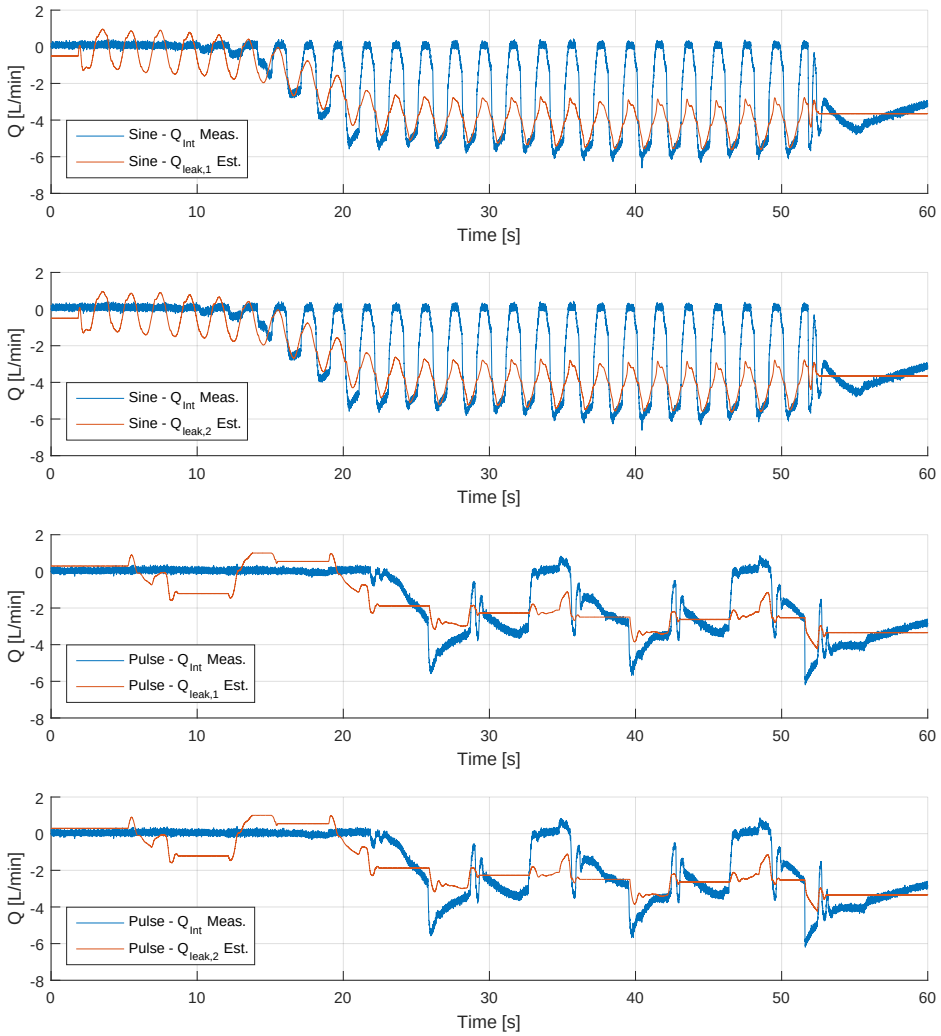

Figure 12.12: Estimation of leakage flows during sine and pulse trajectories.

The performance of the IARC can be observed in fig. 12.13. The two smaller time period graphs show that the IARC is reducing the under- and overshoot error after the estimation converges to the average of the leakage.

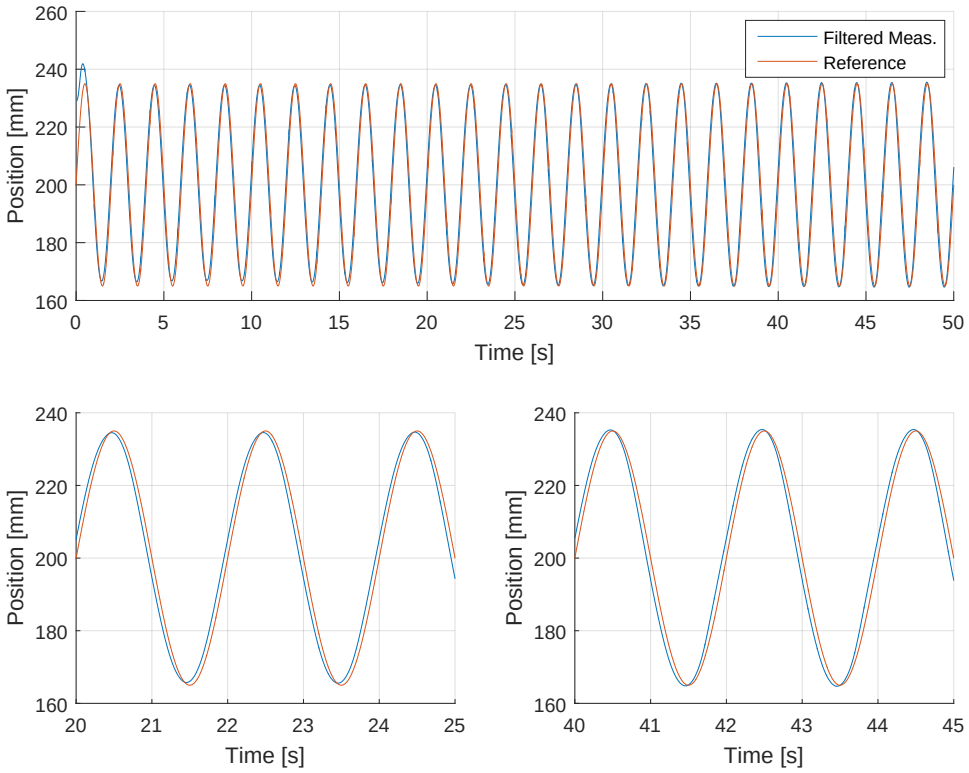

Figure 12.13: Trajectory tracking of filtered position signal.

It was found suspect that the internal leakage dropped to 0 L/min when the cylinder was moving in one direction. This should correspond to equal pressures in both cylinder chambers. The non-filtered cylinder pressure recorded during this test can be seen in fig. 12.14. It can be observed that a pressure difference is always measurable between the two chambers. The pressure in chamber 2 is always larger, due to the area difference between chambers. Because of this the internal leakage in the cylinder is always negative according to the sign convention established in this report. According to the pressure difference the leakage should have a ≈20 % difference in one direction, but instead the sensor shows a zero leakage flow. The uncertainty of the pressure sensor calibration is not large enough to account for total of 12 bar error in pressure measurement. Based on this the sensor measurement are considered suspect. The estimation agrees with the pressure measurements, but no baseline is available, since the other tests suffer from other issues. The filtered position shows an improvement after the estimation has converged to the assumed leakage level. For the pulse trajectory, similar results were observed in position tracking. The increase in error introduced when the leakage was increased was reduced over time by 1-1.5 mm. A graph of the result is shown in App. G.

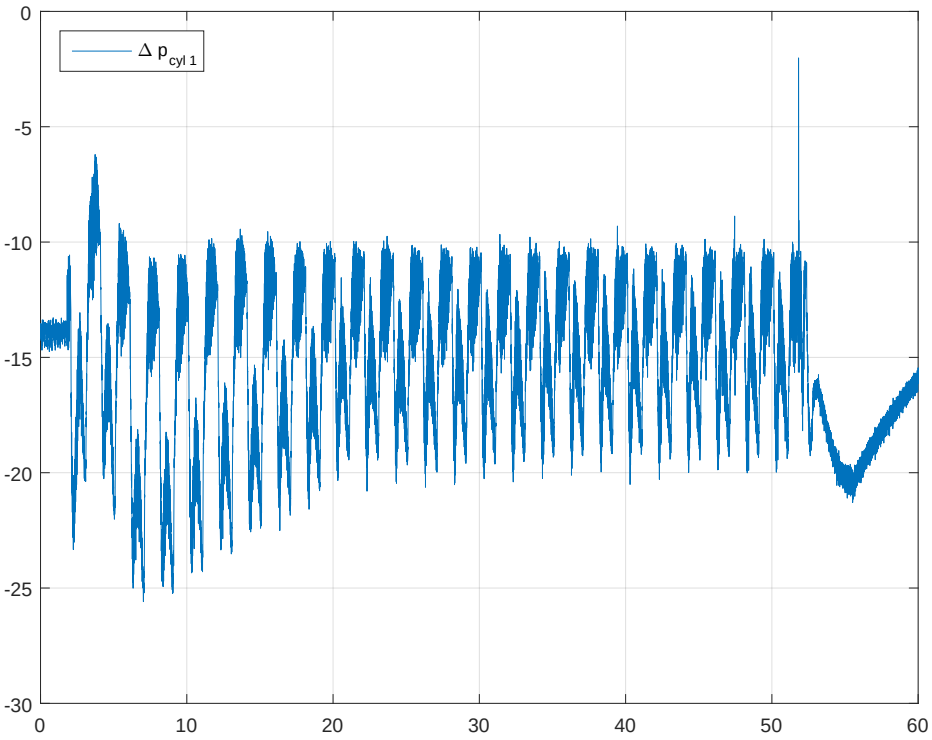

Figure 12.14: Pressure difference between chamber 1 and 2 for cylinder 1.

A test was also done where external leakage of 1 L/min was introduced. No significant impact was observed on the position measurements. The results have been omitted here, but can be found in App. G.

12.7 Test Results Discussion

It can easily be seen that the result in the test results are not identical to the ones obtained through simulation. A number of issues have been found during this testing procedure. Due to time limitations the issues have not been addressed on time to be included in the project. Further testing will be conducted after the project is handed in to further verify the promising simulation results. The issues discovered during this testing are:

- Lack of velocity measurements has lead to excessive filtering which has caused the IARC to perform in a degraded manner. The actual position does not follow the reference trajectory. Instead the filtered signal is attempting to.
- The force controller designed for this project has difficulties delivering forces in one direction. Since the force error is not filtered the output of the force controller is out of phase with the information the IARC and the estimation algorithm are receiving. Because of this variations in mass, viscous friction and Coulomb friction cannot be introduced as intended. The estimation algorithm cannot distinguish between errors in the different force related parameters. The IARC still forces the filtered position to follow the reference to some extent.

- The estimation algorithm can estimate the direction and to some extent the magnitude of the leakage, based on it being able to reduce the error to nominal-like conditions. The changes to performance in the IARC resulting from leakage are then the closest to what was expected to be obtained from these tests. It can be seen that when the magnitude of the leakage is estimated correctly the IARC is able to compensate for the fault. Based on this observation it can be concluded that the simulation results are not false. The method shows promise, but certain issues still need to be addressed. The experimental performance of the algorithm needs to be verified under the same faults as introduced in the simulated test. Nonetheless it is expected that the performance obtained in the simulations is possible.

Part V

Conclusion & Future Work

CHAPTER 13

CONCLUSION

Based on the literature review, the IARC method was chosen to be used as a fault tolerant controller for the considered hydraulic servo system. To determine which faults were of interest, a previous study regarding FMEA of wind-turbines was utilised. Based on the study, it was chosen to consider faults regarding internal- and external leakage, excessive friction, a varying mass, and an increase of the air-ratio in the oil.
A non-linear model of the system was constructed to be used for design and simulations of the control law and estimation algorithm. Furthermore, a linear model of the system was made to investigate frequencies of the system compared to the valve dynamics.
A force controller was designed based on the linear model of the system. The force controller is used to emulate an increased and time-varying mass together with excessive friction in the form of time-varying friction parameters. To emulate the internal- and external leakage flows, user controlled needle-valves on the experimental set-up were used.

Experimental tests were conducted to estimate the nominal friction parameters. The results showed that the parameters were sensitive to small variations in the measured pressures. This resulted in uncertain friction parameters. The friction parameters also depended heavily on the direction of movement. To make sure the IARC was able to handle these variations, the ranges on the friction parameters were set accordingly.
The non-linear model was verified by comparing with laboratory measurements. Similar dynamics were observed between the simulations and experimental results. But, if the measured pressures in each chamber were applied directly into the non-linear model, circumventing the continuity equation, differences were observed. The main issue being that when the model was set to move in the negative direction almost no movement was achieved using the measured pressures. The reason behind the difference was not determined, but a possible reason is a leakage across the valve, allowing the system to move without a force applied in one direction. Observations of the system drifting in one direction when all valves were closed were observed, indicating the valves have a small steady state opening.

Based on the non-linear model and the faults considered, the design and proof of stability of the IARC and estimation algorithm have been conducted. To determine the optimal parameters for the two algorithms, an optimisation algorithm was used. The IARC is proven to be stable for a predefined operation range. The initial ranges were chosen based on the non-linear model. If the ranges were increased, the performance of the system was found to

be increasingly dependent on the performance of the estimation algorithm. Furthermore, to achieve a stable response, user defined parameters had to be changed accordingly. From the information obtained in the verification tests, the initial parameter ranges were expanded and a new controller optimisation was conducted. The resulting range of faults that the control law can tolerate in the form of parameter variations are shown in tab. 13.1. Where D_{21n} and D_{22n} can be considered as the leakage flow in each chamber.

Range	M_{eq}[kg]	B [Ns/m]	F_c [N]	D_{1n} [N]	β^{-1} [bar^{-1}]	D_{21n} [L/min]	D_{22n} [L/min]
$\boldsymbol{\theta_{range,exp}}$	[10 9000]	[0 30000]	[0 3000]	[-500 500]	[10000 4000]$^{-1}$	[-9 1]	[-9 1]

Table 13.1: Parameter Ranges used for experimental testing.

Simulations were conducted in order to investigate the performance of the IARC and possibly point out implementation errors. Plausible noise levels and signal delays were used. These simulations showed that the IARC was noise sensitive. It was found that low-pass filters should be applied to the measurements. Due to velocity sensor issues, a low cut-off frequency was selected for the filters. This was required, in order to obtain a smooth position profile. The position was then differentiated by time to obtain a velocity estimate. The force controller was also found to be noise sensitive, mainly due to an aggressive design. The aggressive design resulted in a marginally unstable force output if filters below 400 rad/s were applied.

The simulation and experimental tests used two trajectories. The first being a pulse trajectory, which moves back and forth with a wait-time between each movement. This trajectory is chosen due to it exciting a wider range of frequencies than a sine curve. Furthermore, the pulse trajectory will have acceleration pulses for short periods of time, resulting in the estimation conditions only being met for short periods of time. The second trajectory used was a sine curve with a frequency of 0.5 Hz. Here the system is accelerated during the whole run, resulting in a continuous estimation of uncertain parameters.

The simulation tests indicated that the IARC was able to compensate for variations in mass, viscous friction, and air-ratio, in the sense that conditions close to nominal were obtained after the system variations had been estimated.
The estimation algorithm had problems estimating variations in the Coulomb friction magnitude. An analysis showed the emulated variation in Coulomb friction affected the estimated values of all the force related parameters. The result of these estimation problems was an inability to determine that the fault has affected Coulomb friction specifically. Even though the estimation algorithm did not estimate each parameter correctly the position error was rejected after some time.
Faults where a leakage flow was introduced as internal- and external leakage showed that the estimation was able to follow the average leakage flow. The estimation was not able to keep up with the relatively rapid changes in leakage due to its pressure dependence, but it managed to converged towards the mean of the signal. The result was that the IARC was not able to converge to nominal conditions. Nevertheless a reduction of the magnitude of the initial error was observed.

During the first laboratory implementation of the IARC, an increased filtering was found to be required. The consequence of the heavy filtering was a reduced performance, due to the large delays introduced in the signal values. It is expected that this problem will be addressed when

a velocity sensor is applied on the system. This will reduce the smoothness requirement of the position signal.
When attempting to emulate faults such as excessive friction and an increased mass, it was found that the force controller is not able to obtain the same performance as the one achieved in the simulations. Due to this, it was not possible to detect the increased mass and increased Coulomb friction. An increase in viscous friction was detected during both the viscous friction emulation and the Coulomb friction emulation.
Based on the experimental tests regarding force related parameters, no conclusion can be made, due to no proper emulation of the introduced faults was observed. The IARC was however able to reduce the increase in error observed when the inaccurately emulated faults were introduced.
For the experimental tests regarding an increased leakage flow, the magnitude of the introduced internal leakage flow was -6 L/min during one movement direction, and close to zero when the cylinder was returning. An investigation of the pressure difference between the two chambers revealed that this should not be the case. The reason being a minimum of 10 bar difference throughout the run, indicating uncertainties of the internal leakage measurement. The estimation algorithm converged towards the maximum magnitude. The result was however, that the IARC maintained a good performance, and reduced the influence from the introduced leakage flow to a minimal. Based on this information it is assumed that the IARC is fault tolerant to leakage related faults.
Air-ratio was not tested experimentally due to it not being possible to emulate an increase on the experimental set-up. The simulation tests regarding air-ratio showed no significant influence at the tested levels.

Based on the simulation , the IARC was found to fault tolerant to the emulated faults regarding increased mass, excessive friction, leakage, and increased air-ratio in the oil. The most difficult fault being for coulomb friction, due to difficulties estimating its value. When tested experimentally, a number of issues prevented solid conclusion on the fault tolerance of the IARC. However, some indications can be seen, due to the estimation algorithm showing converging behaviour during the nominal test and the leakage test. A lot of the issues are known, and are expected to be possible to fix by the time of the presentation of results.

13.1 Future Work

Based on the experimental result, it is desired to test the designed control law with a velocity sensor. This will determine if the hypothesis of it reducing the required filtrations is true. This will potentially increase the performance. Furthermore, it is desired to determine the problem regarding the force controller, and possibly design a new controller to emulate force related faults better experimentally.
Furthermore, it is desired to investigate if a better optimum of the estimation algorithm parameters can be achieved, due to the relatively few generations currently used.
Further studies regarding the real system parameters may improve the verification and validation of the non-linear model. This may allow for an improved optimum of both the control law and estimation parameters to be obtained. Furthermore, the ranges may be determined with more confidence if the real nominal values are known.
Based on the simulation and experimental tests, it was found that the estimation algorithm

had troubles following the leakage during changes in direction, resulting in only a mean of the leakage flow being estimated. It is desired to redesign the estimation algorithm to include a pressure dependant leakage flow parameter. By doing so, the leakage relevant estimated parameter should not change when the leakage area has settled.

BIBLIOGRAPHY

Ahmed-Zaid, Ioannou, Gousman, and Rooney, **1991**. Farid Ahmed-Zaid, Petros Ioannou, Ken Gousman, and Robert Rooney. *Accommodation of failures in the F-16 aircraft using adaptive control.* Control Systems, IEEE, 11(1), 73–78, 1991.

Amirat, Benbouzid, Al-Ahmar, Bensaker, and Turri, **2009**. Yassine Amirat, Mohamed El Hachemi Benbouzid, Elie Al-Ahmar, Bachir Bensaker, and Sylvie Turri. *A brief status on condition monitoring and fault diagnosis in wind energy conversion systems.* Renewable and Sustainable Energy Reviews, 13(9), 2629–2636, 2009.

Balle, Fischer, Füssel, Nelles, and Isermann, **1998**. Peter Balle, Martin Fischer, Dominik Füssel, Oliver Nelles, and Rolf Isermann. *Integrated control, diagnosis and reconfiguration of a heat exchanger.* Control Systems, IEEE, 18(3), 52–63, 1998.

Bodson and Groszkiewicz, **1997**. Marc Bodson and Joseph E Groszkiewicz. *Multivariable adaptive algorithms for reconfigurable flight control.* Control Systems Technology, IEEE Transactions on, 5(2), 217–229, 1997.

Bošković, **2014**. Jovan D Bošković. *A new decentralized retrofit adaptive fault-tolerant flight control design.* International Journal of Adaptive Control and Signal Processing, 28(9), 778–797, 2014.

Fanping Bu and Bin Yao, 2001. Fanping Bu and Bin Yao. Integrated direct/indirect adaptive robust motion control of single-rod hydraulic actuators with time-varying unknown inertia. In *Advanced Intelligent Mechatronics, 2001. Proceedings. 2001 IEEE/ASME International Conference on*, volume 1, pages 624–629. IEEE, 2001.

Fanping Bu and Bin Yuo, 2001. Fanping Bu and Bin Yuo. Desired compensation adaptive robust control of single-rod electro-hydraulic actuator. In *American Control Conference, 2001. Proceedings of the 2001*, volume 5, pages 3926–3931. IEEE, 2001.

Chen, Jiang, and Cui, **2016**. Mou Chen, Bing Jiang, and Rongxin Cui. *Actuator fault-tolerant control of ocean surface vessels with input saturation.* International Journal of Robust and Nonlinear Control, 26(3), 542–564, 2016.

Danfoss. Data Sheet Danfoss. *Pressure transmitters for industrial applications Type MBS 32 and MBS 33.*

Diao and Passino, **2001**. Yixin Diao and Kevin M Passino. *Stable fault-tolerant adaptive fuzzy/neural control for a turbine engine.* Control Systems Technology, IEEE Transactions on, 9(3), 494–509, 2001.

Diao and Passino, **2002**. Yixin Diao and Kevin M Passino. *Intelligent fault-tolerant control using adaptive and learning methods*. Control Engineering Practice, 10(8), 801–817, 2002.

Dorling and Zinober, **1988**. CM Dorling and ASI Zinober. *Robust hyperplane design in multivariable variable structure control systems*. International Journal of Control, 48(5), 2043–2054, 1988.

Farrell, Berger, and Appleby, **1993**. Jay Farrell, Torsten Berger, and Brent Appleby. *Using learning techniques to accommodate unanticipated faults*. Control Systems, IEEE, 13(3), 40–49, 1993.

Subhabrata Ganguli, Andres Marcos, and Gary Balas, *2002*. Subhabrata Ganguli, Andres Marcos, and Gary Balas. Reconfigurable LPV control design for Boeing 747-100/200 longitudinal axis. In *American Control Conference, 2002. Proceedings of the 2002*, volume 5, pages 3612–3617. IEEE, 2002.

Gao, Wang, and Wang, **2015**. Gang Gao, Jinzhi Wang, and Xianghua Wang. *Adaptive fault-tolerant control for feedback linearizable systems with an aircraft application*. International Journal of Robust and Nonlinear Control, 25(9), 1301–1326, 2015.

Henriksen, **2009**. Daniel Henriksen. *Design and Construction of a Facility for Testing Friction in Hydraulic Cylinders*, Aalborg university, 2009.

Hess and Wells, **2003**. RA Hess and SR Wells. *Sliding mode control applied to reconfigurable flight control design*. Journal of Guidance, Control, and Dynamics, 26(3), 452–462, 2003.

Huang, Shi, and Zhang, **2014**. Ji Huang, Yang Shi, and Xue Zhang. *Active fault tolerant control systems by the semi-Markov model approach*. International Journal of Adaptive Control and Signal Processing, 28(9), 833–847, 2014.

HydratechIndustries, **2016**. HydratechIndustries. *Wind Power Pitch System*, 2016. URL `http://www.hydratech-industries.com/En-US/Products/Wind%20Power/Pitch%20System/SiteAssets/Pitch%20systems_140809.gif`. [Online; accessed May 23, 2016].

Inc., **2009**. MOOG Inc. *Direct drive servovalves D633/D634*, 2009.

Jesper Linger, Mohsen Soltani, **2016**. Henric C. Pedersen James Carroll Nariman Sepehri Jesper Linger, Mohsen Soltani. *Reliability based design of fluid power pitch systems for wind turbines*. 2016.

Jin, **2015**. Xu Jin. *Adaptive fault-tolerant control for a class of output-constrained nonlinear systems*. International Journal of Robust and Nonlinear Control, 25(18), 3732–3745, 2015.

Jin, **2016**. Xu Jin. *Adaptive fault tolerant control for a class of input and state constrained MIMO nonlinear systems*. International Journal of Robust and Nonlinear Control, 26(2), 286–302, 2016.

Karpenko and Sepehri, **2003**. M Karpenko and N Sepehri. *Robust position control of an electrohydraulic actuator with a faulty actuator piston seal*. Journal of dynamic systems, measurement, and control, 125(3), 413–423, 2003.

Karpenko and Sepehri, **2005**. Mark Karpenko and Nariman Sepehri. *Fault-tolerant control of a servohydraulic positioning system with crossport leakage*. Control Systems Technology, IEEE Transactions on, 13(1), 155–161, 2005.

Karpenko and Sepehri, **2010**. Mark Karpenko and Nariman Sepehri. *On quantitative feedback design for robust position control of hydraulic actuators*. Control Engineering Practice, 18(3), 289–299, 2010.

Keating, Pachter, and Houpis, **1997**. MS Keating, M Pachter, and CH Houpis. *Fault tolerant control system: QFT design*. International Journal of Robust and Nonlinear Control, 7(6), 551–559, 1997.

Kim, Rizzoni, and Utkin, **2001**. Yong-Wha Kim, Giorgio Rizzoni, and Vadim I Utkin. *Developing a fault tolerant power-train control system by integrating design of control and diagnostics*. International Journal of Robust and Nonlinear Control, 11(11), 1095–1114, 2001.

WE Leithead, DJ Leith, F Hardan, and H Markou, 1999. WE Leithead, DJ Leith, F Hardan, and H Markou. Direct regulation of large speed excursions for variable speed wind turbines. In *Proceedings of European Wind Energy Conference*, 1999.

Liu, Shi, Zhang, and Zhao, **2011**. Ming Liu, Peng Shi, Lixian Zhang, and Xudong Zhao. *Fault-tolerant control for nonlinear Markovian jump systems via proportional and derivative sliding mode observer technique*. Circuits and Systems I: Regular Papers, IEEE Transactions on, 58(11), 2755–2764, 2011.

Maybeck, **1999**. Peter S Maybeck. *Multiple model adaptive algorithms for detecting and compensating sensor and actuator/surface failures in aircraft flight control systems*. International Journal of Robust and Nonlinear Control, 9(14), 1051–1070, 1999.

Peter S Maybeck and Donald L Pogoda, 1989. Peter S Maybeck and Donald L Pogoda. Multiple model adaptive controller for the stol f-15 with sensor/actuator failures. In *Decision and Control, 1989., Proceedings of the 28th IEEE Conference on*, pages 1566–1572. IEEE, 1989.

Maybeck and Stevens, **1991**. Peter S Maybeck and Richard D Stevens. *Reconfigurable flight control via multiple model adaptive control methods*. Aerospace and Electronic Systems, IEEE Transactions on, 27(3), 470–480, 1991.

Mogens Blanke, Michel Kinnaert and Staroswiecki, **2016**. Jan Lunze Mogens Blanke, Michel Kinnaert and Marcel Staroswiecki. *Diagnosis and Fault-Tolerant Control*. 3^{st} edition, 2016.

Amit Mohanty and Bin Yao, 2006. Amit Mohanty and Bin Yao. Integrated direct/indirect adaptive robust control (diarc) of hydraulic robotics arm with accurate parameter estimates. In *ASME 2006 International Mechanical Engineering Congress and Exposition*, pages 39–45. American Society of Mechanical Engineers, 2006.

Mohanty and Yao, **2011**. Amit Mohanty and Bin Yao. *Indirect adaptive robust control of hydraulic manipulators with accurate parameter estimates*. Control Systems Technology, IEEE Transactions on, 19(3), 567–575, 2011.

Moradi and Fekih, **2014**. Mehdi Moradi and Afef Fekih. *Adaptive PID-sliding-mode fault-tolerant control approach for vehicle suspension systems subject to actuator faults*. Vehicular Technology, IEEE Transactions on, 63(3), 1041–1054, 2014.

Musgrave, Guo, Wong, and Duyar, **1996**. Jeffrey L Musgrave, Ten-Huei Guo, Edmond Wong, and Ahmet Duyar. *Real-time accommodation of actuator faults on a reusable rocket engine*. Control Systems Technology, IEEE Transactions on, 5(1), 100–109, 1996.

Niksefat and Sepehri, **2002**. Navid Niksefat and Nariman Sepehri. *A QFT fault-tolerant control for electrohydraulic positioning systems*. Control Systems Technology, IEEE Transactions on, 10(4), 626–632, 2002.

Peter F Odgaard and Kathryn E Johnson, 2013. Peter F Odgaard and Kathryn E Johnson. Wind turbine fault detection and fault tolerant control-an enhanced benchmark challenge. In *American Control Conference (ACC), 2013*, pages 4447–4452. IEEE, 2013.

Parker. Data Sheet Parker. *SensoControl Diagnostic Test Equipment for Hydraulics*.

Patton, Putra, and Klinkhieo, **2010**. Ron J Patton, Devi Putra, and Supat Klinkhieo. *Friction compensation as a fault-tolerant control problem*. International Journal of Systems Science, 41(8), 987–1001, 2010.

Plummer and Vaughan, **1996**. Andrew R Plummer and ND Vaughan. *Robust adaptive control for hydraulic servosystems*. Journal of Dynamic Systems, Measurement, and Control, 118(2), 237–244, 1996.

Polycarpou, **2001**. Marios M Polycarpou. *Fault accommodation of a class of multivariable nonlinear dynamical systems using a learning approach*. Automatic Control, IEEE Transactions on, 46(5), 736–742, 2001.

Polycarpou and Helmi, **1995**. Marios M Polycarpou and Arthur J Helmi. *Automated fault detection and accommodation: a learning systems approach*. Systems, Man and Cybernetics, IEEE Transactions on, 25(11), 1447–1458, 1995.

Prolasa. Data Sheet Prolasa. *Hydraulic Flow Control & Needle Valves*.

Putra and Nijmeijer, **2004**. Devi Putra and Henk Nijmeijer. *Limit cycling in an observer-based controlled system with friction: Numerical analysis and experimental validation*. International Journal of Bifurcation and Chaos, 14(09), 3083–3093, 2004.

Regal Components AB. Data Sheet Regal Components AB. *PS6300 Potentiometer cylinder sensor 50-1000mm*.

Reveliotis and Kokar, **1995**. Spiridon A Reveliotis and Mieczyslaw M Kokar. *A framework for on-line learning of plant models and control policies for restructurable control*. Systems, Man and Cybernetics, IEEE Transactions on, 25(11), 1502–1512, 1995.

Sami and Patton, **2013**. Montadher Sami and Ron J Patton. *Active fault tolerant control for nonlinear systems with simultaneous actuator and sensor faults*. International Journal of Control, Automation and Systems, 11(6), 1149–1161, 2013.

Jong-Yeob Shin, N Eva Wu, and Christine Belcastro, 2002. Jong-Yeob Shin, N Eva Wu, and Christine Belcastro. Linear parameter varying control synthesis for actuator failure, based on estimated parameter. In *AIAA Guidance, Navigation and Control*, 2002.

Shtessel, Buffington, and Banda, **2002**. Yuri Shtessel, James Buffington, and Siva Banda. *Tailless aircraft flight control using multiple time scale reconfigurable sliding modes.* Control Systems Technology, IEEE Transactions on, 10(2), 288–296, 2002.

Sloth, Esbensen, and Stoustrup, **2011**. Christoffer Sloth, Thomas Esbensen, and Jakob Stoustrup. *Robust and fault-tolerant linear parameter-varying control of wind turbines.* Mechatronics, 21(4), 645–659, 2011.

Slotine, Li, et al., **1991**. Jean-Jacques E Slotine, Weiping Li, et al. *Applied nonlinear control*, volume 199. Prentice-Hall Englewood Cliffs, NJ, 1991.

Tao, Joshi, and Ma, **2001**. Gang Tao, Suresh M Joshi, and Xiaoli Ma. *Adaptive state feedback and tracking control of systems with actuator failures.* Automatic Control, IEEE Transactions on, 46(1), 78–95, 2001.

Tao, Chen, and Joshi, **2002**. Gang Tao, Shuhao Chen, and Suresh M Joshi. *An adaptive actuator failure compensation controller using output feedback.* Automatic Control, IEEE Transactions on, 47(3), 506–511, 2002.

Temposonics. Data Sheet Temposonics. *Temposonics®, R-Series Models RP and RH.*

T.O.Andersen, **2007**. M.R.Hansen T.O.Andersen. *Fluid Power Circuits - System Design and Analysis,* Aalborg university, 2007.

Tong, Huo, and Li, **2014**. Shaocheng Tong, Baoyu Huo, and Yongming Li. *Observer-based adaptive decentralized fuzzy fault-tolerant control of nonlinear large-scale systems with actuator failures.* Fuzzy Systems, IEEE Transactions on, 22(1), 1–15, 2014.

Veillette, Medanic, and Perkins, **1992**. Robert J Veillette, JB Medanic, and William R Perkins. *Design of reliable control systems.* Automatic Control, IEEE Transactions on, 37(3), 290–304, 1992.

Vidal, Tutivén, Rodellar, and Acho, **2015**. Yolanda Vidal, Christian Tutivén, José Rodellar, and Leonardo Acho. *Fault diagnosis and fault-tolerant control of wind turbines via a discrete time controller with a disturbance compensator.* Energies, 8(5), 4300–4316, 2015.

Wise, Brinker, Calise, Enns, Elgersma, and Voulgaris, **1999**. Kevin A Wise, Joseph S Brinker, Anthony J Calise, Dale F Enns, Michael R Elgersma, and Petros Voulgaris. *Direct adaptive reconfigurable flight control for a tailless advanced fighter aircraft.* International Journal of Robust and Nonlinear Control, 9(14), 999–1012, 1999.

Wu and Yang, **2015**. Li-Bing Wu and Guang-Hong Yang. *Robust adaptive fault-tolerant tracking control of multiple time-delays systems with mismatched parameter uncertainties and actuator failures.* International Journal of Robust and Nonlinear Control, 25(16), 2922–2938, 2015.

Shu-Fan Wu, Michael J Grimble, and Wei Wei, 1999. Shu-Fan Wu, Michael J Grimble, and Wei Wei. QFT based robust/fault tolerant flight control design for a remote pilotless vehicle. In *Control Applications, 1999. Proceedings of the 1999 IEEE International Conference on*, volume 1, pages 57–62. IEEE, 1999.

Guang-Hong Yang and Dan Ye, 2006. Guang-Hong Yang and Dan Ye. Adaptive Fault-tolerant H/spl sub/spl infin//Control via State Feedback for Linear Systems against Actuator Faults. In *Decision and Control, 2006 45th IEEE Conference on*, pages 3530–3535. IEEE, 2006.

Bin Yao and A Palmer, 2002. Bin Yao and A Palmer. Indirect adaptive robust control of SISO nonlinear systems in semi-strict feedback forms. In *IFAC World Congress, T-Tu-A03*, volume 2, pages 1–6, 2002.

Yao and Tomizuka, 1997. Bin Yao and Masayoshi Tomizuka. *Adaptive robust control of SISO nonlinear systems in a semi-strict feedback form.* Automatica, 33(5), 893–900, 1997.

Yao, Bu, Reedy, and Chiu, 2000. Bin Yao, Fanping Bu, John Reedy, and George TC Chiu. *Adaptive robust motion control of single-rod hydraulic actuators: theory and experiments.* Mechatronics, IEEE/ASME Transactions on, 5(1), 79–91, 2000.

Yao, Bu, and Chiu, 2001. Bin Yao, Fanping Bu, and George TC Chiu. *Non-linear adaptive robust control of electro-hydraulic systems driven by double-rod actuators.* International Journal of Control, 74(8), 761–775, 2001.

Yao, Yang, and Ma, 2014. Jianyong Yao, Guichao Yang, and Dawei Ma. *Internal leakage fault detection and tolerant control of single-rod hydraulic actuators.* Mathematical Problems in Engineering, 2014, 2014.

Yin, Luo, and Ding, 2014. Shen Yin, Hao Luo, and Steven X Ding. *Real-time implementation of fault-tolerant control systems with performance optimization.* Industrial Electronics, IEEE Transactions on, 61(5), 2402–2411, 2014.

Zhang, Parisini, and Polycarpou, 2004. Xiaodong Zhang, Thomas Parisini, and Marios M Polycarpou. *Adaptive fault-tolerant control of nonlinear uncertain systems: an information-based diagnostic approach.* Automatic Control, IEEE Transactions on, 49(8), 1259–1274, 2004.

Zhao, Jiang, Chowdhury, and Shi, 2014a. Jing Zhao, Bin Jiang, Fahmida N Chowdhury, and Peng Shi. *Active fault-tolerant control for near space vehicles based on reference model adaptive sliding mode scheme.* International Journal of Adaptive Control and Signal Processing, 28(9), 765–777, 2014.

Zhao, Jiang, Shi, and He, 2014b. Jing Zhao, Bin Jiang, Peng Shi, and Zhen He. *Fault tolerant control for damaged aircraft based on sliding mode control scheme.* Int. J. Innovative Comput. Inf. Control, 10(1), 293–302, 2014.

Hongcheng Zhou, Dezhi Xu, Daobo Wang, and Le Ge, 2014. Hongcheng Zhou, Dezhi Xu, Daobo Wang, and Le Ge. Adaptive Fault-Tolerant Tracking Control of Nonaffine Nonlinear Systems with Actuator Failure. In *Abstract and Applied Analysis*, volume 2014. Hindawi Publishing Corporation, 2014.

Zhou and Ren, **2001**. Kemin Zhou and Zhang Ren. *A new controller architecture for high performance, robust, and fault-tolerant control.* Automatic Control, IEEE Transactions on, 46(10), 1613–1618, 2001.

Part VI

Appendix

APPENDIX A

LINEAR MODEL

In this section, a linear model of the hydraulic cylinder is developed in order to determine the natural frequency of the system. The dynamics will be used to design a filter for the estimation algorithm. The structure of the linear model will be used to design a force controller, which will be used to emulate force related time varying parameters on the system.

Natural Frequency of the Hydraulic Cylinder

In the linearisation of the hydraulic system, the following assumptions have been made.

- Constant supply & tank pressure.
- Constant bulk modulus.
- Negligible deadband in the valves.

The first assumption can be defended, because accumulators will be in place on the laboratory set-up to filter out some of the supply pressure oscillations. The result will be small variations of supply pressure, which should not have a large effect on the system. The second assumption can be defended, because the majority of the operation of the system will be at a relatively high load pressure. This will lead to a small variation in bulk modulus. The third assumption can be defended, because the valve used in this project is constructed with high requirements on its dynamic response.

In order to linearise the pressure build up equations the flows Q_1 and Q_2 have to expended using Tailor's series. This converts eq. (5.16) and eq. (5.17) into

$$\delta Q_1 = \left.\frac{\partial Q_1}{\partial x_v}\right|_{\delta x_v} + \left.\frac{\partial Q_1}{\partial p_1}\right|_{\delta p_1}$$

$$= \underbrace{k_q\sqrt{p_{S,0}-p_{1,0}}}_{k_{qx1}}\delta x_v - \underbrace{\frac{k_q x_{v,0}}{2\sqrt{p_{s,0}-p_{1,0}}}}_{k_{qp1}}\delta p_1 \tag{A.1}$$

$$\delta Q_2 = \left.\frac{\partial Q_2}{\partial x_v}\right|_{\delta x_v} + \left.\frac{\partial Q_2}{\partial p_2}\right|_{\delta p_2}$$

$$\delta Q_2 = \underbrace{k_q\sqrt{p_{2,0}-p_{t,0}}}_{k_{qx2}}\delta x_v + \underbrace{\frac{k_q x_{v,0}}{2\sqrt{p_{2,0}-p_{t,0}}}}_{k_{qp2}}\delta p_2 \tag{A.2}$$

In order to linearise the system it should be forced to a standstill. This can be done by setting the gradients of the system i.e. $\ddot{x}_p$, $\dot{p}_1$, $\dot{p}_2$ to zero. This lead to the following set of equation to be solved simultaneously:

$$0 = \ddot{x}_p = \frac{A_{p,1}}{M_{eq}}p_{1,0} - \frac{A_{p,2}}{M_{eq}}p_{2,0} - \frac{B}{M_{eq}}\dot{x}_{p,0} \tag{A.3}$$

$$Q_1 = A_{p,1}\dot{x}_{p,0} = k_q x_{v,0}\sqrt{p_{s,0}-p_{1,0}} \tag{A.4}$$

$$Q_2 = -A_{p,2}\dot{x}_{p,0} = -k_q x_{v,0}\sqrt{p_{2,0}-p_{t,0}} \tag{A.5}$$

Here it is assumed that the external force is not present. The velocity chosen for linearisation is 30 mm/s. The reason being that the system will work around 30 mm/s for the majority of the tests. Furthermore the valve opening corresponding to this velocity is $\approx$ 10%. The data sheet of the valve gives the frequency for this opening seen in fig. A.1. A larger valve opening would have a lower bandwidth and would give a higher damping in linear model, which is not necessarily true for all cases. Furthermore the linearisation position has been chosen as -0.1 m. This corresponds to a high frequency of the test cylinder as can be seen in fig. A.1.

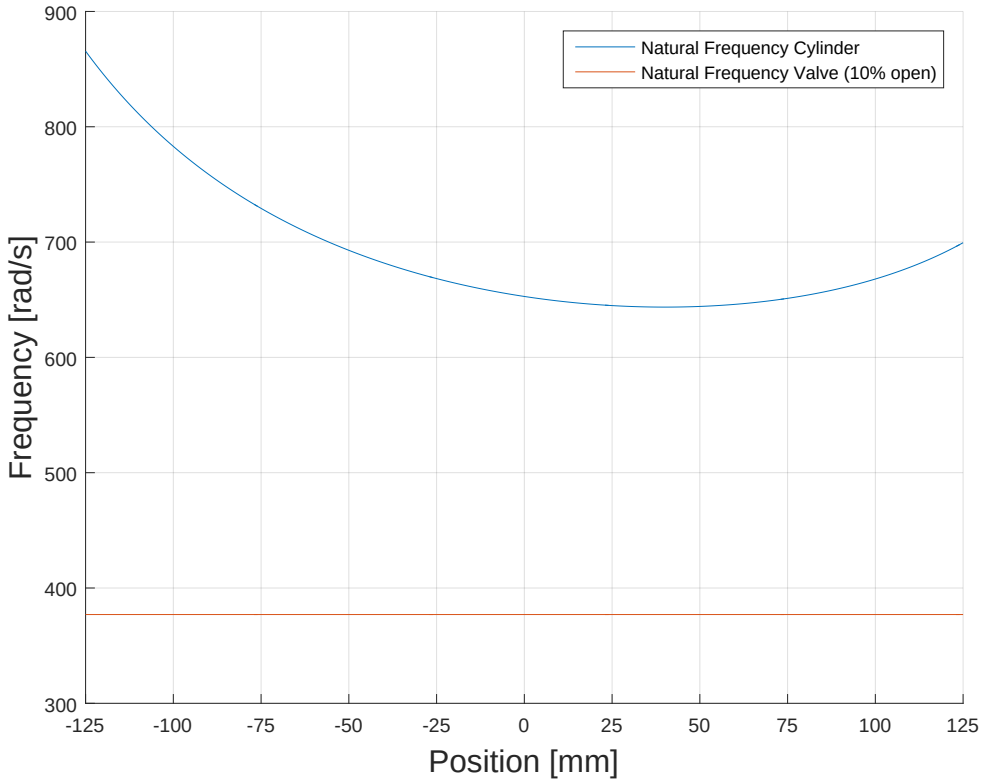

Figure A.1: Cylinder frequency as a function of position.

For the linear model, the following states will be used:

$$x = [p_1 \quad p_2 \quad \dot{x}_p \quad x_p \quad \dot{x}_v \quad x_v]^T \tag{A.6}$$

where x_p is the piston position and x_v is the valve opening.

The resulting linear constants are

$$\boldsymbol{x}_0 = \begin{bmatrix} p_{1,0} \\ p_{2,0} \\ \dot{x}_{p,0} \\ x_{p,0} \\ \dot{x}_{v,0} \\ x_{v,0} \end{bmatrix} = \begin{bmatrix} 54.2[bar] \\ 71.7[bar] \\ 30[mm/s] \\ 25[mm] \\ 0[-] \\ 0.1618[-] \end{bmatrix} \tag{A.7}$$

With these linear constants a state space model has been established as

$$\dot{\boldsymbol{x}} = \mathbf{A}\boldsymbol{x} + \mathbf{B}x_{v,ref} \tag{A.8}$$

$$\boldsymbol{y} = \mathbf{C}\boldsymbol{x} \tag{A.9}$$

The scalar denoted as $x_{v,ref}$ is the reference valve opening. The output $\boldsymbol{y}$ will be a 3×1 vector consisting of force from pressure force, velocity of piston, and position of piston. The matrices in eq. (A.8) and (A.9) are defined as

$$\mathbf{A} = \begin{bmatrix} \frac{k_{qp1}\beta_{eff}}{V_{1,0}} & 0 & \frac{-\beta_{eff}A_1}{V_{1,0}} & 0 & 0 & \frac{k_{qx1}\beta_{eff}}{V_{1,0}} \\ 0 & \frac{k_{qp2}\beta_{eff}}{V_{2,0}} & \frac{\beta_{eff}A_2}{V_{2,0}} & 0 & 0 & \frac{k_{qx2}\beta_{eff}}{V_{2,0}} \\ \frac{A_1}{M_{eq}} & \frac{-A_2}{M_{eq}} & \frac{B}{M_{eq}} & 0 & 0 & 0 \\ 0 & 0 & 1 & 0 & 0 & 0 \\ 0 & 0 & 0 & 0 & -2\zeta_v\omega_{nv} & -\omega_{nv}^2 \\ 0 & 0 & 0 & 0 & 1 & 0 \end{bmatrix} \tag{A.10}$$

$$\mathbf{B} = \begin{bmatrix} 0 \\ 0 \\ 0 \\ 0 \\ \omega_{nv}^2 \\ 0 \end{bmatrix} \tag{A.11}$$

$$\mathbf{C} = \begin{bmatrix} A_p & -A_r & 0 & 0 & 0 & 0 \\ 0 & 0 & 1 & 0 & 0 & 0 \\ 0 & 0 & 0 & 1 & 0 & 0 \end{bmatrix} \tag{A.12}$$

To verify the described linear model, a comparison of the system response of the linear and non-linear model is made. The test is done where the reference normalised valve opening to both models is the linearised valve opening of 0.1618. The initial state values can be seen in (A.7). The comparison between the linear and non-linear models can be seen in fig. A.2.

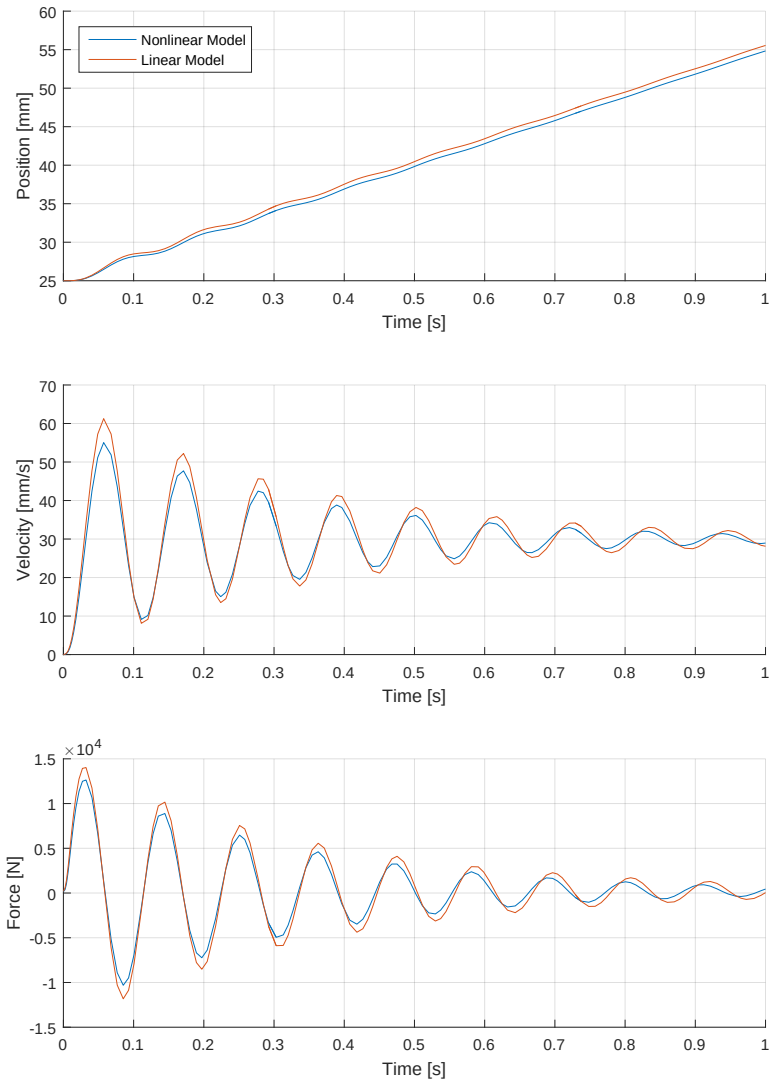

Figure A.2: Comparison of linear and non-linear model system response.

From fig. A.2, the system responses are very similar, and the linear model has almost identical dynamics as those from the non-linear model. Based on this, the linear model is found acceptable, and can be used for force controller design.

It can be seen in the bode diagram A.3, that the natural frequency of the system is 630 [rad/s]. This can be compared with the frequency response of the valve at 10% opening which is 376 [rad/s]. The fact that the fastest frequency response of the valve is slower than the eigenfrequency of the cylinder means that the bandwidth of the valve will be the limiting factor when designing controllers. The design of the force controller, which will simulate an increased

mass in the system can be seen in Appendix chapter B.

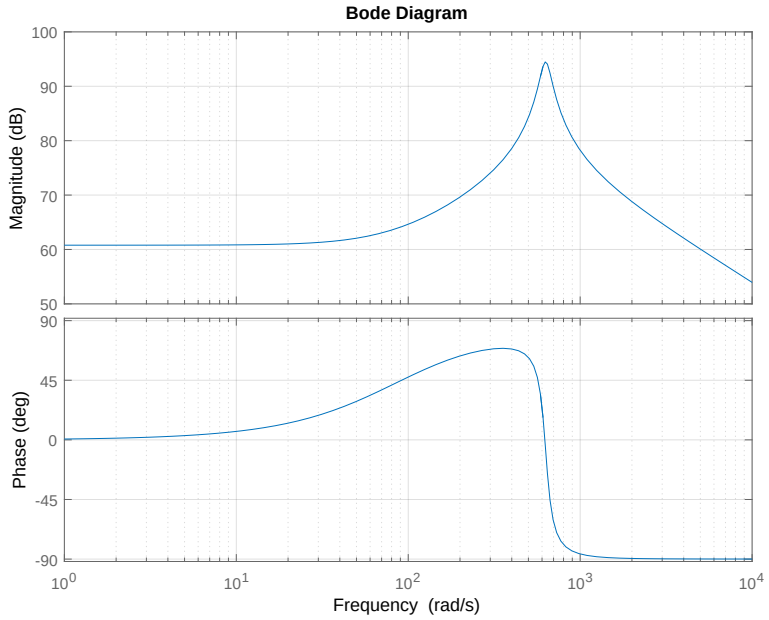

Figure A.3: Bode plot of the transfer function between valve opening and force.

APPENDIX B

FORCE CONTROLLER

In this appendix the design of the controller for the load cylinder will be discussed. The load cylinder will be used to provide a changing force trajectory for the test cylinder. The trajectory is designed to emulate changes in mass and/or friction forces. For this reason a force controller will be designed here. A linear controller has been chosen for the control of this side of the set-up. A simpler control structure can reduce the difficulty of deducing implementation problems in the entire set-up during practical tests.
The reference for the force controller is calculated based on fig. B.1 and eq. (B.2).

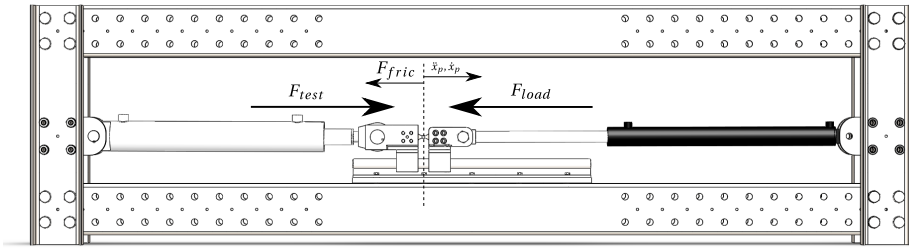

Figure B.1: Diagram of forces relevant to the design of the force controller.

$$\begin{aligned} F_{test} &= M_{ref}\ddot{x}_p + B_{ref}\dot{x}_p + F_{c,ref} \\ &= M\ddot{x}_p + F_{fric} + F_{load} \\ &= M\ddot{x}_p + B\dot{x}_p + F_c + M_{emu}\ddot{x}_p + B_{emu}\dot{x}_p + F_{c,emu} \end{aligned} \tag{B.1}$$

$$F_{load} = M_{emu}\ddot{x}_p + B_{emu}\dot{x}_p + F_{c,emu} \tag{B.2}$$

where the subscript $_{emu}$ is for emulated variations to the nominal system parameters.

In order to design a linear controller for the load cylinder a linear model is required. A state space model similar to the one designed in App. A, with the appropriate changes in dimensions and parameters, is used. The system parameters used for the linear model of the load cylinder will be the emulated sizes, shown in eq. (B.2). The cylinders will be working in opposite directions and the controllers are being tuned to be able to follow a reference with little error. The reference frequency will depend on the acceleration, velocity, and parameter variation

trajectory.
An increase in mass to 6000-9000 kg has been selected as an appropriate load for the system, together with a viscous friction of up to 30000 Ns/m. By having system parameters of this size, a larger percentage of the possible pressure force from the test cylinder will be used. This will reduce the effect of noise in the sensor signals. The magnitude of the noise has been found to be around 500 N. By having a larger force trajectory the effect of this 500 N is smaller. Example of the maximum force available for each cylinder is shown in eq. (B.3) and (B.4).

$$F_{test,max1} = p_s A_1 - p_t A_2 \approx 90000N \tag{B.3}$$
$$F_{test,max2} = p_s A_2 - p_t A_1 \approx 68000N$$
$$F_{load,max1} = p_s A_3 - p_t A_4 \approx 22000N \tag{B.4}$$
$$F_{load,max2} = p_s A_4 - p_t A_3 \approx 13800N$$

where A_1 and A_2 are the areas for the piston and rod chambers on the test cylinder, and A_3 and A_4 are for the piston and rod chambers on the load cylinder.

For the trajectory used when tuning the controller in Chap. 8, acceleration of up to 0.25 m/s^2 is used. If only the maximum mass is emulated, then the load side uses 2250 N or 10-20 % of the available force. The viscous friction force depends on velocity. The valve can deliver flow for velocities up to ≈ 0.15 m/s. To emulate the maximum viscous friction of 30000 Ns/m, the load side uses 4500 N, or 20-30 % of the available force. Furthermore, the maximum emulated coulomb friction is 1500 N. If all parameters are set as maximum, and a maximum acceleration at maximum speed is required, then a total force of 7750 N is required by the load side.
These calculations are assuming the load cylinder will have to emulate the full magnitude of each system parameter, where in reality, the nominal size of the parameters will reduce the size of the emulated parameters. However, it shows that the load cylinder will be able to deliver enough force in both direction to emulate the desired parameters variations. It is expected that the load cylinder will be providing forces of up to 3300 N for the fault trajectory used.
If these relative large system parameters were not emulated, the test cylinder would only be using a low amount of the available force, making it difficult to control precisely due to the sensor noise having a larger influence. Furthermore, if the tested hydraulic servo-system was applied to a wind-turbine, then the increased mass is a more realistic scenario.

A velocity feedforward is applied to reduce the coupling between the cylinders. Without a velocity feedforward the movement of the test cylinder may introduce a pressure build up in the load cylinder, depending on the reaction time of the force controller. The feedforward signal will open the load cylinders valve to allow the appropriate amount of flow. Then the only force the force controller has to produce is the load.

The IARC requires an estimation algorithm in order to operate. Three of the uncertain parameters, which will be estimated, are the mass, viscous friction, and coulomb friction of the system. This means that the non-linear controller will adjust to the appropriate emulated parameters. Furthermore the IARC has been shown to ensure stability, despite incorrect estimation. This is done through the sizing of a non-linear gain according to ranges of possible estimation error. The IARC is stable for non-linear force errors of upto 1000 N. The margin comes from the ranges of D_{1n} and $\tilde{D}_1$. These ranges are effective when the estimation of a

parameter has already reached a limit, but the real parameter is outside it. If the force controller has to emulate a parameter at the range of the estimation, then possible overshoot can cause the real parameter to go outside the range for which the controller is designed to be stable for. In this case overshoot force will be seen from the estimation as a non-linear force. Then the D_{1n} and $\tilde{D}_1$ range will have to be linked to the possible fluctuation of mass due to over/undershoot of the force controller that will be designed here. From the stability range of the IARC (1000 N) and the maximum force required from the force controller (in this case 3300 N), it is found desirable that the force controller has an over/undershoot limit of 30%. Furthermore, a rule of thumb dictates that the load controller has to be faster than the test controller. Otherwise the load cylinder may not be able to provide the desired emulation of parameters. This is the case, because the force controller and the IARC are following the same trajectory. To allow for a better tuning of the IARC the force controller will be tuned aggressively. The maximum possible bandwidth in the system is determined by the valve, which is a limiting factor. For this reason the force controller will be tuned to have a frequency close to the valves. With these considerations in mind the requirement for the force controller, arranged by importance from more to less important, are:

- Bandwidth above 50 Hz
- Overshoot/undershoot under 30%

The load cylinder has been linearised with a velocity of 30 mm/s and at 7 equally spaced linearisation points spanning the entire length of the cylinder. The transfer functions from valve opening to load force for the 7 linear models can be seen in fig B.2.

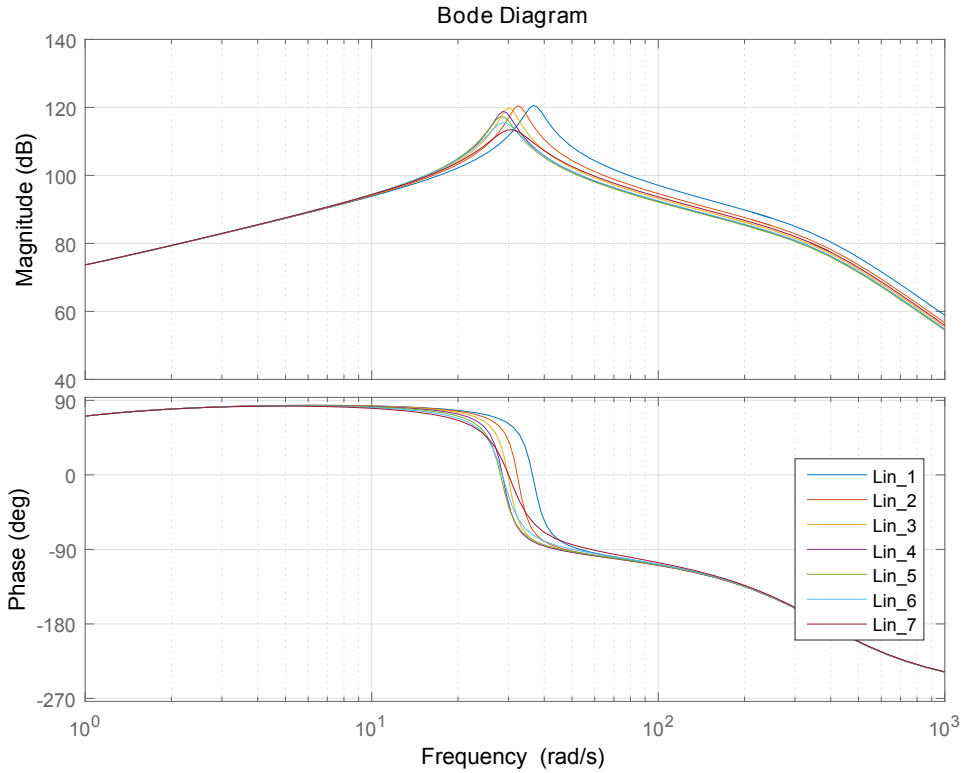

Figure B.2: Bode plot of the transfer functions between valve opening and force for the 7 linearisation points.

The slowest peak in these bode plots is at the 5th linearisation point, which is close to the center of the cylinder. In order to spare time, a PID has been autotuned for the 5th linearisation point using Matlabs 'pidtune' function. The slowest transfer function will be used, because that one will have the smallest safety margins. In the other linearisation points the controller will have a slightly degraded performance, but will still be stable.

A bode plots of the OL systems with the controller can be seen in fig B.3

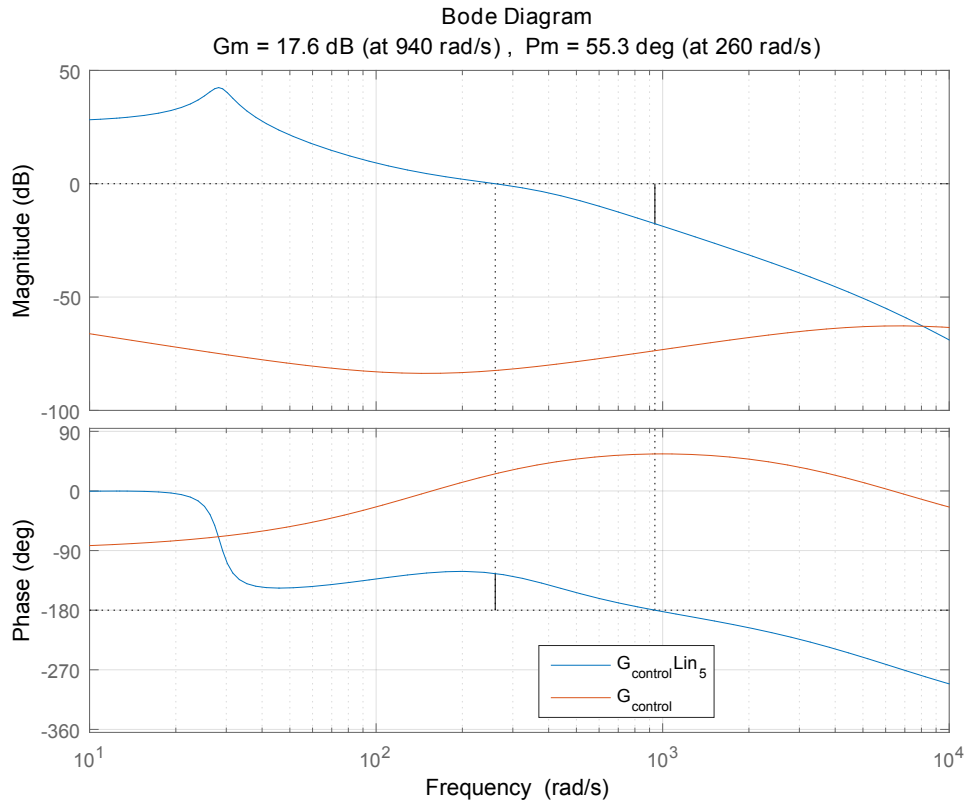

Figure B.3: Bode plot of the OL system with applied force controller and the controller itself.

The autotuned controller is difficult to implement in its initial form, because of the derivative term. The force feedback is based on pressure measurements. These will not be smooth continuous signals, meaning their derivation will be problematic from a numerical simulation perspective. To overcome this problem the controllers will be implemented as a PI-Lead, where the derivative term has been implemented as a lead filter. The effect of the double zero has been removed close to a decade later, by a double pole. This will reduce the effect of the derivative term in the higher frequencies, reducing the sensitivity of the controller to sensor noise. At the same time the zeros introduce a positive phase contribution before the phase crosses 180 deg, in effect delaying it. This allows a higher CL bandwidth of $\approx$ 490 rad/s(78 Hz) to be achieved. The CL response of the system can be seen in fig B.4.

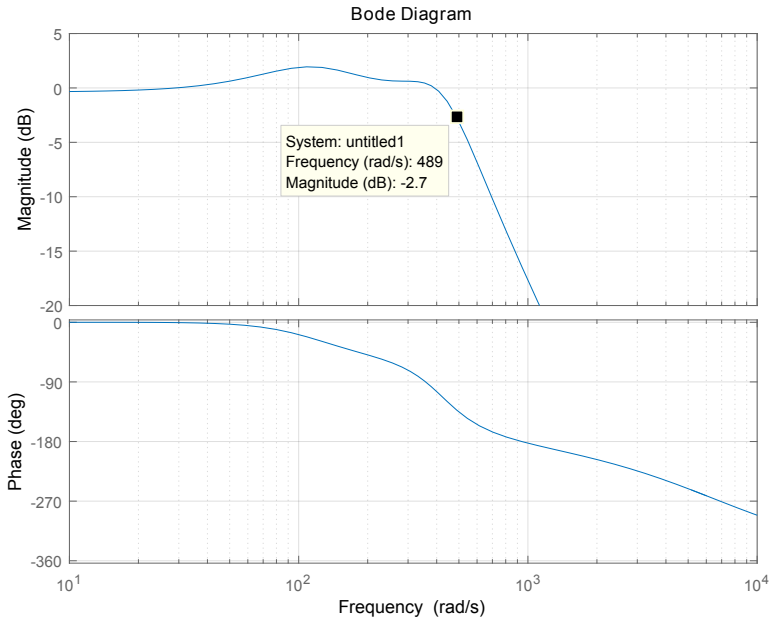

Figure B.4: Bode plot of the CL system with applied force controller.

The peak at the eigenfrequency of the system does not move sufficiently to merit the use of gain scheduling. Fig. B.5, shows the controller applied to the linear model with the fastest eigenfrequency.

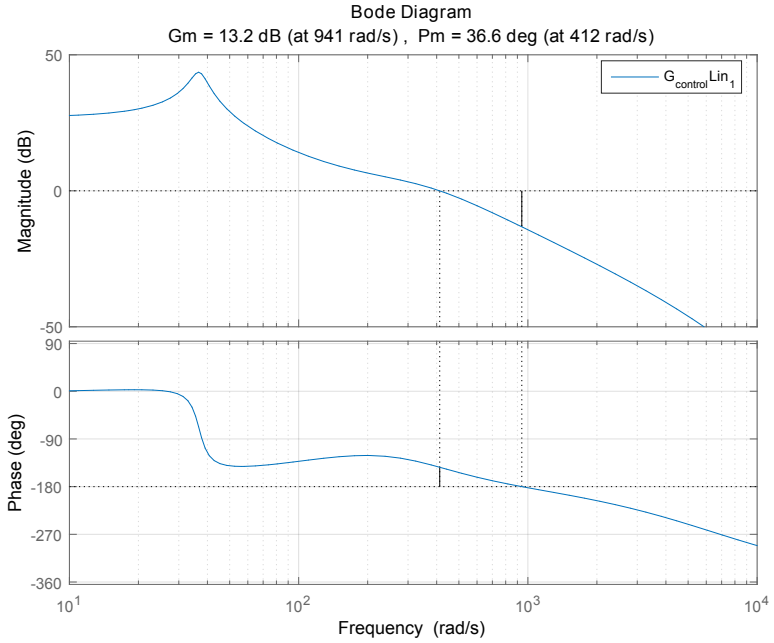

Figure B.5: Bode plot of the OL system Lin_1 with applied force controller.

It is possible to improve the tuning of this controller. The standard desired margins of 6 dB and 45 deg are not achieved. The extra time and effort associated with this has been deemed

inefficient, because the load controller has been found to perform satisfactory in simulations. The errors in force produced by this controller will be within the margins of the estimation algorithm, and the IARC is expected to give a good performance regardless of uncertainties in the system. Furthermore any errors in parameter estimation will be estimated and accounted for by the IARC. Since the emulated parameters are not based on a real case, their exact values are not important as long as their values are within the ranges set for the IARC. Finally the large margin can help avoid instability if any of the systems parameters change.

A step response of the closed loop system with the designed controller can be seen in B.6.

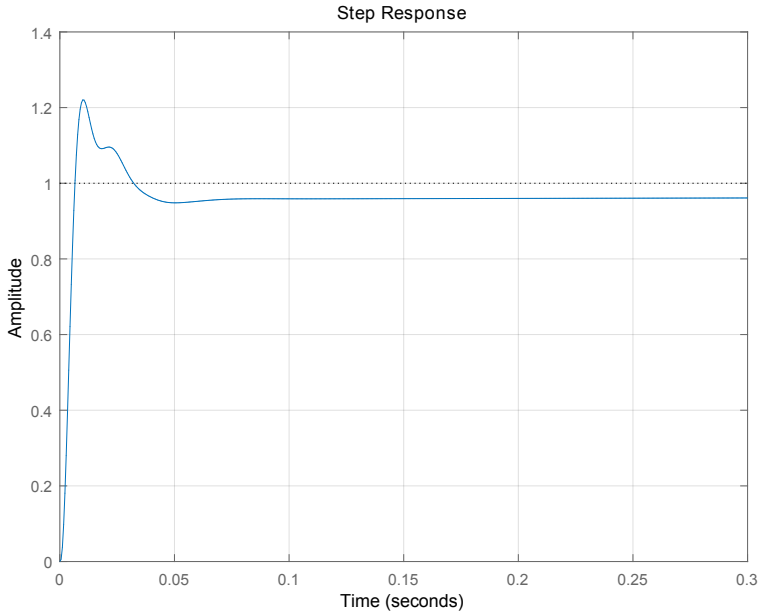

Figure B.6: Step responses of the CL system linearised at middle position with the force controller.

The 20% overshoot of the controller has to be taken into account by the estimation algorithm and the non-linear gain of the IARC. The settling time is 36 ms with a rise time of 4 ms.

The feedforward introduced to help the force controller follow the IARC movement is implemented as a passive feedforward. The feedforward is based on the DC gain from the transfer function of each system. To visualise the structure of the force controller, a block diagram can be seen in fig. B.7.

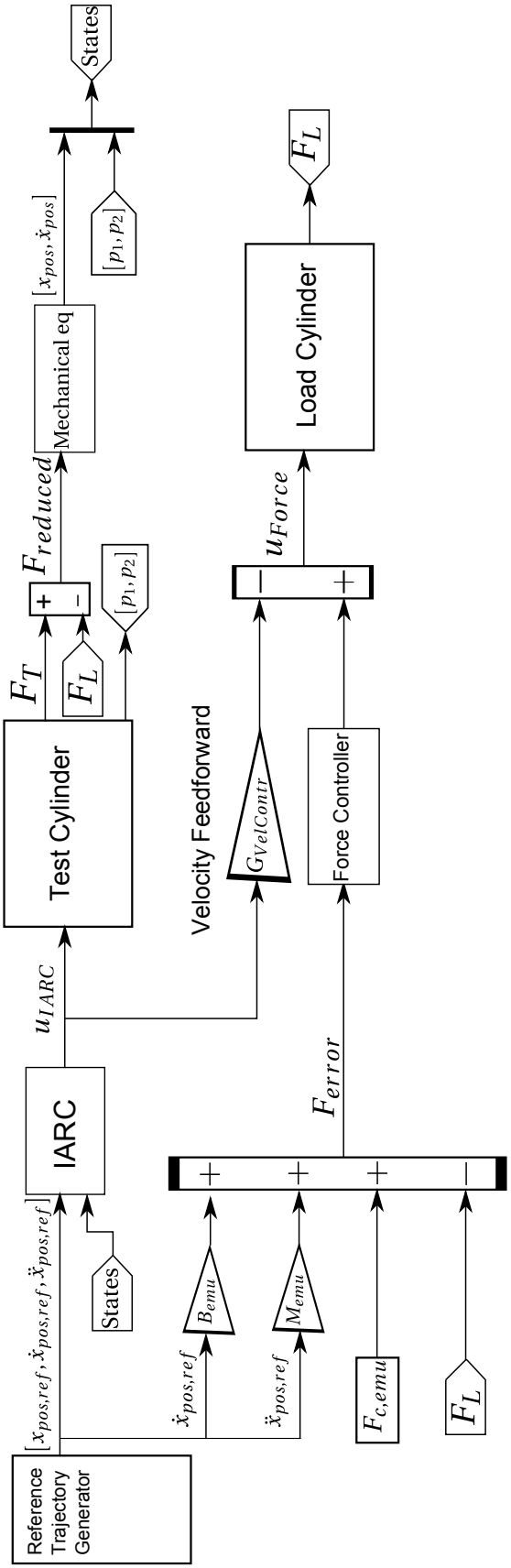

Figure B.7: Diagram of the load cylinder control structure.

APPENDIX C

EXPERIMENTAL PARAMETER DETERMINATION

In this chapter, tests for determination of the nominal system parameters will be described. The system parameters that need to be determined are:

M_{eq}	Equivalent mass of the system	[kg]
B	Viscous friction coefficient and damping	[Ns/m]
F_c	Coulomb friction	[N]
β	Bulk modulus	[Pa]
D_{21n}	Nominal lumped model error, fx. leakage	[m^3/s]
D_{22n}	Nominal lumped model error, fx. leakage	[m^3/s]

where the lumped model error, D_{1n} is considered to be zero, i.e. no load applied, and stribeck does not have an influence.

These have been split up into force and flow parameters, based on whether they can be determined from the force equation, (C.1) or the continuity equations, (C.2)-(C.3). Due to a late order of a velocity sensor, which resulted in a delivery too late for implementation, derivation of the measured position will have to be made to approximate the velocity. It is expected that the velocity obtained by derivation will be less accurate than the measured one, because the position signal will have to be filtered heavily in order to obtain a smooth derivable signal. This filtering will introduce a phase delay between the real and estimated velocities. The velocity obtained by derivation will be accurate enough for these tests, since a constant velocity is required during the testing and the delay will not have an effect.
The acceleration will be estimated in a similar manner by deriving the position twice. The acceleration is needed in order to estimate the mass of the system. The uncertainty of the acceleration estimation would also affect the mass estimation. In order to avoid these uncertain measurements a different method will be used to find the mass of the system. Since the CAD model of the system is fairly accurate it has been decided to obtain the mas through it. From the CAD model, the mass is calculated to be 21.6 kg. However, the piston seals are not included in the CAD model. To compensate for this, a larger mass should be used. It is chosen to use 25 kg as the mass of the system. This is a small mass compared with the forces the cylinders can produce. Errors in mass estimations of ±20 % will have little to no effect, because of the large load forces.

The equations used to estimate the system parameters are:

$$M_{eq}\ddot{x}_p = p_1 A_{p,1} - p_2 A_{p,2} - B\dot{x}_p - F_c \cdot S(\dot{x}_p) + D_{1n} \tag{C.1}$$

$$Q_1 - D_{21n} - \tilde{D_{21}} = A_{p,1}\dot{x}_p + \frac{V_1}{\beta_1}\dot{p}_1 \tag{C.2}$$

$$Q_2 + D_{22n} + \tilde{D_{22}} = -A_{p,2}\dot{x}_p + \frac{V_2}{\beta_2}\dot{p}_2 \tag{C.3}$$

where the stribeck part of the friction force is included in D_{1n}, and external and internal nominal leakage in D_{21n} and D_{22n}.

C.1 Force parameters

C.1.1 Viscous friction and Coulomb friction

To estimate the viscous friction and Coulomb friction, a constant speed test is made, to remove the acceleration term in (C.1). Furthermore, the Stribeck friction should not affect the tests, due to it only being relevant at speeds close to zero. The resulting dynamics are:

$$0 = p_1 A_{p,1} - p_2 A_{p,2} - B\dot{x}_p - F_c \cdot S(\dot{x}_p) \tag{C.4}$$

The measured variables are:

- Position
- Pressure 1 & 2

The tested velocities are ±[50:180] mm/s. Before the velocity tests have been conducted the system has been "warmed up". This consist of a sine-wave trajectory run continuously until the oil of the system reaches close to 50 degrees. This is considered the working temperature of the oil. Throughout the testing the temperature of the oil does not increase significantly. This warm-up procedure should prevent variations in the system parameters due to temperature changes. The velocity is estimated by fitting a first order polynomial function of the position during the movement, where the slope will be equal to the average velocity. An example is shown in fig. C.1.

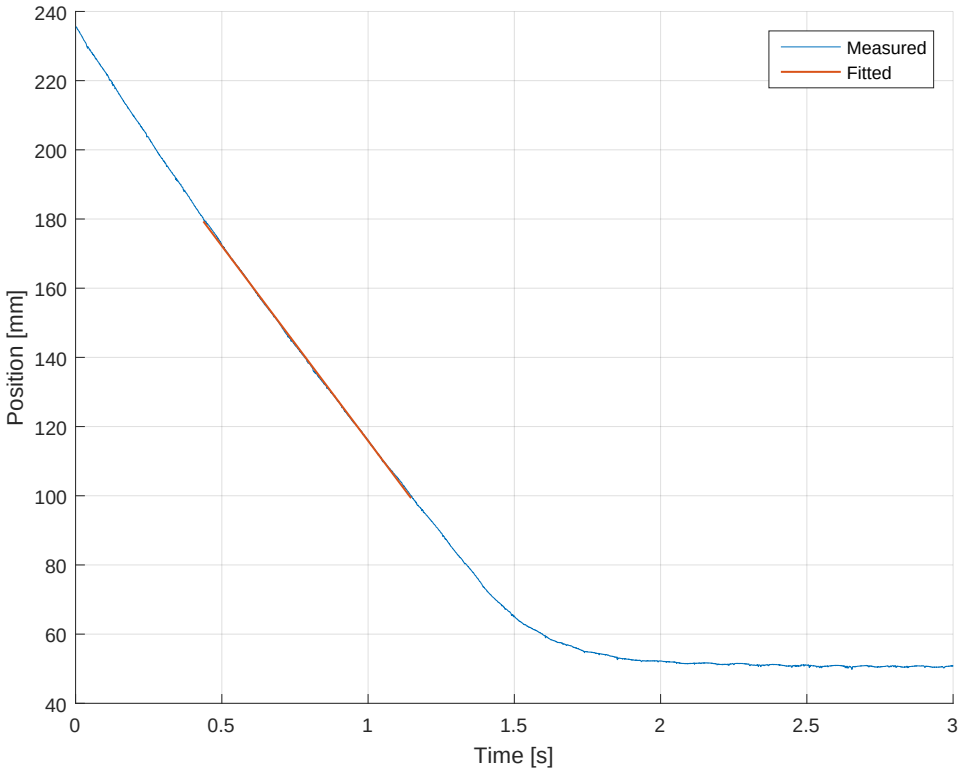

Figure C.1: Measured position compared with linear fit.

From each test, the average velocity and force is determined within the range shown as a red line in fig. C.1. If the forces follows the expected model shown in eq. (C.4), a first order polynomial can be applied for each direction of movement. Since no acceleration is present, during that part of the run, the resulting force provided by the cylinders is equivalent to the friction forces in the system. For each test the resulting force of the pressures is divided by the estimated velocity. The results can be seen in fig. C.2, where each test result is indicated with a cross.

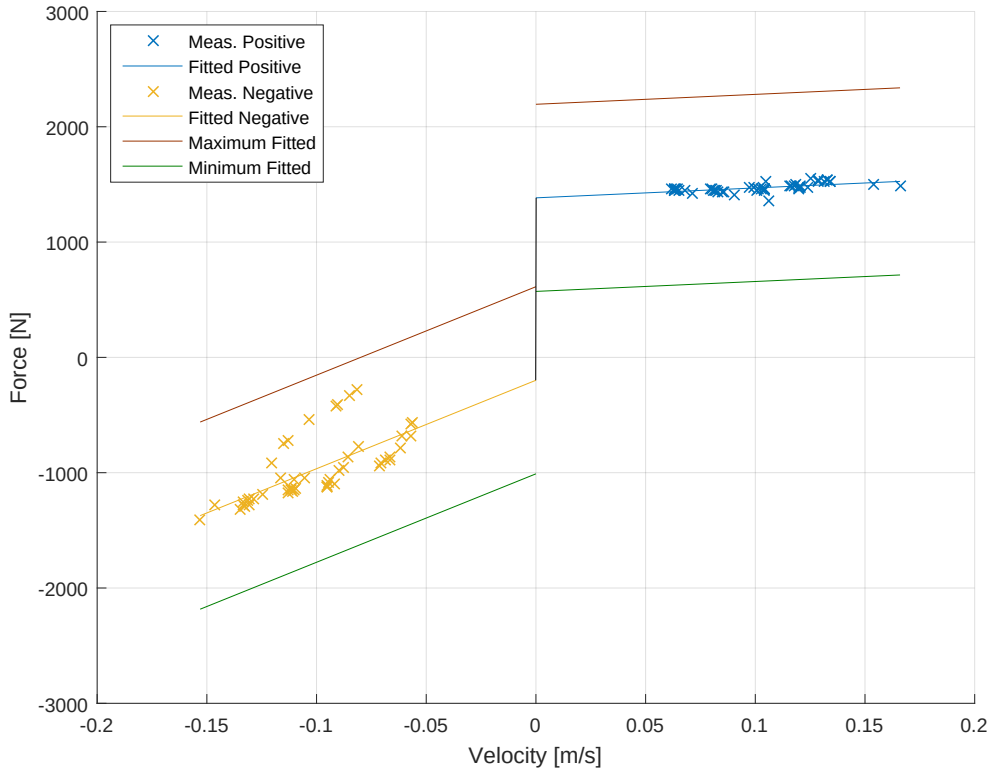

Figure C.2: Friction parameter estimation.

In fig. C.2, the results from 50 runs in each direction with velocities of ±[50:180] mm/s is shown. The force from the cylinders were found to be sensitive to small calibration errors of the sensors. The sensors have been calibrated by forcing a cylinder to push against the maximum position on one side. This results in supply pressure in one chamber, and tank pressure in the other. After the pressures settled the chamber pressure sensor is calibrated to a match the readings of a pressure sensor integrated in the pump station. This pump sensor is the only available benchmark for calibration. This was done at various pressures to reduce calibration errors. However, small errors could still be there, because it difficult to match the two signal when noise and oscillations in the supply pressure of up to 2 bar were present at all times. To determine how sensitive the estimated friction parameters are to errors in the calibration, an estimation, where 0.75 bar is added or subtracted to the pressures, has been made. These are plotted as maximum and minimum in fig. C.2 and correspond to worst cases of wrong calibration, assuming errors of up to 0.75 bar.

Because the relative small errors in the calibration will result in significantly different friction parameters, the estimated values are found to be uncertain. The fitted values are shown in table C.1.1. Min and max for the viscous friction are not shown, because an offset on the measured pressures only results in an offset of the average force. This will not affect the slope of the velocity dependent viscous friction. An error in the gains of the sensor from raw voltage and current measurement to engineering units can result in a uncertainty range of the viscous friction. It is not expected that a gain error is made because that error would have been notice easier during the calibration process, since the calibration has been checked at both 1 bar and

120 bar.

Parameter	Positive Test	Negative Test
$F_{c,min}$	572 N	-613
F_c	1384 N	198
$F_{c,max}$	2195 N	1010
B	859	7670

The estimated values are uncertain, however, due to lack of time to further study the friction parameters and obtain more confident results, these values will be used to compare the dynamics of the experimental set-up and the non-linear model.

C.2 Flow parameters

C.2.1 Leakage flow

To estimate the nominal leakage in the system, it is desired to have precise flow measurements, because the leakage flows are expected to be in the magnitude of 1-2 L/min. These leakage ranges correspond to information from the valve data sheet. The sensors applied on the set-up however, have errors of up to 1 L/min. The error of 1 L/min is based on a calibration data-sheet made by Danfoss for these sensors. The uncertainty on the measurements results in the leakage measurement being unreliable. No baseline is available for better calibration of these sensor so they cannot be made more accurate. Due to this, the nominal leakage flow will be set to 1.2 L/min at 140 bar initially [Inc., 2009]. Since this leakage's dependency on pressure cannot be investigated, a linear dependency is used in the model. When comparing the dynamics of the experimental set-up and non-linear model, variations can be made, if the tendencies indicates a leakage flow in the system.

C.2.2 Bulk modulus

Similar to the leakage flow, the uncertainties on the sensors makes it difficult to determine a proper bulk modulus value. The initially assumed bulk modulus of 7000 bar will be used in the comparison simulation. During this comparison of the pressure dynamics of the experimental set-up measurements with the non-linear model an indications of the correct range for the bulk modulus may be obtained. The nominal air ratio in the oil cannot be determined due to the measurement uncertainties, so it has been assumed zero for the verification.

APPENDIX D

CONTROL AND ESTIMATION PARAMETER OPTIMISATION

No set procedure is available for the tuning of non-linear controllers. So an optimisation algorithm was selected as the best approach for tuning the IARC and the estimation algorithm parameters. The trajectory that will be used for the optimisations is discussed in the first section. The simulation model will use the force controller determined in App. B, to include the delay in emulating an increased mass. The simulation model will not include noise on the measured states, but the effect from including these will be determined in Chap. 11. Section D.2 will be concerned with the control gain optimisation. This optimisation is affected heavily by the severity of the faults the controller has to be stable for. For this reason an analysis is performed. This analysis investigates if the uncertain parameter ranges used are at the limit of what the system can handle. In the third section an optimisation of the parameters for the estimation algorithm is performed.

D.1 Optimisation Trajectory

The trajectory used for the optimisation can be seen in fig. D.1

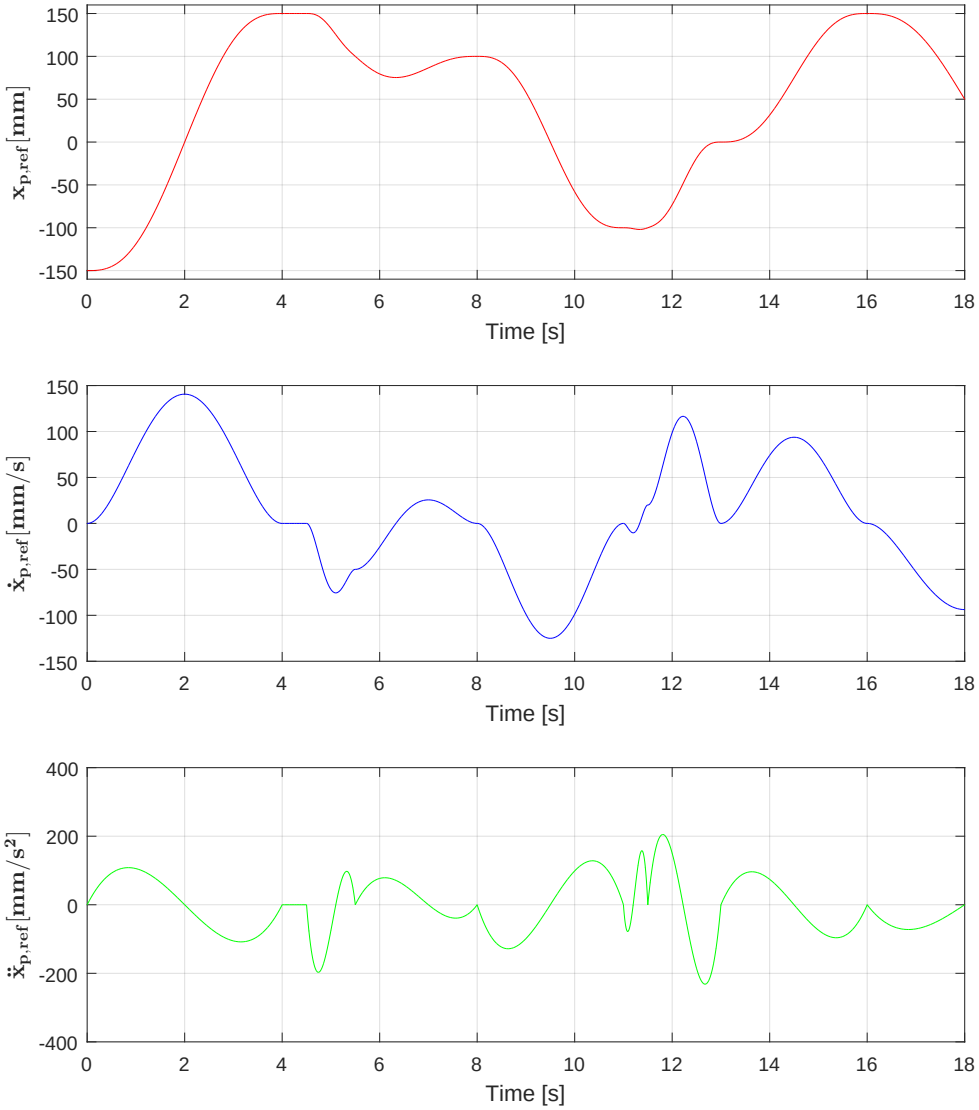

Figure D.1: Position, velocity, and acceleration trajectory used for the optimisation algorithms

By using this trajectory the system will be tested for dynamic scenarios with frequencies of 1-4 Hz on the acceleration. Higher frequencies have not been included because of a desire to not optimise the controller for a high bandwidth. The reason for this is the valve and force controller limits how fast the IARC can operate. At the maximum velocity, the normalised valve opening is ≈0.8.
Simulations where higher frequencies are used will be made in Chap. 11. These are done to determine if the system is stable with the designed controller, if a higher frequency reference is required.

D.2 Control Law Parameter Optimisation

In the appendix section a lot of the information from the main report section 8.2 is repeated in order to make the section easier to read. The important differences are the expended investigation of the effect of ε_2 and ε_3. The performance of the control law depends on the four control gains, k_1, k_2, k_3, and k_{scale}. k_1 is used for the position control, k_2 for the velocity, and k_3 for the acceleration. k_{scale} was introduced in the control law proof to reduce the impact of the velocity error state z_2. These will be used as the optimisation variables:

$$\boldsymbol{x}_{opti} = \begin{bmatrix} k_1 & k_2 & k_3 & k_{scale} \end{bmatrix}^T \tag{D.1}$$

The desired result of the optimisation is to obtain the minimum error of velocity, during trajectory tracking for run without faults. The test starts with an initial error in estimation, shown in table D.1. The cost function to be minimised is based on a simulation using the trajectory in fig. D.1 on the non-linear model and it depends on the Root-Mean-Square (RMS) velocity error ($\dot{e}_p$), calculated as:

$$f_{min}(\boldsymbol{x}_{opti}) = \sqrt{mean\left(\dot{e}_p^2\right)} \tag{D.2}$$

$$\dot{e}_p = \dot{x}_{pd} - \dot{x}_p \tag{D.3}$$

The performance of the controller also depends on the estimation algorithm. For this optimisation an initial error is present in the uncertain parameters. The estimation will then converge to the true values over the course of the simulation. It is possible to give the correct values to the control law directly. This would decouple the two algorithms. The optimisation has not been performed in this manner, because part of the control law is only active when the uncertain parameters have not converged to their real values. The parameters for the estimation algorithm in this optimisation are hand tuned, based on simulation tests. These values are not the optimal values, but the performance is satisfactory for these tests, estimating the correct parameters within 5-10 seconds.
For the first optimisation, relatively large ranges on the uncertain parameters are used, to determine how large a fault spectrum can be tolerated by the control law. The nominal value, initial value and range tested are shown in table D.1.
Furthermore, the values of the user defined constants ε_2 and ε_3 have to be chosen. ε_2 and ε_3 are used in the calculation of the virtual non-linear control laws α_{2s2} and Q_{Ls2}, shown in eq. (D.4).

$$\begin{aligned} \alpha_{2s2} &= -h_2 \tanh\left(\frac{h_2 z_2}{\varepsilon_2}\right) \\ Q_{Ls2} &= -h_3 \tanh\left(\frac{h_3 z_3}{\varepsilon_3}\right) \end{aligned} \tag{D.4}$$

where h_2 and h_3 are the non-linear control gains, defined as:

$$\begin{aligned} h_2 &\geq ||\boldsymbol{\varphi}_{2,max}^T \boldsymbol{\theta}_{range}|| + ||\tilde{D}_{1,max}|| \\ h_3 &\geq ||\boldsymbol{\varphi}_{3,max}^T \boldsymbol{\theta}_{range}|| + ||\dot{\alpha}_{2u,max}(\theta_{5,max} - \theta_{5,min})|| + ||\tilde{D}_{2,max}|| \end{aligned} \tag{D.5}$$

By having a relatively large value of ε_2 and ε_3, the non-linear control gains will only have minimal impact when the estimator is working correctly and no uncertain non-linearities are present. The sizing of ε_2 and ε_3 is also regarding the maximum effect that an error in the estimation and unmodelled non-linear forces will have on the system. From this, having a very large value of ε_2 and ε_3 means the controller will mainly use the linear control gains when no faults and uncertainties are present, which is desirable, but will also result in a large maximum effect when a fault occurs. With these considerations in mind, values of ε_2 and ε_3 has initially been set to 200 and 1 respectively. These values have been chosen from hand tuning and only serve as an initial guess.

The ranges tested are:

Range	M_{eq}[kg]	B [Ns/m]	F_c [N]	D_{1n} [N]	β^{-1} [bar^{-}1]	D_{21n} [m^3/s]	D_{22n} [m^3/s]
Nom. Value	6500	18000	200	0	7000^{-1}	$\approx$-2·10^{-6}	$\approx$ -2·10^{-6}
Ini. est.	7000	16500	120	0	7500^{-1}	0	0
$\boldsymbol{\theta_{range}}$	[10 9000]	[0 30000]	[0 1500]	[-500 500]	[10000 4000]$^{-1}$	[-5 1]/60000	[-5 1]/60000

Table D.1: Nominal value of uncertain parameters, initial estimate used, and uncertain parameter range tested

The optimisation algorithm chosen for this purpose is a standard Genetic Algorithm (GA) from Matlab's Global Optimization Toolbox. The algorithm is slower and more complex than a gradient based optimisation. A gradient based method is not used, because the non-linear nature of the controller and the system prevent the determination of the shape of the cost function. The genetic algorithm has the added benefit of having random initial guesses for the parameters, removing the requirement of having a good user defined initial guess, or multiple tests with different initial guesses. Furthermore the values have been normalised to prevent numerical problems, due to the large difference between the magnitude of k_1 and k_2, and k_3. The values are:

Parameter	Minimum Value	Maximum Value	Normalisation Scale
k_1	1	250	0.05
k_2	1	200	1
k_3	1	1500	$1{\cdot}10^{-10}$
k_{scale}	1	500	1

where the minimum and maximum values have been chosen based on what previous studies have used ([Mohanty and Yao, 2011]), and realistic values from hand tuning.

The algorithm is set to run for 10 generations. By using only 10 generations, it is not certain that the optimum is found. However, the cost function value can give an indication whether the controller can be tuned with this method. By running the reduced version of GA, the time used is decreased significantly, which is desired, due to the amount of settings considered in this section. The conditions that can be varied to improve performance are mainly the size of a fault that can occur ($\boldsymbol{\theta_{range}}$) and the values of ε_2 and ε_3. After proper conditions has been found, a full GA run will be made.

For the GA, a penalty function has been applied, which stops the simulation if control law input of more than 1.5 has been observed. These will stop the simulation if it goes unstable, and possible result in a very slow simulation, delaying the optimisation significantly.

First Optimisation Results

The resulting optimum control gains are shown in table D.2, together with the value of the cost function. The control law input was found to have chattering during the run. The performance can be seen in fig. D.2.

Range tested	k_1	k_2	k_3	k_{scale}	f_{min}
$\boldsymbol{\theta_{range}}$	100.6	17.2	$12.1 \cdot 10^{-10}$	426.2	**13.32**

Table D.2: Optimisation of control law gains result

The RMS velocity error found of 13.9 mm/s in D.2, marked with bold, is quite high, and changes of the user defined parameters should be considered. The system response can be seen in fig. D.2.

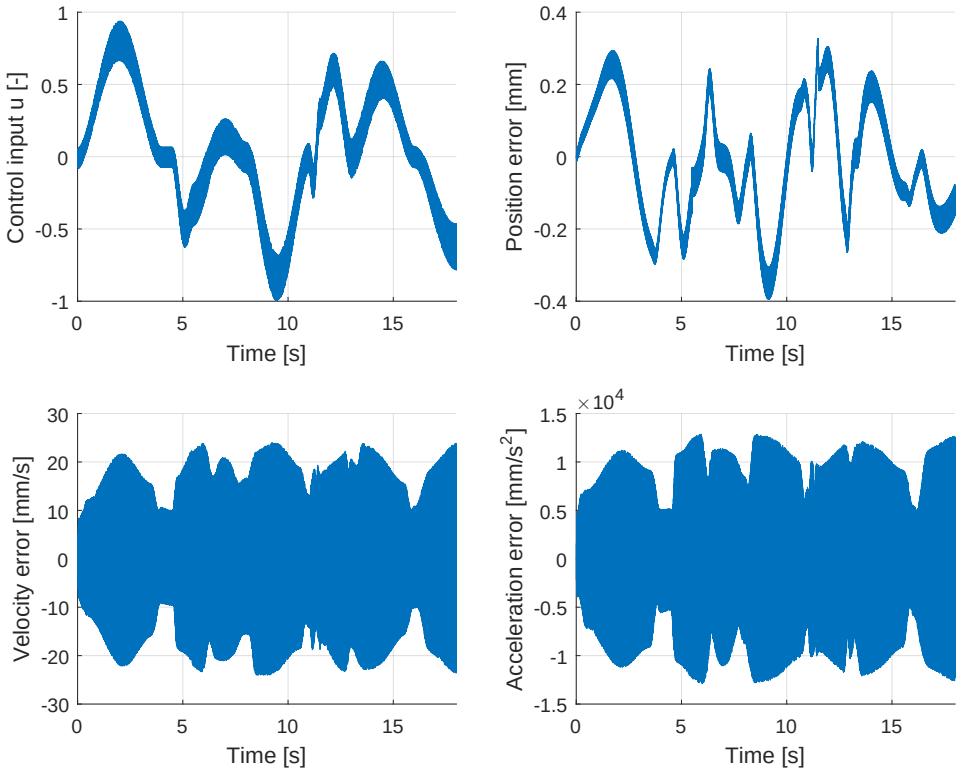

Figure D.2: System performance with initial control gains and uncertain parameter ranges

From fig. D.2 it can be determined that the controller has high frequency chattering causing the acceleration, velocity, and position to chatter. The system also uses a load cylinder to provide a simulation of increased mass, designed in App. B. Either one or both of the controllers is

chattering. A discussion regarding the root of this chatter is done in the following section.

D.2.1 Evaluation of Results

The performance obtained with the control gains found through optimisation were not satisfactory. First it was assumed, that the optimal control gains were found too large, resulting in the chattering effect. The gains were reduced in order to alleviate the problems. The reduction consisted of lowering each gain separately, and in combinations of each other. The reduction of the control gains k_1, k_2 and k_3 did not reduce the chattering significantly, and led to a poorer performance. Tests where a fraction of the magnitude of the non-linear gains h_2, and h_3 were used was also made. These resulted in a significantly reduced chattering. Based on these tests, it is assumed that the non-linear gains are the reason for the chattering behaviour. To investigate these findings further, the control input, u, was split into a linear and feedforward part, and a h_2, h_3 part. The linear and feedforward part contains the terms where the gains k_1, k_2, and k_3, and the scaling factor k_{scale} are used. The control input from both can be seen on fig D.3.

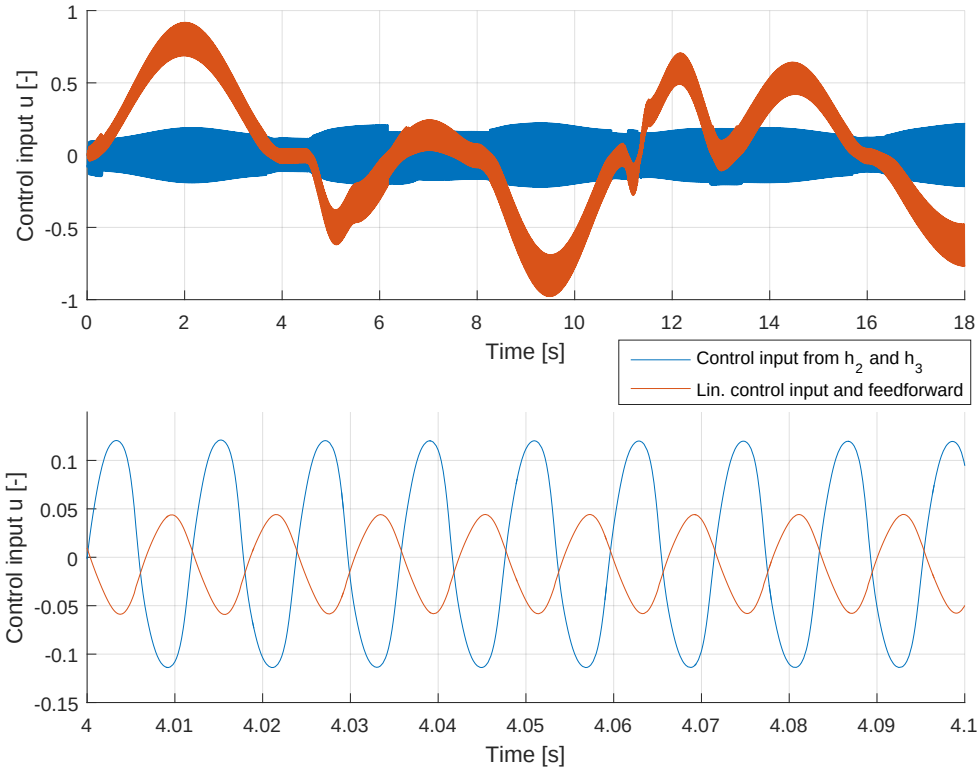

Figure D.3: Comparison of linear and feedforward control input with h_2, h_3 control input

Fig. D.3 shows that a significant part of the chattering on the control input is from the h_2, h_3 control part. From the figure with the enlarged time frame it can be seen that the two signal have a phase shift. The chattering of h_2, h_3 introduce a similar error in the velocity state. The resulting control law has a frequencies of close to 90 Hz, which exceeds the bandwidth

of the valve. To investigate if the non-linear control gains are the reason for the high frequency chatter, methods of reducing the control gains of h_2, and h_3 will be investigated. By reducing these gains, the frequency of the control input may decrease below the valve- and force controller frequency, reducing the chattering and improving the performance.

The magnitude of the gains, h_2, and h_3, are dependent on the selected ranges as seen in (D.6).

$$\begin{aligned} h_2 &\geq ||\boldsymbol{\varphi}_{2,max}^T(\boldsymbol{\theta}_{max} - \boldsymbol{\theta}_{min})|| + ||\tilde{D}_{1,max}|| \\ h_3 &\geq ||\boldsymbol{\varphi}_{3,max}^T(\boldsymbol{\theta}_{max} - \boldsymbol{\theta}_{min})|| + ||\dot{\alpha}_{2u,max}(\theta_{5,max} - \theta_{5,min})|| + ||\tilde{D}_{2,max}|| \end{aligned} \tag{D.6}$$

The magnitude of the gain used for a specific error, z_2 and z_3, is dependent on the size of ε_2, and ε_3. The reason for this is the use of a tanh function for the calculation, see eq. (D.7).

$$\begin{aligned} \alpha_{2s2} &= -h_2 \tanh\left(\frac{h_2 z_2}{\varepsilon_2}\right) \\ Q_{Ls2} &= -h_3 \tanh\left(\frac{h_3 z_3}{\varepsilon_3}\right) \end{aligned} \tag{D.7}$$

This means that there are two ways of reducing the effect of the non-linear gains:

- Reducing the magnitude of h_2 and h_3 through reducing the range of the uncertain parameters, $||\boldsymbol{\theta}_{range}||$
- Reducing the part of h_2 and h_3 which is used at a certain error through the user defined parameters ε_2, and ε_3

These will be investigated in turn. First an analysis is made on the uncertain parameter ranges. The analysis will consist of changing the magnitude of each uncertain parameter range by ± 5% to see which uncertain parameter the cost function value, f_{min} is the most sensitive to. If large changes are introduced in the parameter ranges control values would no longer be valid. This is why only small changes are made in the analysis. The results are shown in fig. D.4. In the second analysis ε_2 and ε_3 have been varied by ± 5%. The results can be seen in fig. D.5.
Parameters causing a significantly larger variation in f_{min} compared to others will be looked into, and a new optimum determined.

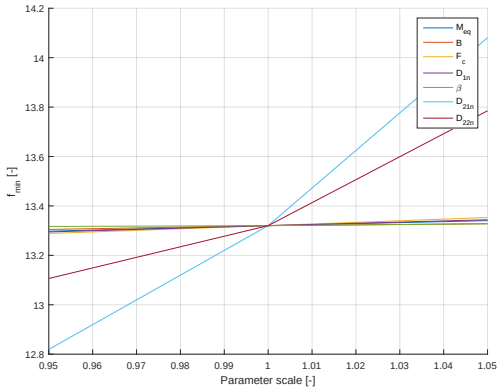

Figure D.4:

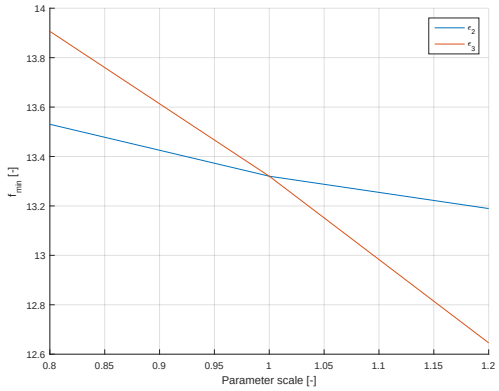

Figure D.5:

Figure D.6: Analysis of uncertain parameter ranges (left) and ε_2 and ε_3 (right)

Uncertain Parameter Range Variation

Fig. D.4 shows that the cost function f_{min} is sensitive to changes of D_{21n} and D_{22n}, which includes the possible leakage ranges of the system. Changes to the other parameter ranges seems to only have minimal effect, and will not be adjusted. The effect from varying the uncertainty range on D_{21n} and D_{22n} will be on the gain h_3.

To investigate to what degree the range should be decreased to reduce the chattering, four new ranges are investigates. The new ranges tested are shown in table D.3, changes are marked with bold text.

Range	M_{eq}[kg]	B [Ns/m]	F_c [N]	D_{1n} [N]	β^{-1} [bar$^-$1]	D_{21n} [m^3/s]	D_{22n} [m^3/s]
$\boldsymbol{\theta_{range,1}}$	[10 9000]	[0 30000]	[0 1500]	[-500 500]	[10000 4000]$^{-1}$	**[-3 1]/60000**	**[-3 1]/60000**
$\boldsymbol{\theta_{range,2}}$	[10 9000]	[0 30000]	[0 1500]	[-500 500]	[10000 4000]$^{-1}$	**[-2 1]/60000**	**[-2 1]/60000**
$\boldsymbol{\theta_{range,3}}$	[10 9000]	[0 30000]	[0 1500]	[-500 500]	[10000 4000]$^{-1}$	**[-1.5 1]/60000**	**[-1.5 1]/60000**

Table D.3: Uncertain parameter ranges tested.

ε_2 and ε_3 variation

Fig. D.5 shows that the cost function is very sensitive to a change in ε_3. Based on this result, changes to the magnitude of ε_3 will be tested to see what performance can be achieved with the initial leakage range.

Similar to the range variation, different magnitudes will be tested. The new values can be seen in table D.4, marked with bold text. The initial test had a ε_3 of 1. This investigation will determine if it is possible to remove the chatter of the signal by increasing the value of ε_3 instead of decreasing the range of the stability proof.

ε with 6 L/min leakage range	ε_2	ε_3
$\boldsymbol{\varepsilon_{3,1}}$	200	**2**
$\boldsymbol{\varepsilon_{3,2}}$	200	**3**
$\boldsymbol{\varepsilon_{3,3}}$	200	**4**

Table D.4: Values for ε tested

The leakage range in the previous test is considered small for the available system. This test will determine if a leakage range of 10 L/min can be obtained. This leakage range corresponds to the difference between the rated value of the valve which 40 L/min and maximum flow during the trajectory following which is 32 L/min. An extra 2 L/min is added for safety. If the relationship from the previous test holds, an even larger ε_3 is required. The values tested are shown in table D.5.

ε with 6 L/min leakage range	ε_2	ε_3
$\boldsymbol{\varepsilon_{3,4}}$	200	**8**
$\boldsymbol{\varepsilon_{3,5}}$	200	**9**
$\boldsymbol{\varepsilon_{3,6}}$	200	**10**

Table D.5: Values for ε tested

D.2.2 Uncertain Parameter Range Variation Results using ε_3=1

The result of the optimisations for a variation of the leakage fault range are shown on table D.2.2, with the ranges mentioned in table D.3.

Range tested	k_1	k_2	k_3	k_{scale}	f_{min}
$\boldsymbol{\theta_{range,1}}$	77.7·0.05	15.2	$15.0 \cdot 10^{-10}$	469	**2.028**
$\boldsymbol{\theta_{range,2}}$	204·0.05	54.5	$125 \cdot 10^{-10}$	125	**0.2139**
$\boldsymbol{\theta_{range,3}}$	224·0.05	92.4	$159 \cdot 10^{-10}$	55.8	**0.1899**

Table D.6: Optimisation of control law gains result - variation of range on uncertain parameters, table D.3

Table D.2.2 shows that reducing the range on D_{21n} and D_{22n} reduced the optimum value of the cost function to only a fraction of the initial value. From the results, it was found that the leakage range should be decreased to 2-3 L/min. The reason for the relative low leakage is mainly its effect on the gain h_3, which seems to be the main reason for the high frequency demand from the control law. The cost function value found for the ranges $\boldsymbol{\theta_{range,2}}$-$\boldsymbol{\theta_{range,3}}$ are very similar, and the difference may be due to the GA stopping after 10 generations. From the result, it is decided to use $\boldsymbol{\theta_{range,2}}$ for further analysis. This range has been chosen because it is a compromise between cost function minimum and leakage range.

The system performance for $\boldsymbol{\theta_{range,2}}$ is shown in fig. D.7.

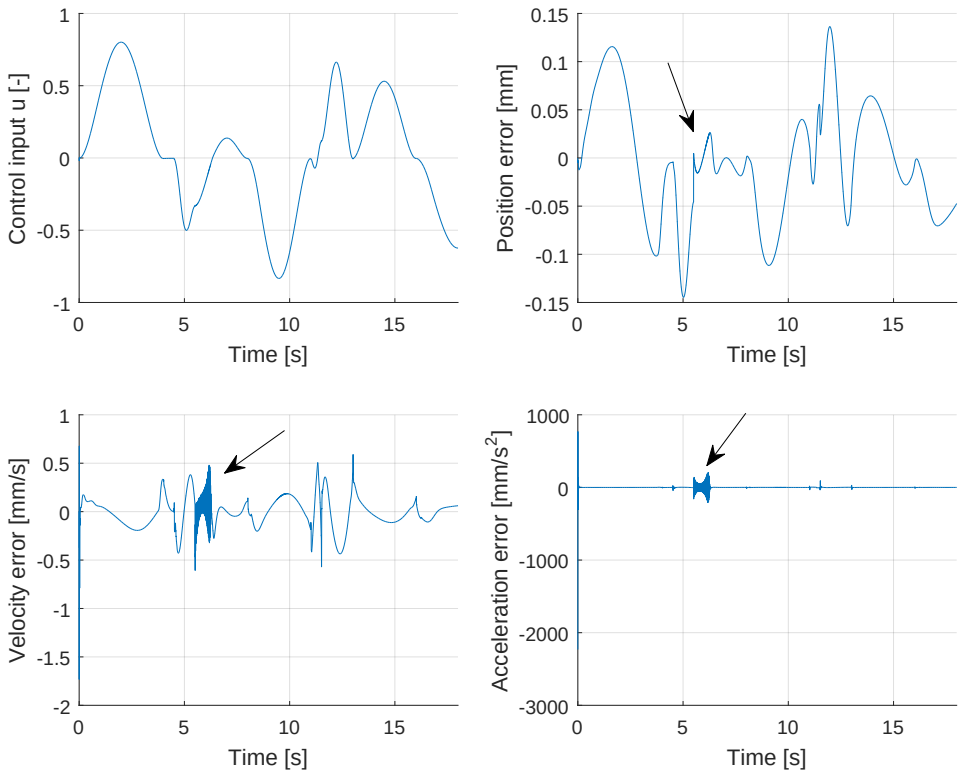

Figure D.7: System performance with $\boldsymbol{\theta_{range,2}}$

From fig. D.7, the chattering of the control input is now almost gone, which results in smoother responses of the velocity and acceleration. The initial error in the system responses are due to the initial pressures not being set ideally, resulting in a large initial acceleration error. This error is quickly rejected by the controller, and has little effect.
At around 6 seconds, marked with an arrow, a problem still occurs regarding high oscillations on the velocity. Further testing showed that the reason for this behaviour is the force controller. The simulation of mass requires an instant change in force direction which is not possible for the force controller. The next best thing is for the force controller to be sufficiently faster than the non-linear controller. It was found that optimising to reduce the acceleration error instead of the velocity error reduced this problem. A possible reason could be that a better correlation between the force controller and the IARC controller is obtained. The new optimum control gains are:

Range tested	k_1	k_2	k_3	k_{scale}	$f_{min}(acc)$
$\boldsymbol{\theta_{range,2}}$	45.8·0.05	62.5	$18.3 \cdot 10^{-10}$	465	**39.28**

Table D.7: Optimisation of control law gains result using RMS of acceleration error as cost function value

The resulting system performance using the control gains from table D.2.2 is shown in fig. D.8.

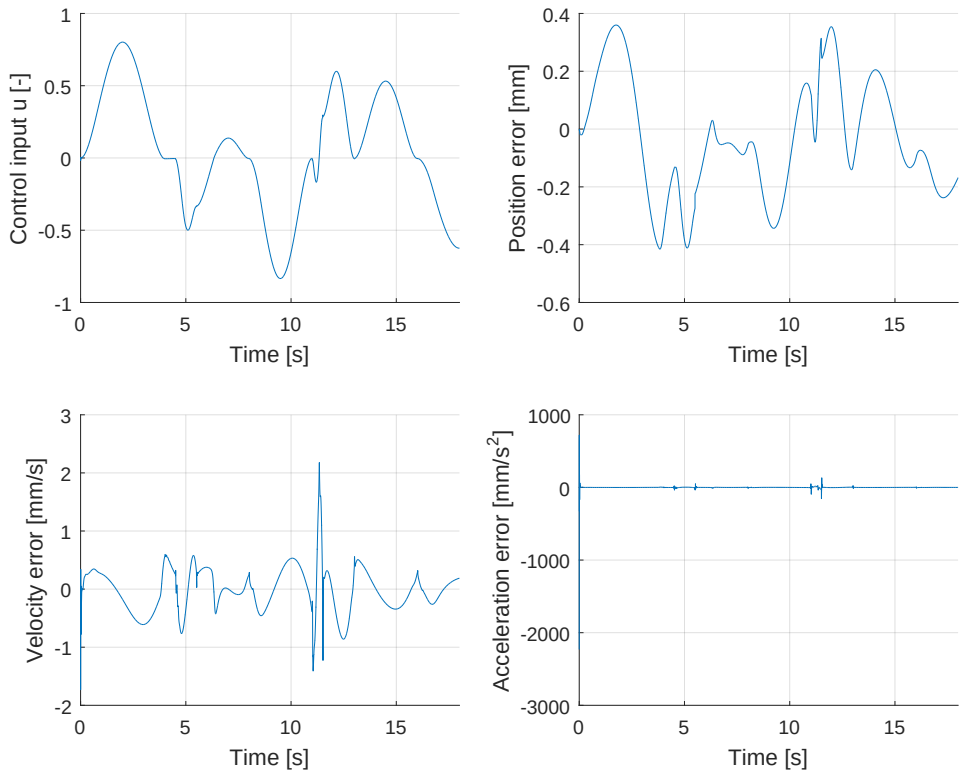

Figure D.8: System response with $\boldsymbol{\theta_{range,2}}$.

Fig. D.8 shows that the high frequency chatter at time ≈6 seconds has been reduced significantly. This indicates that the optimisation using the acceleration error as cost function value results in a more stable control signal. The new control gains in table D.2.2 are lower than those found with the velocity error based cost function. This shows that by using the acceleration error, the controller frequency is reduced.

By using these control gains, the position- and velocity error have been increased. This is however not seen as an issue, because the maximum position error is still below half a millimetre. Errors of these sizes may not be measurable on the experimental set-up, due to a sensor noise within the range of 0.4 mm.

Based on these results, the range of uncertain parameters where a stable response can be achieved, if the ε_3 is kept constant, is $\boldsymbol{\theta_{range,2}}$. To obtain even better control gains, a full GA optimisation will be made under the determined conditions. The GA setting used are the standard in Matlab. The resulting control law parameters are shown in D.2.2 with the performance shown in fig. D.9.

Range tested	k_1	k_2	k_3	k_{scale}	$f_{min}(acc)$
$\boldsymbol{\theta_{range,2}}$	36.0·0.05	285	$17.0 \cdot 10^{-10}$	471	**39.27**

Table D.8: Optimisation of control law gains result using RMS of acceleration error as cost function value

The resulting system performance using the control gains from table D.2.2 is shown in fig. D.9. The full GA run improved the performance sligthly when looking at the cost function value, improved from 39.28 to 39.27. The performance can be seen in fig. D.9.

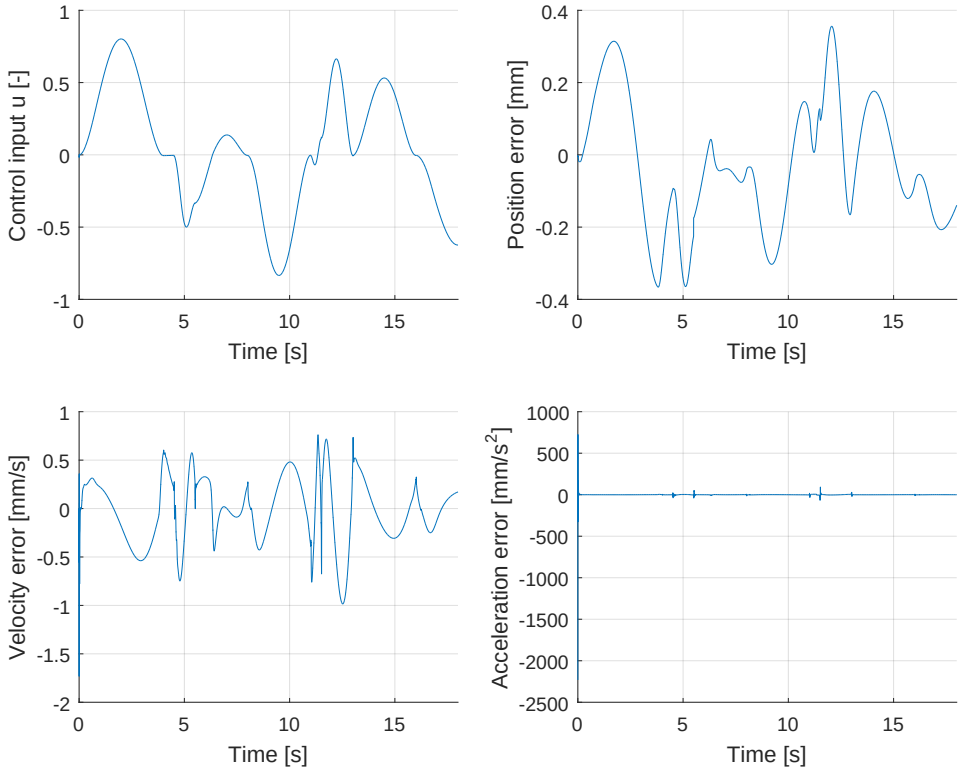

Figure D.9: System response.

These control gains will work for a 3 L/min leakage flow range and a ε_3 of 1. To investigate if a higher leakage flow range can be achieved, a different approach will be used. Here different values of ε_3 will be investigated, to see if a stable system response can be achieved at the initial desired leakage range of 6 L/min, and if possible, also investigate 10 L/min.

ε_3 Variation

Leakage Range of 6 L/min

In the previous section the effect of range size on the performance of the controller was investigated. Here the effect of ε_3 will be investigated. The variations in table D.4 will be used. From the findings in the previous section the RMS of the acceleration error will be used as the cost function value. The result of the optimisations are shown in table D.2.2.

Leakage Range tested, ε	k_1	k_2	k_3	k_{scale}	f_{min}
$6L/min$, $\varepsilon_{3,1}$=2	77.7·0.05	49.3	$24.3 \cdot 10^{-10}$	284	**3961.3**
$6L/min$, $\varepsilon_{3,2}$=3	68.6·0.05	185	$13.2 \cdot 10^{-10}$	194	**40.02**
$6L/min$, $\varepsilon_{3,3}$=4	140 ·0.05	109	$36.0 \cdot 10^{-10}$	339	**39.28**

Table D.9: Optimisation of control law gains result - variation of ε_3 with 6 L/min leakage flow range

The optimums from table D.2.2 shows similar tendencies to what was found when lowering the leakage ranges. A fast decrease of the cost function is achieved until a saturation is reached, which for RMS of the acceleration error is ≈39. For ε_3 of 3 and 4, similar cost function values are found, and the differences may be due to the GA only having run for 10 generations. The effect of varying ε_3 is the maximum effect that an error in the estimation and unmodelled non-linear forces will have on the system. Due to this, it is desired to use a low value, and the lowest value resulting in a ≈40 cost function value is chosen. The chosen ε_3 for further analysis is $\varepsilon_{3,2}$.

The performance for the control gains found with $\varepsilon_{3,2}$ is shown in fig. D.10.

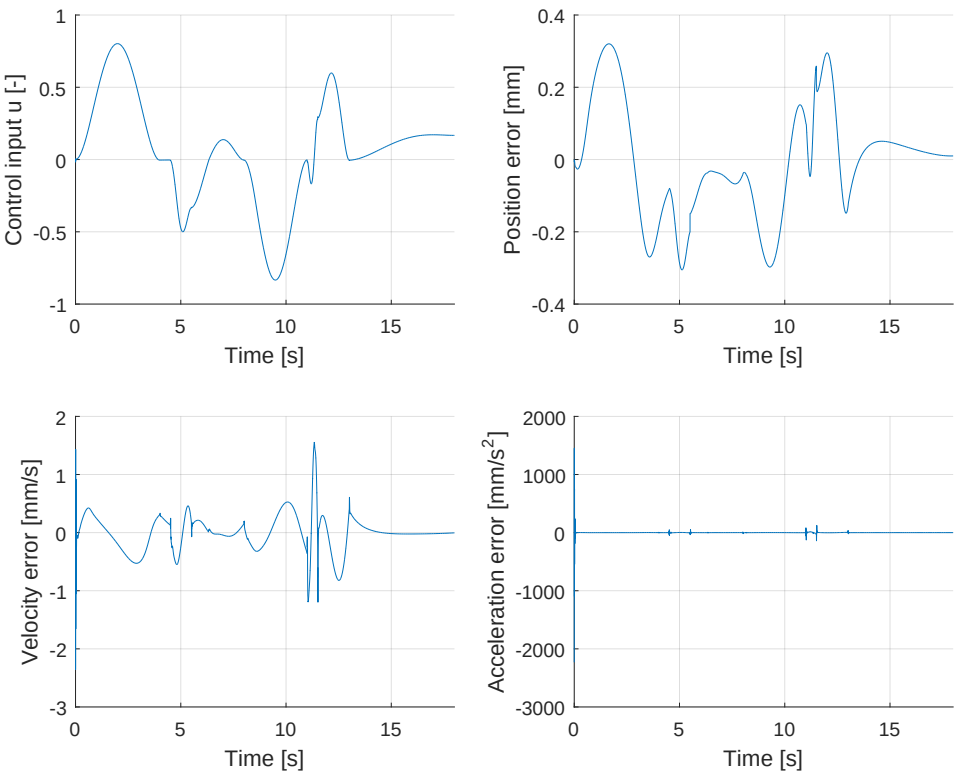

Figure D.10: System response with control gains for $\varepsilon_{3,2}$.

Fig. D.10 shows that the increase of ε_3 has indeed given similar improvements as the decrease of leakage range. The chattering on the control input and error dynamics has been reduced heavily. Similar system response as when $\boldsymbol{\theta_{range,3}}$ is used has been achieved regarding cost function value and the system response when looking at the error plots in fig. D.8 and fig. D.10. With the determined size of ε_3 that results in a stable system, a full GA optimisation will be

made. The result is shown in table D.2.2.

Range tested, ε	k_1	k_2	k_3	k_{scale}	f_{min}
$\boldsymbol{\theta_{range}}$, $\varepsilon_{3,2}$	71.5·0.05	204	$1.0 \cdot 10^{-10}$	578	**40.01**

Table D.10: Full optimisation run of control law gains result

Leakage Range of 10 L/min

The result of the optimisations are shown in table D.2.2.

Leakage Range tested, ε	k_1	k_2	k_3	k_{scale}	f_{min}
$10L/min$, $\varepsilon_{3,4}$=8	38.2·0.05	147	$1.6 \cdot 10^{-10}$	329	**40.21**
$10L/min$, $\varepsilon_{3,5}$=9	50.1·0.05	84.7	$15.5 \cdot 10^{-10}$	414	**39.69**
$10L/min$, $\varepsilon_{3,6}$=10	26.5·0.05	69.1	$4.4 \cdot 10^{-10}$	251	**39.47**

Table D.11: Optimisation of control law gains result - variation of ε_3 with 10 L/min leakage flow range

From the cost function values, similar cost function value has been achieved. It is desired to have ε_3 as low as possible, because it reduces the maximum error if the estimation algorithm is not working. To show to what degree the difference of the three ε_3 has, a comparison is made, where the estimation algorithm is giving an estimate of 1 L/min, with the real leakage being down to -9 L/min. The result is shown in fig. D.11

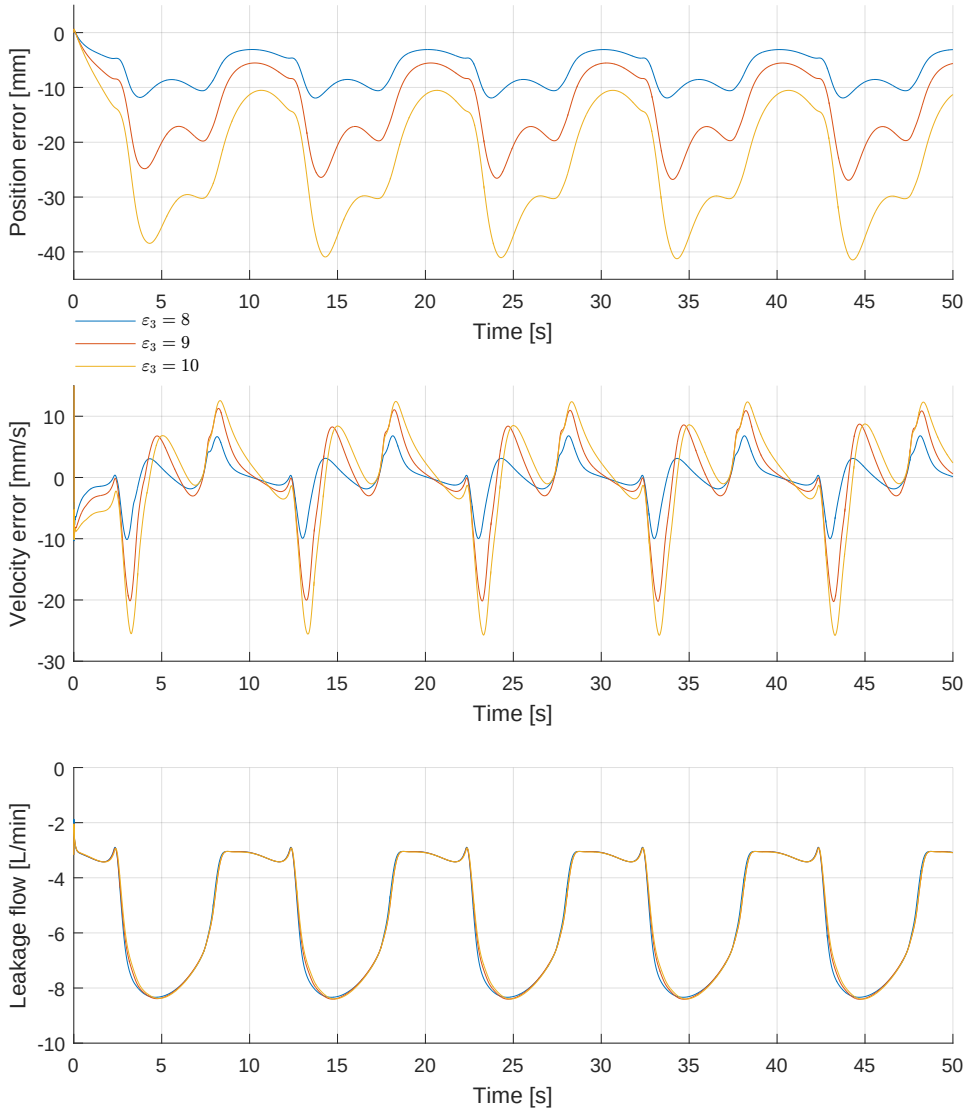

Figure D.11: Comparison of system response at large leakage estimation error.

In fig. D.11, the difference is found to be up to $\approx$ 10 mm position error increase when ε_3 is increased by 1. Based on these findings, it is chosen to use $\varepsilon_{3,4} = 8$ for further analysis.

The performance is shown in fig. D.12.

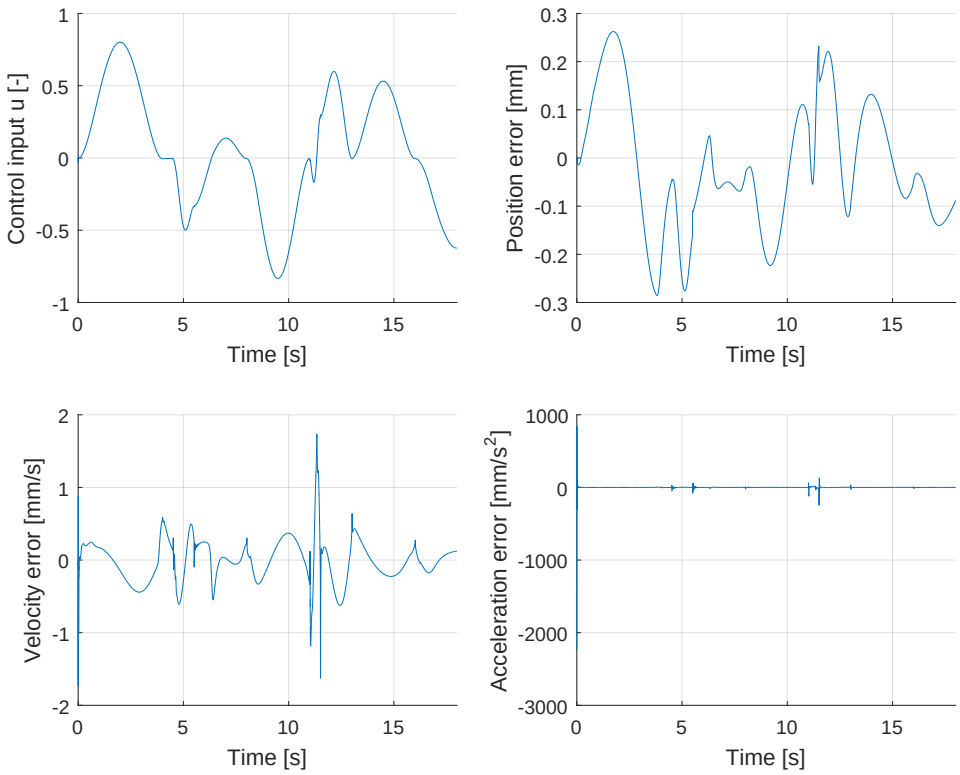

Figure D.12: System response with control gains for $\varepsilon_{3,4}$.

In fig. D.12 good performance is achieved with similar error magnitudes as for the previous leakage ranges investigated. The full GA run resulted in the following control parameters:

Range tested, ε	k_1	k_2	k_3	k_{scale}	f_{min}
$\boldsymbol{\theta_{range}}$, $\varepsilon_{3,4}$	76.5·0.05	129	$35.0 \cdot 10^{-10}$	197	**40.18**

Table D.12: Full optimisation run of control law gains result

D.2.3 Control Law Result Discussion

The optimisation and analysis, done up to this point, has been focused on performance and stability of the control law. The increase in ε_3 has lead to a larger range of faults, which can be handled by the algorithm. But the actual effect of ε_3 can be seen when the maximum estimation error is present. The increase in ε_3 should be associated with a larger maximum error in z_2 and z_3 and it can be seen in fig. D.11 that the assumption holds.

Based on the performance shown in fig. D.11, it is found acceptable to use a ε_3 of 8, and by doing so allow a leakage flow range of 10 L/min. The increased leakage range will allow the controller to work under larger leakage faults, which is desirable. A ε_3 than 8 would require a decrease in the leakage range. This is not desirable and the error introduced when the estimation algorithm is not working is found an acceptable trade-off.
The last analysis made before the estimation algorithm parameters are to be found, is to see what effect an incorrect estimation of all parameters will have on the system. For this test, the

mass and friction related parameters are inserted as maximum to the control law, while the simulated system will be using minimum values. The performance result can be seen in fig. D.13.

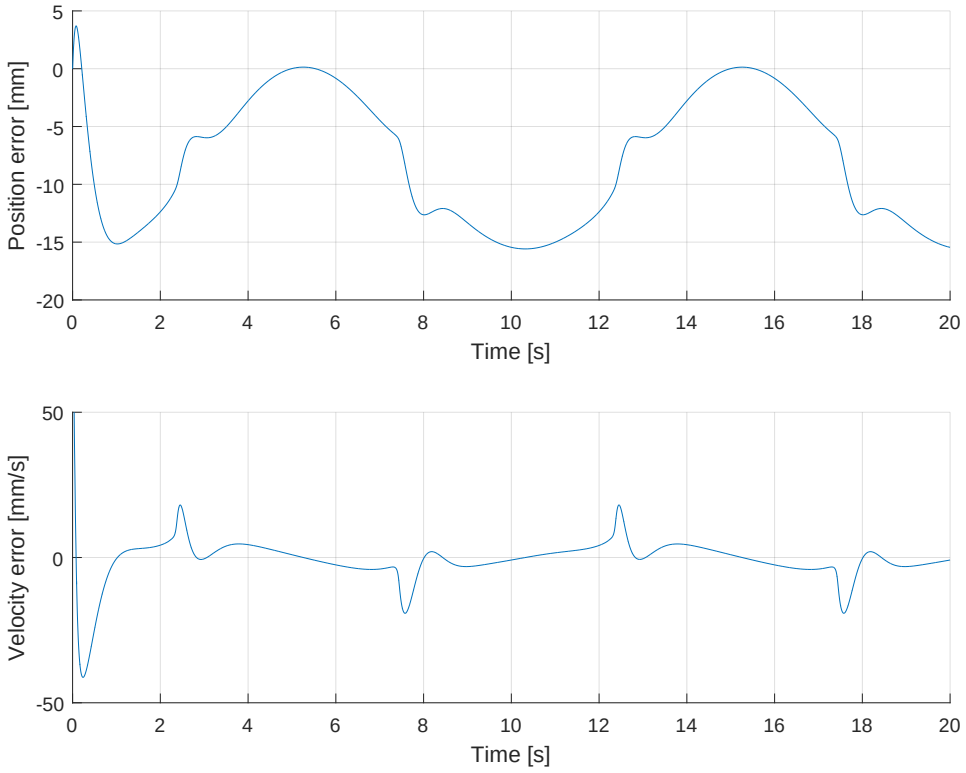

Figure D.13: System response with large estimation errors for all parameters.

In fig. D.13, the system now has position errors of up to 15 mm. The magnitudes of the errors may change if different scenarios are tested. For example if the control law uses minimum flow of -9 L/min, and the system has 1 L/min leakage, or if the control law uses minimum mass, with the simulated system using maximum. All possible estimation errors have not been investigated, so conclusions cannot be made on what is the largest possible error. These tests do however give an indication regarding the systems stability under the influence of large errors in the estimation algorithm.

Based on these findings, the control law found for a leakage flow range of 10 L/min will be used for implementation. In the following section, estimation algorithm parameters will be determined.

D.3 Estimation Algorithm Parameter Optimisation

In this appendix section the detailed optimisation of the estimation algorithm parameters is shown. A large part of the information is repeated in sec. 8.3. This information has not been removed here, in order to allow the section to be read more easily. The important

difference is the table inclusion of the table showing the upper and lower boundaries of the optimisation algorithm. Furthermore simulation results where all the faults occur during the same test is shown. For the estimation algorithm, the control parameters determined in the previous section will be used. The piston movement trajectory used is the same. For the estimation algorithm optimisation, a number of faults have been introduced, to emulate time-varying tendencies of the uncertain parameters. For the emulation of mass-, viscous friction-, Coulomb friction-, and disturbance changes, a load trajectory will be used. To emulate a time-varying bulk modulus, a slow variation in the air ratio of the oil is introduced. For the leakage, an increasing internal leakage area is used. A visual depiction of the parameter trajectory is shown in fig. D.14 and fig. D.15.

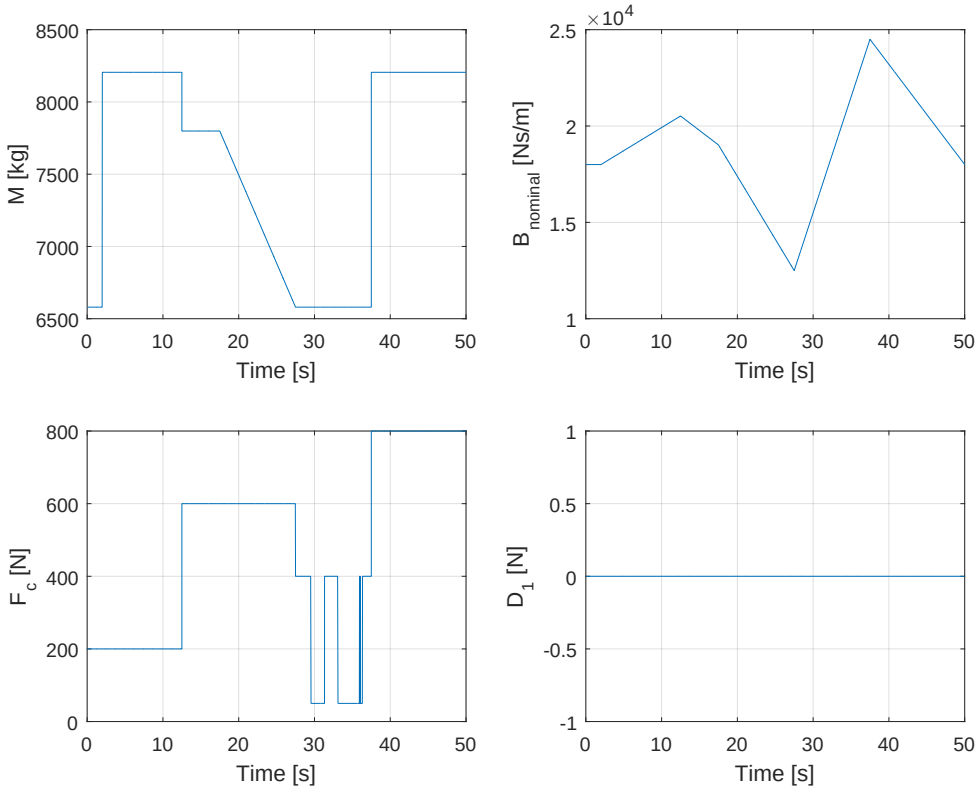

Figure D.14: Force fault related parameter variations.

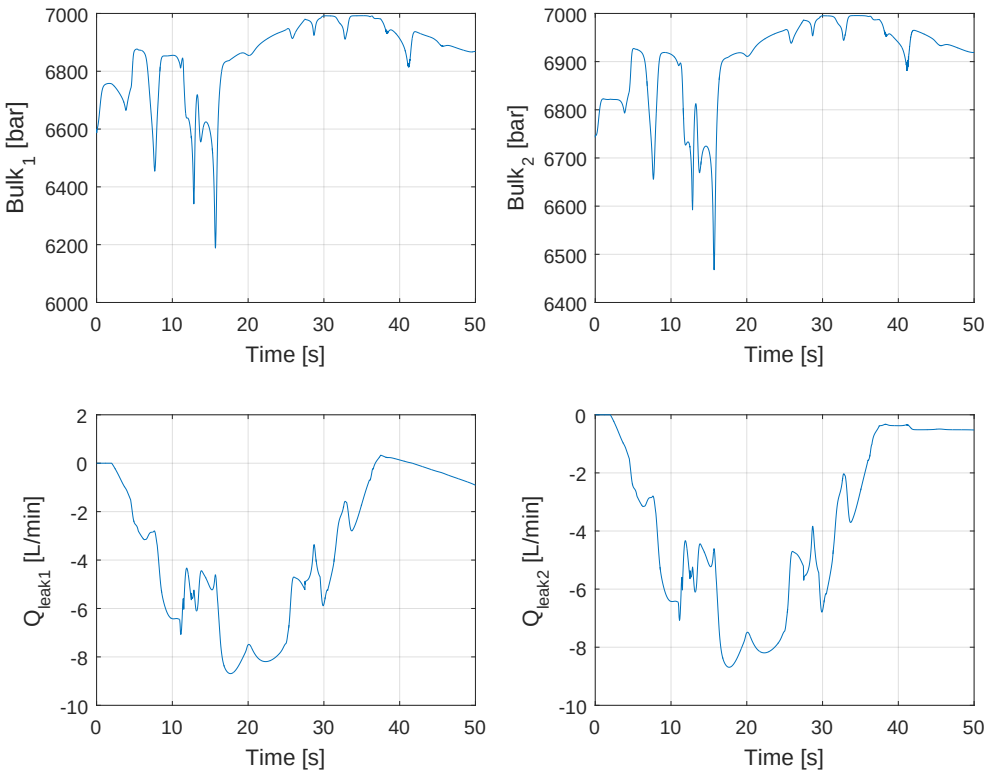

Figure D.15: Flow fault related parameter variations.

As can be seen in fig. 8.3 and 8.4, all uncertain parameters are varied during the run. This is done because some of the parameters of the estimation algorithm are not independent, and should be chosen simultaneously.

The optimisation variables are:

$$\boldsymbol{x}_{opti} = [\boldsymbol{\Gamma}(0) \quad \dot{\boldsymbol{\theta}}_M \quad \boldsymbol{\nu} \quad \boldsymbol{\alpha} \quad \boldsymbol{\rho}_M \quad \boldsymbol{\rho}_l]^T \tag{D.8}$$

where the variable vectors contain multiple elements, written explicitly in table D.13. The upper and lower bounds for the optimisation parameters, are shown in table D.13. Here a number of notations are introduced: $A_{a;,b,c}$ corresponds to the matrix element for matrix number a at row b column c, and $_M$ for maximum, $_l$ for minimum.

	Parameter	Minimum Value	Maximum Value	Normalisation scale
Initial estimation gain	$\Gamma_{1;1,1}(0)$	1	5000	1
	$\Gamma_{1;2,2}(0)$	1	5000	1
	$\Gamma_{1;3,3}(0)$	1	5000	1
	$\Gamma_{1;4,4}(0)$	1	3000	1
	$\Gamma_{2;1,1}(0)$	1	3000	10^{-12}
	$\Gamma_{2;2,2}(0)$	1	3000	10^{-4}
	$\Gamma_{3;2,2}(0)$	1	3000	10^{-4}
Maximum rate of change	$\dot{\theta}_{M;1}$	1	400	20
	$\dot{\theta}_{M;2}$	1	400	70
	$\dot{\theta}_{M;3}$	1	400	2
	$\dot{\theta}_{M;4}$	1	400	20
	$\dot{\theta}_{M;5}$	1	400	10^{-8}
	$\dot{\theta}_{M;6}$	1	400	10^{-6}
	$\dot{\theta}_{M;7}$	1	400	10^{-6}
Normalisation factor	ν_1	0	1	1
	ν_2	0	1	1
	ν_3	0	1	1
Forgetting factor	α_1	0	1	1
	α_2	0	1	1
	α_3	0	1	1
Maximum eigenvalue	$\rho_{M,1}$	1	2000	10^4
	$\rho_{M,2}$	1	2000	10^4
	$\rho_{M,3}$	1	2000	10^4
Minimum eigenvalue	$\rho_{l,1}$	1	20	10^{-2}
	$\rho_{l,2}$	1	20	10^{-10}
	$\rho_{l,3}$	1	20	10^{-10}

Table D.13: Upper and lower boundaries for estimation algorithm optimisation

where the initial $\mathbf{\Gamma}$ and maximum rate of change, $\dot{\boldsymbol{\theta}}_M$, is assumed equal for the bulk modulus in each chamber. Furthermore, the maximum rate of change has been set as the maximum absolute magnitude, i.e., the same maximum rate of change is used when increasing and decreasing a parameter. The ranges and scales set on the parameters are based on what previous studies have obtained, together with what has been found to be the correct magnitude for the system available for this project.

The cost function is defined as eq. (D.9), to obtain a minimisation of the error between the real parameters and estimated parameters. A scaling, $weight_i, i = 1:7$, has been applied to make the algorithm weigh the parameter equally. D_{1n} error scale is zero, resulting in it not being included in the cost function. This is done due to the reference being zero during the whole run. If D_{1n} is included, it will interfere in the three other force related parameters in a negative way, due to it trying to reduce the variations in D_{1n} to become as small as possible. This hypothesis was tested and the result from an optimisation with a weight larger than zero on D_{1n} resulted in slower convergence of the mass, viscous friction, and Coulomb friction being increased significantly. Because these are found to be more important parameters, it is chosen to not include the D_{1n} in the cost function.
A different approach that could be used is a minimax approach, where the optimisation tries to decrease the parameter with the largest error first, then the next and so forth. This was tried to

be implemented, however, the results obtained showed significantly worse performance than the GA results.

$$f_{min}(\boldsymbol{x}_{opti}) = \sum_{i=1}^{7} \sqrt{mean\left((\tilde{\theta}_i \cdot weight(i))^2\right)} \tag{D.9}$$

$$weight = \begin{bmatrix} \frac{1}{5000} & \frac{1}{10000} & \frac{1}{900} & 0 & 7000 \cdot 10^5 & 12 \cdot 10^4 & 12 \cdot 10^4 \end{bmatrix}^T \tag{D.10}$$

The optimisation algorithm chosen is the GA, with the same reasoning as for the control law optimisation with the optimisation function being very non-linear, and GA not being dependent on a good initial guess. The simulation required for the estimation algorithm is very time consuming. A full optimisation run with 2600 generations was determined to be unfeasible. Instead, a 10 generations optimisation run which required 4 days was performed. The parameters determined here may not be the optimum due to the relatively low amount of generations. However, the parameters will be analysed and the performance will be determined. The results from the optimisation is shown in tab. D.14.

type	Parameter	Optimum value	Normalisation scale
Initial estimation gain	$\Gamma_{1;1,1}(0)$	4250	1
	$\Gamma_{1;2,2}(0)$	2690	1
	$\Gamma_{1;3,3}(0)$	2890	1
	$\Gamma_{1;4,4}(0)$	2140	1
	$\Gamma_{2;1,1}(0)$	48.4	10^{-12}
	$\Gamma_{2;2,2}(0)$	3140	10^{-4}
	$\Gamma_{3;2,2}(0)$	3060	10^{-4}
Maximum rate of change	$\dot{\theta}_{M;1}$	279	20
	$\dot{\theta}_{M;2}$	240	70
	$\dot{\theta}_{M;3}$	320	2
	$\dot{\theta}_{M;4}$	197	20
	$\dot{\theta}_{M;5}$	164	10^{-8}
	$\dot{\theta}_{M;6}$	198	10^{-6}
	$\dot{\theta}_{M;7}$	159	10^{-6}
Normalisation factor	ν_1	0.148	1
	ν_2	0.010	1
	ν_3	0.023	1
Forgetting factor	α_1	0.979	1
	α_2	0.639	1
	α_3	0.621	1
Maximum eigenvalue	$\rho_{M,1}$	1190	10^4
	$\rho_{M,2}$	1290	10^4
	$\rho_{M,3}$	1030	10^4
Minimum eigenvalue	$\rho_{l,1}$	9.32	10^{-2}
	$\rho_{l,2}$	6.86	10^{-10}
	$\rho_{l,3}$	14.3	10^{-10}

Table D.14: Optimised estimation algorithm parameters

The optimum values in table D.14 has a few noticeable factors. The first one is the low initial

estimation gain for bulk modules ($\Gamma_{2;1,1}(0)$) which indicates that the normalisation factor might be sat a bit high compared to the others. The optimum value is however not equal to the minimum, indicating the optimum is still inside the range sat. For the normalisation factors, ν_2 and ν_3 are found to be almost zero, resulting in almost no normalisation being used. ν_1 is optimised to 0.148, indicating the force relevant parameters can benefit from having some normalisation. The forgetting factor has been optimised to 0.979 and ≈0.6, indicating the estimation algorithm is benefiting from having a relative large forgetting factor.

To determine the estimation performance for each parameter without any influence from variations of others, the tests are conducted with a variation in only one parameter for each run. The estimation performance for time-varying variations of each parameter be seen in fig. D.16 and D.17. These figures will show the performance if the possible fault occurring is only affecting one parameter.

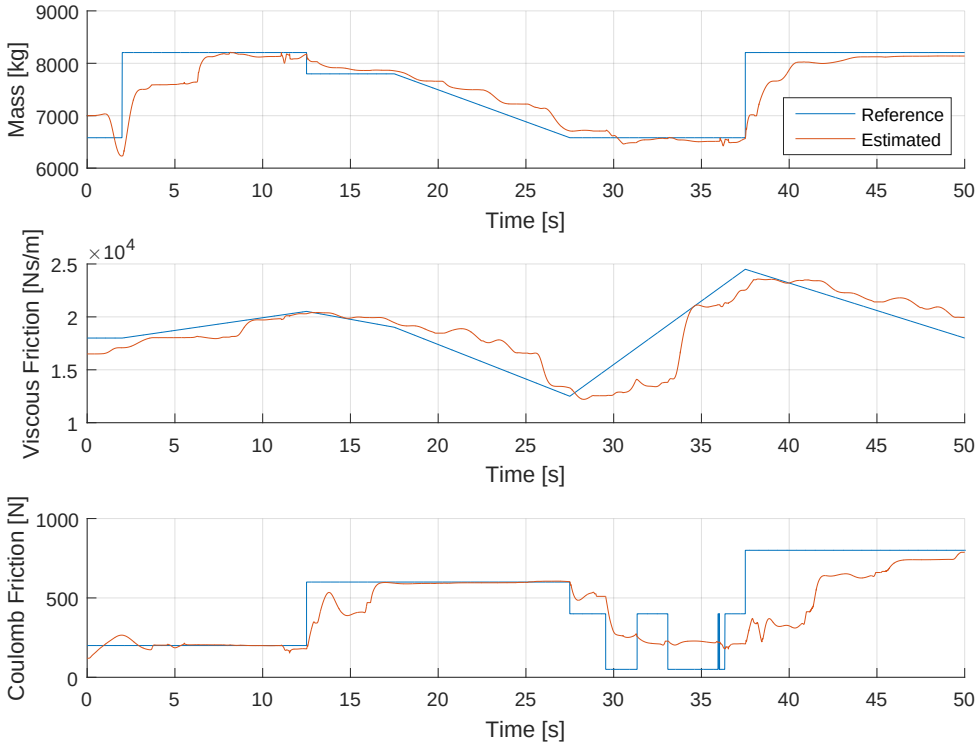

Figure D.16: Parameter estimation of mass, viscous friction and Coulomb friction

The mass estimation in fig. D.16 shows that the estimation algorithm is able to follow the variations emulated, with a 2-5 seconds delay for a step variation. It should be noted that the movement trajectory used is the same as for the estimation optimisation, meaning there are time periods with low or no accelerations. Without any acceleration, the estimation algorithm may have difficulties estimating. An example is at time 4 seconds, the reference acceleration is zero for 0.5 seconds, possible resulting in the mass estimation stopping to converge.
For the viscous friction, similar conditions apply, with the estimation algorithm being able to follow the reference, with some issues at ≈27-34 seconds, which is a period in time where a low

reference velocity occurring, possible being the reason.
The Coulomb friction has some difficulties, however, it follow the tendencies.
The last uncertain parameter D_{1n} is not shown, due to the reference being zero.

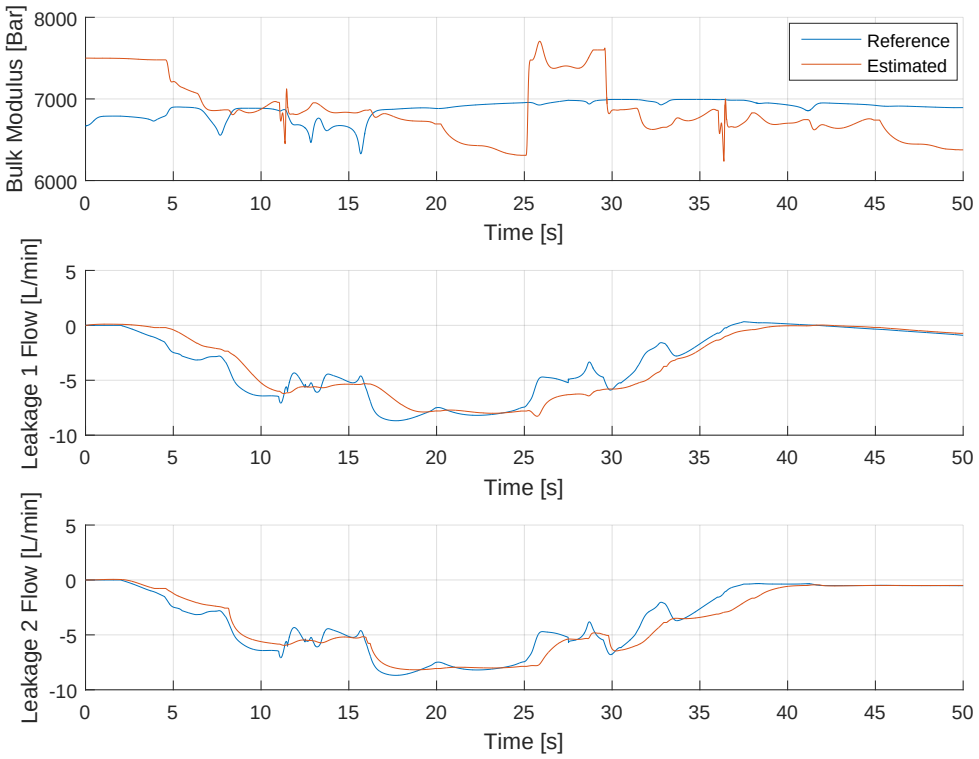

Figure D.17: Parameter estimation of bulk modulus, leakage flow 1 and leakage flow 2

The bulk modulus estimation in D.16 shows that the algorithm has some difficulties estimating the reference value, while still being somewhat close to the reference value. A possible explanation to the difficulties is the low pass filter applied on the pressure measurements to allow an approximation of the pressure dynamics removing the high frequency variations. However, if the cut off frequency in the filter is increased too much, problems regarding noise can appear.
The leakage flows follows the reference quite well with a small delay or offset.

A simulation where all parameters are varied as is the case for the fault trajectory used during determining the estimation parameters is shown in fig. D.18 and D.19.

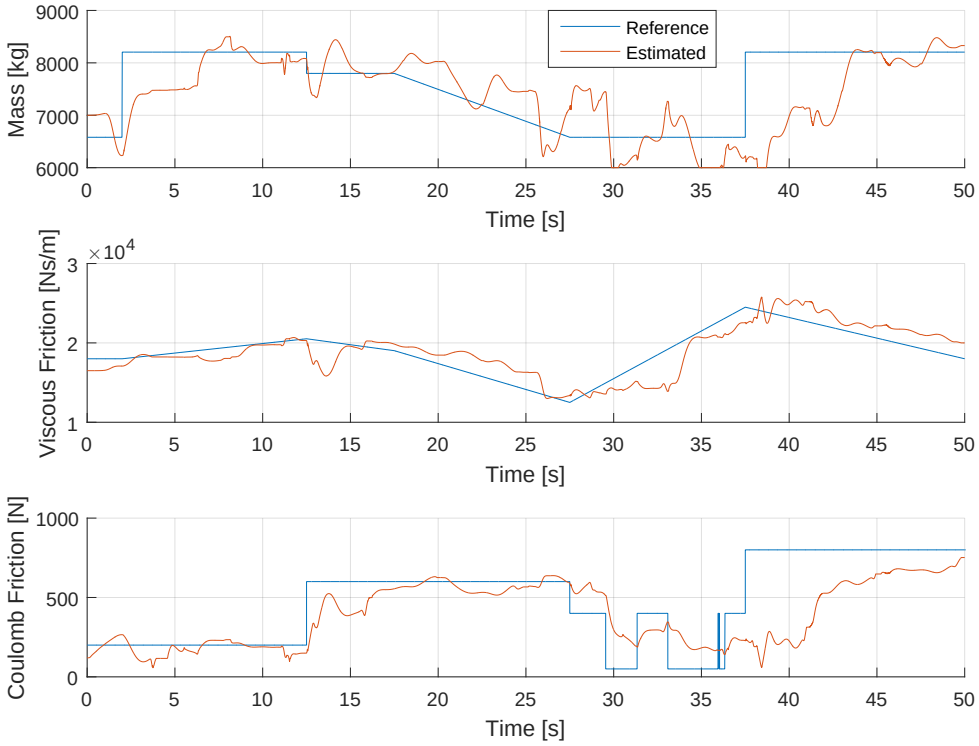

Figure D.18: Parameter estimation of mass, viscous friction and Coulomb friction

Similar tendencies in the estimation is obtained in fig. D.18 to what was observed when each parameter was varied individually. The main difference is the mass estimation having some problems, indicating its the most affected by variations in other parameters.

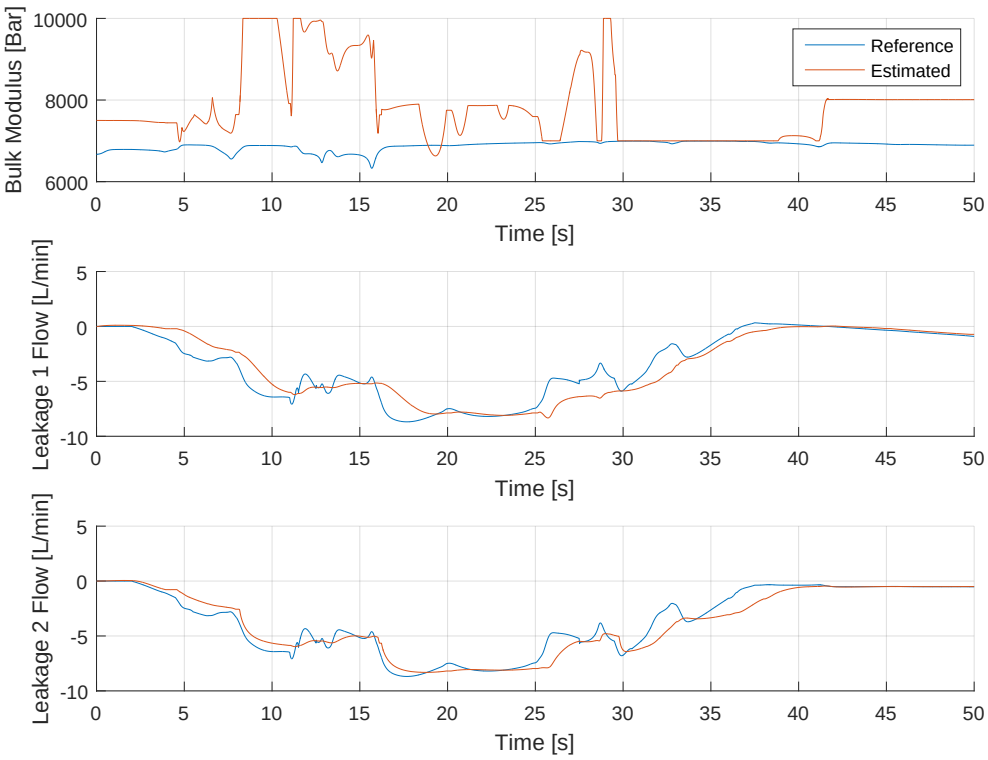

Figure D.19: Parameter estimation of bulk modulus, leakage flow 1 and leakage flow 2

In fig. D.19, the leakage flows are barely affected by the other parameter variations, obtaining almost identical results to what was found when only the leakage flow was varied. The bulk modulus is effected heavily. A reason may be the leakage flow variations, causing pressure differences affecting the bulk modulus.

APPENDIX E

IMPLEMENTATION

In order to apply the IARC controller on the friction testbench provided by AAU, several steps have to be taken. A Real Time (RT) system has been established E.1. The RT computer will conduct the calculations required by the controller. A laptop with LabView will be used to interact with the RT system. It will provide user access to control gains, trajectory selection and will allow the states of the system to be monitored. The control law and estimation algorithm have to be discretized to difference equations, which can be implemented in the RT system shown in sec. E.2. A number of fittings have been increased in size in order to replace one of the cylinders with a larger one.

E.1 Labview RealTime

This implementation is based on a Labview Real-Time(RT) sample project. The sample project provides a framework for easier implementation of a RT controller. In depth understanding of the full code is not the focus of this project, which is why only a general explanation will be provided here. The virtual instrument in which the controller has been implemented will be explained more thoroughly in sec. E.1.2. The general explanation can be seen below.

E.1.1 Broad View

The program consists of eight parallel loops. These loops are executed on two targets. One being the RT PC and the other-a laptop through which the commands will be sent. The loops which get executed on the laptop are

- Event Handling Loop
- Message Loop
- Monitoring Display Loop

The event handling loop produces messages based on the events in the main user interface(UI). These events consist of start/stop commands, changes in controller gains, trajectory loading and others.
These messages are then sent to the RT PC by the Message Loop.
The monitoring loop displays messages and data acquired from the RT loop. This information can consist of system health messages and system parameter values i.e. position measure-

ments, pressure measurements and so on. The Message Loop sends messages through the network streams. The network connection is achieved via an Ethernet cable and a switch. The monitoring loop executes at 100 Hz frequency, since it is of lower priority than the actual control loop. The loops which get executed on the RT desktop are

- Control Loop
- UI Command Handling Loop
- Message Handling Loop
- Watchdog Loop
- System Health Monitoring Loop

The Message Handling Loop receives and sends messages through the network connection. The user commands are received in this loop and rerouted to the UI Command Handling Loop. The UI Command Handling Loop then send the appropriate commands and values to the Control Loop.
The control loop is a while loop, which executes with a 1 kHz frequency. The loop is synchronised to execute at the same time as the scan engine. In this way the latest values are used in the control loop. The control loop is where the estimation algorithm, the IARC, and the force controller algorithm will be executed. The loop receives values from a EtherCAT slave chassis, when the scan engine reads the sensor measurements. Then based on these measurements the calculations of these three algorithms have to be executed within one millisecond. The outputs of the control loop are sent back to the EtherCAT slave chassis, which then converts them to analog voltage signals for the two MOOG valves, which control the flow in the system. The control loop is the main focus of this implementation so it will be examined in greater detail in sec. E.1.2.
Every time the control loop is executed it send a signal to the Watchdog loop. If this loop does not receive a signal in time, it assumes that a problem has occurred and stop all loops.
A graphic representation of the programs structure can be seen in fig. E.1

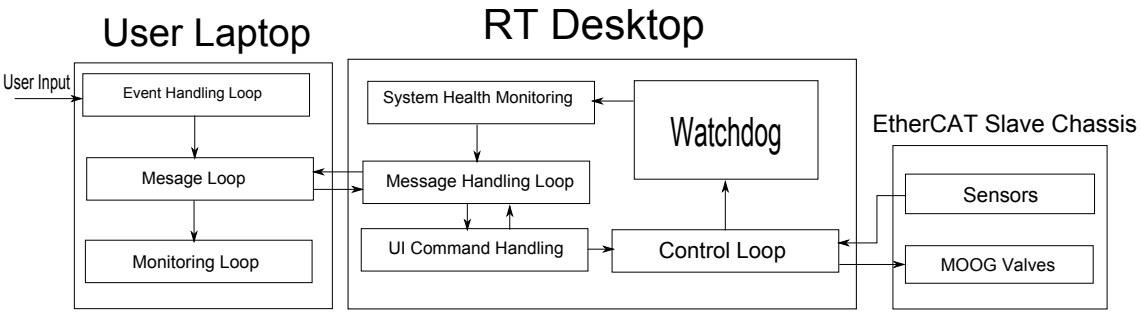

Figure E.1: Graphical representation of the RT project used for controller implementation.

Furthermore a RT lossless First-In First-Out (FIFO) buffer records all relevant information on the RT target. The content of the buffer is sent to the user laptop through the network. The buffer ensures that no information is lost when the faster RT loops sends information to slower loops running on the laptop. When the appropriate command is given through the UI, the content of the buffer is flushed through a TDSM virtual instrument, which writes it to a file. The data recorded in the file contains sensor measurements, system outputs, system health, loop variable and the exact time step at which this information has been recorded. The information from these log files will be the experimental results data used in this project.

E.1.2 Controller Loop

A schematic of the control loop can be seen in fig. E.2.

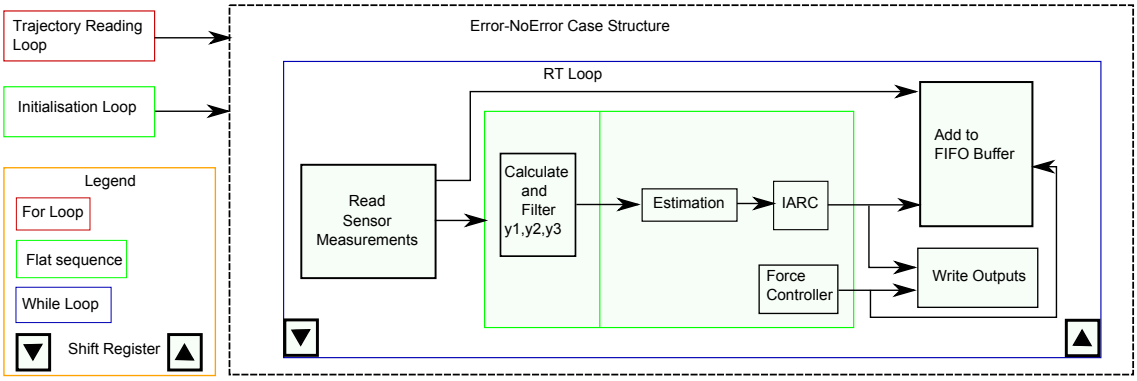

Figure E.2: Graphical representation of the Controller virtual instrument.

The Trajectory Reading For Loop reads the trajectory file from the hard drive of the RT PC once and converts it to an array. The trajectory contains both the trajectory for the IARC and the Force controller. In the program the data is defined as a cluster of data which is then connected to the controller VI's. The inclusion of all data connections between the VI's would make the figure difficult to read, which is why they have been omitted.
The Initialisation Flat Sequence structure is run once at the beginning of the program. It defines the width of the FIFO buffer, it configures the scan engine and defines the number of CPU that will be available for the computations.

The Error-No error Case Structure switches between two cases based on an input. If the structure receives an error message it stops the RT loop. It is not possible to exit the error case without the intervention of the user. This structure is an extra security feature. This error can be tripped by attempting to give out more output voltage than 10 V to the Moog valves, reading sensor measurements outside the user predefined range, inconsistencies during the initialisation sequence or finished late flags.

The RT loop, marked in blue, is synchronised to the scan engine thanks to the initialisation sequence. It is set to run at 1 kHz, so whenever the scan engine acquires new measurement values the control structure is executed and a new output is given. Once the Read Measurements VI has read, filtered and transformed the sensor measurement to the correct engineering units it sends them to the flat sequence in which the estimation and control are executed. This flat sequence structure contains VI's with the algorithms explained in sec. 7.1. The calculation in conducted in Labview's formula nodes. To reduce computational time no mathematical functions are called. For this reason matrix multiplications have been implemented by manually multiplying and adding the appropriate elements. It was decided to test if the discrete implementation was valid, before it was tested on the set-up. To do this the resulting code ,which is similar in syntax to Matlab's, is copied into an estimation and controller Simulink functions. These are set to execute at 1 kHz intervals. The comparison between the continuous and discrete implementation of the algorithms shows nearly identical results. From these result it is concluded that the discrete implementation is valid and the laboratory results should agree with the simulation results in chap. 11. After the flat sequence is executed and both controller have calculated appropriate valve openings, the control signals

are sent to the EtherCat slave chassis to be converted to an analog voltage signal for the Moog valves.

The RT FIFO buffer records the control values, the measurements on which the values were calculated, system health information and the time step at which these have been recorded. Through a UI command this buffer can be emptied into a data file. The width of the buffer is selected in the initialisation sequence. This defines how many variables can be recorded at each time instant. This has been set to 90. Each group of 10 variables has been selected to record a different group of signals i.e. group 0-10 contains system information, while group 80-89 contains the estimation vector. This allows for easier reading of the data.

The difference equations in the control VI's require values from the previous iteration of the while loop. Shift registers act similar to Matlabs zero-order hold blocks. The signals whose previous values are required are sent to these shift registers. The force controller requires values from more than one iteration ago, so some signals are held for several iterations. Specific signal connections have not been shown in the figure to preserve the readability of the figure.

This concludes the explanation of the implementation. The code can be seen in the attached files.

E.2 Discretisation of force controller and filters

Force controller

To implement the designed controller in LabView, a discrete form of the continuous controller is required. In Matlab Different methods are available for discretisation of continuous equations. The Tustin method is suited for applications where "You want good matching in the frequency domain between the continuous- and discrete-time models". Based on the descriptions, the Tustin method is chosen, due to it being desired to achieve a good matching in the frequency domain.

The continuous load controller that is to be discritised is:

$$G_{force}(s) = \frac{2.195 \cdot 10^{-7} \cdot s^2 + 6.551 \cdot 10^{-5} s + 0.004889}{2.25 \cdot 10^{-8} \cdot s^3 + 0.0003 \cdot s^2 + s} \tag{E.1}$$

To discretise, the Matlab function $c2d$ is used, which discretises the continuous controller using a chosen method with a user defined sampling time. For the real-time pc used on the set-up, a 1 kHz sampling time will be used, which will also be used here. The result of the discretisation is:

$$G_{force}(z) = \frac{8.072 \cdot 10^{-5} \cdot z^2 - 8.779 \cdot 10^{-5} \cdot z + 1.195 \cdot 10^{-5}}{z^3 - 1.003 \cdot z^2 + 0.002547 \cdot z - 1.62 \cdot 10^{-6}} \tag{E.2}$$

To verify that the discretisation is working as intended and the sampling frequency is sufficient, a comparison of a step response to the two controllers on the system is made. The result can be seen in fig E.3

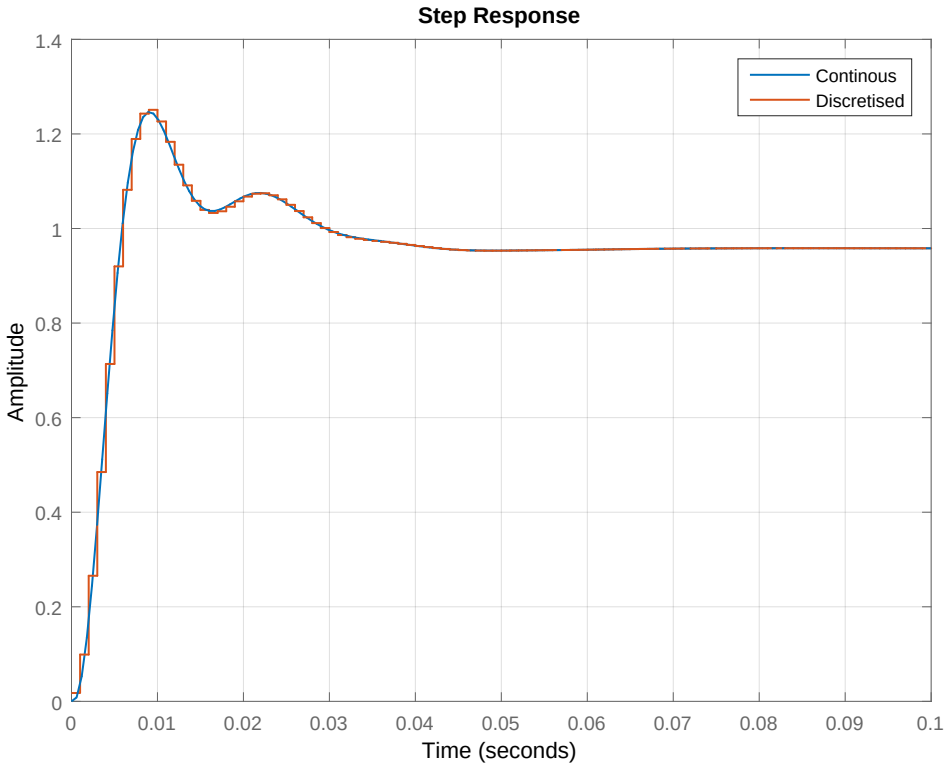

Figure E.3: Comparison of continuous and discrete step response.

From fig. E.3, the discretisation has little effect. The discrete version follows the continuous step response, and converges to the same value. From this, a sampling frequency of 1 kHz is found acceptable for the force controller, and the Matlab function is working as desired. The controller has to be converted to a difference equation in order to be implemented in NI's Labview. This can be done in the following manner

$$Output(z) = G_{force}(z) \cdot E(z) \tag{E.3}$$

$$Output(z) = \frac{8.072 \cdot 10^{-5} \cdot z^2 - 8.779 \cdot 10^{-5} \cdot z + 1.195 \cdot 10^{-5}}{z^3 - 1.003 \cdot z^2 + 0.002547 \cdot z - 1.62 \cdot 10^{-6}} E(z) \tag{E.4}$$

$$\begin{aligned} &\left(z^3 - 1.003 \cdot z^2 + 0.002547 \cdot z - 1.62 \cdot 10^{-6}\right) \cdot Output(z) \\ &= \left(8.072 \cdot 10^{-5} \cdot z^2 - 8.779 \cdot 10^{-5} \cdot z + 1.195 \cdot 10^{-5}\right) \cdot E(z) \end{aligned} \tag{E.5}$$

where E(z) denotes error in the z-domain. The following conversion can be implemented, where (k) corresponds to the current value, (k-1) corresponds to the previous iteration value and so forth.

$$\begin{aligned} &Output(k) - 1.003 \cdot Output(k-1) + 0.002547 \cdot Output(k-2) - 1.62 \cdot 10^{-6} \cdot Output(k-3) \\ &= 8.072 \cdot 10^{-5} \cdot E(k-1) - 8.779 \cdot 10^{-5} \cdot E(k-2) + 1.195 \cdot 10^{-5} \cdot E(k-3) \end{aligned} \tag{E.6}$$

Isolating for $Output(k)$ leads to

$$\begin{aligned} Output(k) =& 8.072 \cdot 10^{-5} \cdot E(k-1) - 8.779 \cdot 10^{-5} \cdot E(k-2) + 1.195 \cdot 10^{-5} \cdot E(k-3) + \\ &+ 1.003 \cdot Output(k-1) - 0.002547 \cdot Output(k-2) + 1.62 \cdot 10^{-6} \cdot Output(k-3) \end{aligned} \tag{E.7}$$

This is the force controller which has been implemented in NI's Labview.

Filters

The filter used in the estimation algorithm is a Butterworth filter. In LabView, the discretisation of a Butterworth filter can be done automatically, and no discretisation is therefore required.

E.2.1 Velocity Sensor Problem

The desired velocity sensor mentioned in Chap. 10 was ordered too late, and will not arrive until a few days before the end of this project. However, because the system is not required to move at high frequencies, the performance may still be satisfactory by estimating the velocity based on position measurements. Currently, a position sensor is applied on the load cylinder. This sensor has a noise level of ≈ 0.4 mm.

The noise levels of the position sensor have been verified by a test on the experimental set-up. The position was put in steady state. The standard deviation was found to be 0.33 mm, which validates the use of 0.4 mm in the simulation. Furthermore, the noise levels used for the pressure transducers and transmitters were verified to correspond to a standard deviation of 0.5-0.8 bar for the test cylinder, and 0.5-1.3 bar for the load cylinder. These levels agree with 0.75 for the test cylinder and 1.2 for the load cylinder.

To estimate the velocity, a time derivative of the position feedback is required. In order to obtain a somewhat smooth signal, further filtering is required. The filter applied on the position feedback is a second order filter, with cut-off frequencies at 15 and 5 Hz. A comparison between the simulated velocity, the simulation of velocity measured by a sensor, and the estimated velocity based on derivation of position is shown in fig. E.4, where the reference used is the pulse-like trajectory.

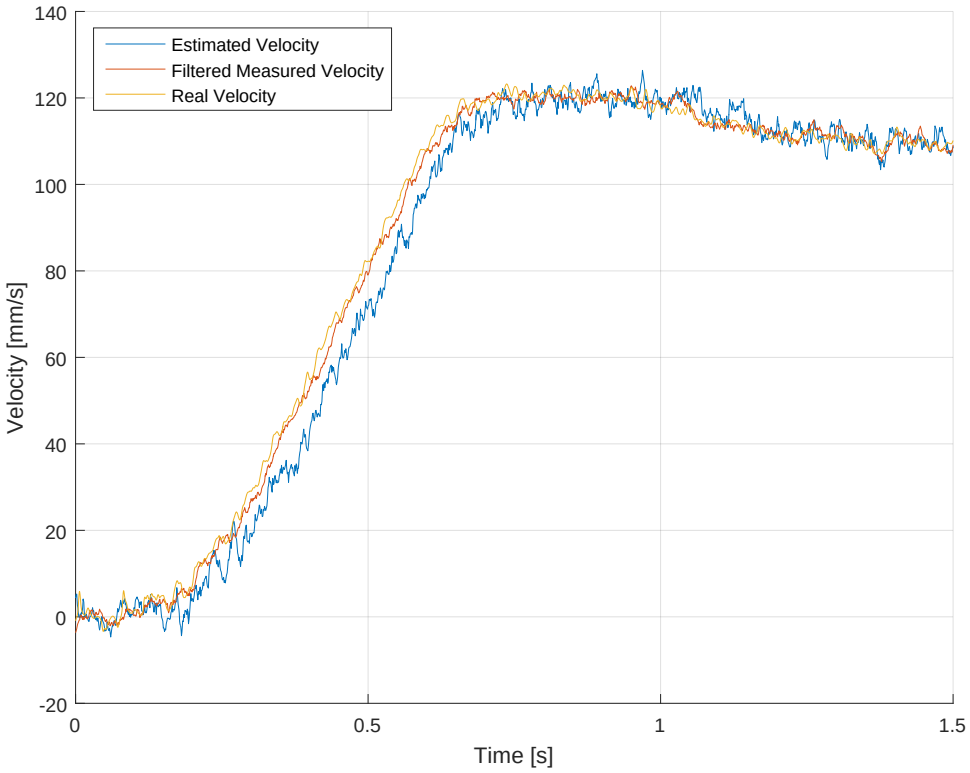

Figure E.4: Measured compared to Estimated Velocity

In fig. E.4, the estimated velocity has slightly more noise. The estimated velocity lags behind the other two signals, because of the extra filtering.

The system performance achieved by using the estimated velocity has been compared to the which would be achieved with a velocity sensor. It is found that the resulting position error depends on the frequency of the trajectory. For slower frequency references, the impact is less, because the velocity has lower frequency changes which can pass through the filter. Figures showing the system response to the pulse reference and sine curve reference regarding position errors are shown in fig. E.5 and E.6 respectively. No faults have been introduced during these tests.

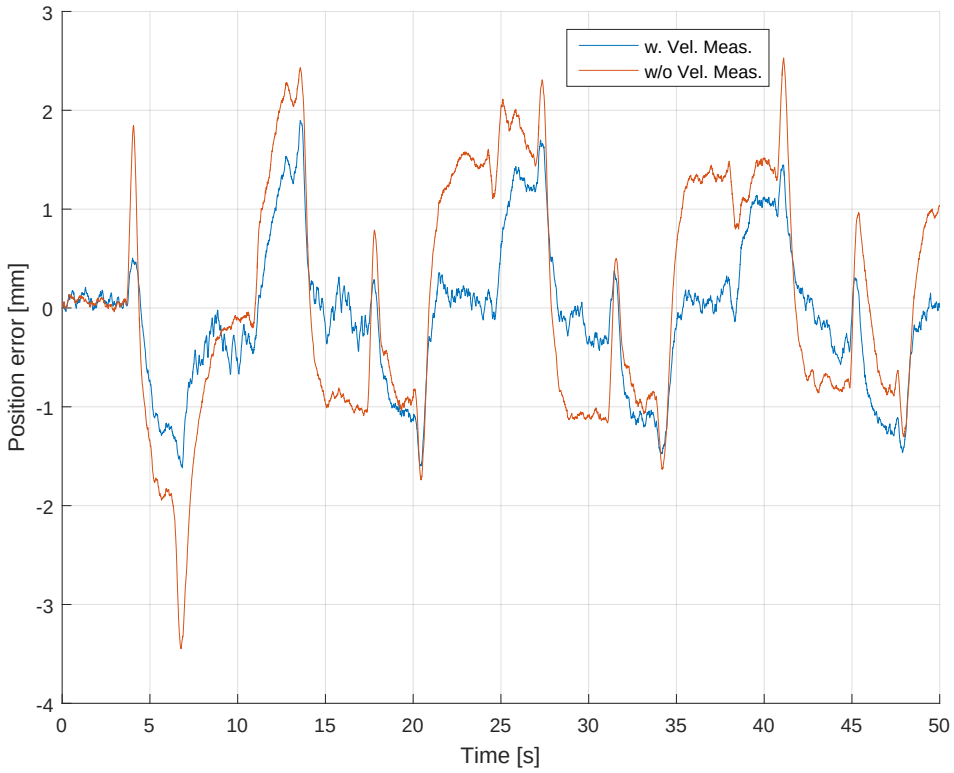

Figure E.5: Measured compared to Estimated Velocity

For the step response shown in fig. E.5, the increased delay introduced from the required estimation of velocity has reduced the performance for a nominal run. The response is however found to be sufficient for comparing nominal conditions and faulty conditions.

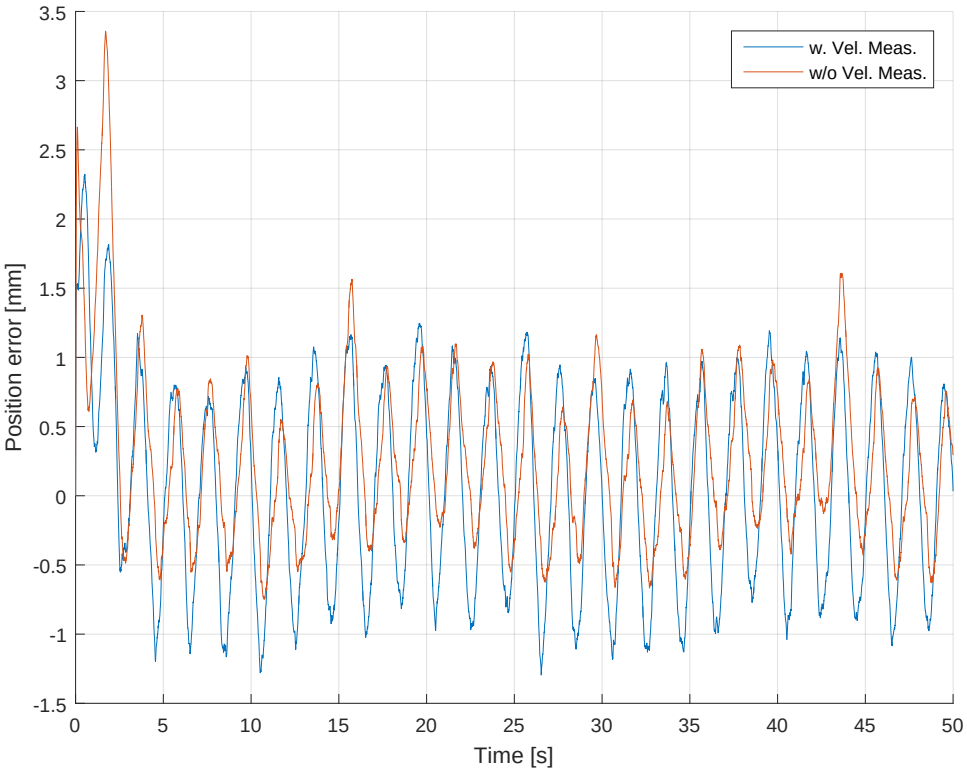

Figure E.6: Measured compared to Estimated Velocity

For the sine-curve reference with a frequency of 0.5 Hz, shown in fig. E.6, the performance is similar. The response without velocity measurement has a larger initial error. However, after 5 seconds similar or better performance compared to the response using velocity measurements can be observed.

Based on these simulations, satisfactory system performance can still be obtained without a dedicated velocity sensor. Depending on the frequency of the trajectory an increase in position error can be expected. The system is still stable, and the IARC can be tested on the set-up.

APPENDIX F

SUPPLEMENTARY SIMULATION RESULT

F.1 System Response without Measurement Filters

To determine the effect of noise, a simulation with the noise levels from the datasheet explained in the Chap. 10 is made. Fig. F.1 shows the system performance compared to the reference, and fig. F.2 shows the pressure forces from each chamber. The plotted values are the simulated system values, ergo the chatter in the figures is not noise, but real parameter chatter.

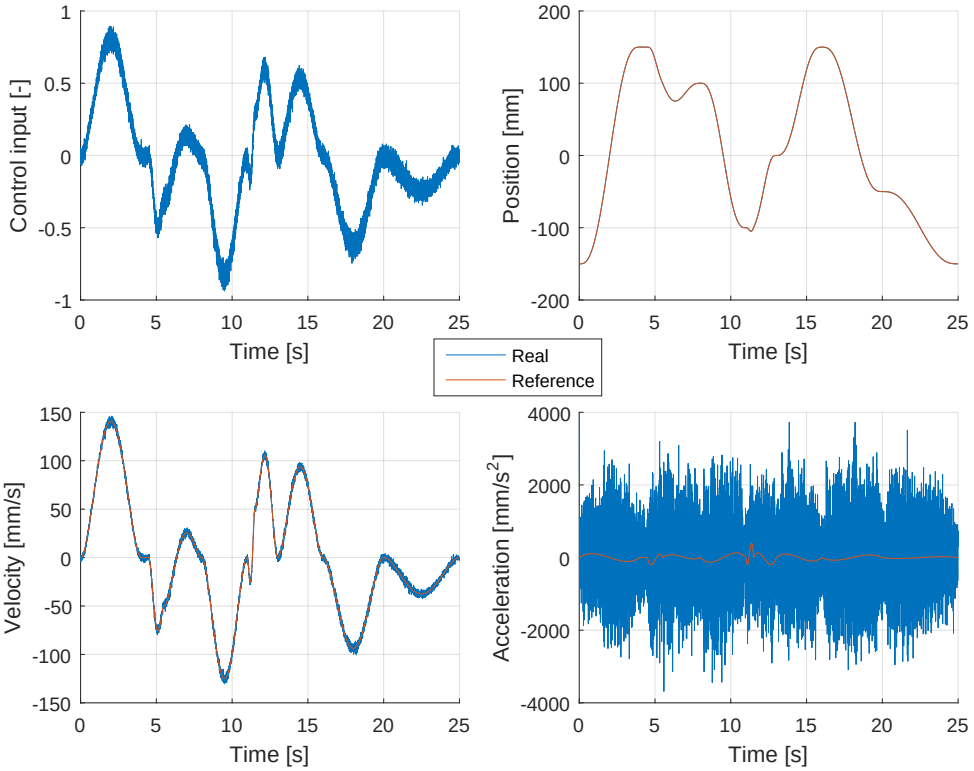

Figure F.1: System performance with simulated noise in the feedback signals.

Fig. F.1 shows that position is barely affected by the noise levels. The velocity has some

fluctuations. The acceleration is fluctuating heavily. This could be the result of both the IARC and the force controller being sensitive to noise or possibly amplifying each others problems. Based on these observations, the IARC is assumed to be sensitive to noise. This could be expected due to the control structure consisting of feedforwards and proportional controllers, which sees the full effect of the noise.

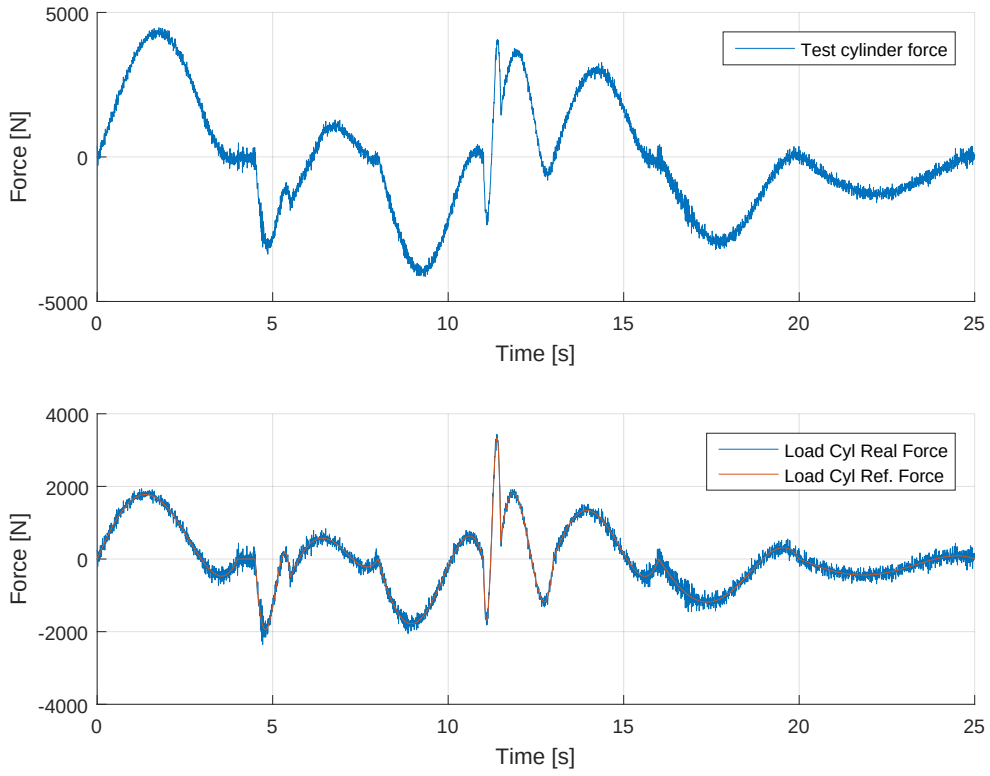

Figure F.2: System performance with noisy measurements.

In fig. F.2 the force from both cylinders is influenced by the noisy signal, resulting in chattering of ≈ 300 N.

F.1.1 System Response with Measurement Filters

The result from the previous subsection are considered unsatisfactory. In order to attempt to reduce the amount of control chatter, the measurement of the system have been filtered with first order low pass filters. For the IARC measured inputs, a cut-off frequency of 15 Hz is used. A low cut-off frequency is chosen to reduce the chattering significantly, which is found desirable. For the force controller, a cut-off frequency of 400 rad/s has been tested. The reason for the relative high cut-off frequency of 400 rad/s is the aggressive control design, which may give stability problems if a lower frequency is chosen. The force controllers lead filter delays the natural 180 deg crossover of the system. This crossover would occur at 40 rad/s but is delayed to 941 rad/s as can be seen in app. B, fig. B.5. Since a filter would affect the phase of the system a decade before its cut-off frequency, any filters with a cut-off frequency below 400 rad/s can potentially cause instability. The system response can be seen in fig. F.3 and fig. F.4.

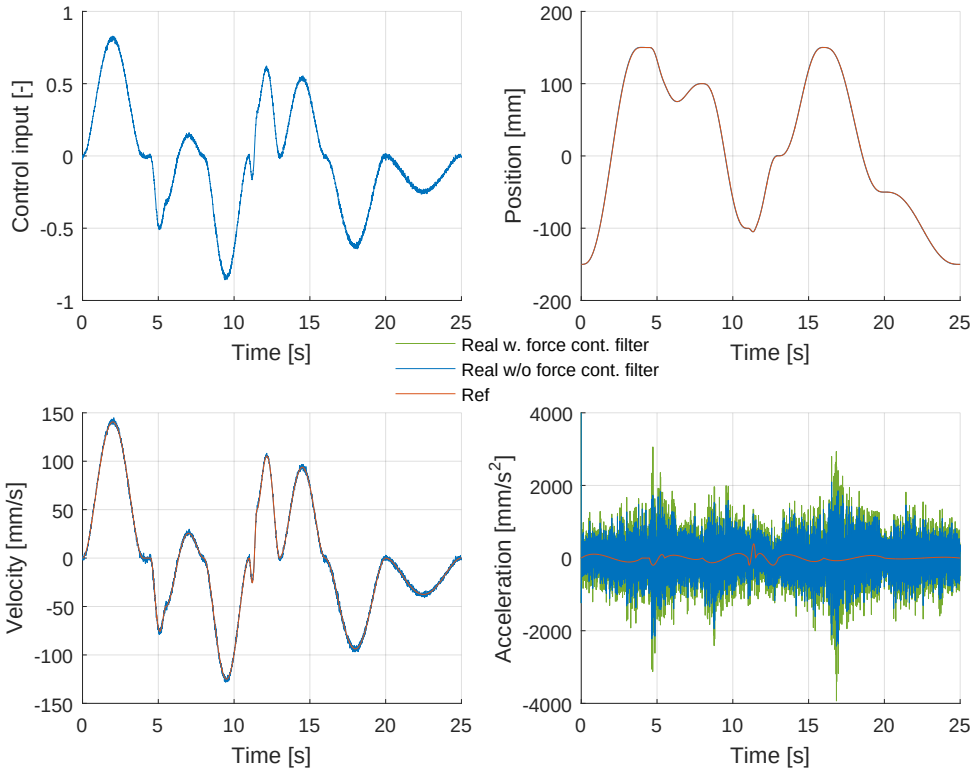

Figure F.3: System performance with filtered noisy measurements.

In fig. F.3 the chattering in the system response has been significantly reduced, when considering the control input, and velocity response. For the acceleration, it was found that the use of a filter on the force controller did not improve the system response. In fig. F.3 it can be seen that for the acceleration, an increase in error was obtained. It is assumed that the high cut-off frequency of the filter does not reduce noise as intended, but the introduced delay in the response of the controller has a negative impact on the performance. Based on this, filtering the input to the force controller may need to be reconsidered. Before a choice is made, the force output from each cylinder is investigated.

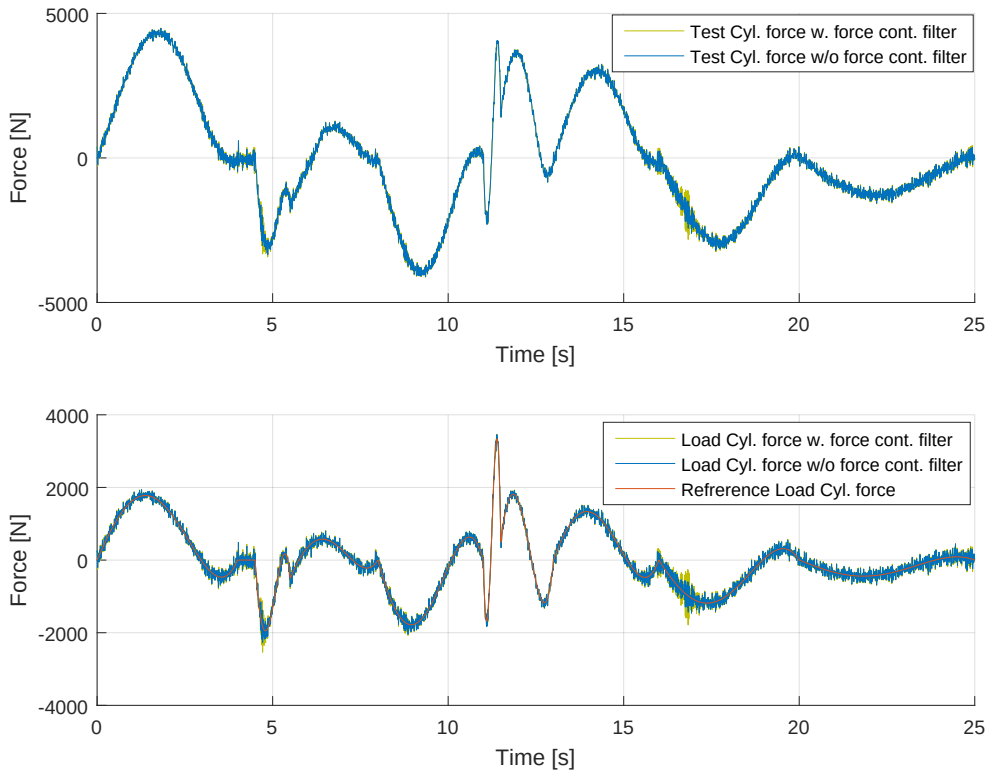

Figure F.4: System performance with filtered noisy measurements.

Similar to the acceleration, the introduction of a filter of the measured pressures used in the force controller has not improved the response in the form of a reduced chattering. Based on these results, it is chosen not to filter the force controller input. Before a choice is made on the IARC inputs, a higher frequency test is made.

F.1.2 Influence of Filtering on Performance for Higher Frequency Trajectories

The low cut-off frequency of the filters has shown itself to be beneficial in the previous tests, but it can introduce problems if the system has to follow higher frequency trajectories. An FFT has shown that the previous trajectory contains frequencies under 4 Hz. This is why the 15 Hz cut-off frequency has not interfered with the trajectory following. A test where a large sine wave with a 0.5 Hz frequency is combined with smaller but faster sine waves to produce a velocity trajectory. The response can be seen in fig F.5. The 5 Hz sine wave is replaced with a 10 Hz sine at time 2 seconds.

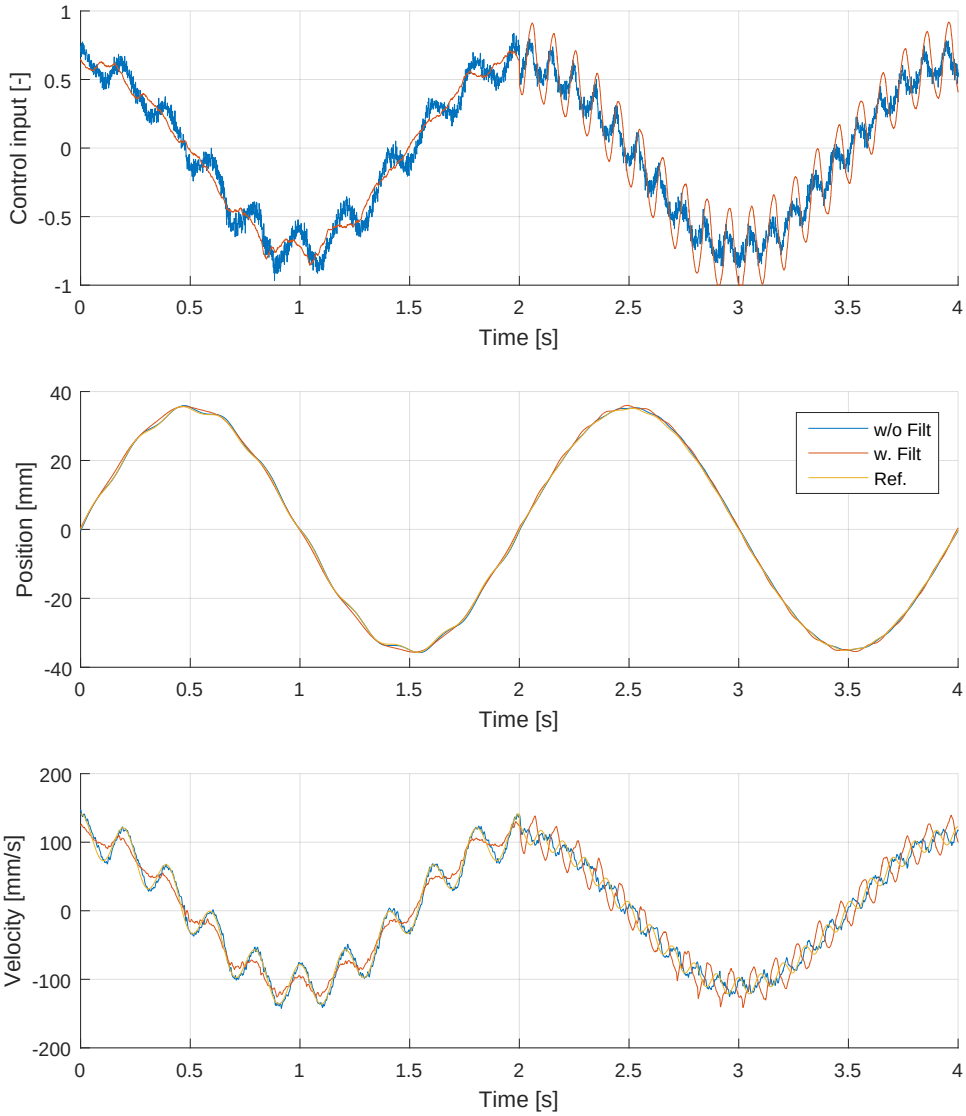

Figure F.5: Higher frequency test of 5 Hz initially and 10 Hz after 2 seconds.

In fig. F.5, the system response without any filter applied is able to follow the velocity reference for both cases with minimal error. The response with filter has some issues, due to the low cut-off frequency of the low pass filter applied to the measurements. This is one of the consequences of applying a somewhat heavy filtering of the measurement inputs. However, looking at the control inputs from the IARC, the filtered response has significantly reduced chatter, resulting in a smooth signal compared to the non-filtered. It is desired to have a smooth control signal, because chatter increases the rate of wear of the valve. Furthermore it can lead to pressure oscillations.

If this controller is to be applied on a wind-turbine pitch like system, it is not expected to require a trajectory at frequencies 0.40-1.75 Hz [Vidal et al., 2015] [Leithead et al., 1999]. The test however, shows that if the chattering is not an issue, or improved sensors and/or better

force control response is obtained, then a higher frequency trajectory can also be followed. Based on these findings, it is decided to use the filtered measurements for further analysis, due to it not being desired to have chattering.

F.1.3 Noise Influence on Estimation

To determine if the estimation algorithm is able to estimate the uncertain parameters under noisy conditions, the estimation of an initial mass error is shown in fig. F.6.

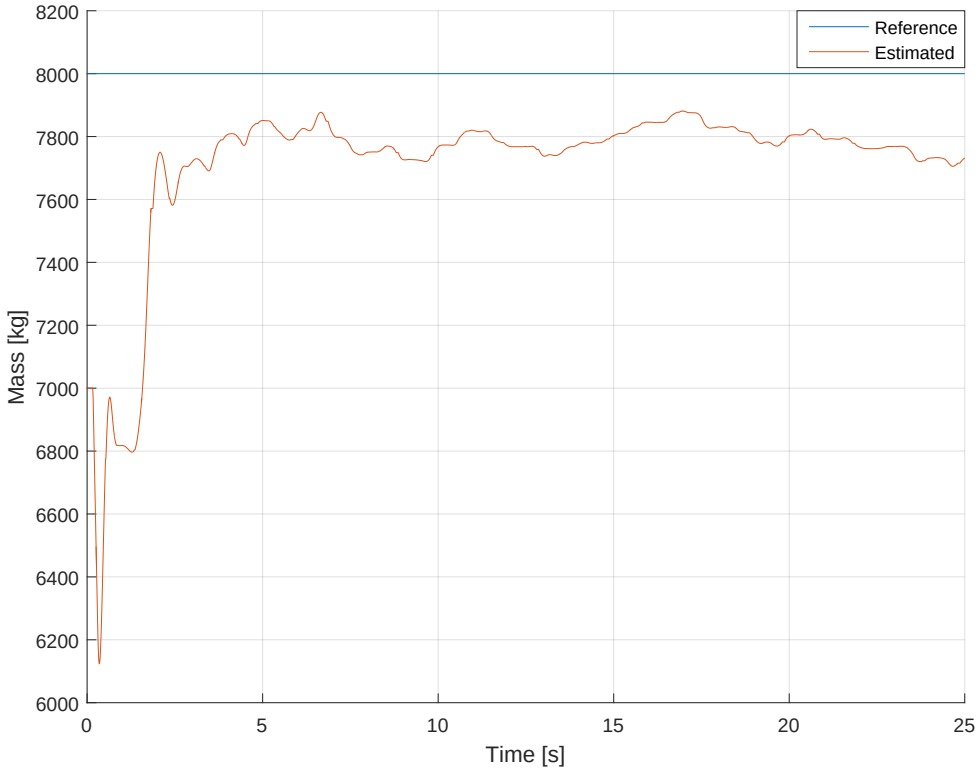

Figure F.6: Mass estimation comparison using a 0.5 Hz sine curve as reference trajectory.

In fig. F.6, the estimation has some initial issues, however, over time it is able to converge close to the correct value. Performance is not reduced compared with the noiseless simulations. This shows that the 3rd order filter applied is working as desired, filtering the noise while keeping the system dynamics.

Based on these results it is found that due to the influence from noise, a low pass filter with a 15 Hz cut-off frequency should be applied to the measured inputs of the IARC. With this filter the estimation is not affected, but the chatter of the IARC is reduced significantly. No filter will be applied to the force controller. Attempts to down-tune the force controller and either reduce its sensitivity to noise or allow a filter to be applied have not worked. All force controllers tuned with a lower bandwidth have shown stability issues when paired with the IARC.

F.2 Nominal Performance

Optimisation Trajectory

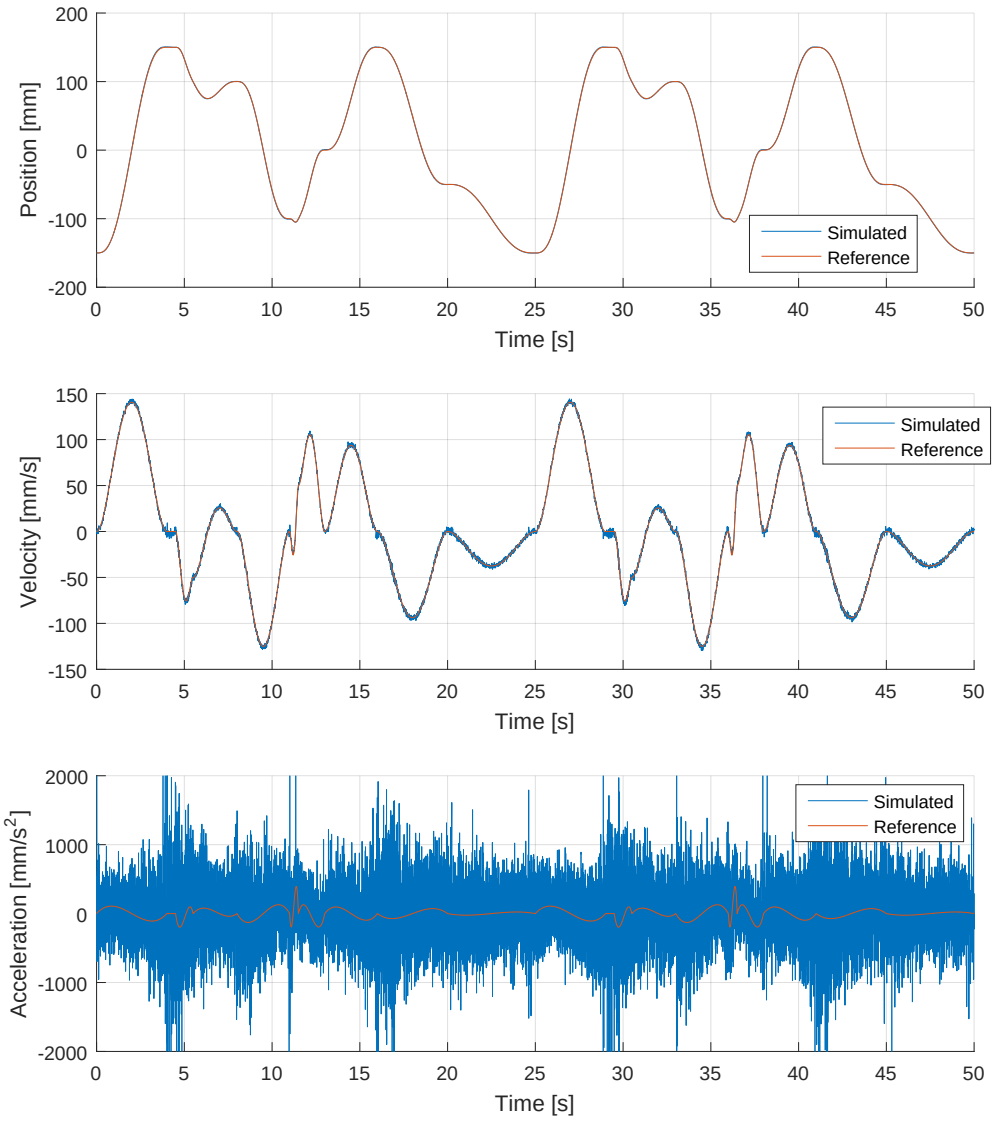

Figure F.7: Nominal performance for the trajectory used for optimisation.

The performance achieved with this trajectory during a nominal run can be seen in the table below

Parameter	Maximum error	RMS error
Position [mm]	1.3	0.64
Velocity [mm/s]	10	1.75

Table F.1: Trajectory following information for dynamic trajectory benchmark.

Pulse Trajectory

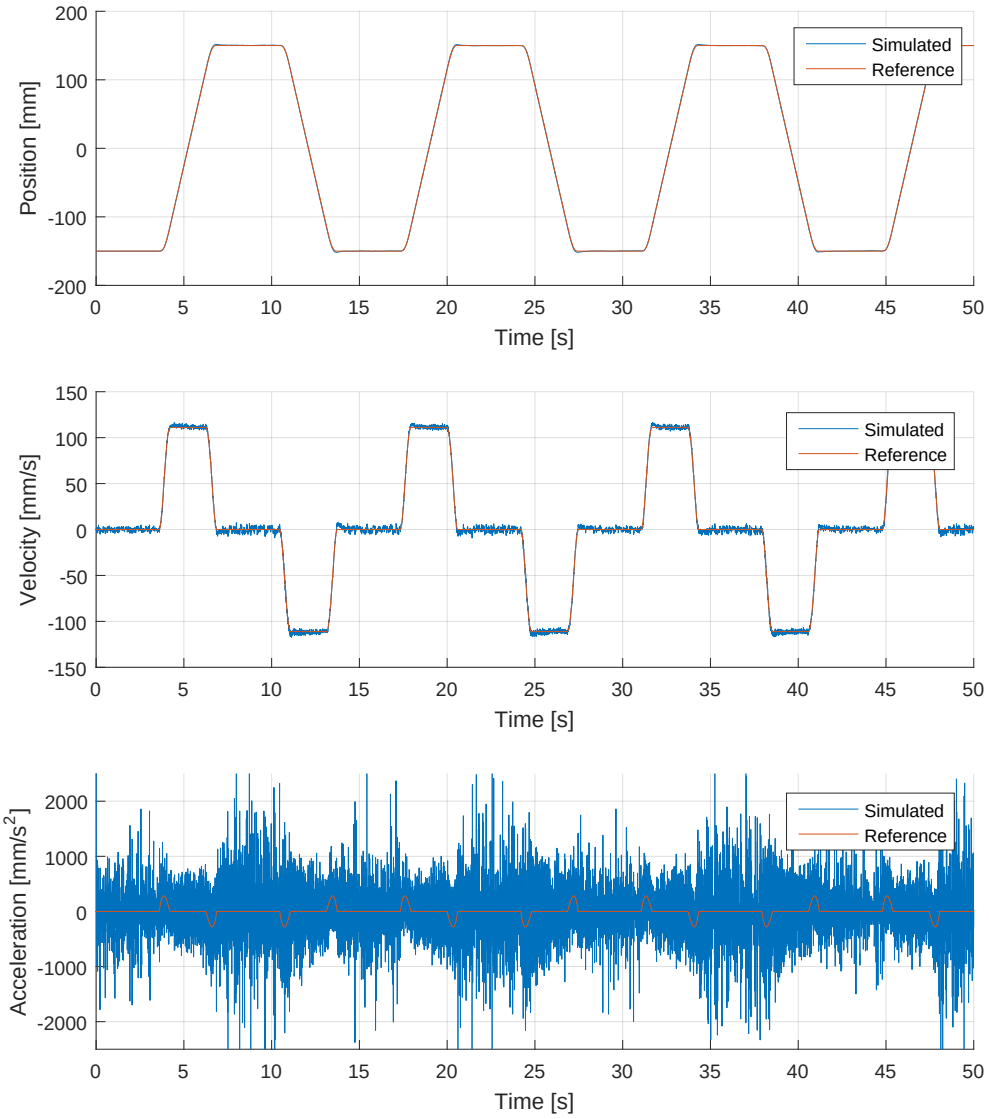

Figure F.8: Nominal performance for a pulse trajectory.

The performance achieved with this trajectory during a nominal run can be seen in the table below

Parameter	Maximum error	RMS error
Position [mm]	1.90	0.73
Velocity [mm/s]	9.27	1.88

Table F.2: Trajectory following information for Pulse-like trajectory benchmark.

Sine curve Trajectory

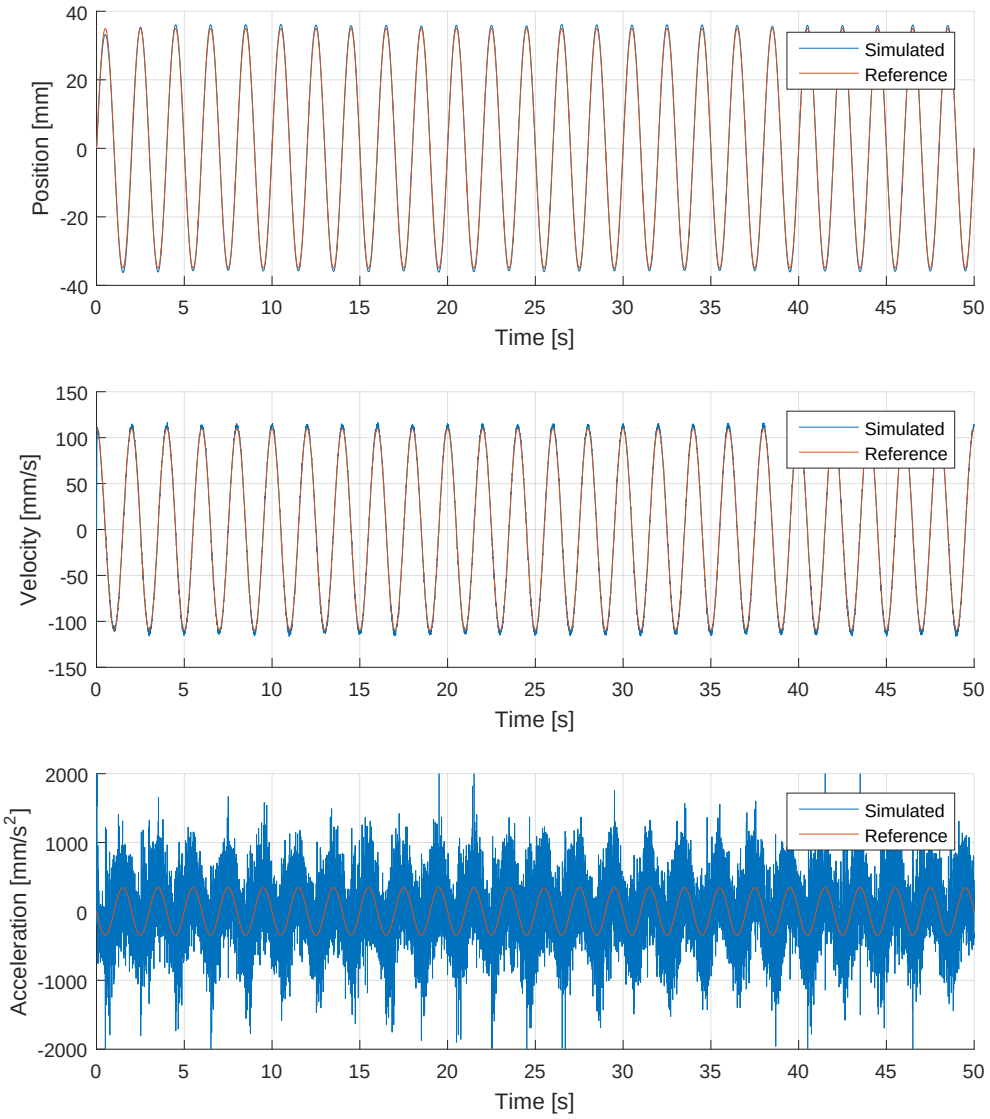

Figure F.9: Nominal performance for a sine curve trajectory.

The performance achieved with this trajectory during a nominal run can be seen in the table below

Parameter	Maximum error	RMS error
Position [mm]	1.96	0.70
Velocity [mm/s]	8.13	2.58

Table F.3: Trajectory following information for Sine-curve trajectory benchmark.

F.3 Pulse reference

Mass

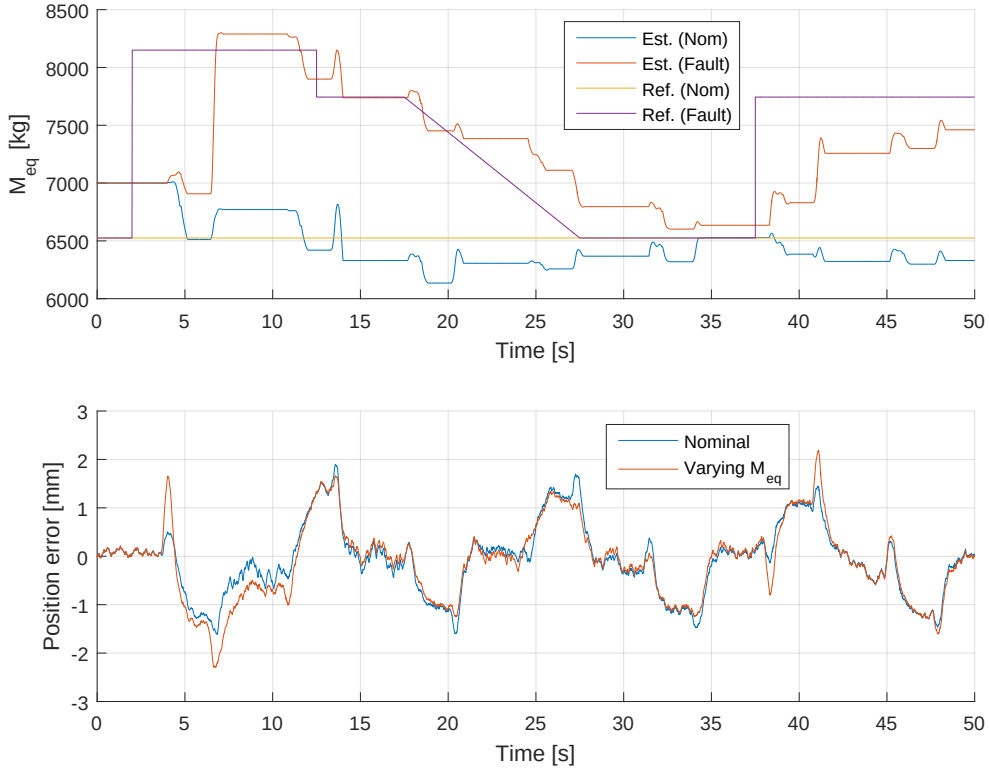

Figure F.10: Performance when affected by a step change in Mass.

The following performance is observed during a mass fault handling test

Error	e_{RMS} Nominal[mm]	e_{max} B[mm]	e_{RMS} B[mm]	e_{max} B[mm]
Position [mm]	0.73	1.90	0.79	2.19

Table F.4: Trajectory following information for Pulse-like trajectory and mass fault.

Viscous Friction

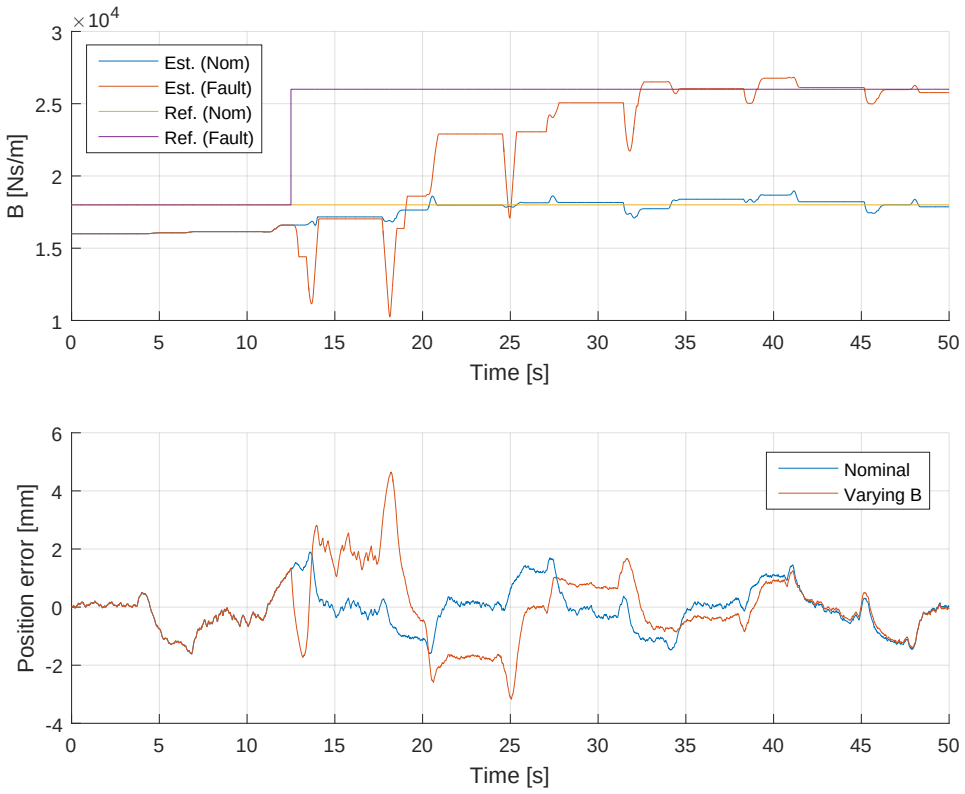

Figure F.11: Performance when affected by a step change in viscous friction.

The following performance is observed during a viscous friction fault handling test

Error	e_{RMS} Nominal[mm]	e_{max} B[mm]	e_{RMS} B[mm]	e_{max} B[mm]
Position [mm]	0.73	1.90	1.17	4.65

Table F.5: Trajectory following information for Pulse-like trajectory and viscous friction fault.

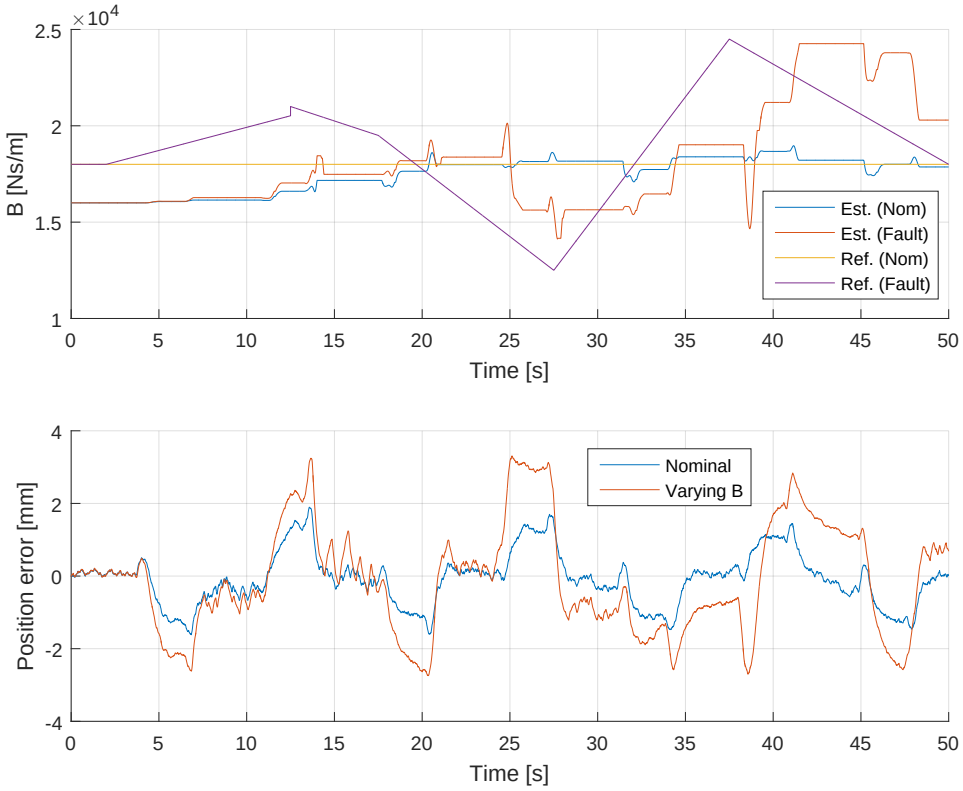

Figure F.12: Performance when affected by ramp changes in viscous friction.

The following performance is observed during a viscous friction fault handling test

Error	e_{RMS} Nominal[mm]	e_{max} B[mm]	e_{RMS} B[mm]	e_{max} B[mm]
Position [mm]	0.73	1.90	1.49	3.31

Table F.6: Trajectory following information for Pulse-like trajectory and viscous friction fault.

Coulomb Friction

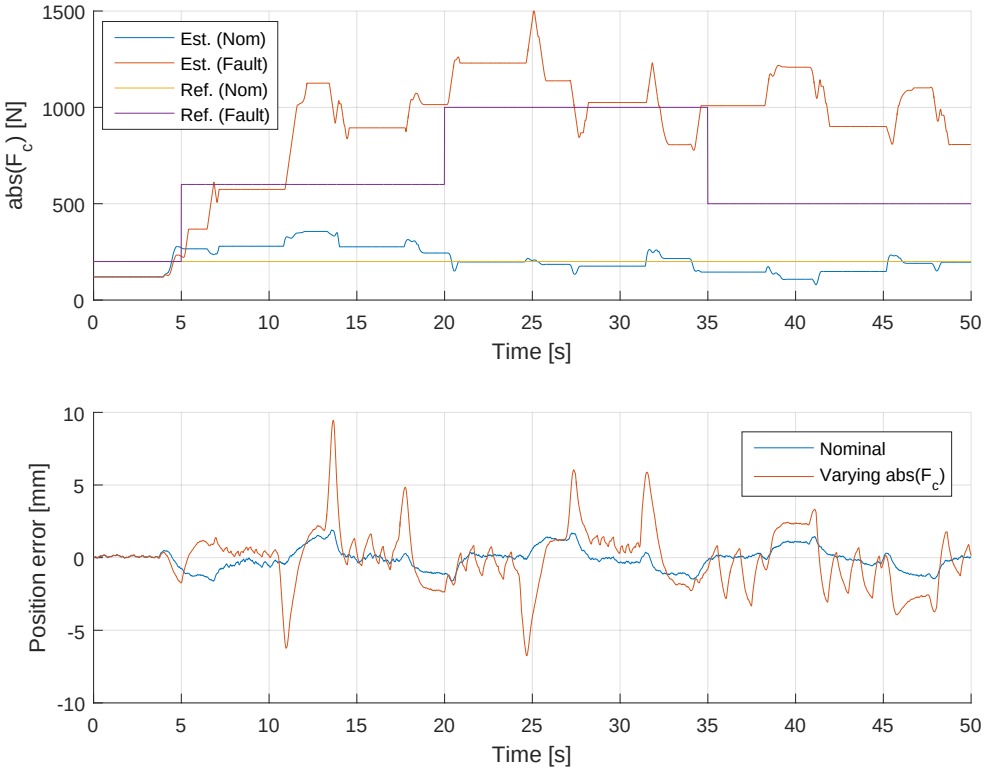

Figure F.13: Performance when affected by a varying Coulomb friction.

The following performance is observed during a Coulomb friction fault handling test

Error	e_{RMS} Nominal[mm]	e_{max} B[mm]	e_{RMS} B[mm]	e_{max} B[mm]
Position [mm]	0.73	1.90	2.04	9.45

Table F.7: Trajectory following information for Pulse-like trajectory and Coulomb friction fault.

Air-ratio

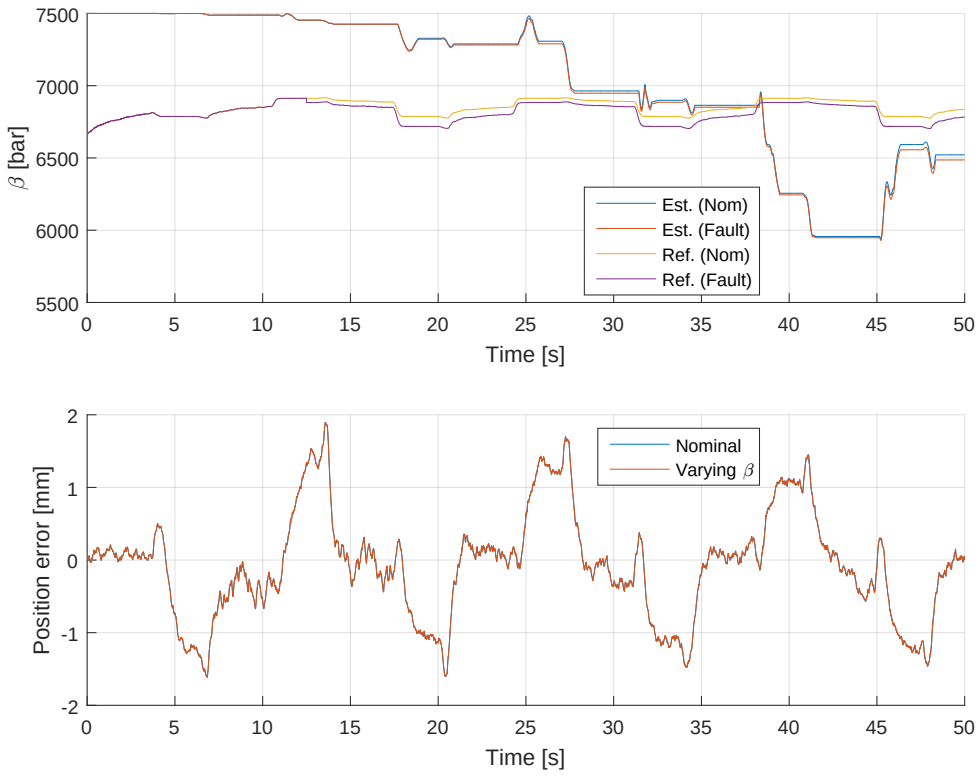

Figure F.14: Performance when affected by a varying air-ratio.

The following performance is observed during an Air-ratio fault handling test

Error	e_{RMS} Nominal[mm]	e_{max} B[mm]	e_{RMS} B[mm]	e_{max} B[mm]
Position [mm]	0.73	1.90	0.73	1.90

Table F.8: Trajectory following information for Pulse-like trajectory and Air-ratio friction fault.

APPENDIX G

SUPPLEMENTARY EXPERIMENTAL RESULTS

G.1 Pulse trajectory following with internal leakage

The position following of the IARC when an internal leakage of 6 L/min was introduced can be seen in fig. G.1. A small improvement can be seen after the estimation algorithm converges to the assumed leakage value.

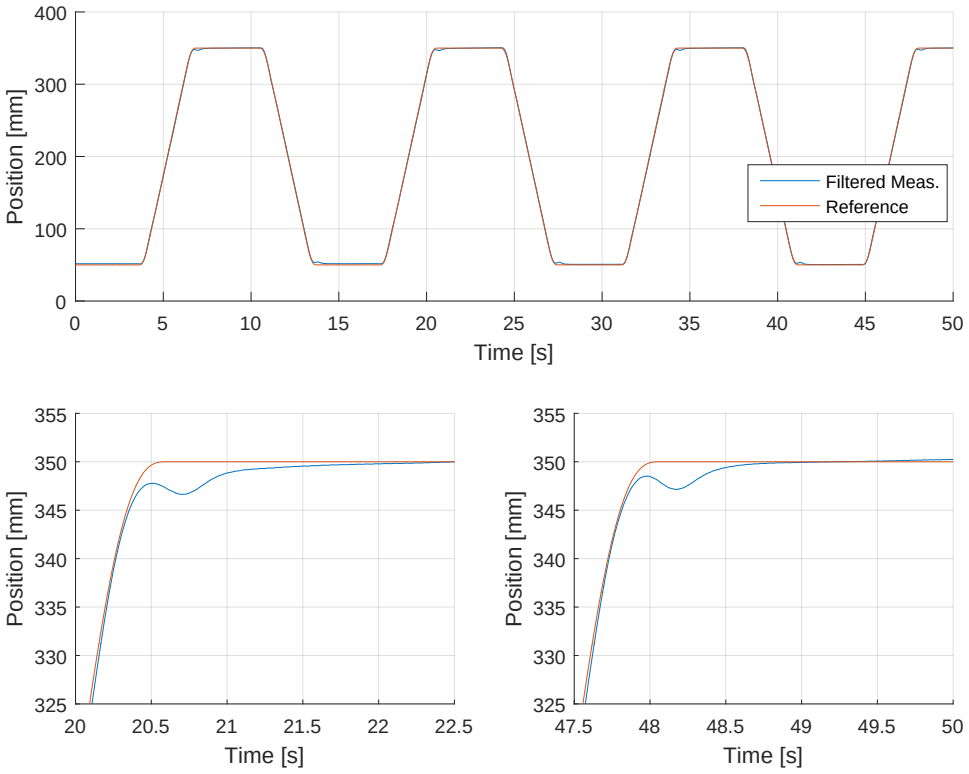

Figure G.1: Results with initial filters.

G.2 External Leakage Test

The result of the estimation algorithm during test for external leakage can be seen in fig. G.2. The external leakage was introduce by manually opening a needle valve from either one or both chambers to tank. The estimation algorithm had problems and an increase in leakage in one chamber appeared in both chamber estimations. Because the leakage introduced was comparatively small(0.5 L/min), the impact on position was minimal as can be seen in fig. G.3. Because the algorithm estimated leakages in both chambers the result from increasing chamber 2 external leakage had the same results

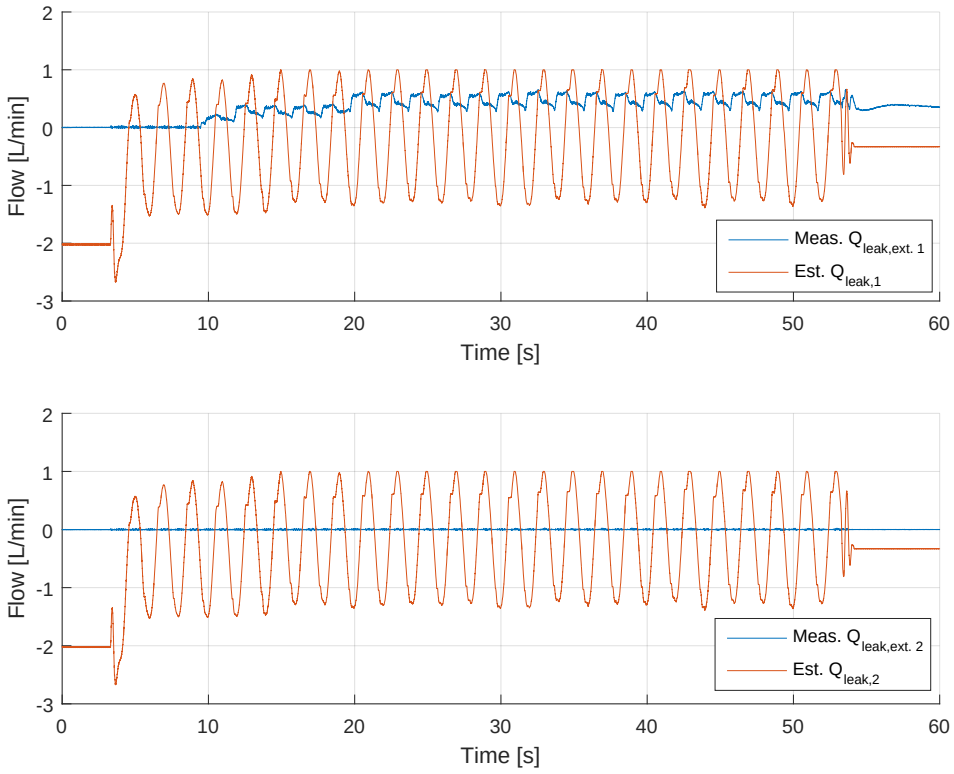

Figure G.2: Results with initial filters.

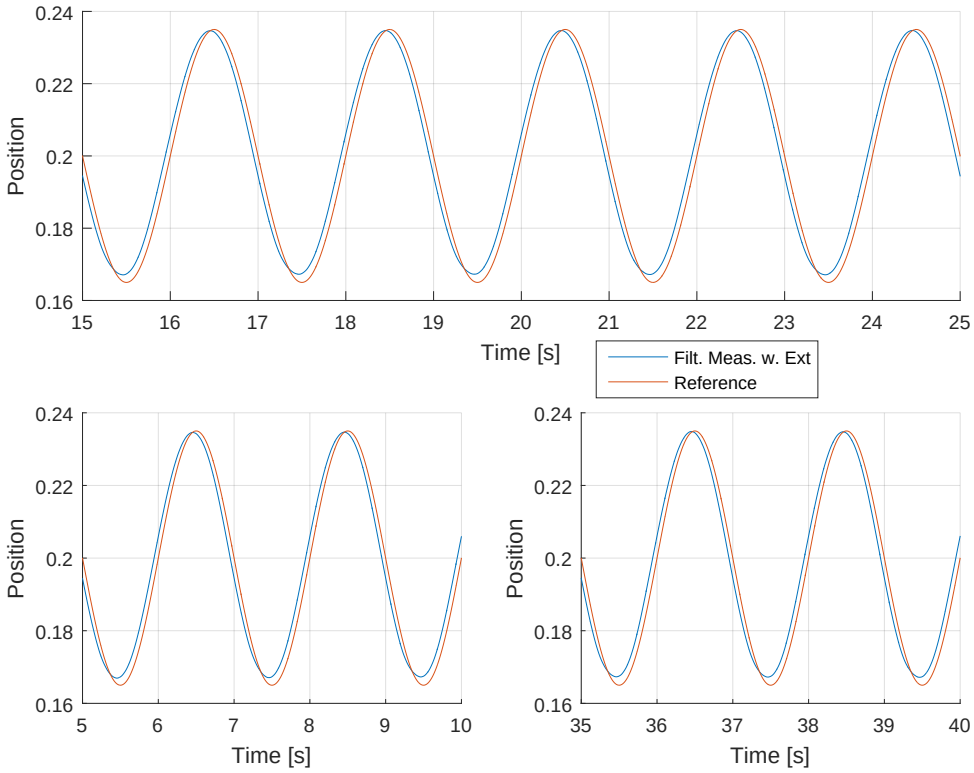

Figure G.3: Results with initial filters.

APPENDIX H

LITERATURE REVIEW

In this Appendix, an extension of the review of the methods and findings for the articles reviewed in Chap. 3 is made. A lot of the information from the report chapter is repeated. The main difference is the expanded information for articles that were found not relevant.

H_∞ control

A common design methodology for PFTC, is to use robust controllers in order to obtain stability and disturbance attenuation, both when the system operates normally and when faults occur. As discussed in the introduction chapter, passive FTC methods do not change the control structure or controller parameters when a fault occurs. Instead they are designed in a way, which is robust to faults, disturbances and modelling errors within certain bounds. H_∞ is but one of the methods that can be used to obtain robust control. It is used as an example of what can be achieved with such methods, because Linear Quadratic Regulators and other optimal control methods share many of the same limitations.

In [Veillette et al., 1992] it is shown that an H_∞ controller can be design to deal with either actuator or sensor faults. The design is possible provided the remaining non-faulted part of the system is able to stabilise the whole system. Furthermore the system is only robust towards the failures included in the design phase. No numerical examples are given in the article, since it is more theoretically focused, but the authors conclude that increase the robustness of the method also increase the H_∞ bound i.e. it reduces the performance of the system.

In the study [Zhou and Ren, 2001] a new architecture for the H_∞ design approach is found. A parametrisation for an Linear Time Invariant (LTI) system based on the sufficient condition for existence of stable H_∞ controller is determined. An internal model is included to determine if a fault has occurred by comparing measurement and internal model output data. A performance controller is designed for the optimal case, allowing a less conservative design. The performance of the controller is then augmented by a feedback from the internal model when faults or uncertainties are present. This feedback is designed to ensure stability. Since hydraulic system have inherent non-linearities and uncertainties in their parameters this robust modi-

fication of the control law would be constantly active. This means that the controller would always be operating under less than optimal conditions, thus degrading the performance of the system.

H_∞ has also been introduced as a method for AFTC. In [Huang et al., 2014], a H_∞ controller is applied, where a semi-Markov process is used in the system fault modelling. This system is able to accommodate for different types of faults, which includes sensor and actuator faults. The controller is recalculated based on the results of the semi-Markov modelling. The semi-Markov method is useful for modelling abrupt random changes in the system according to the article. The controller and system modelling was applied to a vertical take-off and landing vehicle, where an actuation fault of 50% was applied. Based on the tests, there were some improvements that the study would like to continue working on, which includes using a higher order feedback to potentially remove a steady state error, which occurred in the example. Furthermore, an improved control performance for systems with uncertainties is of interest. The study proved stochastic stability of the system, but no performance criteria is considered.

Quantitative Feedback Theory

The FTC method Quantitative Feedback Theory (QFT) has been used both as a passive and active FTC for hydraulic systems in studies from 2002-2010. Their findings are mentioned below:

The article [Niksefat and Sepehri, 2002] utilises QFT on a linearised electro hydraulic servo system. The faults considered were sensor failure, and servo-valve and supply pump faults. The faults were modelled as uncertainties for the control design. The proposed controller was tested experimentally on a electro hydraulic servo system, where the system was found robust to the sensor fault. One test included a completely failed sensor, while another considered a faulted sensor, which was delivering four times the actual position measurement, with an inclusion of random noise with an amplitude of 40 % of the actual measurement. The system was stable in both cases, but it could not correct the error in the first, while it was still able to reject the noise in the second. Actuator fault in the servo-valve (25 % change in output- tested as sensor reading four times the correct values) and the supply pressure (55-400 % of operating point, tested as drop from 103 bar to 41 bar) were also tested, the controller was able to compensate for the fault and achieve good responses. Another fault tested was a model uncertainty of 5% in piston effective area and 65 % in viscous damping coefficient.

The article [Karpenko and Sepehri, 2005] investigates the use of QFT for increasing leakage in actuator piston seals for a electro-hydraulic positioning system. For the control design, a linearised model of the system is required. The study proposes a way to remove the requirement of a fault detection from a previous study [Karpenko and Sepehri, 2003]. In the previous study, the increased leakage was corrected by use of multiple controllers, where each QFT controller was designed for a given range of leakage, which resulted in the requirement of fault detection to determine the level of leakage in the system. [Karpenko and Sepehri, 2005] establishes a fixed-gain linear time invariant FTC via QFT, which is able to maintain performance despite a degrading effect of fluid leakage across the actuator piston. The size of the fault considered

corresponded to a loss of 25 % effective area of the piston seal. The controller was however not compared to the one determined in the previous study, but to a nominal controller. Here the FTC QFT was found to be four times faster in response time, under the faulted conditions, while giving the same performance under nominal conditions. The drawback of the proposed controller is the need for a priori defined leakage range fault, and if chosen too small, the controller does not have the guaranteed performance.

The study [Karpenko and Sepehri, 2010] investigates an approach to reduce the over-design of QFT algorithms due to the linearisation. The proposed method is using a linear time invariant equivalent modelling approach, which captures the important properties of non-linear hydraulic actuator frequency responses. Two QFT control laws are proposed for different fluid power applications. The first controller uses a proportional structure and is well suited for applications with noisy sensors or highly dynamic reference commands. The second controller incorporates an integrator and is suited for applications where static errors due to un-modelled non-idealities are present. The controllers were tested on a hydraulic ram where different load springs (0-80 kN/m) were attached. The controllers were also tested with various parameter uncertainties, but no specific values have been mentioned. The proposed controller worked well for all tests, with the proportional having a slight overshoot and able to be within 5 % of the desired value and the integrator being more tight and having zero steady state error due to the integrating term.

QFT has also been proposed as a control strategy for aircraft, the studies are briefly described beneath:

The study [Keating et al., 1997] establishes a frequency domain based QFT robust control system design for aircraft. The design consists of a MISO longitudinal channel and a MIMO lateral direction channel. The faults under consideration were varying flight conditions and damage to aerodynamic control surfaces. The controller however is only able to be robust for up to 25% loss of elevator surface area. It was shown that reasonable aircraft control is maintained up to loss of 50% but tracking and stability specifications will no longer be met. The reason given is the large bandwidth of longitudinal channel sampling rate effect and sensor noise problems, not limitations of QFT.

The article [Wu et al., 1999] proposes to use QFT to design a controller for an aircraft due to it not requiring the use of gain scheduling and involves a simple low-order fixed controller. To use QFT, the control system is converted into a set of LTI MISO plants, that are controlled using QFT designed controller. The aircraft control surface loss is considered as a model uncertainty and can therefore be included in the QFT approach. For the simulations, a 50 % loss of elevator surface was tested, and the proposed controller resulted in a maximum deflection of 0.58 degree, which is better than the original controller, which had approximately 0.85 degree deflection. The proposed controller gives the designer a more versatile solution, where a trade-off between system performance specification and controller complexity can be made.

Based on these articles, QFT is found to be an useful tool for hydraulic systems, which is of

interest in this study, when linear or close to linear faults are considered in addition to the range of uncertainty and fault condition being known beforehand. The above articles provide proof that the method can deal with 50% loss of efficiency in actuators. The problem however occurs when more non-linear faults are included. The increased uncertainty bounds can result in a very conservative controller design, depending on the severity of the non-linearities. This should be taken into consideration when the choice of control algorithm is to be made. Furthermore, since the main plus of this method is the ability to provide robust performance without the addition of complicated schemes and strategies for FDI, it is expected that these will not be added to a system that will be controlled by QFT. The simplicity is a plus, but depending on the system, the benefits of FDI and FDD can greatly outweigh this plus.

Adaptive Control

A large number of studies, regarding adaptive control design used for FTC, have been made, because of the inherent properties of the adaptation theory. Different methods have been developed to achieve the desired adaptive properties. Papers describing some of them will be presented in the following section.

The study described in [Maybeck and Pogoda, 1989], [Maybeck and Stevens, 1991], and [Maybeck, 1999] is regarding the development of an improved multiple model approach for aircrafts. The two older articles use a multiple model adaptive controller, where seven controllers are made. A specific controller is used depending on the current state of the faults in the system. The faults and failures considered are single and double actuator and sensor faults/failures. In [Maybeck, 1999] the method is improved to a multiple model adaptive estimation. For detecting faults, a bank of Kalman filters is used, together with a blending of the output of the filters by using a probability-weighted average. If multiple failures occur, a hierarchy structure will be used to keep the number of used filters to a minimum. Based on the detected fault, the control uses a back end algorithm to redistribute control signals from failed control surfaces to non-failed control surfaces instead. The method is able to detect faults in less than a second based on tests on a precise aircraft model.
The problem with applying this control structure to the system available for this project is the lack of multiple actuators and sensors. The lack of redundant hardware makes the control algorithm not relevant. The fault detection method by using Kalman filter however might have potential.

The article [Tong et al., 2014] involves observer-based adaptive decentralised fuzzy FTC of a non-linear large-scale system with actuator failures. The faults and uncertainties considered are unmeasured states, unknown non-linear functions and actuator faults modelled as loss of effectiveness. The control design method is done by combining a backstepping technique with the non-linear tolerant-fault control theory. The simulated system used for testing is a model of two inverted pendulums connected by a spring. The existing adaptive decentralised control approaches made prior to this study are able to control the same system, however, only if no actuator faults occurs, which is where this approach is superior. The future work proposed is to simplify the design. Other studies using similar methods have been made for hydraulic sys-

tems. Because of this, this study will not be investigated further.

The studies [Yao et al., 2000] [Bu and Yuo, 2001], [Yao et al., 2001], [Bu and Yao, 2001], [Yao and Palmer, 2002], [Mohanty and Yao, 2006], and [Mohanty and Yao, 2011] investigates the use of Adaptive Robust Controller (ARC) for hydraulic systems with uncertain parameters, hard to model non-linearities, and disturbances. These includes parameters such as bulk modulus, leakage and friction forces. For testing and examples, a three degree of freedom robot has been used. The most recent study [Mohanty and Yao, 2011] proposes to use indirect ARC, (IARC), which is able to separate parameter estimation and control law. By doing this, the parameter estimation from the previous studies has been improved regarding estimation time. The reason for this, is the separation allowed the use of a better method than a gradient approach. A requirement for the proposed algorithm is a known range on the parameters investigated and a adaptation range. The resulting IARC is shown to be superior to both industrial controllers, and the ARC and direct ARC, (DARC), used in the previous studies. The test for the comparison of IARC and DARC consisted of moving a load of 22.7 kg in a swinging motion, where seven parameters were estimated by the algorithm. The IARC was able to estimate the parameters in 1.5-10 seconds, depending on the parameter.

The article [Balle et al., 1998] investigates FTC for heat-exchanger. The proposed control method is based on the fuzzy model type Takagi-Sugeno, together with a FDT based on self-organising fuzzy structure. The control algorithm is a non-linear model adaptive predictive controller. The faults considered were faults in sensors, namely the temperature (can detect 2 $^{\circ}C$ errors and higher - the nominal temperature in the system is approximately 30-50 $^{\circ}C$), fan speed (can detect faults larger than 15 %), and flow rate sensors (can detect higher than 2 m^3/h - flow rates in system are 3-8 m^3/h)). Based on experimental tests on a thermal plant, the fault detection was working for most cases which resulted in the controller being able to compensate for it. There was however a problem distinguishing between a fault on the fan speed sensor and flow rate sensor.

The articles [Tao et al., 2002] and [Tao et al., 2001] are regarding systems with unknown parameters and in the presence of unknown actuator faults. The base plant considered is an LTI plant. The method used for controller design is an effective output feedback controller structure for the actuator failure compensation. The new feature in [Tao et al., 2002] is a stable adaptive law to derive parameter adaptation in the presence of parameter uncertainties, which gives more relaxed conditions. The controller proposed in [Tao et al., 2002] is tested on a Boing 747 model. Actuator failures were considered and in order to emulate them a controller value would be stuck at a specific number. First one controllers output was stuck at 50% , and then later a second controller stuck at -100%, leaving only one controller working. A failure regarding stuck actuators was also tested, where instead of having the controller 1 and 2 go close to zero, be stuck at a specific value used at a specific time. A combination of the two was also tested. The results showed that the controller worked as intended and was able to compensate for the failures.

[Bošković, 2014] develops a new decentralised retrofit adaptive fault tolerant control design for non-linear models in flight control. The proposed controller is designed to accommodate

loss of effectiveness failures in flight control actuators, and achieve accurate estimation of failure related parameters. The control design is based on local estimation of loss of effectiveness parameters and to generate local retrofit control signals to accommodate the failures. Simulations are made of a F/A-18 aircraft under the actuator fault mentioned. The proposed controller is compared to a fully centralised design and a decentralised estimation with centralised control. The fault that was tested was the variation of three actuator gains from a normalised value of 1 to 0.01. The proposed controller had a significantly superior parameter estimation, however with a slightly worse tracking performance compared to the decentralised estimation and centralised control. Future work proposed is extending it to handle sensor faults and structural damage.

The study [Yao et al., 2014] is regarding internal leakage for a single-rod hydraulic actuator. The article proposed two controllers, one for the nominal system with small faults, and a FTC for the severe faults. The controller designed is based on parameter adaptive methodology, with a learning mechanism. For the system investigated in the article the learning mechanism only has one uncertain parameter, internal leakage. The designed controller is simulated on a double-rod hydraulic actuator model. The internal leakage faults tested were abrupt and incipient cases with a leakage parameter corresponding to an increase of 50 to 200% of the nominal leakage (calculated under the assumption the load pressure is equal to supply pressure), which was detected in 6 seconds and compensated for a few seconds later. An issue with this method is the lack of friction related faults and only considering one uncertain parameter.

The article [Yin et al., 2014] investigates an integrated design of FTC systems with application to Tennessee Eastman (TE) benchmark. The proposed fault-tolerant architecture is a data driven design whose core is an observer/residual generator based realisation of the Youla-parametrisation of all stabilisation controllers. The FTC is then achieved by an adaptive residual generator for the on-line identification of the fault diagnosis relevant vectors, and an gradient based optimisation approach for the on-line configuration of the parameter matrix. The benefits of the proposed design is a fault tolerant architecture that can be reconfigured on-line, together with the on-line calculation cost reduced to minimal. The faults considered were actuator faults, process faults and sensor faults. The performance and effectiveness of the proposed schemes has been demonstrated by using the TE benchmark model. The FTC was compared to a standard PI controller, which showed that the FTC was superior to the PI controller when faults occurred. They reduced the variance in the control signal from 0.1387 to 0.0020 by using the proposed FTC. The control signals are applied to valves, so by decreasing the frequency and chattering, the valves life-time would also increase.

[Wise et al., 1999] proposes a direct adaptive reconfigurable flight control approach. The reconfigurable control law is based on a dynamic inversion controller in an explicit model following architecture. An on-line neural network is used to adaptively regulate the error between the desired response model and the actual vehicle response. An on-line control allocation scheme generates individual control selector commands to yield the moments commanded by the controller, while prioritising critical axis and optimizing performance objectives such as manoeuvre load alleviation. An on-line system identification module generates estimates of the vehi-

cle's stability and control derivatives for use in control allocation and command limiting. The reconfigurable control laws are demonstrated by comparing their performance to a dynamic inversion control law when unknown failure/damage are induced. The comparison is made using simulations, where the proposed controller was able to cope with class 1 failures/damage very well, and was satisfactory for class 2. Some issues were present, however including the pilot as a control aid was suggested as a way to improve the conditions. Furthermore, including an FDI to locate the faulty components was found to improve performance. Proposed future work is testing it experimentally.

The study [Bodson and Groszkiewicz, 1997] compares three adaptive algorithms for a multi variable model reference control. The controllers compared are: Indirect adaptive control, direct adaptive control (both input- and output error direct), and least-squares adaptation algorithm. The indirect algorithm required 45 parameters versus the 27 required for input error direct method for the specific application. This is considered a handicap for identification matrices. The output error direct method, also required 45 parameters, but it has a more rigid stability conditions than the other two. A proposed least-square adaptation method can only be used with the indirect and input error direct algorithms. The usage of least square algorithm results in a faster convergence, furthermore, a new algorithm for this has been tested where a forgetting term is added. For the design, all states are assumed measurable. The faults considered in design and simulations are actuator failure or surface damage (size not mentioned). Based on simulations on a full non-linear model of a twin-engine jet aircraft, the input error direct algorithm with the new proposed least-squares algorithm is found preferable. The article did not consider noise, input saturation or the implementation of the algorithm to systems where some of the states are not available for measurement.

[Plummer and Vaughan, 1996] proposes an adaptive control based on pole placement for electro-hydraulic positioning systems. For the design, a linearisation of the system is required. The method is considered indirect and uses a strategy to switch off adaptation if the trace of the covariance matrix becomes too large. System identification is done off-line to determine the plant model structure and reduce the number of parameters adapted on-line and to obtain initial estimates and variances for controller start-up. Faults tested include a change in supply pressure from 160 to 40 bar and vice-versa. Dead oil was introduced into the circuit reducing the natural frequency equivalent to an increased load mass, a reverse of this is also made, where external oil is initially there and then removed. From these tests, the adaptation happens rapidly and is able to compensate the fault.

[Yang and Ye, 2006] investigates FTC for linear time-invariant systems. The proposed control is based on adaptive H_∞ design. The new indirect adaptive FTC design method is made via state feedback and is presented for actuator fault compensations. The design is developed in the framework of linear matrix inequality approach. A comparison between the proposed controller and a fixed gain version was tested on a nominal system and a system with an outage on the first actuator. From the simulations, the proposed adaptive H_∞ has better performance in both situations and has more relaxed conditions than the standard H_∞ design with a fixed gain.

The article [Chen et al., 2016] investigates FTC for an ocean surface vehicle. The faults considered on the system are parameter uncertainties and unknown disturbances. The method used for the adaptive tracking control design is backstepping technique and a Lyapunov synthesis method. The initial development is incorporating the actuator configuration matrix and then considering actuator saturation gains. The result is a method similar to the standard backstepping design, but with an auxiliary system added to handle saturations and faults in actuators. For testing the controller, a simulation is made on a model based on a 1:70 scaled supply vessel, called Cybership 1. The firsts steps include a disturbance applied to the ship in the form of wave currents, which tests the systems ability to compensate for a changing system. A comparison of a FTC design with and without adaptation is made, where the controller with adaptation was found superior. Another test is made to test the fault tolerance, where an actuator is set to fail at 120 seconds. Given the systems conditions of having only two out of three controllers working, and therefore reaching saturation, it nonetheless met satisfactory performances.

The studies [Jin, 2015] and [Jin, 2016] analyses FTC for MIMO non-linear systems, which are tested as a simulation for a model of a two degree of freedom robotic manipulator. The brief review here will be based on [Jin, 2016] due to it being a continued work of [Jin, 2015]. The faults considered in the design are both multiplicative and additive actuator faults. The input constraints can be asymmetric, and state constraints can be time-varying. To handle state constraints, a Barrier Lyapunov function (BLF) is used, and for analysis of input constraints an auxiliary system is used. For the control design, a backstepping approach is used together with BLF and auxiliary system. The proposed controller is simulated under different scenarios of actuator faults, both multiplicative and additive. The results shown are the systems ability to estimate the faults and ability to be within the constraints while following the reference.

[Gao et al., 2015] is regarding FTC for feedback linearisable systems. The system used for testing is a pendulum and an air-breathing hypersonic vehicle, where actuator faults will be considered. The controller is a robust controller with applied adaptive terms to relax the need for precision of several parameters in the actuator faults. Furthermore, a chattering free FTC law is designed, which showed good performance for restricting the parameter estimation drifting. For the simulation of the pendulum, the system was tested with an 0.85 efficiency of the actuator, and 100 tests were conducted using a Monte Carlo simulation with random actuator efficiencies in the range from 0.5 to 1. A comparison between using and not using the chattering free control law, showed that while the tracking performance is similar, the chattering of the control input was reduced as intended.
The aircraft simulation was conducted with the following efficiencies: Actuator one 0.74, actuator two 0.71, together with an uncontrollable action parameters of 2.57(bounds of parameter defined as [0,3]) and 0.13(bounds [0,0.2]) for actuator one and two respectively. Under these conditions, the nominal controller was not able to maintain the tracking performance of the velocity. Furthermore, a 100 simulations were made with a randomly varying efficiency and uncontrollability, with efficiency of 0.7-1.0 and uncontrollability parameters of 0-3 and 0-0.2. Based on these, the proposed control law was shown to have good tracking performance, and it was suggested to use the chattering free version.

[Zhou et al., 2014] investigates FTC for non-affine non-linear systems. A model approximation method is developed to bridge the gap between affine and non-affine control systems. As a basis for the adaptive FTC, a joint estimation approach based on unscented Kalman filter is used, which estimates both failure parameters and states simultaneously by using the argument state vector composed of the unknown faults and states. To show the performance of the proposed controller, a simulation of a 3 degree of freedom fighter aircraft is utilised. The fault tested is a change in thrust efficiency going from 1 to 0.2 in 20 seconds and rising back to 1 in 20 seconds. The reference speed is set to 300 m/s. By using the nominal controller, an error up to approximately 30 m/s is obtained, but with the fault tolerant controller, the error is not visible. Furthermore, the fault estimation of the FTC is able to converge to the true fault value.

The article [Wu and Yang, 2015] looks into FTC for linear systems with mismatched parameter uncertainties, external disturbances, multiple time-delays state perturbations, and actuator faults. The upper bound of the perturbations, uncertainties and disturbances are assumed to be unknown. The proposed FTC design is an adaptive robust tracking controller. To test the proposed controller, a model of a B747 is used. A simulation was made, where the third actuator failed after 6 seconds, and the first actuator had a 20 % loss in efficiency, furthermore an unknown disturbance is applied for the full test (sinus wave function, no specific frequency or amplitude mentioned). From the tests, the system was able to estimate the parameters and its ability to keep the tracking error at minimal. It was compared to a non FTC, which did not work well when faults were introduced.

The study [Ahmed-Zaid et al., 1991] looks into FTC for a F-16 fighter with surface or hardware failure. The proposed controller is designed with a hybrid adaptive linear quadratic control scheme. For the design, a reduced order model is utilised, however, it should match the full-order model for the frequency range of interest. For the simulations, a failure on the pitch control channel was tested by applying a 100 times higher dynamic pressure as input to the gain scheduling blocks. The proposed controller was compared to a standard non-FTC controller, where the proposed controller was found superior. The other faults and failures tested were: Failure in the horizontal stabilizer, and bank-to-bank reversal attempts using lateral stick commands with stabiliser failure. From these, the proposed FTC is found superior, and is able to better cope with the failures applied.

Sliding mode control

Sliding Mode theory has received a lot research attention, due to its relatively simple design and implementation and highly robust properties making it a good candidate for FTC applications. Application using sliding mode controllers or observers are presented here.

In [Kim et al., 2001] the authors have developed an integral sliding mode controller for a combustion engine. The article utilises the integrated term of the controller to determine and isolate faults and then uses observers with fault hypothesis to isolate the fault. One hypotesis is that there is a sensor fault, while the other is that there is an actuator fault. The different fault produce different residuals, which allows the authors to distinguish between them. A valida-

tion simulation has been performed in the article, where a valve fault is introduced, increasing the output of the valve by 15 %, at the 38 engine cycle. Within 2 cycles the fault is accommodated. Also a sensor fault is introduced at the same time, but the controller does not drift with the sensor fault and the result remain within the desired values. The design appears to be a valid approach with the possibility of detecting and accommodating actuator and sensors faults. Even though the system discussed in the article is not a hydraulic cylinder there are similarities to the task of this project and the method proposed is deemed relevant.

There are multiple works devoted to sliding mode control in the aviation industry. In [Shtessel et al., 2002] a tailless fighter jet is considered. The plant is linearised and abrupt faults are considered. Both actuator fault and control surface loss is presented as augmentations of the input matrix in a state space representation. Then the triple loop continuous SMC designed in this work is shown to be stable under loss of 30 % of a left elevator area and 50 % of a pitch flap by tracking a manoeuvre reference with little to no error. The boundary layer preventing chatter in the control signal is continuously adjusted by the most inner loop of the controller. The multiple level controller in this article is very complex and requires an over-actuated system due to the nature of flight control systems. With the most outer loop of the controller allocating control effort to the actuators it is possible to accommodate the major faults tested in the article, but the task this project aims to solve will probably not require this level of complicated control and furthermore will not have redundant actuators.

In [Hess and Wells, 2003] the SMC method is applied to an F-18 aeroplane with a focus on the methods sensitivity to neglected high order dynamics. Where the previous study varied the boundary layer, this one proposes the use of an asymptotic observer to reject the chatter in the control signal. The article claims that such an observer "serves as a high frequency bypass loop in the SMC system". The fault tested in the article is an abrupt 50 % loss of stabilator. The authors show they have achieved better performance with the SMC method than with a classical controller synthesised through loop shaping. Furthermore they claim that the asymptotic observer can reduce the sensitivity to high order dynamics and structural modes neglected in modelling, thus reducing some of the minuses of sliding mode controllers.

In the study [Zhao et al., 2014a] an adaptive sliding mode scheme has been proposed, for both fault identification and fault-tolerant control of near space vehicles. For determining fault parameters, an adaptive observer design is used, which is found to accurately estimate the parameters on-line. The adaptive sliding mode controller is able to work for both actuator dynamic faults and control effector damage. The proposed controller and observer have been tested in simulations, where different faults are tested. The result is that the controller is able to compensate for the faults tested. A saturation of the switching algorithm, within certain bound around zero error, has been selected as a method for removing the chattering action normally exhibited by SMC.

A more mathematical approach was taken in [Liu et al., 2011], where instead of a specific system the authors treat non-linear Markovian jump systems with time delays. The article uses an augmented sliding mode observer called proportional and derivative sliding mode observer to

accurately estimate both system states and sensor faults. Then they implement an observer based feedback controller and prove stability by Lyapunov-like analysis. Simulation results have been omitted from the article due to space issues, but the authors claim that the method has been verified and has been able to stabilise the CL system. Furthermore the method only deals with sensor faults. While a valid approach for sensor faults a different control should be considered to deal with actuator faults as well.

Such a method is proposed in [Patton et al., 2010], where a sliding mode observer is combined with a sliding mode controller in order to deal with abrupt actuator faults. The authors propose the use of this method to deal with the hard to model friction effect such as Stribeck effect and Coulomb friction. The system under consideration was an inverted pendulum with a DC motor for actuation of the sled. The authors of the article claim that the proposed methods are less complex, than constructing accurate friction models, while still being able to deal with the problem. Laboratory test show that the method is viable and shows promising results. The article proposes further study of this method on a non-linear system.

[Zhao et al., 2014b] investigates adaptive sliding mode for a linearised aircraft model. The fault considered on the aircraft is structural damage at the vertical tail damage or loss, and has also considered outer disturbances. For the controller to work at a given drop in system efficiency, the system has to have compensated from the error within 50 seconds. From the simulations, the system was tested with a range of efficiency losses in the range of 0-0.6, where the system was able to compensate for the error within 50 seconds for efficiency losses of up to 0.5. For future work, an increase in the amount of efficiency loss that can be compensated for is desired.

The article [Moradi and Fekih, 2014] is regarding FTC for a full-scale car suspension. The proposed control is an adaptive PID for each wheel subsystem, where a tracking signal is made from a sliding mode controller to each of the subsystems to mitigate the 3 degree of freedom arising from road undulations. The proposed controller is tested on a full-scale vehicle dynamic model with active suspension system with 7 degrees of freedom. The faults considered are actuator faults and uncertainties. To test the uncertainties, 20 % uncertainty was added to 18 parameters, and a 1 % uncertainty to tire stiffness. From this test, the system was able to handle the system with only slightly less tracking performance than for a nominal model. For faults, a test for each of the wheel subsystem was made where one received zero control signal. Further tests were made were a varying efficiency was applied to the actuators. The result from these tests were that the proposed controller was found superior to those used in previous studies. For further studies, the use of observers instead of measuring states is desired.

Linear Parameter Variation

The study [Sloth et al., 2011] investigates FTC for wind turbines. The method used is Linear Parameter Variation (LPV), where different design strategies are compared. The strategies used are active, passive, and nominal. Furthermore, a robust controller is designed. For the optimisation problem involved in the passive and robust controllers, bilinear matrix inequalities are solved instead of linear matrix inequalities due to unmeasured parameter variations. For

comparing the controllers, a non-linear simulation model of a wind turbine is used. A nominal and a faulty case were simulated, with the fault being a low pressure in the pitch system. From this, the robust controller and nominal controller showed similar performance, however, both had a greater loss in performance, when a fault was introduced, with robust being the better here. For the faulty case, the active showed a better performance than the passive, and it was also easier to solve the optimisation algorithms for the active. However, the active does require having fault diagnosis.

[Shin et al., 2002] investigates FTC for aircraft with actuator failures, which are assumed to fail one at a time in the study. The proposed controller is a LPV controller based on LMI optimisations, which are based on estimated failure parameter with pre-defined estimation error bounds. The conservatism of LPV control synthesis methodology is reduced by using a scaling factor on the uncertainty block, which represents the estimated parameter uncertainties. The estimations are done using a Kalman filter. For testing of the proposed controller, a comparison to a H_∞ controller is made. The actuator fault considered is having the performance parameter at the following values at different times: [1, 0.01, 1, 2], where 1 corresponds to the nominal case. The simulations shows that the proposed controller is superior to the H_∞ design and able to cope with the faults satisfactory.

[Ganguli et al., 2002] proposes a FTC for a Boeing 747. The proposed controller design is an LPV using a quasi-LPV model based on Jacobian linearisation approach. The controller uses three signals, two measured and a fault identification signal from an FDI module. The actuator faults considered in the simulations are lock-in-place and float (the control signal is floating around zero, thus becoming ineffective). It is assumed that an FDI is able to detect the faults immediately, and send a signal to the controller. From these tests, the controller was able to maintain stability and desired tracking and good disturbance rejection, but the immediate detection and diagnosis assumption can be a possible problem for the implementation of this method.

Intelligent Systems

[Sami and Patton, 2013] investigates a strategy for fault tolerant tracking control (FTTC) based on robust fault estimation and compensation of simultaneous actuator and sensor faults, which have a bounded first time derivative. The contribution from this study is a new architecture based on a combination of actuator and sensor Takagi-Sugeno proportional state estimators augmented with proportional and integral feedback fault estimators together with a Takagi-Sugeno dynamic output feedback control capable of time-varying reference tracking. The requirement for this method is that the non-linear system can be modelled in Takagi-Sugeno fuzzy inference form.

[Diao and Passino, 2001] investigates FTC for a turbine engine. They use a hierarchical learning structure in the form of Takagi-Sugeno fuzzy systems. Based on this, a FTC scheme is designed based on stable adaptive fuzzy/neural control, where the learning capabilities capture unknown dynamics caused by faults. The designed controller is tested as both indirect and

direct adaptive control case. Based on simulations on a component level model simulation of a turbine engine. The faults tested were having an initial engine variation of -0.3 % to 0.2 % together with an engine deterioration of 10 %. The results showed that both could compensate for the fault as they learned over time, with the direct case resulting in more oscillations compared to the indirect case. The same authors also utilised this method for the adaptive estimation based on neural networks in their article [Diao and Passino, 2002], which also dealt with FTC. The systems considered are input-output feedback linearisable time-varying nonlinear systems. The fault tolerance was improved by using a multiple model structure of expert supervisory schemes to do the fault-diagnosis.
The proposed control algorithm is tested on a precise model of a jet engine.The faults tested were a deterioration of the engine and initial engine variation, from -0.5 % to 0.5 %, another fault tested is an abrupt large compressor hub fault. The results showed the control algorithm was able to learn and obtain an improving performance over time.

[Zhang et al., 2004] proposes a way to unify the methodology for detecting, isolating and accommodating faults in a class of non-linear dynamic systems. Three controllers are proposes, one for the nominal system, one during fault detection and one during fault isolation. An adaptive tracking design is proposed, which uses neural networks to approximate the unknown fault function. It is enhanced by the use of adaptive bounding design technique. The proposed methodology is tested as a simulation using two tanks with fluid flow. The faults simulated are abrupt, and specifically leakage in tank 1 (modelled as an orifice with 0.01 m radius circular shape) and model uncertainties (bound of $5{\cdot}10^{-5}/\mathrm{A}_s$). The two tanks are identical with a cross section of 0.0154 m^2, and a water level of 0.2333 m is desired. A comparison between the proposed controller and the proposed controller not using FDI was made, and the results showed the controller, using FDI information, was superior to a system not using FDI information. The future work proposed is to extend the design to a larger class of non-linear systems and fault, together with cases were not all state variables are available for measurements, which is a current requirement.

[Farrell et al., 1993] investigate the possibility of applying FTC that can accommodate unanticipated unspecified faults to a water vehicle. Improvement was noticed in the performance of the vehicle with each completion of the prespecified trajectory. The error of 6 degrees in the heading of the vehicle, which was present on the first pass, was reduced to nearly 0.5 within 9 passes of the trajectory. This kind of training requires the vehicle to always be operating under the same conditions, which was considered insufficient in the study, so another test was conducted. A number of training phases, consisting of a 1000 second each was performed. The trajectory was randomly varying between runs in all degrees of freedom. After each training phase a helical benchmark trajectory was tested. After 5.6 hours of learning the variance of the estimation error was decreased by a factor of 10 in some degree of freedom. The article concludes that a constraint of 4 inputs per mapping is the reason for the reduced improvement in the other degrees of freedom. The article concludes that by assuming a more general form for the post-fault system model a learning algorithm will take longer estimate the error but will be able to learn and accommodate a greater number of faults.

[Reveliotis and Kokar, 1995] presents a learning framework, which is able to "learn" local models and recognise that a change in these models behaviour has occurred and finally control the plant on which it is applied. Once it establishes a model the framework would store it in a data base, meaning if the plant deviates from the behaviour of the current model a new one is learned, but if it returns to a certain behaviour the stored model is used. The system under consideration was a mass-spring system. Part of the range of motion of the mass in an air environment and part was in a liquid environment, thus the damping in the system changed abruptly. The article shows that the learning controller performed better than a standard PID controller, which was designed for the liquid environment. The article further investigates the limitations of the framework associated with noise in the measurement.